Permittivity Measurement of Biological Tissues and Open-ended Coaxial Probe Measurement Method Analysis

Matković, Anđela

Doctoral thesis / Disertacija

2024

UNIVERSITY OF SPLIT
FACULTY OF ELECTRICAL ENGINEERING, MECHANICAL ENGINEERING
AND NAVAL ARCHITECTURE

Anđela Matković

PERMITTIVITY MEASUREMENT OF BIOLOGICAL TISSUES AND OPEN-ENDED COAXIAL PROBE MEASUREMENT METHOD ANALYSIS

DOCTORAL THESIS

Split, 2024.

UNIVERSITY OF SPLIT
FACULTY OF ELECTRICAL ENGINEERING, MECHANICAL ENGINEERING
AND NAVAL ARCHITECTURE

Anđela Matković

Permittivity Measurement of Biological Tissues and Open-ended Coaxial Probe Measurement Method Analysis

DOCTORAL THESIS

Split, 2024.

The research reported in this thesis was carried out at the Department of Electronics and Computing, University of Split, Faculty of Electrical Engineering, Mechanical Engineering and Naval Architecture.

Supervisor: prof. dr. sc. Antonio Šarolić, FESB, University of Split, Croatia
Dissertation number: 199

BIBLIOGRAPHIC INFORMATION

Keywords: dielectric permittivity measurement, open-ended coaxial probe, electromagnetic modeling and simulation, microwave frequency range, biological tissue, brain tissue Cole–Cole models, human and animal ex vivo measurements, permittivity preservation
Scientific area: Technical sciences
Scientific field: Electrical engineering
Scientific branch: Electronics
Institution of PhD completion: FESB, University of Split, Split, Croatia
Supervisor of the thesis: prof. dr.sc. Antonio Šarolić
Number of pages: 165
Number of figures: 19
Number of tables: 6
Number of references: 94

Committee for assessment of doctoral dissertation:

1. Prof. dr. sc. Ivan Marinović, University of Split, FESB
2. Prof. emer. dr. sc. Vesna Roje, University of Split, FESB
3. Assoc. prof. dr. sc. Maja Škiljo, University of Split, FESB
4. Prof. dr. sc. Davor Bonefačić, University of Zagreb, FER
5. Asst. prof. dr. sc. Raquel Cruz Conceição, University of Lisbon, IBEB

Committee for defense of doctoral dissertation:

1. Prof. dr. sc. Ivan Marinović, University of Split, FESB
2. Prof. dr. sc. Zoran Blažević, University of Split, FESB
3. Assoc. prof. dr. sc. Maja Škiljo, University of Split, FESB
4. Prof. dr. sc. Davor Bonefačić, University of Zagreb, FER
5. Asst. prof. dr. sc. Raquel Cruz Conceição, University of Lisbon, IBEB

Dissertation defended on: 24.6.2024.

Permittivity Measurement of Biological Tissues and Open-ended Coaxial Probe Measurement Method Analysis

Abstract:

This doctoral thesis presents the studies of the open-ended coaxial probe permittivity measurement method, with the emphasis on its application to biological tissues in the microwave frequency range. A measurement study was conducted on human, bovine, and porcine ex vivo samples, resulting in Cole–Cole permittivity models of the measured brain tissues for each species. The study also revealed intra- and interspecies variations and the impact of tissue degradation. The study on tissue permittivity preservation investigated the effect of freezing and thawing on the permittivity of bovine tissues, including brain tissues, muscle, and liver. The statistical significance of the permittivity change due to a freeze-thaw cycle was dependent on the frequency range and the tissue investigated. Due to the observed complexity of measurement of biological tissue permittivity and preservation thereof, a comprehensive model was developed to enable the analysis of the entire measurement process. This encompassed computer electromagnetic modeling, simulations, and postprocessing calculations using a simple capacitive-load model which was validated by measurements. The entire model produced negligible errors and, despite minor deficiencies at lower frequencies, the simulations yielded accurate results, especially for physiological saline, which approximates high water content biological materials. The outcomes of these studies enhance the existing knowledge on dielectric properties of biological tissues, particularly human brain tissues, and provide valuable insights into the open-ended coaxial probe measurement method.

Keywords:
dielectric permittivity measurement, open-ended coaxial probe, electromagnetic modeling and simulation, microwave frequency range, biological tissue, brain tissue Cole–Cole models, human and animal ex vivo measurements, permittivity preservation

Mjerenje permitivnosti bioloških tkiva i analiza metode mjerenja koaksijalnom sondom s otvorenim krajem

Sažetak:

Ovaj doktorski rad objedinjuje studije o metodi mjerenja permitivnosti koaksijalnom sondom s otvorenim krajem, s naglaskom na njenu primjenu na biološka tkiva u mikrovalnom frekvencijskom području. Mjerna studija provedena je na ex vivo uzorcima ljudskog goveđeg i svinjskog tkiva, što je rezultiralo razvojem Cole–Cole modela permitivnosti izmjerenih tkiva mozga za svaku vrstu pojedinačno. Studija je također ukazala na varijacije permitivnosti unutar i između vrsta te utjecaj propadanja tkiva na permitivnost. Studija o očuvanju permitivnosti tkiva istraživala je utjecaj procesa smrzavanja i odmrzavanja na permitivnost goveđih tkiva, što je uključivalo tkiva mozga, mišić i jetru. Statistička značajnost promjene permitivnosti zbog ciklusa smrzavanja i odmrzavanja ovisila je o frekvencijskom rasponu i ispitivanom tkivu. Zbog uočene složenosti mjerenja permitivnosti bioloških tkiva i njenog očuvanja, razvijen je opsežan model koji omogućuje analizu cjelokupnog mjernog procesa. On obuhvaća računalno elektromagnetsko modeliranje, simulacije i naknadne izračune korištenjem jednostavnog kapacitivnog modela koji je potvrđen mjerenjima. Cjeloviti model je rezultirao zanemarivim pogreškama i, unatoč manjim nedostacima na nižim frekvencijama, simulacije su dale točne rezultate, ponajviše za fiziološku otopinu, čija permitivnost je približna permitivnosti bioloških materijala s visokim sadržajem vode. Rezultati ovih studija unapređuju postojeće znanje o dielektričnim svojstvima bioloških tkiva, posebice tkiva ljudskog mozga, i pružaju važne spoznaje o metodi mjerenja koaksijalnom sondom s otvorenim krajem.

Ključne riječi:
mjerenje dielektrične permitivnosti, koaksijalna sonda s otvorenim krajem, elektromagnetsko modeliranje i simulacije, mikrovalno frekvencijsko područje, biološko tkivo, Cole–Cole modeli tkiva mozga, ex vivo mjerenja ljudskih i životinjskih uzoraka, očuvanje permitivnosti

I would like to express my gratitude to my supervisor Antonio Šarolić
for his guidance and mentorship. I appreciate the time and effort invested in me.
I am grateful to my family and friends for always being by my side.
And a very special thank you to my other half for all his love and support.

Contents

Abstract iv
Sažetak v
Contents viii
List of Tables x
List of Figures xi
List of Acronyms and Symbols xiii

1. INTRODUCTION 1

- 1.1. Motivation, Objectives and Hypotheses 1
- 1.2. Scientific Methods and Contributions 4
  - 1.2.1. Measurement Experiments 5
  - 1.2.2. Computer Simulations 7
- 1.3. Published Papers 8
- 1.4. Outline 8

2. DIELECTRIC THEORY, CHARACTERIZATION AND MEASUREMENTS 10

- 2.1. Dielectric Materials 10
- 2.2. Dielectric Relaxations 14
  - 2.2.1. Dielectric Relaxation Models 15
  - 2.2.2. Dielectric Polarization Mechanisms 16
  - 2.2.3. Relaxation Regions in Biological Tissue 18
- 2.3. Dielectric Measurement Methods 20
  - 2.3.1. Transmission Methods 20
  - 2.3.2. Free Space Methods 21
  - 2.3.3. Resonant Methods 22
  - 2.3.4. Open-Ended Coaxial Probe Method 22

3. PERMITTIVITY OF BIOLOGICAL TISSUES 24

- 3.1. References for Permittivity of Biological Tissues 24
- 3.2. Dielectric Properties of Brain Tissues 26
- 3.3. Preservation of Permittivity of Biological Tissues 34

4. MODELING OF THE OECP MEASUREMENT METHOD 40

- 4.1. Microwave Measurements 40
- 4.2. Equivalent circuit model of an OECP 43

4.3. Computer Electromagnetic Modeling and Simulation 50
  4.3.1. FEKO 51
  4.3.2. CST 52
  4.3.3. Modeling, Simulation and Validation of the Complete Measurement Process. 53

5. SCIENTIFIC CONTRIBUTIONS OF PUBLICATIONS 62

5.1. Publication 1: Complex Permittivity of Ex-Vivo Human, Bovine and Porcine Brain Tissues in the Microwave Frequency Range 63
  5.1.1. Abstract 63
  5.1.2. Scientific Contributions 64
  5.1.3. Authors Contribution 64
  5.1.4. Supplementary Materials 64
5.2. Publication 2: The Effect of Freezing and Thawing on Complex Permittivity of Bovine Tissues 65
  5.2.1. Abstract 65
  5.2.2. Scientific Contributions 65
  5.2.3. Authors Contribution 66
5.3. Publication 3: Dielectric Permittivity Measurement Using Open-Ended Coaxial Probe—Modeling and Simulation Based on the Simple Capacitive-Load Model 66
  5.3.1. Abstract 66
  5.3.2. Scientific Contributions 67
  5.3.3. Authors Contribution 67

6. CONCLUSION 68

BIBLIOGRAPHY 70

APPENDIX A 77

APPENDIX B 102

APPENDIX C 115

List of Tables

Table 3.1. The number of measurement points on brain tissues per tissue and species type. *30*
Table 3.2. Single pole Cole–Cole parameters for measured brain tissues. *30*
Table 3.3. Average standard deviation for measured white matter, grey matter, and cerebellum of all brain samples. *33*
Table 4.1. Cole–Cole parameters of the analyzed saline solutions. *54*
Table 4.2. Calculated upper frequency limits given for common commercial coaxial probes. *61*
Table 5.1. CRediT roles and definitions. *62*

List of Figures

Figure 2.1. Complex permittivity in a complex plane. 13
Figure 2.2. Real and imaginary part of permittivity as a function of frequency. (Adapted from [33]) 13
Figure 2.3. Cole–Cole diagram. 16
Figure 2.4. Dielectric polarization mechanisms. (Adapted from [41]) 17
Figure 2.5. $\boldsymbol{\alpha}$*,* $\boldsymbol{\beta}$*,* $\boldsymbol{\gamma}$*, and* $\boldsymbol{\delta}$ *relaxation regions in biological tissue. (Adapted from [43])* 19
Figure 2.6. Free space measurement method in its a) transmission configuration and b) reflection configuration. 21
Figure 2.7. Examples of commercial open-ended coaxial probes: probes manufactured by Keysight [24] (top row) and probes manufactured by SPEAG [47] (bottom row). 23
Figure 3.1. Frequency dependent real and imaginary part of permittivity for cancellous bone [28]. 25
Figure 3.2. Grey matter permittivity comparison of averaged bovine brains (B), averaged human brains (H) and a porcine brain (P) as well as comparison with the published data from 31
Figure 3.3. Permittivity change in human grey matter for brain H1 on day 2 and day 3. 34
Figure 3.4. Measurement setup which includes the dish supported by polystyrene on top of a weight scale for the sample of bovine (a) brain white matter, (b) brain grey matter, (c) liver, and (d) muscle. 36
Figure 3.5. Percent change in ε' *and* ε'' *for bovine white matter before freezing below -18 °C in a commercial freezer and after thawing.* 37
Figure 3.6. Percent change in ε' *and* ε'' *for bovine white matter before freezing in liquid nitrogen and after thawing* 38
Figure 4.1. OECP represented as a general two-port network with incident (a_1 *and* a_2*) and reflected (*b_1 *and* b_2*) waves. Adapted from [77].* 41

Figure 4.2. OECP measurement setup with indicated Port 1 and Port 2 planes. ..42

Figure 4.3. ε' and ε'' results for 0.5 M saline obtained from the: measurement software (“measured”), postprocessing with simple capacitive-load model (“capacitive model”) and dispersion model (“Cole–Cole dispersion”). 55

Figure 4.4. ε' (top) and ε'' (bottom) relative error of the simple capacitive-load model with respect to the measurement result obtained from the measurement software, for water and saline solutions. 56

Figure 4.5. ε' (top) and ε'' (bottom) relative error of the simple capacitive-load model with respect to the set permittivity value. 59

Figure 4.6. Electric field lines in a coaxial cable operating in a) TEM mode b) TE_{11} mode. 61

List of Acronyms and Symbols

Acronyms

EM	electromagnetic
EMF	electromagnetic fields
FEM	finite element method
FIT	finite integration technique
MLFMM	multilevel fast multipole method
MoM	method of moments
MUT	material under test
MW	microwave
OECP	open-ended coaxial probe
SEP	surface equivalent principle
TE	transverse electric
TEM	transverse electromagnetic
TLM	transmission line matrix method
VEP	volume equivalent principle
VNA	vector network analyzer

Greek symbols

$\boldsymbol{\alpha}, \boldsymbol{\beta}, \boldsymbol{\gamma}, \boldsymbol{\delta}$	biological dispersion regions
α	exponent parameter representing the broadening of relaxation
β	exponent parameter representing the asymmetry of relaxation; phase constant
Γ	reflection coefficient
δ	loss angle
ε	complex permittivity
ε'	real part of the permittivity
ε''	imaginary part of the permittivity
ε_0	vacuum permittivity

ε_∞	infinite frequency permittivity
ε_r	complex relative permittivity
ε_s	static permittivity
η	intrinsic impedance of a medium
λ	wavelength
μ	complex permeability
μ_0	vacuum permeability
μ_r	complex relative permeability
σ	equivalent conductivity
σ_s	static conductivity
τ	relaxation time
χ	electric susceptibility
ω	angular frequency

Roman symbols

A_1, A_2 and A_3	calibration coefficients
a	radius of the outer conductor of a coaxial probe
B	susceptance
b	radius of the inner conductor of a coaxial probe
C	capacitance
c	saline concentration
D	electric flux density
E	electric field
f	frequency
f_rel	relaxation frequency
G	conductance
H	magnetic field strength
J	total current density
j	imaginary unit ($j^2 = -1$)
n	refractive index
P	dielectric polarization
S_{11}, S_{12}, S_{21}, and S_{22}	two-port network scattering parameters
t	temperature

V_+	incident voltage phasor
V_-	reflected voltage phasor
Y	admittance
Y_0	characteristic admittance
Z	impedance
Z_0	characteristic impedance

1. INTRODUCTION

This doctoral thesis aims to contribute to the existing body of knowledge about the dielectric spectroscopy of biological tissues using an open-ended coaxial probe as the chosen measurement method. The research presented herein is a compilation of three scientific papers published in renowned journals that have an impact factor greater than the median of journals within the research field. The thesis provides original scientific contributions in the scientific field of electrical engineering. The three publications are cohesive in their topic and relevant in the context of emerging biomedical applications and technologies. All findings are disclosed in published papers listed in Chapter 1.3. The introduction concludes with the outline of the subsequent chapters.

1.1. Motivation, Objectives and Hypotheses

Complex dielectric permittivity (hereafter: permittivity) is a physical property of a material whose real part describes the dielectric polarization (i.e., the ability of the material to store electrical energy), and the imaginary part describes losses in the material exposed to an electric field. As permittivity is a quantity that varies with frequency, the dielectric properties of a material should preferably be known in a wide frequency band.

Dielectric characterization of materials in the microwave (MW) frequency range is required for many existing applications and technologies as well as emerging technologies such as the next generation of wireless communications that require the extension of this knowledge to the millimeter frequency range. Knowledge of the dielectric properties of materials is needed and researched in the context of various industries: development of medical sensors [1], diagnostic and therapeutic medical procedures [2], dosimetry [3], food industry [4], construction industry [5], vegetation analysis [6], art evaluation [7], microwave remote sensing [8], soil bioremediation [9] and other industries.

Dielectric characterization of tissues can be utilized in a wide range of applications within the medical field, particularly in diagnostic and therapeutic applications. It provides valuable insights into the electrical properties of biological tissues, which can be indicative of their physiological and pathological states. Diagnostic applications include examples such as quantification of edema in brain tissues [10], assessment of burn depth [11], monitoring of skin healing processes [12], assessment of lymphedema [13], etc. One of the more recent diagnostic applications is the ability to distinguish healthy from malignant tissues based on their permittivity contrast. For some applications, such as the skin cancer diagnosis [14], it is possible to diagnose it completely non-invasively. It has been shown that tumor tissues display a larger real part of the permittivity due to a higher water content, so, in theory, it should be possible to distinguish tissues only according to their complex permittivity values as was already shown for dog tissues [15], human breast tissue [16], human colon tissue [17], and human liver tissue [18]. Conducting the differentiation process with the help of a dielectric probe is a faster and non-invasive alternative to the standard biopsy procedure. Furthermore, understanding the dielectric properties of tissues is essential for safe and effective application of electromagnetic fields (EMFs) in treatments such as hyperthermia and thermal ablation. Hyperthermia and thermal ablation are techniques that involve targeted tissue heating using radiofrequency and MW radiation. Hyperthermia involves exposing body tissues to temperatures in the range of 40–45 °C with the aim of destroying cancer cells or making them more sensitive to radiation and other antitumor agents [19]. In thermal ablation, the desired temperatures range from 50 °C to over 100 °C, resulting in cell death due to necrosis caused by thermal coagulation [20], [21]. It should be emphasized that permittivity varies with temperature, therefore it is crucial to understand how the tissue permittivity changes during the hyperthermia or thermal ablation procedure. Both procedures should be properly planned in order to maximize the heating of the target tissue while simultaneously protecting the surrounding healthy tissue from thermal damage. As tissue heating is primarily determined by the dielectric properties of the tissue, proper planning of the procedure requires the existence of an extensive database with the permittivity of all tissues.

Lastly, permittivity characterization of human tissues is also necessary for an accurate assessment of human exposure to electromagnetic fields in the context of the harmful effects of EMFs on the human body. The primary harmful effect in the MW frequency range is tissue heating caused by the absorbed electromagnetic energy [22], [23]. Considering that the absorbed electromagnetic energy is directly related to the dielectric properties of the exposed tissues, it is necessary to know the permittivity of various human tissues for which a dosimetry study is performed.

For a complete dielectric characterization of a material, which is required for the aforementioned applications, the permittivity should be measured and known in a wide frequency range. One of the most commonly used methods for measuring the permittivity of biological tissues is the open-ended coaxial probe (hereafter: OECP) measurement method. The OECP measurement method is a wide-band, non-destructive and non-invasive measurement method that is suitable for both ex vivo and in vivo measurements. It consists of a coaxial transmission line that is terminated with an open end. The electromagnetic wave propagates along the line and is reflected, partially or completely, when it encounters a mismatch between the open end of the probe and the material in contact with the open end of the probe. The reflected wave is measured at different frequencies and postprocessed to obtain the permittivity as the final desired result. The advantage of this method is its simplicity because it requires minimal handling of the sample and its preparation. In recent years, most research has been done with commercial probe kits. A common commercial probe for measuring biological samples is the Keysight Slim Form Probe [24]. It is a frequent choice of researchers due to its small diameter making it suitable for smaller tissue samples and because it can be autoclaved and therefore used in vivo [25]. Even though numerous studies were made with the OECP, there are still challenges that arise during measurements [25]. Some artefacts in the measurement results as a consequence of unwanted physical phenomena are still unsolved. They affect the accuracy and frequency range of the coaxial probe, and thus limit its wider application. Some of these limitations arise from the probe itself, such as the limitation of the measured volume, while some limitations are related to the peculiarities of measuring biological samples, such as sample heterogeneity and probe pressure with regard to the tissue consistency. A better understanding of the limitations of the probe, which arise precisely from insufficiently researched physical phenomena, will enable more precise and reliable measurements.

Due to all of the above, the motivation of this doctoral thesis is twofold: the first objective is to enhance the current knowledge of the permittivity of biological tissues by publishing the results of the systematic measurement experiments, and the second goal is to analyze and model the OECP measurement method along with the physical phenomena that affect the accuracy of the measurements, and consequently the frequency range of the probe, which is limited precisely by the deterioration of accuracy at both ends of the frequency range.

The first hypothesis of this thesis is that none of the references for tissue permittivity can be considered as absolutely accurate data. While these references serve as valuable sources, it is essential to recognize their inherent limitations. The complexity of measuring the dielectric properties of biological tissues, coupled with the intraspecies and interspecies variations, contributes to the uncertainty associated with the measured permittivity values. The difference may arise due to the natural variability in the tissue composition and physiological processes occurring in the tissue. Notably, age and health status of tissue donors play a role, but additional considerations extend to post-excision handling procedures. Following the tissue excision, a dynamic process unfolds: continuous dehydration and decay which alter the dielectric properties of tissue. Consequently, efforts to minimize these alterations are crucial for the accurate assessment. The aforementioned points suggest that citing permittivity data from any reference should be done with caution. Moreover, it is necessary to determine the possible variability of the measured permittivity results for various tissues through a systematic analysis. As a part of this thesis, the possibility of long-term preservation of ex vivo tissue permittivity will be examined. In summary, the research behind this hypothesis underscores the need for rigorous methodologies, standardized protocols, and an awareness of the intricacies involved in tissue permittivity measurements which should contribute to the advancement of the bioelectromagnetic research and the potential clinical applications.

The second hypothesis explored in this thesis pertains to the feasibility of constructing a comprehensive model for the permittivity measurement process. This includes the modeling of the probe itself, the measured material under test (also known as the MUT), and the subsequent processing of the measured quantity to obtain the complex dielectric permittivity as the final result, and the validation of the complete model by measurement. With this model and additional measurement experiments, it will be possible to analyze the physical phenomena that affect the accuracy and the frequency range of measurements performed with a coaxial probe. In summary, this research contributes to the advancement of dielectric characterization techniques by providing a systematic framework for modeling and analyzing complex dielectric permittivity measurements using the OECP. By addressing these aspects, the accuracy and reliability of measured permittivity will be enhanced.

1.2. Scientific Methods and Contributions

In alignment with the predefined study objectives, our research methodology is split into two complementary approaches: measurement experiments and computer simulations. These methods synergistically contribute to a comprehensive investigation of the OECP measurement method, providing insight into its applications and inherent limitations. Measurement experiments enable acquiring empirical data through controlled experiments where the physical interactions between the probe and the measured material are directly observed, providing valuable information. Computer simulations allow manipulation of a multitude of parameters—

ranging from geometric dimensions of the probe to material properties—enabling the exploration of the OECP behavior under diverse measurement setups. Computer simulations support a systematical investigation of the impact of each parameter, facilitating a deeper understanding of the probe performance.

1.2.1. Measurement Experiments

The measurement system was comprised of an OECP connected to a vector network analyzer (VNA) by a coaxial transmission line. Measurements were made using a commercial dielectric probe from Keysight Technologies Inc. named Slim Form Probe [24] which has a nominal frequency range from 0.5 GHz to 50 GHz. The probe was connected to the FieldFox N9927A (Keysight Technologies Inc.) [26] VNA by a phase-stable coaxial cable Sucoflex 404 (HUBER+SUHNER AG, Herisau, Switzerland). Measurements were limited between 500 MHz, due to the lower frequency limit of the used probe, and 18 GHz, due to the upper frequency limit of the used VNA. Throughout the entirety of the measurement process, the probe was securely affixed to its stand in a vertical orientation. This ensured that the probe remained stationary during all measurements, thereby eliminating any potential errors or inconsistencies that could arise from inadvertent movements. MUTs were strategically positioned atop a block of polystyrene foam. The foam served to distance the MUTs from a metallic laboratory jack situated beneath it, thereby preventing any potential interference. MUTs were lifted with the help of a laboratory jack until in contact with the probe. That way, any drift in the measured results due to the movement of the probe or cables was eliminated. Between measuring different MUTs, the probe was cleaned with 70% ethyl alcohol to prevent cross contamination and ensure the best results. The setup was periodically calibrated, and also recalibrated in regular intervals with the refresh calibration option available in Keysight Materials Measurement Suite N1500A [27], where one calibration standard out of the three is chosen for recalibration. The recalibration was done with deionized water as its properties gave the most stable results during the measurement process.

The measurement methodology included measuring the reflection coefficient on the plane of the VNA connector where the probe is connected via the associated adapters and cables. The permittivity was obtained through two distinct approaches. The first approach was to use the associated computer software that is designed for use with the commercial probe. For the Slim Form Probe, the complementary software is Keysight Materials Measurement Suite [27]. The use of commercial software obscures the algorithm used to derive the permittivity from the reflection coefficient from the user, thereby preventing any choice in the de-embedding model used. The accuracy of the measured permittivity is contingent upon the suitability of the model for the specific configuration of the probe and the material being measured, as well as the frequency range of the measurement. The second methodology involved storing the measured reflection coefficient for subsequent mathematical processing to derive the permittivity of the MUT. This approach allows for the selection of the postprocessing model through which the permittivity is calculated from the measured reflection coefficient. Given that the final calculated permittivity is dependent on the selected model, a comparison was made within this thesis between the results obtained by the simpler model and those obtained by complex model embedded in the commercial measurement software. This comparative analysis served to highlight the impact of the model selection on the final calculated permittivity. The measured materials were different homogeneous liquid samples: deionized water and saline solutions of varying concentrations, depending on the required dielectric properties of the liquid for a particular analysis. In order to reduce the number of unknowns during measurement, only materials with well-defined and known dielectric characteristics were used.

In addition to homogeneous liquid samples, different biological samples were also measured. Measurements conducted on biological samples primarily focused on brain tissues. The VIF project "Measurements in Bioelectromagnetism" (M-BEM) received ethical approval for the conduct of research from the Ethics Committee of KBC Zagreb, thereby enabling the acquisition of ex vivo samples of the human brain for permittivity measurements. Three different brain tissues were measured: white matter, grey matter, and cerebellum. The permittivity of these three tissues was shown in a study by Gabriel and associates [28] and in the IT'IS database [29]. A comparative analysis of the permittivity of human and animal brain tissues was also undertaken. As highlighted in previously published measurement studies, biological samples are most frequently measured using the Keysight Slim Form Probe, which has an outer diameter of only 2.2 mm [25]. Therefore, as part of this doctoral thesis, biological samples were also measured with the Keysight Slim Form Probe. The smaller diameter of this probe enables better resolution when measuring samples consisting of several different types of tissue. An example of such a measurement would be the differentiation of grey and white matter on a cross-sectional sample of the brain.

Lastly, the preservation of permittivity by freezing the biological samples was investigated. The analysis was done on animal tissue samples due to the easier availability of animal samples compared to human samples. Given that it has been demonstrated in the literature [30] that the success of preserving permittivity will depend on the type of tissue, the research was carried out on several types of tissue: primarily white and grey brain matter as tissues of interest, but additionally on muscle and liver as the results could be compared with those from the literature [30]. An analysis was conducted for two distinct freezing methods. The first method involved conventional slow freezing in a freezer at a temperature of -18 °C, while the second method involved rapid freezing with liquid nitrogen, which is nominally at the temperature of -196 °C. The analysis examined whether there was a difference in the preserved permittivity with regard to the final freezing temperature, but also the speed of reaching the freezing temperature.

1.2.2. Computer Simulations

While physical experiments offer the most authentic representation of potential measurement challenges, they do not permit the evaluation of all conceivable configurations of the probe and the MUT for all observed physical phenomena. Conversely, in silico experiments, encompassing computational modeling and simulations, provide a versatile methodology for systematically varying a broad spectrum of parameters of interest. The configuration of the probe and the measured material were electromagnetically modeled and simulated using two different electromagnetic simulation programs: 3DS CST Studio Suite [31] and Altair FEKO [32]. 3DS CST Studio Suite is primarily used for studies done in the time domain, while Altair FEKO is suited for simulations done in the frequency domain. Particular attention was devoted to exploring the simulation tools themselves, the model segmentation procedure, and the parameters of the numerical method used to solve the model, with the aim of achieving the most accurate simulation results.

The results obtained from the electromagnetic simulation were postprocessed using the selected equivalent circuit of the probe and the MUT, in order to derive the permittivity as the final result. This constituted the final phase of modeling the entire measurement procedure. The equivalent circuit selected was a simple capacitive model, as our premise was to validate whether that equivalent circuit could model all significant physical phenomena. The objective of such an approach was to obtain the simplest model capable of analyzing all physical phenomena pertinent to the measurement of biological tissues in the investigated frequency range.

Within the computer model, parameters such as the dimensions of the coaxial probe (including the width of the coaxial line, the length of the coaxial line, and the depth of immersion of the probe into the sample), the dimensions and shape of the measured sample, and the permittivity of the sample can be easily manipulated. Special attention was paid to modeling and simulation parameters that had the greatest influence on the resulting permittivity. Although the in silico experiments were modeled after the geometry corresponding to the Slim Form Probe, the results and conclusions derived from the study are applicable to other probe geometries, provided the electrical lengths are comparable.

1.3. Published Papers

A list of the published papers which form the basis of this dissertation's contribution is given below.

i. A. Matković, A. Kordić, A. Jakovčević, and A. Šarolić, "Complex Permittivity of Ex-Vivo Human, Bovine and Porcine Brain Tissues in the Microwave Frequency Range," Diagnostics, vol. 12, no. 11, p. 2580, Oct. 2022, doi: 10.3390/diagnostics12112580.
ii. A. Matković and A. Šarolić, "The Effect of Freezing and Thawing on Complex Permittivity of Bovine Tissues," Sensors, vol. 22, no. 24, p. 9806, Dec. 2022, doi: 10.3390/s22249806.
iii. A. Šarolić and A. Matković, "Dielectric Permittivity Measurement Using Open-Ended Coaxial Probe—Modeling and Simulation Based on the Simple Capacitive-Load Model," Sensors, vol. 22, no. 16, p. 6024, Aug. 2022, doi: 10.3390/s22166024.

1.4. Outline

The introductory chapter delineates the underlying motivation and hypotheses of this thesis, as well as the research methodology employed. The subsequent chapter provides a brief theoretical foundation of the dielectric permittivity of materials, ranging from the interaction of the electric field with dielectric materials to an in-depth exploration of the polarization mechanisms. The chapter concludes with a succinct overview of the most common dielectric measurement methods with the emphasis on the OECP measurement method. The third chapter recapitulates the general knowledge on biological tissue measurements while highlighting the most cited permittivity databases. The scientific contributions of this thesis in the form of published permittivities of biological tissues are put into perspective while emphasizing the demand for more systematically performed and reported measurements. Additionally, the concept of tissue preservation by freezing was critically evaluated within the second scientific contribution of this thesis. In the fourth chapter, the theoretical basis of the OECP measurement method was laid out with the emphasis on postprocessing the measured reflection coefficient. As the final permittivity result differs depending on the postprocessing method used, several postprocessing variations will be presented. The final scientific contribution of this thesis, in the form of a comprehensive simulation and postprocessing model, will be disclosed at the end of this chapter. Chapter 5 includes the abstracts as well as scientific contributions and author contributions enumerated for all three publications that constitute this doctoral thesis. Closing with Chapter 6, all scientific findings are summarized along with a glimpse into potential directions for future work. Finally, relevant literature is cited in the bibliography, and the publications that form this dissertation are attached (Appendices A – C).

2. DIELECTRIC THEORY, CHARACTERIZATION AND MEASUREMENTS

The central theme of this thesis revolves around the dielectric characterization of materials, with a particular emphasis on biological tissues. The initial subchapter will provide a comprehensive introduction to the theory of dielectric materials, elucidating their interaction with electric fields. This theoretical foundation will serve as a primer for the subsequent discussions. Following the introductory primer, the chapter will transition into a detailed exploration of the various polarization mechanisms. This subchapter will delve into the underlying causes of these mechanisms, providing a thorough understanding of their origins and effects. A portion of this discussion will be dedicated to correlating these mechanisms with the relaxations observed in biological tissues offering insight into the behavior of biological tissues under the influence of electric fields. The chapter will close with a summary of the diverse methods employed for dielectric measurements. The section will not only provide an overview of the various techniques but also justify the selection of the open-ended coaxial probe measurement method for the research conducted within this thesis as the advantages and suitability of this method will be highlighted.

2.1. Dielectric Materials

Electric flux density $\boldsymbol{D}$ in C/m^2 is related to the electric field $\boldsymbol{E}$ in V/m via the constitutive relation which has the following form in the vacuum [33]:

$$\boldsymbol{D} = \varepsilon_0 \, \boldsymbol{E} \tag{2.1}$$

where ε_0 is the permittivity of the vacuum and approximately equals 8.854×10^{-12} F/m. For isotropic dielectric mediums, the equation takes the following form:

$$\boldsymbol{D} = \varepsilon \, \boldsymbol{E}. \tag{2.2}$$

ε is the permittivity of a medium and is related to the electric susceptibility as follows:

$$\varepsilon = \varepsilon_0 \, (1 + \chi) \tag{2.3}$$

where χ is the electric susceptibility and is a measure of the electric polarization property of a material. All dielectric materials exhibit a phenomenon known as polarization, which is the alignment of bound charges within the material in response to an external electric field. Upon the application of an electric field, there is a discernible shift in the positive and negative charges within the dielectric material, with each moving in the opposite direction. Bound charges do not move freely through the material, but rather, they shift slightly from their equilibrium positions, causing a local charge imbalance. This shift results either in the creation of electric dipoles or reorientation of existing electric dipoles, leading to a net polarization within the material. This polarization enhances the material's ability to store electrical energy and is represented by the polarization vector $\boldsymbol{P} = \varepsilon_0 \chi \boldsymbol{E}$. The electric flux density can then be expressed as [33]:

$$\boldsymbol{D} = \varepsilon \boldsymbol{E} = \varepsilon_0 (1 + \chi) \boldsymbol{E} = \varepsilon_0 \boldsymbol{E} + \varepsilon_0 \chi \boldsymbol{E} = \varepsilon_0 \boldsymbol{E} + \boldsymbol{P}. \tag{2.4}$$

The dielectric permittivity of a material is more commonly regarded in the form of relative permittivity. Relative permittivity is a dimensionless quantity defined as the ratio of the permittivity of the material to the permittivity of free space (or vacuum permittivity) [34]:

$$\varepsilon_r = \frac{\varepsilon}{\varepsilon_0} = 1 + \chi. \tag{2.5}$$

This normalization process facilitates a more convenient comparison of the material's dielectric properties relative to those of a vacuum. Thus, the relative permittivity serves as a standardized measure, providing a more meaningful and comparative understanding of the material's dielectric behavior.

Previous equations are valid for the simplest class of materials, characterized by homogeneity, isotropy, linearity, and frequency independence. Obviously, not all materials display those properties. In the case of inhomogeneous materials, the permittivity is not uniform but rather depends on the specific location within the material. This spatial variation in permittivity introduces additional complexity to the analysis. Anisotropic materials present another layer of complexity, as their permittivity varies depending on the direction of the applied electric field. This directional dependence necessitates a more nuanced understanding of the material's behavior under different orientations of the electric field. Nonlinear materials, on the other hand, exhibit a permittivity that is not a constant but a function of the magnitude of the electric field. This nonlinearity introduces additional factors into the analysis, as the response of the material changes with the strength of the applied field. Lastly, while frequency-dependent permittivity is a characteristic inherent to most materials, there are instances where this dependency can be disregarded. Specifically, if the change in permittivity over the relevant frequency range is not significant, the material can be treated as frequency-independent for the purposes of the analysis. Materials that do exhibit significant frequency-dependent permittivity are referred to as dispersive materials, and their analysis requires consideration of this frequency dependence.

It is important to note that permittivity is actually a complex value with its real and imaginary part. By convention, the imaginary part is defined with a negative sign:

$$\hat{\varepsilon}_{\mathrm{r}} = \varepsilon_r' - j\varepsilon_r''. \tag{2.6}$$

In this thesis, akin to established conventions in physics literature, the term "permittivity" is employed to specifically refer to the complex permittivity denoted by $\hat{\varepsilon}$, or, in the context of normalization to a dimensionless quantity, the term "permittivity" is equivalent to the complex relative permittivity $\hat{\varepsilon}_{\mathrm{r}}$, and will be used accordingly throughout this thesis without further visual emphasis in the form of complex notation. Equation 2.6 can now be inserted into the fourth Maxwell's equation:

$$\nabla \times \boldsymbol{H} = j\omega\boldsymbol{D} + \boldsymbol{J} \tag{2.7}$$

$$= j\omega\varepsilon_0\varepsilon_r\boldsymbol{E} + \sigma_s\boldsymbol{E} \tag{2.8}$$

$$= j\omega\varepsilon_0\varepsilon_r'\,\boldsymbol{E} + (\omega\varepsilon_0\varepsilon_r'' + \sigma_s)\boldsymbol{E} \tag{2.9}$$

$$= j\omega\left(\varepsilon_0\varepsilon_r' - j\varepsilon_0\varepsilon_r'' - j\frac{\sigma_s}{\omega}\right)\boldsymbol{E} \tag{2.10}$$

where:

$\boldsymbol{H}$ is magnetic field strength in Am^{-1},

$\omega = 2\pi f$ is the angular frequency in s^{-1},

$\boldsymbol{J}$ is the total current density in Am^{-2} and

σ_s is the static conductivity in Sm^{-1}.

In the context of electromagnetic wave propagation and material behavior, Equation 2.10 highlights the interplay between the real and imaginary components of complex permittivity. Specifically, the real component represents the storage of the electrical energy in the material, while the imaginary part ε_r'', along with static conductivity σ_s, describes the absorption of energy and losses in the material. Two distinct types of losses are present: the first represents the dielectric damping in the material, while the second represents the losses due to static conductivity σ_s. Static conductivity can be made up of several different conduction mechanisms, but ionic conductivity is the most common one [35]. During OECP measurements, the sources of losses are indifferentiable and are presented using a single quantity ε_r''. Therefore, when presenting the results for ε_r'' they will also include contributions from ionic conductivity. Researchers sometimes quantify these losses using metrics such as the loss tangent or loss factor [36]:

$$\tan\delta = \frac{\varepsilon_r''}{\varepsilon_r'}, \tag{2.11}$$

where δ is the loss angle. This loss factor is actually a quotient of energy lost per cycle versus energy stored per cycle. To better visualize the complex permittivity, it is sometimes represented in a complex plane, where the real and imaginary components exhibit a 90° phase shift as shown in Figure 2.1. The angle δ is formed between the sum complex permittivity vector and the positive segment of the real axis.

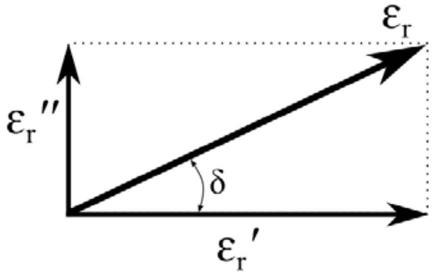

Figure 2.1. Complex permittivity in a complex plane.

Typically, complex permittivity is visualized by plotting its real and imaginary components as functions of frequency. However, since the equivalent conductivity σ is linked with the imaginary part of relative permittivity through $\sigma = \omega\varepsilon_0\varepsilon_r''$, it is not uncommon to see plots of real part of relative permittivity and equivalent conductivity. In those cases, the displayed conductivity is the sum of all loss mechanisms: ionic and dielectric. The resulting conductivity profile provides a comprehensive view of how energy dissipates within the material as a function of frequency. Notably, this behavior varies significantly depending on the specific material properties and the frequency range under consideration.

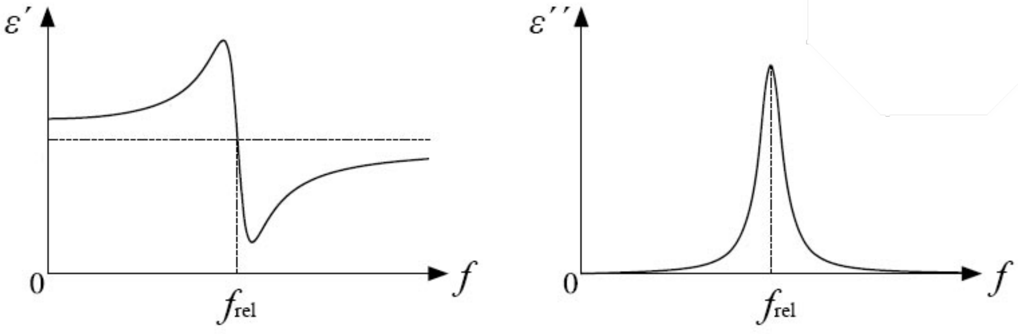

Figure 2.2. Real and imaginary part of permittivity as a function of frequency. (Adapted from [33])

An illustrative example of the complex permittivity dispersion occurs around the resonant frequency, often referred to as the relaxation frequency f_{rel}. This phenomenon is depicted in Figure 2.2., where ε' and ε'' exhibit distinct behaviors as the frequency varies.

Real materials exhibit multiple resonant frequencies, each intricately linked to distinct polarization mechanisms. These phenomena are comprehensively explored in the subsequent chapter.

2.2. Dielectric Relaxations

Dielectrics exhibit specific behavior when subjected to an electric field. Their polarization dynamics depend on several factors, including the nature of bound charges and the internal structure of the dielectric. Within a dielectric, electric charges remain bound—they cannot move independently over macroscopic distances. Consequently, when an external electric field is applied, no net electric current flows. However, the field subtly nudges positive charges in the direction of the field, while negative charges shift in the opposite direction. This results in the formation of tiny electric dipole moments within the atoms and molecules constituting the dielectric. The time needed for dielectric polarization or relaxation varies on several factors:

- Size of bound charges: Larger bound charges take longer to respond to the applied electric field due to their greater inertia.
- Interaction with surroundings: The dielectric’s environment influences the polarization process.
- Applied electric field: When the applied electric field is alternating (as is the case in this thesis), charges continuously strive to align themselves with the changing field direction.

If the time between the alteration of the electric field is shorter than the time needed for a bound charge to realign itself, then the charge will start lagging. The contribution of that bound charge polarization will diminish with increasing frequency until it disappears completely. The loss factor will correspondingly peak at each critical frequency. That process is represented by a relaxation process which is characterized by the relaxation time τ which corresponds to the relaxation frequency $f_{rel} = \frac{1}{2\pi\tau}$. Relaxation time is the time required for dipoles to become oriented in the electric field [36]. The magnitude and the relaxation frequency i.e., the relaxation time, of each mechanism is unique for different materials.

2.2.1. Dielectric Relaxation Models

There are several different mathematical equations that model the relaxation behavior in terms of the frequency-dependent complex permittivity. The simplest one is the Debye model, named after Peter Debye [37]:

$$\varepsilon_r = \varepsilon_\infty + \frac{\varepsilon_s - \varepsilon_\infty}{1 + j\omega\tau}, \tag{2.12}$$

where ε_∞ is the permittivity at a high frequency limit, also called the infinite frequency permittivity and ε_s is the permittivity at a low frequency limit, also called the static permittivity. This model is suitable for the relaxation of polarization in an isotropic and homogeneous material. The Debye model assumes that the medium is comprised of uniform polar molecules that rotate without mutual interaction, resulting in a single relaxation time. Although it shows excellent agreement with the empirical data for the polar liquids, the model is not valid for complex materials which have more convoluted relaxation time. The Cole–Cole model [38] was introduced as an empirical model that better fits the dielectric relaxation in polymers which have broader dispersion curves and lower maximum loss:

$$\varepsilon_r = \varepsilon_\infty + \frac{\varepsilon_s - \varepsilon_\infty}{1 + (j\omega\tau)^{1-\alpha}}, \tag{2.13}$$

where α is a number between 0 and 1. When the exponent parameter α equals 1, the Cole–Cole model reduces to the Debye model. If α is less than 1, the relaxation is stretched, extending over a wider range of frequencies than Debye relaxation. This flexibility makes the Cole–Cole model applicable to a wide range of materials with different dielectric properties. Other materials for which the Cole–Cole model can be applied include biopolymers, colloidal systems, living cells, porous materials, and liquid crystals. It can also be used for rocks, soils, and disseminated ores.

As an alternative plot of real and imaginary part of complex permittivity versus frequency, a Cole–Cole diagram is sometimes employed [38]. It plots the imaginary part of the permittivity on the vertical axis and the real part on the horizontal axis while keeping the frequency as the independent parameter as shown in Figure 2.3. The frequency moves counterclockwise on the semicircle.

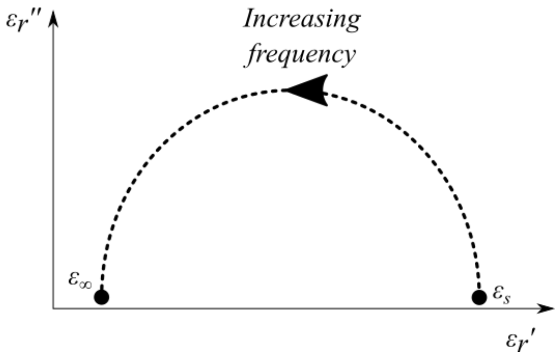

Figure 2.3. Cole–Cole diagram.

For materials with a single relaxation frequency, the Cole–Cole plot exhibits a semicircular arc. When a material has multiple relaxation processes, the Cole–Cole diagram becomes more intricate. Instead of a simple semicircle, multiple overlapping semicircles can be observed. Each semicircle represents a distinct relaxation mechanism with its own characteristic frequency and relaxation time. Deviations from circular symmetry are also possible if the distribution curve is not symmetrical [36]. If the broadening of the dispersion curve is asymmetrical, it is more appropriate to use the Davidson–Cole relaxation model [39]:

$$\varepsilon_r = \varepsilon_\infty + \frac{\varepsilon_s - \varepsilon_\infty}{(1 + j\omega\tau)^\beta}, \tag{2.14}$$

where β is a number between 0 and 1. This model reduces to the Debye equation for $\beta = 1$. In other cases, the dispersion curve will become asymmetrical. This model was introduced to describe dielectric relaxation in materials such as silicate glasses, organic glasses, and some polymers which have asymmetrical nature of the dielectric loss peak. Combining both the asymmetry and the broadening of the dielectric dispersion curve, the Havriliak–Negami model was developed with both α and β exponential parameters [40]:

$$\varepsilon_r = \varepsilon_\infty + \frac{\varepsilon_s - \varepsilon_\infty}{(1 + (j\omega\tau)^{1-\alpha})^\beta}. \tag{2.15}$$

The model was initially used to describe the dielectric relaxation of some polymers. Polymers often exhibit complex dielectric behavior due to their molecular structure and interactions. The Havriliak–Negami model was able to capture these complexities, providing a more accurate description of their dielectric properties. However, its applicability extends beyond polymers and includes various types of amorphous solids, liquids, and other complex materials.

2.2.2. Dielectric Polarization Mechanisms

When dielectric material is placed in the electric field, multiple polarization mechanisms can be active at the same time, depending on the frequency of the applied electric field. The exact permittivity value is dependent on the polarization mechanisms active at the observed frequency. Different categorizations and terminologies for the polarization mechanisms can be found in the literature. This chapter will give an outline of four polarization mechanisms: interfacial, dipolar, atomic, and electronic polarization. Their approximate frequency range and effect on both real and imaginary part of the permittivity is shown in Figure 2.4.

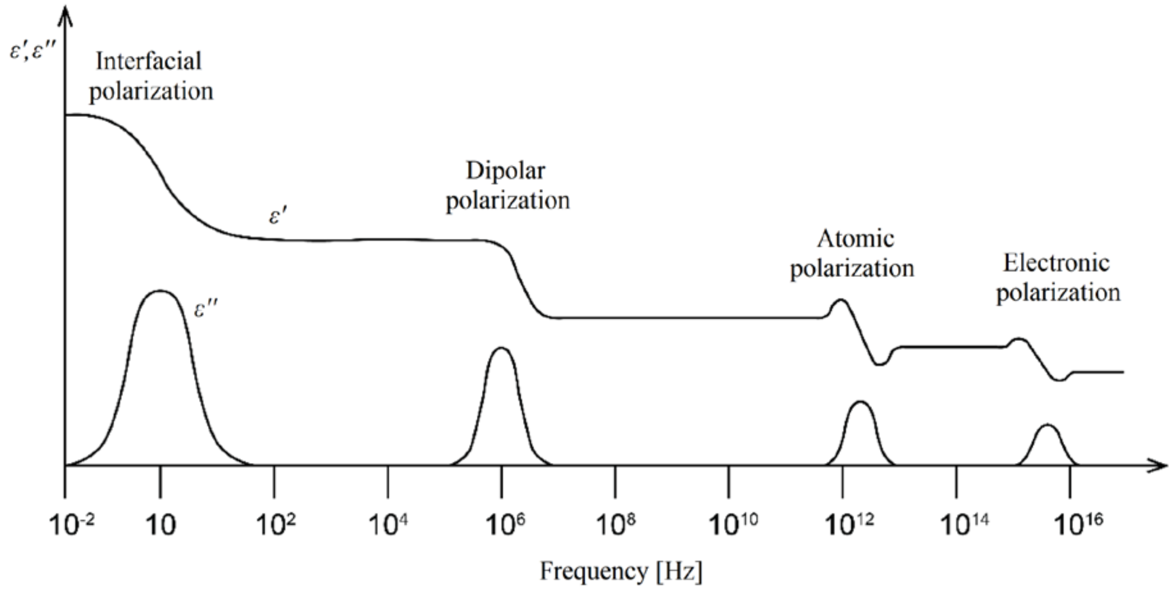

Figure 2.4. Dielectric polarization mechanisms. (Adapted from [41])

Interfacial polarization, also known as Maxwell-Wagner-Sillars polarization or space charge polarization, occurs in heterogeneous materials where the charge accumulation at the interfaces of the material leads to the formation of electric dipoles. Interfacial polarization is significant in materials such as suspensions, colloids, biological materials, and phase-separated polymers. The field distortion caused by the accumulation of these charges increases the overall capacitance of a material which appears as an increase in the real part of the permittivity. The separation of charges occurs either at inner dielectric boundary layers (mesoscopic scale) or at the external electrode-sample interface (macroscopic scale). This type of polarization is most significant at low frequencies because at low frequencies charges have sufficient time to accumulate at the interfaces of the material causing an increase in the real part of the permittivity. At higher frequencies this mechanism ceases to exist because the charges do not have sufficient time to accumulate and the displaced charges are scarce compared to the dimensions of the conducting region [36].

Dipolar or orientation polarization is observed in dielectric materials with permanent dipole moments. When subjected to an external electric field, these materials respond by aligning their intrinsic dipoles along the field direction. In the absence of an external field, these dipoles exhibit random orientations due to thermal motion. This type of polarization is most significant in polar molecules, such as water and certain polymers. Dielectric relaxation of the orientation polarization occurs in the MW frequency range with the order of relaxation time between 1 and 100 picoseconds [36].

Atomic or ionic polarization is caused by the displacement of positive and negative ions within the crystal lattice of dielectric materials. This displacement creates a dipole moment and leads to polarization. The magnitude of the induced dipole depends on the charge and mass of the ions. Its dielectric relaxation effect i.e., resonance, is visible in the infrared spectrum and corresponds to the relaxation times in the order of 0.1 to 1 picosecond [42]. For certain dry solids, this effect may even be observable at lower frequencies, such as MW frequencies [36].

Electronic polarization is observed in all non-conducting materials when subjected to an external electric field. Within an atom or molecule, positive and negative charges (electrons and nuclei) are distributed around their equilibrium positions. When an external electric field is applied, these charge centers experience displacement in opposite directions. Electrons respond rapidly to changes in the electric field, leading to swift adjustments in charge distribution. As a result, electronic polarization contributes significantly at the highest frequencies. The relaxation time associated with electronic polarization is exceptionally short, typically in the order of femtoseconds. Unlike other polarization mechanisms, electronic polarization occurs in all dielectric materials, regardless of their specific composition. Even simple insulators exhibit electronic polarization due to the inherent charge distribution within their atomic or molecular structures. At frequencies below the resonant frequencies of both electronic and atomic polarization, their contributions to both real and imaginary part of the permittivity are negligible [36].

2.2.3. Relaxation Regions in Biological Tissue

In the study of biological tissues, one of the key factors to consider is the existence of natural electrical boundaries. These boundaries are primarily formed by cell membranes, which are crucial components of biological cells. Cell membranes, composed of a bilayer of phospholipids, serve as the boundary between the interior of the cell and the extracellular environment. Due to their unique structure and composition, cell membranes exhibit a certain degree of electrical resistance and capacitance. As a result of these inherent electrical properties, when an external electric field is applied to biological tissues, specific polarization mechanisms occur. These polarizations mechanisms give rise to four major relaxation regions named ***α***, ***β***, ***γ***, and ***δ*** dispersions as shown in Figure 2.5.

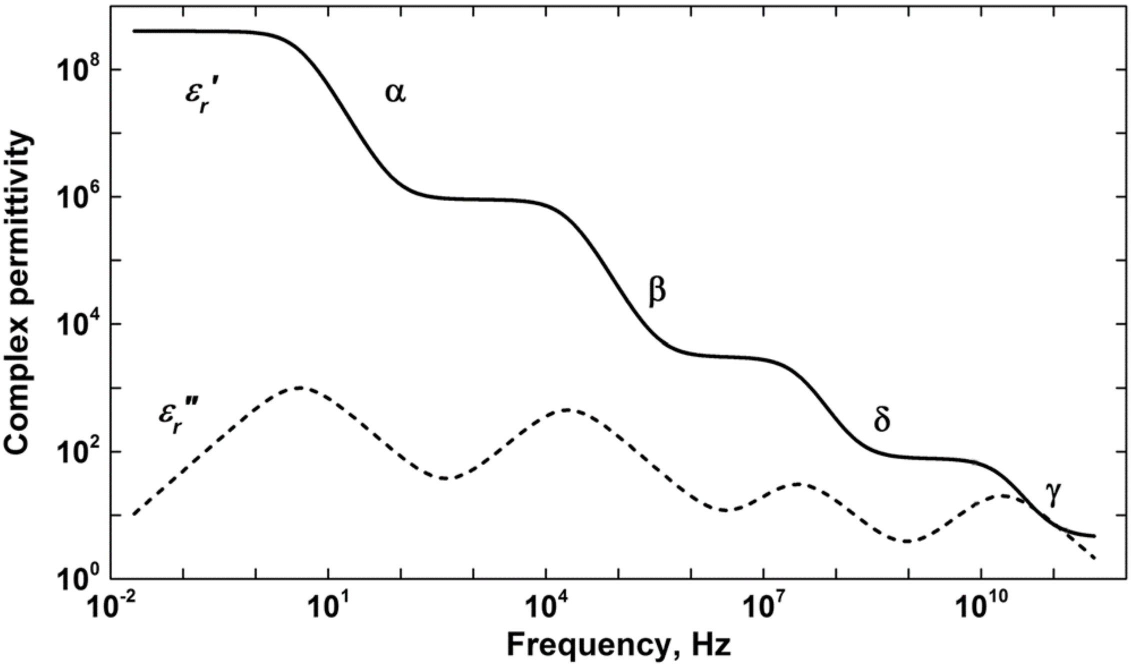

Figure 2.5. ***α***, ***β***, ***γ***, *and* ***δ*** *relaxation regions in biological tissue. (Adapted from [43])*

The ***α*** dispersion arises in the lowest frequency range, from 10 Hz up to 10 kHz which corresponds to the relaxation time of ca. 6 ms. It originates from the counterion polarization mechanisms when the ions flow tangentially over the cell surfaces [42].

The ***β*** dispersion takes place in the vicinity of cellular and intracellular membranes which function as an interface of two different dielectric properties. Membranes cause the separation and accumulation of charges which can be correlated with the interfacial polarization mechanism. The ***β*** dispersion is highly dependent on the membrane characteristics, such as membrane thickness, permittivity, and conductivity, and the properties of the surrounding medium. This dispersion arises around 10 kHz and is noticeable up to 10 MHz which corresponds to the relaxation time of approximately 300 ns. This dispersion disappears when the increase in frequency makes the intracellular structures more electrically similar [42]. Likewise, destroying the cell membranes also causes the disappearance of the ***β*** dispersion.

Moving up the frequency range, the next dispersion encountered is the ***δ*** dispersion. Its origin is connected to the interaction of bound water molecules with other molecules, most commonly proteins and other large molecules with dipolar moments [42]. Bound water, as the name suggests, is bound to other molecules and is unable to rotate as freely as unbound water and thus has a longer relaxation time. This relaxation region is sometimes further subdivided into sub-dispersions depending on whether the water is tightly or loosely bound [44]. The $\boldsymbol{\delta}$ dispersion occurs within the 0.1 to 5 GHz frequency range, while its magnitude is relatively small compared to the previous two dispersions.

The last dispersion is the $\boldsymbol{\gamma}$ dispersion which can be observed at frequencies above 0.1 GHz and is associated with the dipole polarization. This dispersion occurs because of the reorientation of free water molecules and is thus affected by the water content of the biological tissue [42].

2.3. Dielectric Measurement Methods

There are many methods developed for measuring dielectric properties of materials as dielectric measurements can be performed over a wide range of frequencies, from extremely low frequencies to the terahertz range. Each method has its own advantages and disadvantages, and the choice of method depends on the specific requirements of the measurement, such as the frequency range, properties of a sample material, and the desired accuracy. Therefore, a comprehensive understanding of these methodologies and their respective strengths and weaknesses is necessary for a confident selection of a suitable measurement method. The subsequent subchapters will briefly define several of the most common methods for dielectric spectroscopy, which include transmission methods, free space methods, resonant methods and the OECP method as a method of choice.

2.3.1. Transmission Methods

This method involves propagation of an electromagnetic wave through a transmission line that encapsulates the MUT. As the electromagnetic wave propagates along the transmission line, it experiences reflection and transmission at points of discontinuity. These discontinuities are caused by changes in the impedance of the line, which, in turn, are caused by the changes in the permittivity of the material within the line. The transmitted (S_{21}) and reflected (S_{11}) signals are subsequently measured using a network analyzer. The complex permittivity of the material is then calculated from the amplitude and phase of these waves. It is noteworthy that both permittivity and permeability can be computed from the measured scattering parameters. This method is suited for materials that can be shaped or machined into the specific geometries required for the transmission line as the sample is placed inside a section of a transmission line. The MUT must fit in the line without any air gaps, as these can compromise the accuracy of the measurement. Calibration is necessitated to transition the measurement plane from the VNA connector to the surface of the MUT. This method is suitable for materials that have medium to high loss and can be employed over a broad frequency spectrum, from direct current (DC) to microwave frequencies. However, a significant limitation of this method is the destructive nature of sample preparation, coupled with the potential for air gaps if the sample is not impeccably machined to conform to the dimensions of the transmission line [45].

2.3.2. Free Space Methods

The free space method is a non-contact and non-destructive technique for measuring the permittivity of materials. It involves transmitting an electromagnetic wave through the free space and into the material under test. The transmitted and reflected waves are then measured using antennas and a network analyzer, and the complex permittivity of the material is calculated from these measurements. The two variations of the free space method are its transmission and reflection configuration as shown in Figure 2.6.

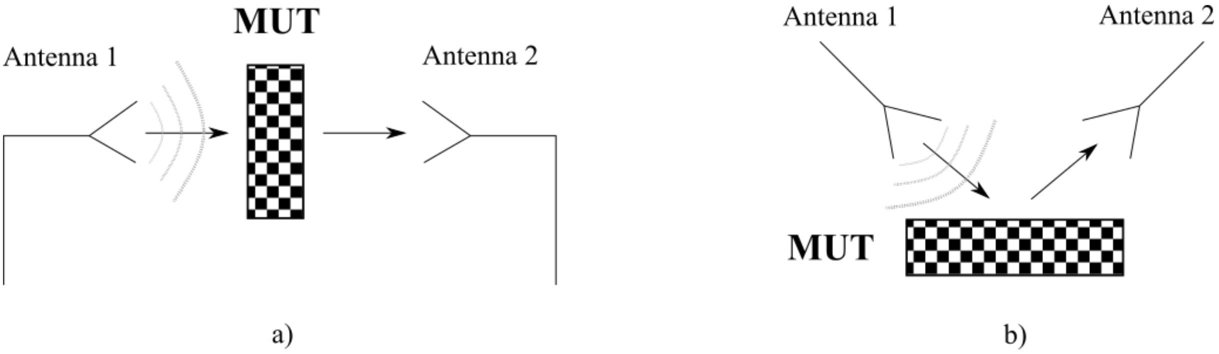

a)

b)

Figure 2.6. Free space measurement method in its a) transmission configuration and b) reflection configuration.

The method is suitable for measuring the permittivity of large, solid materials that cannot be easily inserted into a transmission line or resonant cavity. It also makes it suitable for measuring the permittivity of materials that may be damaged by contact with a probe, or that need to be measured at high temperatures that would damage the equipment used on contact. However, this method does present certain limitations. It requires a large, open space for the placement of the antennas and the MUT. It also requires the material to be large enough to completely contain the propagation path of the electromagnetic wave radiated from the antenna, which can pose a challenge for smaller samples [45]. This method works best with low loss materials, while lossy MUTs should be kept thin to facilitate transmission.

2.3.3. Resonant Methods

Dielectric spectroscopy, when conducted using resonant methods, is generally characterized by a high degree of precision, attributable to the inherent sensitivity of these techniques. Many types of resonant methods exist, including but not limited to reentrant cavities, split cylinder resonators, cavity resonators, and Fabry-Perot resonators. All of those resonant methods are based on the principle of resonance within electromagnetic cavities and are thus narrowband. When an electromagnetic wave is confined within a cavity, it can form standing wave patterns, or modes, at specific frequencies. These frequencies are known as the resonant frequencies of the cavity. The introduction of a material into the cavity induces a change in both the resonant frequency and the quality factor of the cavity. The method involves the measurement of the change in the cavity's resonant frequency and quality factor pre- and post- the insertion of the MUT. The permittivity of the material is then calculated from the measured resonant frequency and quality factor using the cavity perturbation equations. This method is particularly suited for measurements of small samples. However, it necessitates the material to be machined into a specific shape to conform to the cavity shape, which is a significant limitation [45]. Another drawback is that, despite its simplicity in application, this method requires complex calculations which include solving transcendental equations and additional corrections to acquire accurate results.

2.3.4. Open-Ended Coaxial Probe Method

The OECP method, a common technique falling under the reflection methods, traces its origins back to the open waveguide measurements first pioneered by Bailey and Swift in 1968 [46]. Their theoretical model incorporated a circular waveguide with an infinite flange, which radiated into a lossy dielectric backed by a ground plane. As the waveguide presents additional frequency limitations with its cutoff frequency on the lower limit, it was subsequently replaced with the coaxial probe thus developing the OECP method. This method involves bringing the open end of the coaxial probe in contact with the MUT. The method is based on the study of the fringing electric field at the open end of the coaxial line and its transformation caused by the dielectric in contact with the open end. Therefore, the MUT functions as a load to the open end of the coaxial line. The probe is connected to a network analyzer which sends a signal into the material and measures the reflected wave. The reflection coefficient at the probe tip, which is intrinsically a function of the complex permittivity of the material, is then determined from this measurement. It is important to note that the OECP method is limited to the measurement of permittivity and does not extend to permeability, as it only measures one scattering parameter: the reflection coefficient. While it is extensively employed for measuring the permittivity of liquids and semi-solids, its applicability to rough-surfaced solids may be compromised due to the potential for air gaps. The research presented within this thesis is focused solely on this measurement method as it is the most appropriate method for measuring the permittivity of biological tissues. The non-destructive nature of the OECP method ensures that the biological tissue remains unaltered and undamaged during the measurement process. Furthermore, the simplicity and ease of implementation of the method, which does not necessitate a complex measurement setup beyond the probe kit and the VNA, make it a preferred choice.

Figure 2.7. Examples of commercial open-ended coaxial probes: probes manufactured by Keysight [24] (top row) and probes manufactured by SPEAG [47] (bottom row).

The popularity of the OECP method has been further reinforced by the availability of commercial probe kits such as the Keysight Dielectric Probe Kit [24] and SPEAG Dielectric Assessment Kit [47] as shown in Figure 2.7.

3. PERMITTIVITY OF BIOLOGICAL TISSUES

This chapter explores the knowledge that is compiled within the most frequently cited permittivity databases. While the databases offer a wealth of information, the chapter also brings to light the limitations and gaps in the current knowledge base. It emphasizes the need for further research and investigation to address these shortcomings, particularly in the context of specific types of tissues such as brain tissues. The chapter also delves into the practical aspects of permittivity measurements, discussing the challenges associated with maintaining the integrity of biological tissues during storage and handling. It underscores the importance of proper tissue handling and preservation in ensuring the accuracy and reliability of permittivity measurements.

3.1. References for Permittivity of Biological Tissues

A commonly cited source of permittivity values of biological tissues is a three-part study published by Gabriel et al. in 1996 [28], [48], [49]. The study is a compilation of the results of measurements conducted on different human and animal tissues, either by Gabriel herself or taken from previously published literature. The final result is a four pole Cole–Cole frequency-dependent parametric model of the real and imaginary part of the permittivity which best matches all the measurement results for a particular tissue. The four pole model was chosen because each pole corresponds to one of the four biological dispersion mechanisms covered in Chapter 2.2.3. The final equation for the complex permittivity of each tissue is given by:

$$\varepsilon_r = \varepsilon_\infty + \sum_{n=1}^{4} \frac{\varepsilon_{sn} - \varepsilon_\infty}{1 + (j\omega\tau_n)^{1-\alpha_n}} + \frac{\sigma_s}{j\omega\varepsilon_0}, \tag{3.1}$$

where σ_s represents only the static conductivity in S/m as opposed to the equivalent conductivity σ. The frequency range of the final models spans from 10 Hz to 20 GHz, although the authors state that the model is reliable only for frequencies above 1 MHz. An example of a one such final model is shown in Figure 3.1 for cancellous bone. The figure illustrates the data obtained by measurements on the ovine tissue [28] (represented by grey solid and dashed lines), alongside measurement data from previously published studies on the bovine and human cancellous bone (represented by circles and triangles). The final approximate parametric model is represented by a black solid and dashed line. The figure reveals a few shortcomings of this study. The most significant drawback is the reliance on ovine tissue results for the final permittivity model, despite the models from this study being predominantly used to model human tissues. A systematic analysis comparing the permittivity of the same tissue types across different species (animal and human) has yet to be conducted. Furthermore, the final model is approximated from only a few discrete measurement points across the frequency range. The measurements compiled in the study [28] were conducted on tissues that were at different temperatures. While it is known that temperature variations can impact permittivity, no temperature correction was applied to the permittivity measurements. Thus, the previously mentioned permittivity results for cancellous bone are a compilation of measurements conducted on a sheep skull at 37 °C, a human tibia at 27 °C, and a bovine femur at an unspecified temperature.

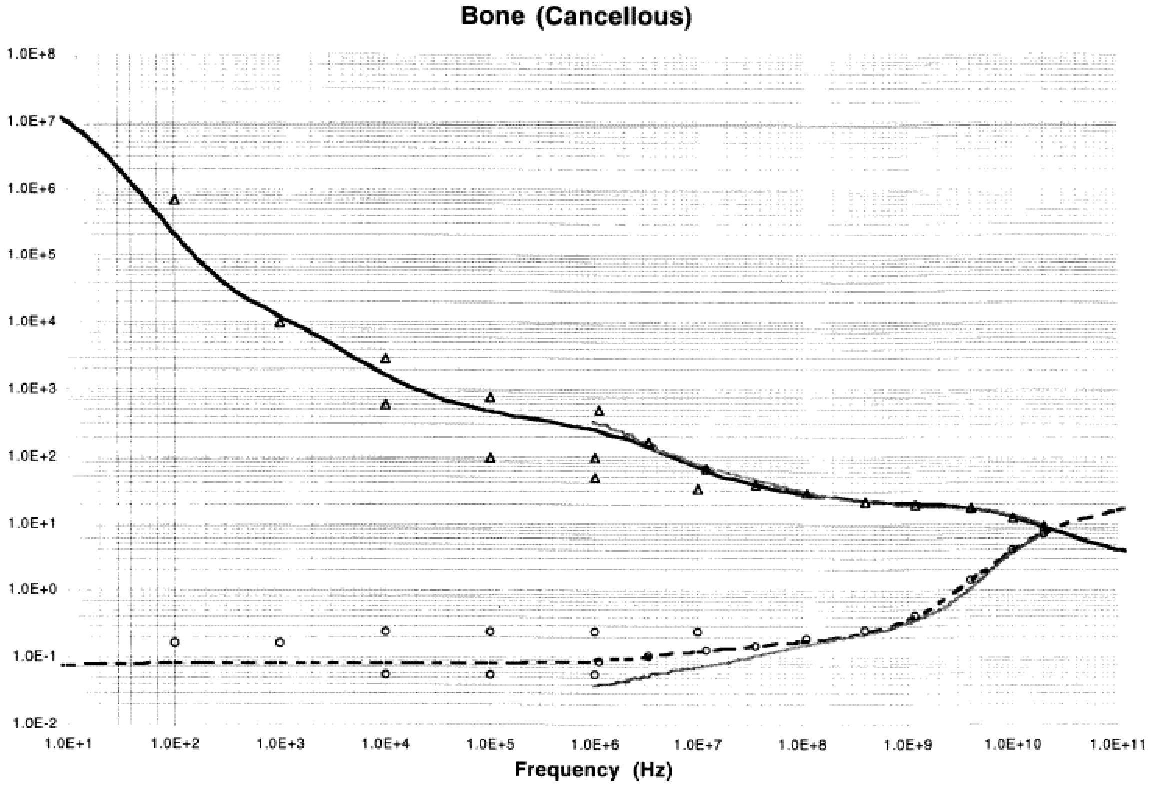

Figure 3.1. Frequency dependent real and imaginary part of permittivity for cancellous bone [28].

The permittivity and frequency scales in Figure 3.1 are represented on a logarithmic scale, spanning an extensive frequency range from 1 Hz to 100 GHz, and a permittivity range from 0.01 to 100,000,000. The broad scope of the logarithmic scale inherently limits the precision with which results can be interpreted from the graph, thus raising questions about the level of accuracy that can be anticipated when referencing these findings. For some frequency points where data have been taken from several different measurement studies, a deviation of an entire order of magnitude is visible. An example of such deviation is between the measured and the referenced data at 1 MHz. Although the coarseness of this scale partially hides these deviations, a comparison of the exact numerical values reveals that the disparities in the results are far from negligible. These deviations of the results from the model accentuate its approximate nature.

In addition to the study published by Gabriel et al., another frequent reference for tissue permittivity in the literature is the IT'IS database [29]. In addition to the dielectric properties of tissues, this database also provides data on their density, thermal parameters, acoustic parameters, and other properties. The database undergoes regular updates, with the most recent one occurring in February 2022. However, the dielectric properties of the majority of tissues in the IT'IS database were taken from the aforementioned study published by Gabriel et al. [28]. Only five biological samples (adrenal gland, intervertebral disc, lymph node, salivary gland, and urine) have been updated with more recent measurement studies conducted by Peyman and Gabriel on porcine tissues [50], [51]. This indicates that the permittivity values of majority of tissues, available in the IT'IS database [29], have not been updated since 1996, which is a direct consequence of the lack of new systematic measurements.

The need for wider and systematic measurement studies was also expressed in a review paper from 2022 [52], which compiled all published measurement studies of the permittivity of biological tissues. The authors concluded that the publication of systematically measured data on the dielectric properties of human tissues, which are currently lacking, as well as the expansion of the frequency range of measured tissues, is of immense importance not only for biomedical applications but also for the human protection from non-ionizing radiation.

3.2. Dielectric Properties of Brain Tissues

The measurement of permittivity in brain tissues presents a significant challenge due to the invasive nature of these measurements and the often-indistinct boundaries between different types of brain tissues. Permittivity data for brain tissues from the IT’IS database [29] originates from the Gabriel measurement study [28]. The values for brain tissues in the frequency range from 500 MHz to 18 GHz in Gabriel [28] were compiled from the literature published prior to 1996:

- Steel and Sheppard [53] measured dielectric properties of white and grey matter of a rabbit specimen at 20 °C and 37 °C between 1 and 4 GHz and between 7.5 and 18 GHz,
- Thurai et al. [54] measured dielectric properties of a mouse cerebral cortex at 37 °C from 10 MHz to 5 GHz,
- Kraszewski et al. [55] measured a cat brain cortex from 100 MHz to 8 GHz at 36 °C as well as a rat brain from 100 MHz to 12 GHz at 32 °C, both measured in vivo,
- Burdette et al. [56] measured samples of a canine brain in situ at 2450 MHz with the temperatures ranging from 25 °C to 40 °C with 1 °C increments,
- Xu et al. [57] measured dielectric properties of a canine white and grey matter at 20 °C at 10 discrete frequencies from to 0.1 GHz 11 GHz,
- Stuchly et al. [58] measured white and grey matter of feline specimens in vivo at 33 °C at frequencies from 10 MHz to 1 GHz,
- Foster and Schepps [15] measured canine white and grey matter at 37 °C from 0.1 GHz to 18 GHz.

The study also included Gabriel’s own measurement results done on ovine white matter, grey matter and cerebellum measured at 37 °C, as well as for human white matter and grey matter obtained from autopsies and measured also at 37 °C. While the ovine tissue results are reported in detail as comprehensive sets of measurement results measured in a continuous frequency range from 10 Hz to 20 GHz, the human tissues are reported only for a few frequency points. Gabriel states [28] that the parameters of each model were adjusted to correspond to a close fit between the model and the most comprehensive data set available for the particular tissue. Observing the models for the white matter, grey matter and cerebellum in [28], it is evident that they are primarily based on the ovine results, which represent the most comprehensive data set for these particular tissues.

There are only four published studies measuring human brain tissues and fluids more recent than Gabriel (1996) [28], namely: [59], [60], [61], [62]. Out of those four studies, only the latter two measured and reported values of dielectric permittivity in the microwave range, which is of greatest interest for therapeutic, diagnostic, and dosimetry applications. The first study [61] conducted measurements on the dielectric properties of grey matter in the frequency range of 800–2450 MHz, with tissue temperatures ranging between 18 and 25 °C. The results indicated a slightly higher conductivity of human grey matter at body temperature compared to previous literature. It suggested that brain models may need to be updated to reflect the properties of human brain tissue more accurately. The second study [62] measured the dielectric properties of 20 freshly removed pineal glands less than 20 hours after death. A high-resolution numerical model of the brain region surrounding the pineal gland was developed based on real human tissue valid in the frequency range from 0.4 GHz to 6 GHz and at temperature of 18 °C. Both studies by Schmid et al. [61], [62], although valuable, cannot be used to update the database because they were made in too narrow frequency range, so it is not possible to extrapolate a model suitable for a wide frequency range based on them. They acknowledged that the data reported by different authors are often difficult to compare due to differences in the investigated sample, such as the measurement procedure (i.e., in vivo, in situ or in vitro), tissue origin (i.e., species), postmortem age of the tissue, treatment of the tissue after excision, and tissue temperature at the time when the measurements took place. The authors advocated that the best approach for estimating dielectric data of living human body tissue seems to be obtaining data based on human tissue measured as soon as possible after death, combined with corresponding in vivo investigations in large mammals.

That is why, in our study [63], we measured permittivities of three different brain tissues of both large mammalian and human specimens. The publication, and its supplementary materials in the form of Cole–Cole models of brain tissues, serve as a valuable resource for microwave imaging and all related procedures relying on MW electromagnetic (EM) radiation. The existence of a dielectric contrast between healthy and pathological brain tissues has been well-documented, particularly in the detection of brain hemorrhage [64]. In the MW frequency range, blood exhibits a much higher dielectric permittivity compared to other brain tissues. Consequently, mapping the high contrast regions within the brain can directly indicate bleeding, a common consequence of a hemorrhagic stroke. In the context of stroke diagnosis, it is crucial for medical professionals to be certain that the observed increase in permittivity is caused by pooled blood rather than other potential brain pathologies. This underscores the importance of defining the expected range of dielectric properties of healthy human brain tissues. Saied et al. [65] presented a novel method for detecting stages of Alzheimer’s disease based on the permittivity change observed in the frequency range from 200 MHz to 3 GHz. Dielectric measurements were done on brain tissues with severe Alzheimer’s disease pathology. The comparison was made with the permittivity values from the aforementioned study [61] and the IT’IS database [29]. The study found that dielectric properties in diseased brain tissues differed from those in healthy ones. Additionally, there was an increase in the contrast as the volume of the affected brain regions increased. The reconstructed images successfully highlighted the brain areas impacted by Alzheimer’s disease, confirming that dielectric spectroscopy presents a promising non-invasive technique for monitoring the progression of brain pathology. Another noteworthy application is microwave beamforming for hyperthermia treatment of brain tumors, in particular pediatric brain tumors [66]. Beamforming is planned to create localized heating in the brain by controlling the interference of transmitted electromagnetic waves. This procedure requires meticulous planning and precise knowledge of the dielectric properties of brain tissues, as it relies on the constructive interference of electromagnetic waves and their selective absorption to achieve localized heating solely in the target tumor tissue. It has been shown that the technique is sensitive to the underestimation of dielectric properties [66]. For a successful hyperthermia treatment planning, even non-target tissues must be accurately defined as they may also be inadvertently heated during the treatment. A study by Schooneveldt et al. [67] showed that not taking the cerebrospinal fluid dielectric behavior into account when planning brain tumor hyperthermia may lead to erroneous predictions of severe hot spots. Likewise, exact permittivity of brain tissues is also necessary for hyperthermia treatment planning of non-brain head and neck tumors to prevent unnecessary heating of brain tissues [68]. One of the more recent hyperthermia studies of the head and neck region highlighted the importance of the relationship between the absorbed electromagnetic power and tumor response [69], a subject that could be resolved by deeper understanding of physical properties of target tissues including their dielectric properties.

The aim of our work [63] was to report the measurement data for dielectric properties of brain tissues for several species, including humans, providing enough supporting information about our measurement protocol and tissue properties. In this study, three types of brain tissues from three different species were measured, namely: white matter and grey matter (both from cerebrum), and cerebellum. Despite the cerebellum comprising of both white and grey matter, it was treated as a singular tissue entity in this study. It was due to the fact that white and grey matter are intertwined in the cerebellum, rendering them indistinguishable by the probe. This approach aligns with conventional practices in the literature [28], [29]. In total, we acquired two different human brains (hereafter referred to as H1 and H2), three different bovine brains (B1, B2 and B3), and one porcine brain (P). Cerebellum was intact only in the human brain specimens (H1 and H2) and one bovine brain specimen (B1). Other animal brain specimens were fractured by splitting into two hemispheres during slaughter. This was especially damaging to the delicate cerebellum tissue located in the center so the measurements on cerebellum could not be performed. Human tissues were obtained from hospital autopsies at the Department of Pathology and Cytology, University Hospital Centre Zagreb. The study was performed under ethical approval from the Ethics Committee of the University Hospital Centre Zagreb.

The measurements were performed on homogeneous regions of either white or grey matter, when such regions were clearly visible on the sample. The regions with visually indistinguishable white and grey matter were avoided. Within these constraints, each sample was measured at as many points as possible to obtain better accuracy. The number of measurement points per tissue is shown in Table 3.1.

Table 3.1. The number of measurement points on brain tissues per tissue and species type.

SPECIES	BRAIN	AGE	WHITE MATTER	GREY MATTER	CEREBELLUM
Human	H1	50 years	14	15	15
	H2	84 years	18	10	5
Bovine	B1	<12 months	72	70	13
	B2	<12 months	38	32	-
	B3	<12 months	38	32	-
Porcine	P1	Unknown	38	40	-

The average measured permittivity for each species and each tissue was fitted to a single pole Cole–Cole model. The Cole–Cole fits were derived in Microsoft Excel using Equation 3.1, producing the best fits predominantly based on the least-squares fitting, with additional manual adjustments for a better fit at the highest measured frequencies. The derived parameters are listed in Table 3.2.

Table 3.2. Single pole Cole–Cole parameters for measured brain tissues.

		$\boldsymbol{\varepsilon_\infty}$	$\boldsymbol{\varepsilon_s}$	$\boldsymbol{\alpha}$	$\boldsymbol{\sigma_s}$ **[S/m]**	$\boldsymbol{\tau}$ **[ps]**
Porcine Brain	White Matter	5	31	0.09	0.47	5.4
	Grey Matter	3	45	0.05	0.80	6.2
Bovine Brain	White Matter	5	34	0.09	0.48	5.6
	Grey Matter	5	51	0.05	0.85	6.8
	Cerebellum	5	47	0.10	0.80	7.0
Human Brain	White Matter	2	36	0.13	0.50	5.8
	Grey Matter	5	51	0.05	0.90	7.1
	Cerebellum	3	47	0.08	0.83	6.5

Permittivity results for the grey matter for human, bovine and porcine brain are shown in Figure 3.2. The mean permittivity values for bovine brains align closely with those of human brains, while the measurements for porcine brains deviate from the aforementioned two. Notwithstanding these differences, it is crucial to highlight that the change in $\varepsilon_{\mathrm{r}}'$ and $\varepsilon_{\mathrm{r}}''$ with frequency across all measurements exhibits a degree of similarity. A parallel observation can be made for white matter, although for the sake of clarity, these results are not included here but can be found in Appendix A.

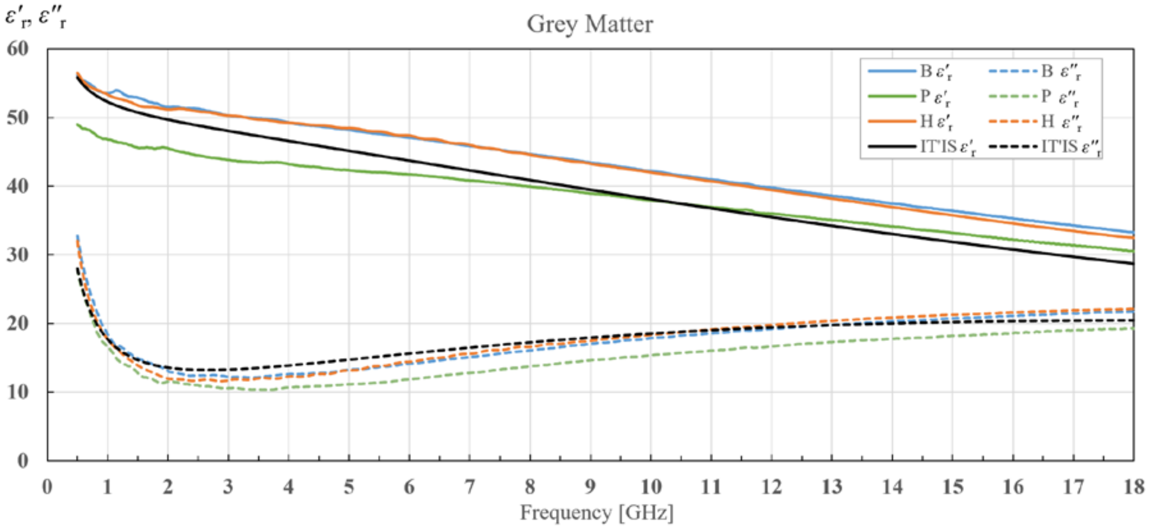

Figure 3.2. Grey matter permittivity comparison of averaged bovine brains (B), averaged human brains (H) and a porcine brain (P) as well as comparison with the published data from the IT'IS database [29].

It should be taken into consideration that our measured data is compared with the data from the IT'IS database which is based on the measurements of different species at different temperatures, predominantly exceeding 30 °C. Consequently, the comparison, although indicative, should be interpreted with a degree of caution. However, there are not enough published data on permittivity of brain tissues of various species measured at various temperatures in a relevant and continuous frequency range to make a direct comparison to a corresponding set of data. In general, the published data for all three measured brain tissues in this study are considerably dated and scarce. This is particularly true for human tissues where, to the best of our knowledge, there are no reported data on human white matter, grey matter and cerebellum measured in the continuous frequency range of this study.

There is a noticeable interspecies variability for all three measured brain tissues between the porcine brain and both human and bovine brains. The averaged results for the real part of the permittivity of bovine brain white and grey matter are similar to the averaged results for human brain white and grey matter. The imaginary part of the permittivity shows greater difference, but the results are still comparable. Both human and bovine white and grey matter show greater deviation from the porcine brain white and grey matter than from each other. The permittivity data for cerebellum are only available for human and bovine brains and they display noticeable differences between bovine and human cerebellum in both real and imaginary parts of the permittivity. It should be remarked that the permittivity trends, with respect to frequency, are similar for all three measured species when comparing the same brain tissue.

All three bovine brains show similar permittivity values for both grey and white matter. This uniformity is anticipated given that all specimens originate from healthy individuals of comparable age. Despite the negligible intraspecies variability observed in bovine grey and white matter, the results derived from human brain tissues suggest a different narrative. There is an apparent difference in all three measured tissues (grey and white matter and cerebellum), where the results for H2 are consistently higher than for H1 for both the real and imaginary parts of the permittivity. The most obvious difference between H1 and H2 is their age, although this may not necessarily be the most influential factor. There are no comprehensive studies done on age-related permittivity changes of brain tissues beyond the comparisons between the young (immature) and the adult (fully matured) brain. Consequently, we sought to identify the cause of this disparity by examining studies that investigate the water content of brain tissues in older adults. The rationale for this was the known fact that the permittivity of biological tissues, in this frequency range, is predominantly determined by their water content. As demonstrated in [70], tissues with higher water content exhibit higher permittivity, given that water possesses the highest permittivity value compared to any other tissue constituent. This also explains why grey matter, with a water content of approximately 83%, has a larger overall permittivity and equivalent conductivity than white matter, which has a water content of around 69% [70]. Accordingly, our results suggest that all three brain tissues taken from brain H2 had a higher water content than those taken from H1. The study by Gullet et al. [71] revealed that the extracellular free water within white matter increases with normal aging and can even serve as an indicator of cognitive decline. Free water refers to the water molecules that are freely diffusing without being hindered or restricted by tissue membranes. Increases in the free water are connected with the accumulation of extracellular water, which may occur due to processes such as atrophy, edema, or neurodegenerative disease. The increase in free water causes a decrease in the white matter integrity [71]. Thus, a reasonable explanation for the difference in permittivity of brains H1 and H2 could be in the changes that were ongoing in the elderly brain, leading to an increase in extracellular free water. This is particularly relevant because the permittivity of biological tissue in the gigahertz frequency range is primarily influenced by the γ biological dispersion, i.e., the polarization of free water molecules, as outlined in Chapter 2.2.3.

Lastly, it is worth acknowledging that there is a factor of variability of the measured dielectric properties even when the tissues are considered homogenous. Therefore, the measured permittivity results can vary greatly when measured at different locations on the same specimen. The measurement study by Schmid et al. [61] indicates that the observed extent of standard deviation is around 6% for the real part of the permittivity and between 8% and 10% for the imaginary part of the permittivity. This variability is hypothesized to stem from a combination of biological variances within the tissue and differences in tissue temperature at the measurement sites. Similarly, Gabriel et al. [28], [48], [49] report that the variability of their results was within the range of ±5%, and they further suggest that the variation in tissue properties within a species may well surpass variations between species. This introduces an additional layer of uncertainty that should be factored in when comparing measurement results from seemingly identical specimens. The above applies not only to our measurement results, but also to all published results from the literature, which should always be taken with some reservation. The average standard deviations for the measured brain tissues are presented in Table 3.3. The reported standard deviation of our data is within the expected standard deviation caused by the natural variation of the biological tissues, a phenomenon that is also evident in other reported ex vivo measurements.

Table 3.3. Average standard deviation for measured white matter, grey matter, and cerebellum of all brain samples.

Brain sample	**White Matter**		**Grey Matter**		**Cerebellum**	
	ε_r'	ε_r''	ε_r'	ε_r''	ε_r'	ε_r''
H1	2.4	1.1	2.9	1.6	3.9	2.3
H2	8.1	4.5	3.1	1.9	2.1	1.5
B1	3.0	1.4	3.1	1.9	6.0	3.6
B2	2.1	0.9	1.7	0.9	-	-
B3	2.1	1.1	2.3	1.5	-	-
P	2.6	1.3	1.2	4.9	-	-

In the course of this study, we used the opportunity to measure the same human white and grey matter samples over the course of three days, to examine the effects of tissue degradation on its permittivity. For the permittivity of H1 measured on day 2 and day 3, we calculated the percent change in permittivity relative to the permittivity measured on day 1 for both white and grey matter separately. The results for grey matter are shown in Figure 3.3. The average percent change for the real part of the permittivity was -11.19% and -28.55% for day two and three, respectively. The average percent change for the imaginary part was -15.29% and -32.81%, for day two and day three, respectively.

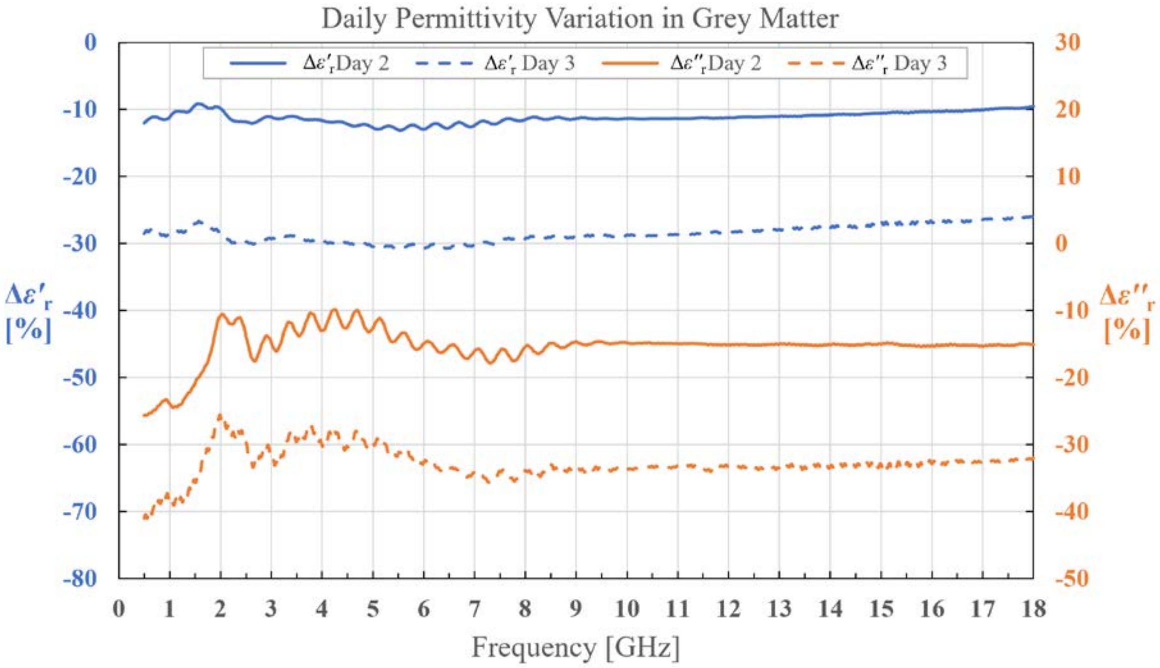

Figure 3.3. Permittivity change in human grey matter for brain H1 on day 2 and day 3.

There is a clear trend of increase in magnitude of the average change in permittivity from day 2 to day 3 for both ε_r' and ε_r''. The results confirm that there is an increase in tissue degradation over time. The decrease in ε_r' and ε_r'', which correlates with the decrease in equivalent conductivity σ, for both day 2 and day 3 could be explained by the loss of water in the tissue, i.e., dehydration. This observation is in line with the expectations and severely limits the usability of samples that are not freshly excised. The results warrant the need for tissue preservation, which is the subject of the following subchapter.

3.3. Preservation of Permittivity of Biological Tissues

Given that most of the measurements of biological tissues in the literature were made on ex vivo tissue, the time elapsed since the excision of that tissue from the donor's body should also be taken into account. Ex vivo tissues are prone to dehydration and deterioration over time, which then makes it impossible to measure the actual value of the permittivity of that tissue. Even when the measurements are conducted immediately post-excision, the inevitable onset of dehydration and deterioration, especially in the case of a large number of specimens awaiting measurement, poses a significant challenge. As demonstrated by Shahzad et al. [72] on a mouse liver sample, a mere 3.5 hours of dehydration can alter both the real and imaginary part of the permittivity by more than 25%. Given these circumstances, the development of a method to preserve ex vivo tissue for an extended period would be highly advantageous. However, conventional preservation methods employed in pathology, such as immersion in formalin and other solutions, invariably alter the permittivity of the preserved tissue due to the absorption of these solutions into the tissue [73]. An alternative preservation strategy, borrowed from the food industry, involves freezing the tissue to inhibit deterioration. This approach enables the tissue sample to be frozen immediately after excision and thawed just prior to measurement. Savazzi et al. [30] conducted an investigation to determine whether the freezing and thawing process impacts the permittivity of biological tissues. Samples of chicken muscle and beef liver and adipose tissue were tested. Although the results were measured in a continuous range from 0.5 to 8.5 GHz, the results are presented and analyzed only in three discrete frequency points: 2.5 GHz, 4.5 GHz, and 6.5 GHz. The permittivity of the three tissues was measured at room temperature, before and after freezing and thawing. The findings revealed that certain tissues, such as muscle, exhibited a significant difference in permittivity before freezing and after thawing, while other tissues, such as adipose tissue, showed no statistically significant difference. The liver displayed a significant difference at some frequencies but not at others. The authors concluded that the freeze–thaw cycle results in an increase in the complex permittivity for high-water content tissues, while low-water content tissues did not have a significant change in complex permittivity. The outcomes of this study led to the conclusion that it is necessary to conduct a preliminary study for each tissue of interest in order to be sure whether the permittivity of that particular tissue can be preserved by freezing.

Building upon the preceding research, and the findings of our previous studies [63], [74], it became evident that the preservation of biological tissues and the subsequent impact on their permittivity is a complex issue that warrants further investigation. Motivated by these observations and the gaps in current knowledge, our research study aimed to delve deeper into the effects of freezing and thawing on the permittivity of brain tissues specifically. The findings of our study [75] are presented in the following section. For a more comprehensive understanding, please refer to Appendix B.

Our study [75] focused on the bovine tissues only: brain, liver, and muscle. Bovine tissues were chosen due to the availability of large healthy tissue samples. We expected that the changes in the bovine tissues' permittivity that would occur as a result of the freezing and thawing process would similarly influence the corresponding human tissues. Our expectancies were further reinforced by our previous study [63] that showed that the complex permittivities of bovine and human white matter and grey matter were very similar. In comparison with the similar freezing study [30], we introduced liquid nitrogen as an additional fast-freezing method and expanded the upper-frequency limit to 18 GHz. Furthermore, we reported both the results and the statistics continuously in the whole frequency range instead of just several discrete frequency points. Another distinction of this study is the introduction of brain tissues into the experiment, as the brain tissue was the primary interest of our previous tissue measurement campaign [63]. The muscle and liver are rather homogenous tissues that served well for the additional investigation and control of the freezing and thawing method. Additionally, we did not find any published references that examined the permittivity changes of biological tissues after freezing and thawing using liquid nitrogen.

We acquired two entire bovine brains, two entire lobes of bovine livers from two different specimens, and two bovine muscles from two different specimens from a local butcher. Figure 3.4. shows the measurement setup and a sample of each of the four measured tissue types. The precise weight scale in the setup was included to control the pressure that the probe exerted on the samples as the pressure was held constant during measurements.

(a) (b) (c) (d)

Figure 3.4. Measurement setup which includes the dish supported by polystyrene on top of a weight scale for the sample of bovine (a) brain white matter, (b) brain grey matter, (c) liver, and (d) muscle.

After the initial measurements on fresh samples, these samples were subjected to freezing either below -18 °C with the use of a commercial freezer or frozen by immersing in liquid nitrogen, nominally at -196 °C. The bovine brain, muscle, and liver that were frozen and stored in the freezer were labeled as B1, M1, and L1, respectively. Conversely, those that were frozen and stored in the liquid nitrogen tanks were labeled as B2, M2, and L2. These samples were subjected to a freezing duration of 3 days, followed by thawing in a water bath set to the ambient temperature of 25 °C, post which their permittivity was measured again. Finally, the results were processed to compare the permittivity at the same temperature of 25 °C before freezing and after thawing.

The results were processed as the average of all the measurement points across all samples of the identical tissue type, thereby enhancing the statistical robustness of the results. The results were separated into two categories: the percent permittivity change for samples B1, L1, and M1 and the percent permittivity change for samples B2, L2, and M2. The percent change was favored over the absolute change, given that the permittivity exhibited significant variation with frequency; thus, the absolute change would not yield information on the significance of the change. Additionally, polynomial fitting was performed to mitigate the narrowband fluctuations, which were a consequence of the imperfections of the setup and did not reflect the actual change in permittivity due to the freezing process. The results for bovine brain white matter are shown in Figure 3.5 and Figure 3.6 for freezing in a commercial freezer and freezing in liquid nitrogen, respectively.

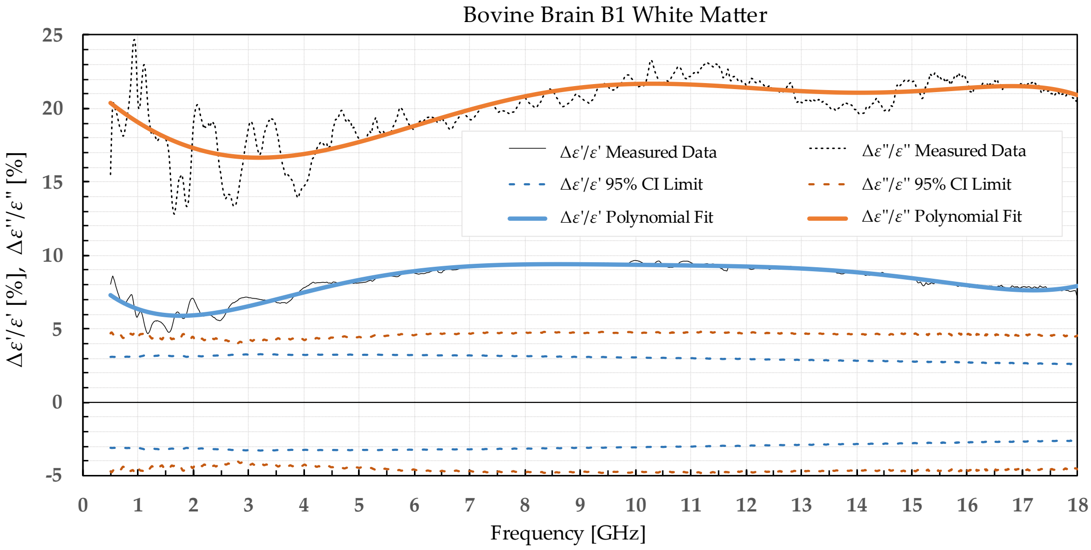

Figure 3.5. Percent change in ε' and ε'' for bovine white matter before freezing below -18 °C in a commercial freezer and after thawing.

The dashed orange and blue lines delineate the boundaries of a statistical test for easier assessment of statistical significance. The statistical test used was the unpaired *t* test as the two populations did not exhibit a difference in the standard deviation. Their *t* values were calculated for each frequency point of each tissue type and for each freezing method. The calculated values were compared to the values from the table of critical *t* values chosen for a two-tailed test with a significance level of 0.05, i.e., the confidence interval of 95%. The limits of the decision criterion for statistical significance in the change of permittivity with the used 95% CI *t* test are represented with dashed lines in Figure 3.5 and Figure 3.6.

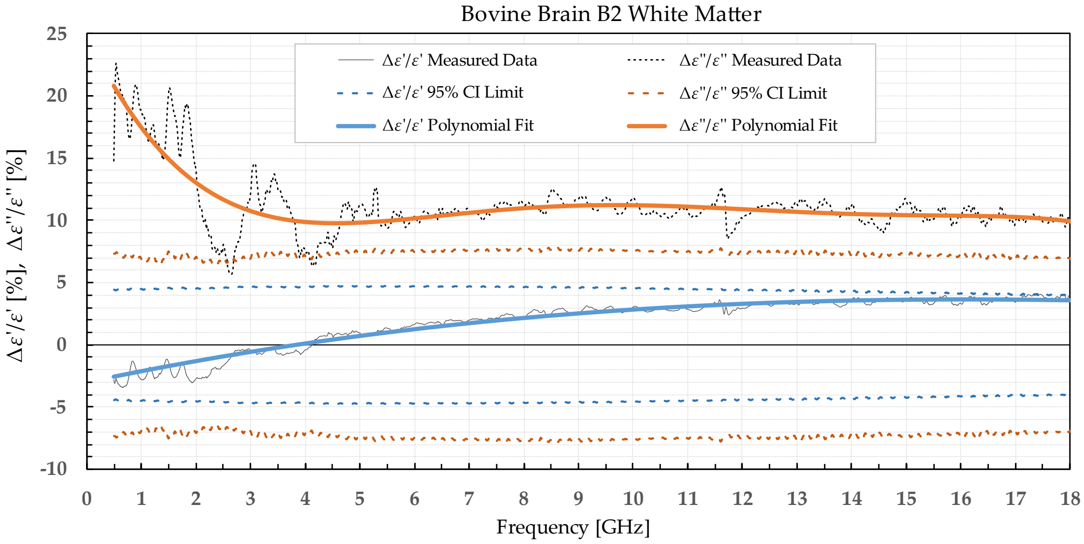

Figure 3.6. Percent change in ε' and ε" for bovine white matter before freezing in liquid nitrogen and after thawing.

The permittivity of white matter from brain B1 displayed a significant difference before and after freezing in a commercial freezer across the entire measured frequency range for both real and imaginary part of the permittivity. Freezing the white matter from brain B2 in liquid nitrogen and subsequent thawing caused a significant difference across the entire measured frequency range in ε'' while the ε' of the white matter did not display significant change across the entire frequency range. There are no consistent trends for the changes in permittivity of different tissues frozen with the same method. For the figures with the exact percentage changes in permittivity for all tissues refer to Appendix B.

Comparison of our measured permittivity difference for muscle and liver tissue before and after freezing with the results of a similar study [30] showed several consistent patterns in the changes in permittivity. For instance, in the aforementioned study [30], the permittivity of the muscle tissue exhibited an increase post-thawing for both real and imaginary part of the permittivity. This observation aligns with our results for muscle sample M1 which was frozen in a commercial freezer. Additionally, the permittivity results for the liver tissue indicated a significant difference for ε'', but not for ε' [30], which is also consistent with our findings [75]. Unfortunately, unlike muscle and liver tissue, there is an absence of a similar study on the effect of freezing the brain tissues to which we could compare our results. Our results suggest that both freezing methods produce a statistically significant change in permittivity, at least in some part of the measured frequency range. Nevertheless, depending on the application and the preferred frequency range, the permittivity change might be acceptable. If the acceptable percent change is set to, e.g., 10%, the measured permittivity change is satisfactory for liver, muscle (but only when frozen in a commercial freezer), and grey matter. Conversely, the permittivity change in white matter and muscle frozen in liquid nitrogen is not acceptable, but solely due to the change in ε'' which exceeds the set limit.

4. MODELING OF THE OECP MEASUREMENT METHOD

The existing literature on the measurement studies of biological samples underscores that the permittivity results for the same tissues can exhibit significant differences across different studies. To ensure the precision of the measured permittivity, it is necessary to properly define the primary sources of error when measuring the permittivity of biological samples. To gain a better understanding of potential error sources, it is essential to construct a comprehensive model of the entire measurement methodology. This encompasses the entire process from measuring the reflection coefficient to de-embedding the permittivity from the measured results while modelling both the probe and the measured material. Proper modeling enables the isolation of specific error sources and their easier clarification. Physical phenomena that cause these errors can appear in both biological and non-biological materials alike, so the analysis of these phenomena can be carried out on non-biological samples. This was exemplified in the research conducted within this thesis, where the measured materials were non-biological, but their permittivities were analogous to those of high-water content biological tissues. This chapter will review the literature that emphasizes the modeling of the OECP measurement method, while simultaneously situating the research conducted within this thesis within a broader context.

4.1. Microwave Measurements

In a coaxial probe at sufficiently high frequencies, both the voltage wave and the current wave comprise of two components: the incident wave propagating towards the load (open end), and the reflected wave propagating towards the generator. The reflected wave arises when the incident wave is reflected back from the open end of the coaxial probe. The voltage reflection coefficient Γ at point z is defined as the ratio of the reflected voltage phasor V_- and the incident voltage phasor V_+ [76]:

$$\Gamma = \frac{V_-\,(z)}{V_+(z)} = \frac{V_{0-}\;e^{-j\beta z}}{V_{0+}\;e^{+j\beta z}}\;, \tag{4.1}$$

where V_{0-} and V_{0+} represent the reflected and incident voltage phasors at the open end and $\beta = 2\pi/\lambda$. In analyzing the reflection properties, the origin of the axis z is at the open end of the probe, and the positive direction of the axis is from the open end to the generator i.e., VNA. The relationship between the input impedance Z_i and the input reflection coefficient Γ_i at the VNA port is given by:

$$Z_i = Z_0 \frac{1+\Gamma_i}{1-\Gamma_i} \text{ or } \Gamma_i = \frac{Z_i - Z_0}{Z_i + Z_0}. \tag{4.2}$$

Whereas input admittance and reflection coefficient at the same point on the transmission line are related with the following equation:

$$Y_i = Y_0 \frac{1-\Gamma_i}{1+\Gamma_i} \text{ or } \Gamma_i = \frac{Y_0 - Y_i}{Y_0 + Y_i}. \tag{4.3}$$

Z_0 and Y_0 represent the characteristic impedance and admittance of both the transmission line and the VNA. By combining these equations with the de-embedding equivalent circuit models, which will be discussed in detail in Chapter 4.2, one can deduce the complex permittivity from the measured reflection coefficient. The coaxial line cannot be considered an ideal transmission line as there would be additional unaccounted reflections and losses. A more accurate approach is to treat the entire transmission line between the VNA and the open end as a general two-port network, as shown in Figure 4.1. Note that this two-port network includes the transmission line within the probe, as well as the coaxial cables connecting the probe to the VNA, i.e., encompassing all components between Port 1 and Port 2 marked in Figure 4.2.

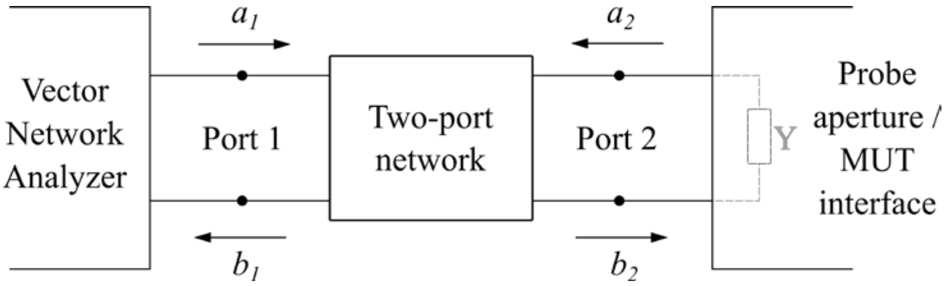

Figure 4.1. OECP represented as a general two-port network with incident (a_1 and a_2) and reflected (b_1 and b_2) waves. Adapted from [77].

N-port networks are unambiguously characterized by their scattering parameters. In the context of a two-port network, the scattering parameters are denoted as S_{11}, S_{12}, S_{21}, and S_{22}. S-parameters of the two-port network, represented in matrix form, are given by [78, pp. 4–10]:

$$\begin{bmatrix} b1 \\ b2 \end{bmatrix} = \begin{bmatrix} S_{11} & S_{12} \\ S_{21} & S_{22} \end{bmatrix} \times \begin{bmatrix} a1 \\ a2 \end{bmatrix} \tag{4.4}$$

They can also be written as two linear equations:

$$b_1 = S_{11}a_1 + S_{12}a_2 \tag{4.5}$$

$$b_2 = S_{21}a_1 + S_{22}a_2 \tag{4.6}$$

where:

a_1 and a_2 represent the incident signal at each port,

b_1 and b_2 represent the signal reflected from each port,

$S_{11} = b_1 / a_1$ with $a_2 = 0$ is the input reflection coefficient with a matched output,

$S_{22} = b_2 / a_2$ with $a_1 = 0$ is the output reflection coefficient with a matched input,

$S_{21} = b_2 / a_1$ with $a_2 = 0$ is the forward transmission coefficient with a matched output,

$S_{12} = b_1 / a_2$ with $a_1 = 0$ is the backward transmission coefficient with a matched input.

The reflection coefficient is measured at the plane of the coaxial port of the VNA as indicated by Port 1 in Figure 4.1 and Figure 4.2. The initial requirement is to translate the reflection coefficient to the plane of the interface between the MUT and the open end of the probe, denoted as Port 2 in Figure 4.1 and Figure 4.2.

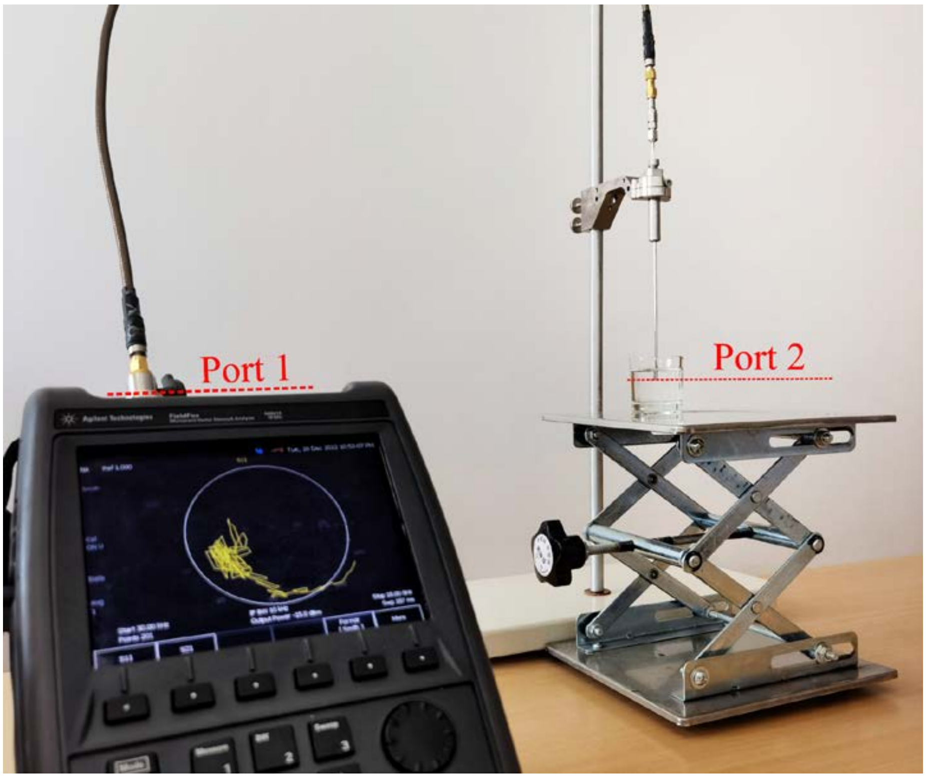

Figure 4.2. OECP measurement setup with indicated Port 1 and Port 2 planes.

Following the notation from the Equation 4.4, the required reflection coefficient Γ_{MUT} is defined as the ratio a_2/b_2, while the reflection coefficient obtained at the VNA plane Γ_{m} is defined as the ratio b_1/a_1. Γ_{MUT} can be calculated from Γ_{m} and the previously measured scattering parameters of the two-port network as follows [77]:

$$\Gamma_{MUT} = \frac{\Gamma_m - S_{11}}{S_{22}\Gamma_m + S_{12}S_{21} - S_{11}S_{22}} \; . \tag{4.7}$$

The number of unknown variables determines the required number of equations, which subsequently defines the necessary number of MUTs for calibration. For each well-defined MUT (n = 1, 2, 3, …, N) it is possible to calculate the exact Γ_{MUTn} using Equation 4.7 and measuring Γ_{mn} at Port 1. For Equation 4.7, there are three unknown variables that need to be independently determined: S_{11}, S_{22}, and the product $S_{12}S_{21}$. Scattering parameters are then defined as follows [77]:

$$S_{11} = \frac{\Gamma_{m3}\Gamma_{MUT1}\Gamma_{MUT2}(\Gamma_{m1} - \Gamma_{m2}) + \Gamma_{m2}\Gamma_{MUT3}\Gamma_{MUT1}(\Gamma_{m3} - \Gamma_{m1}) + \Gamma_{m1}\Gamma_{MUT2}\Gamma_{MUT3}(\Gamma_{m2} - \Gamma_{m3})}{\Gamma_{MUT1}\Gamma_{MUT2}(\Gamma_{m1} - \Gamma_{m2}) + \Gamma_{MUT3}\Gamma_{MUT1}(\Gamma_{m3} - \Gamma_{m1}) + \Gamma_{MUT2}\Gamma_{MUT3}(\Gamma_{m2} - \Gamma_{m3})}, \quad (4.8)$$

$$S_{22} = \frac{\Gamma_{MUT1}(\Gamma_{m2} - S_{11}) + \Gamma_{MUT2}(S_{11} - \Gamma_{m1})}{\Gamma_{MUT1}\Gamma_{MUT2}(\Gamma_{m2} - \Gamma_{m1})}, \quad (4.9)$$

$$S_{12}S_{21} = \frac{(\Gamma_{m1} - S_{11})(1 - S_{22}\Gamma_{MUT1})}{\Gamma_{MUT1}}. \quad (4.10)$$

In the process of determining the unknown scattering parameters, Port 2 is terminated with three standard loads. These loads allow for the calculation of the reflection coefficient of the material under test Γ_{MUT} and the measurement of the reflection coefficient of the probe Γ_m. The standard loads typically used for calibration are short circuit, open circuit, and a known MUT. The calculated Γ_{MUT} is derived from Equation 4.3 where the admittance of the circuit is calculated based on the chosen equivalent circuit and the value of its components. This implies that the permittivity of the MUT can only be calculated if the admittance of the equivalent circuit is known. Therefore, a detailed discussion of the equivalent circuit model of an OECP will be provided in a subsequent chapter.

4.2. Equivalent circuit model of an OECP

There are various mathematical relations that facilitate the conversion of the reflection coefficient into complex permittivity, most of them rely on modelling the admittance of the open end of the probe. The easiest way to model the impedance of an open end involves the use of a lumped element equivalent circuit. Utilizing a VNA to characterize the admittance of the OECP, it is expected that the frequency-dependent admittance measured under steady-state conditions will be indistinguishable from that of a linear network. Such a network could be a parallel or series combination of resistors, inductors, and capacitors. The impedance Z or the admittance Y of the coaxial aperture is a function of the complex permittivity of the MUT. In the past, a few variations of the equivalent model of the probe aperture admittance have been developed with the aim of making the measurements more precise. The two most prevalent models are the capacitive model and the antenna (or radiation) model. It is expected that the obtained results will largely depend on the equivalent circuit employed in the analysis.

The simple capacitive model, which serves as the basis of the calibration method described in Chapter 4.1, was first developed by Stuchly et al. [79] in 1974. The original model consisted of a shunt lumped capacitor, the capacitance of which was dependent on the permittivity value of a measured material. In their work, Stuchly et al. introduced the concept of C_0, defined as the capacitance of a coaxial probe when it is left open in the air, i.e., with no MUT. This capacitance was supposed to model the discontinuity at the termination of the coaxial line where the fringing field lines penetrate the MUT. Subsequent research by the same group [80], [81], led to the expansion of this model, incorporating an additional capacitance connected in parallel. The reasoning behind the introduction of two distinct capacitances was to differentiate between the fringing fields within the probe (in the dielectric of the probe), modeled by the first capacitance C_1, and the fringing fields outside of the probe (in the MUT), modeled by the second one C_2. It is worth mentioning that in certain literature sources, C_1 is occasionally denoted as C_f and referred to as the fringing capacitance. Similarly, C_2 is sometimes denoted as $C_0\varepsilon_r$ to highlight the dependence of the outside fringing field on the permittivity of the MUT. Moreover, it is important to underscore that the capacitances are not static values, but also functions of frequency [81]. The admittance stemming from this model is given by:

$$Y = j\omega C_f + j\omega\varepsilon_r C_0. \tag{4.11}$$

With the complex admittance, and consequently the impedance, explicitly defined, the reflection coefficient at the probe aperture can be easily obtained using the following equation:

$$\Gamma_{MUT} = |\Gamma|^{j\Phi} = \frac{1 - j\omega Z_0(\varepsilon_r C_0 + C_f)}{1 + j\omega Z_0(\varepsilon_r C_0 + C_f)} \, . \tag{4.12}$$

Consequently, complex permittivity of the measured material, denoted as ε_r for the simple capacitive circuit can be extracted using the following equation:

$$\varepsilon_r = \frac{1 - \ \Gamma_{MUT}}{j\omega Z_0 C_o(1 + \Gamma_{MUT})} - \frac{C_f}{C_0} \, . \tag{4.13}$$

The upper frequency limit of this model is inherently constrained by the undesirable radiation effect that arises when the dimensions of the open end of the probe become comparable to the operating wavelength. Given that the equivalent circuit of this model does not account for radiation effects, errors in the results as the frequency increases are an inevitable consequence. This simplified equivalent circuit entirely disregards the radiation losses, which can be modeled with an additional conductance term. It has been demonstrated that for high-permittivity MUTs, such as biological tissues, the conductance term must be included at lower frequencies than those estimated from the analysis of the coaxial probe left in the air [81].

This limitation served as the motivation for the development of the antenna model, first published by Brady et al. [82]. The antenna model perceives the open-ended coaxial probe as a functional antenna radiating in the lossy medium; therefore, this model is occasionally labeled as the radiation model. It substitutes the admittance of the probe aperture with the previously defined capacitances C_1 and C_2, and additionally incorporates a parallel-connected conductance G. The equivalent circuit from [82] yields the following formula for a normalized admittance at the probe aperture plane:

$$\frac{Y}{Y_0} = j\omega Z_0 C_1 + j\omega Z_0 C_2(\omega, \varepsilon_r) + Z_0 G(\omega, \varepsilon_r). \tag{4.14}$$

For frequencies that are sufficiently low, resulting in large wavelengths relative to the probe dimensions, C_2 can be considered frequency independent and simplified to $C_2(\omega, \varepsilon_r) = \varepsilon_r C_0$. The additional conductance is both frequency dependent and permittivity dependent: $G(\omega, \varepsilon_r)$. Conductance G equals to $G_0\ \varepsilon_r{}^{5/2}$, where G_0 is the free-space radiation conductance [82]. This allows for rewriting of Equation 4.14 as:

$$\frac{Y}{Y_0} = j\omega Z_0 C_1 + j\omega Z_0 C_0 \varepsilon_r + Z_0 G_0\ \varepsilon_r{}^{\frac{5}{2}}. \tag{4.15}$$

The fractional exponent of the complex permittivity can be traced back to the equations for admittance of a coaxial aperture in an infinite conductive plane radiating into semi-infinite space, as given by Marcuvitz [83, pp. 213–216] in 1951. The admittance of a coaxial line at the open end consists of conductance G and susceptance B connected in parallel. If the radius of the outer conductor of the probe is denoted as a, and the radius of inner conductor is denoted as b, the normalized conductance G is given by:

$$\frac{G}{Y_0} = \frac{1}{\ln\frac{a}{b}} \int_0^{\frac{\pi}{2}} \frac{d\theta}{\sin\theta}\ [J_0(\beta a \sin\theta) - J_0(\beta b \sin\theta)]^2\,, \tag{4.16}$$

which, if both a and b are much smaller than wavelength, can be simplified to:

$$\frac{G}{Y_0} \approx \frac{2}{3}\frac{1}{\ln\frac{a}{b}} \left[\frac{\pi^2(b^2 - a^2)}{\lambda^2}\right]^2. \tag{4.17}$$

From Equation 4.17, it is clear that the conductance is inversely proportional to the fourth power of frequency. Normalized susceptance is given by:

$$\frac{B}{Y_0} = \frac{1}{\pi \ln\frac{a}{b}} \int_0^{\pi} [2\,Si\,(\beta\sqrt{a^2 + b^2 - 2\,ab\,cos\,\phi} - Si\left(2\,\beta a \sin\frac{\phi}{2}\right) - Si\,(2\,\beta b \sin\frac{\phi}{2})]\,d\phi\ , \tag{4.18}$$

which can also be simplified if both a and b are much smaller than the wavelength:

$$\frac{B}{Y_0} \approx \frac{8(a+b)}{\lambda \ln \frac{a}{b}} \left[E\left(\frac{2\sqrt{ab}}{a+b} \right) - 1 \right] . \tag{4.19}$$

The function *Si(x)* represents the sine-integral function, and the function *E(x)* represents the complete elliptic integral of the second kind. Equation 4.19 shows that the susceptance is proportional to the first power of frequency.

The simplifications in Equation 4.17 and Equation 4.19 are valid if:

$$\lambda > \frac{2(a-b)}{\gamma_1} , \tag{4.20}$$

where γ_1 is determined from the first root of the Bessel-Neumann combination $\chi = \chi_{01}$:

$$\chi = \frac{\pi}{\frac{a}{b} - 1} \gamma_1 . \tag{4.21}$$

The value of χ_{01} can be found in Table 2.3 in [83, p. 74]. For the Slim Form Probe, which has an outer radius of approximately 0.840 mm and an inner radius of approximately 0.255 mm, the value of χ_{01} equals 1.234, which yields the value of $\gamma_1 = 0.901$. Following Equation 4.20, the wavelength should exceed 1.299 mm for the simplifications to be valid. In other words, the simplifications should hold true for the Slim Form Probe if the frequency is below the 230 GHz limit. As the operating range of the Slim Form Probe is only up to 50 GHz, the usable frequency range for the equations is well below the limit.

Marcuvitz [83, p. 216] states that the circuit parameters have been obtained with the assumption of a principal mode at the aperture, and that their error should be less than 10 percent, which is not negligible. The errors decrease for larger values of the ratio of a and b. The applicability of the equations given by Marcuvitz [83] for modeling the admittance of the OECP is questionable because they are suited for a coaxial line terminating in the plane of an infinite metallic screen. Therefore, the model should correspond to the OECP with an infinite metallic flange, which is clearly not the case with real-world probes. Although most of the publications that cite these equations overlook the drawbacks, the authors in [84] explicitly state that the absence of the infinite ground plane has little effects on the results. They cite the theoretical analysis done by Bahl and Stuchly [85] that does state that the effect of the ground plane is negligible. However, the analyzed coaxial probe was actually a monopole antenna as it had an extruded central conductor, whereas the OECPs used today have a central conductor that is flush with the outer conductor.

As the equivalent circuit parameters given in Equation 4.17 and Equation 4.19 are valid only for a probe radiating into free space, an additional transformation is needed for conditions where the probe is pressed against a sample of $\varepsilon_{\mathrm{r}} \neq 1$. The transformation is based on the Deschamps theorem [86], which is suitable for antennas in a conducting medium, therefore the coaxial probe will be regarded to as an antenna. The theorem states that the impedance of an antenna normalized to that of the medium takes the same value at frequency ω in a medium of index n as it does at frequency $n\omega$ in a medium of index 1. The theorem yields the following relation in equation form:

$$\frac{Z_1(\omega, \varepsilon_r\varepsilon_0, \mu_r\mu_0)}{\eta_1} = \frac{Z_2(n\omega, \varepsilon_0, \mu_0)}{\eta_2} \tag{4.22}$$

where η is the intrinsic impedance of a medium (also called wave impedance) and equals:

$$\eta = \sqrt{\frac{j\omega\mu}{\sigma + j\omega\varepsilon}}\ , \tag{4.23}$$

where $\mu = \mu_r\mu_0$ is the complex magnetic permeability of a medium which reduces to $\mu_0 = 4\pi \text{ x } 10^{-7}$ H/m for nonmagnetic materials which have the relative permeability μ_r equaling 1. The refractive index of a medium, denoted as n, is given by:

$$n = \sqrt{\varepsilon_r\mu_r}\ , \tag{4.24}$$

For nonmagnetic materials, which are the focus of this thesis, this simplifies to $n = \sqrt{\varepsilon_r}$. Equation 4.22, when applied to a nonmagnetic antenna medium, simplifies to:

$$\frac{Z_1(\omega, \varepsilon_r\varepsilon_0, \mu_0)}{\sqrt{\frac{\mu_0}{\varepsilon_r\varepsilon_0}}} = \frac{Z_2(\omega\sqrt{\varepsilon_r}, \varepsilon_0, \mu_0)}{\sqrt{\frac{\mu_0}{\varepsilon_0}}}\ , \tag{4.25}$$

which can be rewritten as:

$$\sqrt{\varepsilon_r}\, Z_1(\omega, \varepsilon_r\varepsilon_0, \mu_0) = Z_2\left(\omega\sqrt{\varepsilon_r}, \varepsilon_0, \mu_0\right). \tag{4.26}$$

Here, subscript 1 denotes the impedance of an antenna situated in a conducting medium, and subscript 2 signifies the impedance of an antenna in the free space. Transforming Equation 4.25 for admittance as the parameter of interest results in:

$$Y_1(\omega, \varepsilon_r\varepsilon_0, \mu_0) = \sqrt{\varepsilon_r}\, Y_2\left(\omega\sqrt{\varepsilon_r}, \varepsilon_0, \mu_0\right). \tag{4.27}$$

This can be interpreted as follows: the admittance of an antenna at the frequency ω surrounded by a medium of complex relative permittivity ε_r equals the admittance of an antenna in free space at frequency $\omega\sqrt{\varepsilon_r}$ multiplied by $\sqrt{\varepsilon_r}$.

By scaling the frequency dependence of the free-space conductance of the coaxial probe from Equation 4.17 according to Equation 4.27, the frequency is multiplied by $\sqrt{\varepsilon_r}$ before exponentiation, yielding $(\sqrt{\varepsilon_r})^4 = \varepsilon_r^2$. The entire conductance is subsequently multiplied by $\sqrt{\varepsilon_r}$ resulting in a $G\ \varepsilon_r^{\frac{5}{2}}$ addend as is seen in Equation 4.15.

However, the Deschamps transformation presents certain caveats that question the applicability of the theorem to the open-ended coaxial probe problem. Deschamps [86] states that the theorem is not applicable to aperture antennas unless the transition of the medium from ε_0 to ε_r is carried out inside the coaxial probe before its open end. As a result, the fields in the interface between two mediums can be represented by the principal modes only. In all other cases, i.e., when the medium is modified only outside of the coaxial probe, the field in that aperture usually contains higher-order modes and Equation 4.27 can only be used as an approximation.

The aforementioned drawbacks of the derivation of the expanded equivalent circuit model were also pointed out in other works such as Grant et al. [87] which stated that little confidence can be attached to such procedure and that a more rigorous treatment is required. Similarly, Mosig et al. [88] criticized the methodology, stating that the Marcuvitz's formula cannot be generalized to the OECP configuration as the error increases for high permittivity and lossy dielectrics.

Beyond these limitations, there is an additional drawback of the proposed antenna model. As a result of the fifth order of Equation 4.15, there are five potential solutions, but not all of them should have a physical significance, i.e., $\varepsilon' > 1$ and $\varepsilon'' > 0$. Because the fifth order in Equation 4.15 adds additional complexity, the majority of published measurement studies opt for the simpler, purely capacitive, model.

Marsland and Evans [84] compared the two admittance models by postprocessing the results of dielectric liquid measurements in the frequency range from 50 MHz to 2.6 GHz with each model. The probe used in measurements was characterized by an inner conductor diameter of 1.63 mm and an outer conductor diameter of 5.28 mm. The data derived from ethanediol measurements revealed an improvement in accuracy when the admittance model with incorporated conductance was used. Interestingly, this improvement was also evident at the lowest measured frequencies, thereby raising the question of whether the improvement could be attributed to the additional calibration standard necessary for the expanded admittance model. The additional standard used was methanol which has a similar dielectric dispersion to that of ethanediol. The improvement in results is even more questionable upon observing the permittivity results for 0.15 M saline, where the disparity between the two admittance models was not as significant. Consequently, the authors concluded that the results derived from the simpler admittance model were satisfactory for their intended application, leading to the decision to conduct future work using the simpler model.

The two models were also experimentally analyzed by Ruvio et al. [89] using liquid samples. The frequency range of the measurements was from 0.5 GHz to 4.5 GHz and the probe used was Keysight Slim Form Probe. Although the antenna model turned out to be somewhat more accurate, the authors emphasized that, due to its complexity and the absence of a unique solution, it is not suitable for samples with a wide range of permittivity values, such as biological tissues. The antenna model yields five distinct solutions for each frequency point and given the intricate nature of dielectric properties of biological tissues; it would be challenging to determine with certainty which solutions should be discarded. Furthermore, compared to a simple capacitive model, a more complex antenna model requires an additional calibration standard. This adds to the complexity and potential uncertainty in the application of the antenna model.

It is important to highlight that the frequencies examined in the studies [84], [89] were consistently below the maximum operating range of the probe and possibly below the frequency at which the radiation becomes significant, particularly in the case of study [89]. As such, the precise advantages in terms of accuracy when utilizing the expanded admittance model remain to be verified. Further research is required to determine the conditions under which the expanded model may offer improved performance.

An alternative calibration method, proposed by Bao et al. [90], does not necessitate the knowledge of the lumped-element model components even though it is based on the simple capacitive model. Instead, it operates with the complex constants designated as A_1, A_2 and A_3 which implicitly include the values of lumped elements. By measuring the reflection coefficient Γ_m of a probe terminated with the MUT, the complex permittivity of the measured material can be expressed as:

$$\varepsilon_r = \frac{A_1 \Gamma_m - A_2}{A_3 - \Gamma_m}. \tag{4.28}$$

The values of A_1, A_2 and A_3 can be determined purely from the measured reflection coefficients of the standard terminations during calibration. Each of these constants is a frequency-dependent complex value. The most straightforward method to calculate all three parameters is if one of the calibration standards is a short circuit. In this scenario, it is only necessary to calculate the values of A_1 and A_2 , as A_3 is equivalent to the measured reflection coefficient of the short termination. The equations for the other two parameters are:

$$A_1 = \frac{\varepsilon_a\,(\Gamma_m^s - \Gamma_m^a) - \ \varepsilon_b\,(\Gamma_m^s - \Gamma_m^b)}{\Gamma_m^a - \Gamma_m^b}, \tag{4.29}$$

$$A_2 = \frac{\varepsilon_a\,(\Gamma_m^s - \Gamma_m^a)\Gamma_m^b - \ \varepsilon_b\,(\Gamma_m^s - \Gamma_m^b)\Gamma_m^a}{\Gamma_m^a - \Gamma_m^b}. \tag{4.30}$$

In these equations, the subscripts of complex permittivity and the superscripts of measured reflection coefficient denote the calibration standard in question: standard a, b, or short circuit standard s. Upon obtaining these three complex constants, the unknown complex dielectric constant can be calculated using Equation 4.7 from Γ_m.

4.3. Computer Electromagnetic Modeling and Simulation

The process of computer electromagnetic modeling and simulation in the context of the OECP measurement method involves the application of mathematical principles and methods to predict various characteristics of the coaxial probes. These characteristics include parameters such as impedance, scattering parameters, and power losses, among others. Modeling open-ended coaxial probes presents a higher degree of complexity due to the need to account for the interaction between the probe and its environment. Despite this complexity, the basic approach aligns with that used for modelling other antenna types. This approach involves segmenting the probe and its surroundings into smaller sections, followed by the calculation of the electromagnetic field at each section using Maxwell's equations.

Two primary simulation methods for solving Maxwell's equations are utilized in this context: frequency domain simulation and time domain simulation. The software package used for the frequency domain analysis within this thesis was Altair FEKO [32], while Dassault Systems CST [31] was used for the time domain analysis. Time domain simulations involve the direct solution of Maxwell's equations in the time domain, employing techniques such as the Finite-Difference Time-Domain (FDTD) method. The electromagnetic response of the system is calculated as a function of time. One of the key advantages of using the time domain method is the inherent broadband nature of the results, which reduces the need for multiple simulations. Conversely, frequency domain simulations solve Maxwell's equations in the frequency domain using techniques such as the Finite Element Method (FEM). The system response is calculated at specific frequencies. The primary advantage of frequency domain solvers is their ability to easily simulate advanced material models, such as dispersion or loss, without being as memory intensive as their time domain counterparts. Both time domain and frequency domain simulations offer unique advantages and are chosen based on the specific requirements of the analysis. The choice of the simulation method is crucial in accurately predicting the behavior of the OECP and achieving reliable measurement results.

4.3.1. FEKO

FEKO is a comprehensive 3D EM simulation software developed by Altair Engineering [32]. The acronym FEKO originates from the German phrase *Feldberechnung für Körper mit beliebiger Oberfläche*, which translates to "field calculations involving bodies of arbitrary shape". The software's default numerical method for solving modeled structures is the Method of Moments (MoM), which provides a full-wave solution for integral form of Maxwell's equations. The MoM effectively transforms the governing equation of a boundary-value problem into a matrix equation, thereby facilitating its solution. This transformation involves the projection of an integral equation into a system of linear equations using discrete surface meshes. Consequently, the configuration of the coaxial probe and the MUT is represented as a set of smaller, simpler mesh elements, enabling the easier calculation of current distribution. While the MoM is highly effective for analyzing metallic structures, it is less suitable for inhomogeneous structures or higher frequencies due to the expansion of the number of mesh cells.

As the model of coaxial probe with the MUT comprises of both metallic and dielectric media, it is considered a complex model. The default MoM solver in FEKO incorporates two methods specifically designed for solving problems with models that involve dielectric bodies: the Surface Equivalence Principle (SEP) and the Volume Equivalence Principle (VEP). SEP establishes a relationship between an arbitrary current distribution within an imaginary closed surface and an equivalent source on the surface. It introduces equivalent electric and magnetic currents on the surface of a closed dielectric body, which can be arbitrarily shaped and discretized using triangles. This principle is frequently used to simplify the analysis of radiating structures such as antennas. VEP, on the other hand, extends MoM for the modeling of dielectric bodies with a volume mesh, which can be arbitrarily shaped and discretized into tetrahedra and cuboids. For complex problems that cannot be adequately solved by a single solver, FEKO offers hybridized solvers to efficiently analyze electrically large problems. A common hybrid solver is the combination of MoM and FEM. In this hybrid setup. FEM is utilized for modeling the dielectric media, while the metallic parts are modeled using MoM. FEM subdivides a large system into smaller, simpler parts known as finite elements, collectively referred to as a mesh. The governing differential equations are applied individually to each element, and the equations for each element are assembled into a global system of equations. Following the application of known conditions at the system boundaries, the global system of equations is solved to obtain the field variable at each node. This approach allows for a comprehensive and accurate analysis of complex electromagnetic systems. However, within our research, this hybridized solver was unsuitable as the FEM used for solving the dielectric parts was not compatible with the waveguide port used as an excitation in our model. Therefore, the modeling of dielectric media in the MoM formulation was performed using the SEP.

4.3.2. CST

CST Studio Suite [31] is a high-performance 3D EM simulation software package for designing, analyzing, and optimizing electromagnetic components and systems. It provides an integrated design environment equipped with tools for the design and optimization of devices operating across a broad frequency spectrum, ranging from static to optical frequencies. The software suite offers multiple robust solver modules, each offering distinct advantages within their respective domains. These solvers are based on various numerical methods, including FEM, MoM, Multilevel Fast Multipole Method (MLFMM), Finite Integration Technique (FIT), Transmission Line Matrix Method (TLM) and others. For the simulations conducted within our research, the FIT was employed.

The Finite Integration Technique is a full-wave iterative technique used for solving electromagnetic problems. This technique offers a spatial discretization scheme for Maxwell’s integral equations, rendering them suitable for computer simulations and allowing for the simulation of real-world electromagnetic field problems with complex geometries. The initial step of the FIT method involves confining the electromagnetic field problem, which usually represents an open boundary problem, to a bounded spatial region. Subsequently, the computational domain is decomposed into a locally finite number of simple geometric cells, such as tetrahedra or hexahedra. This method allows for the inclusion of two different materials within a single grid cell, resulting in a reduction in the resource requirements, which is particularly important for complex heterogeneous structures. Following this decomposition, a computational matrix is derived, which can then be efficiently solved in the time domain.

4.3.3. Modeling, Simulation and Validation of the Complete Measurement Process

In our research [91], we have successfully demonstrated and validated that the dielectric permittivity measurement method using open-ended coaxial probe in the microwave frequency range can be completely and reliably modeled and simulated using computational electromagnetic modeling and simulations, followed by the postprocessing calculations based on the simple capacitive-load model. The validity of this model was examined with respect to the dimensions of the probe, the frequency range, and the characteristics of the MUT. As was previously stated, within this thesis, we have modeled the flangeless Slim Form Probe in the microwave frequency range from 0.5 to 18 GHz. The frequency range of up to 18 GHz analyzed in this study represented a significant extension with respect to the previous studies.

The initial phase of the investigation entailed the empirical validation of the simple capacitive-load model by physical measurements. This phase examined how accurate the aforementioned model is in defining the admittance of the coaxial open end terminated by the MUT. Specifically, it evaluated how the measurement results derived from the simple capacitive-load model agree with the measurement results obtained by a more complex load model embedded in the manufacturer's measurement software. In the probe specifications, the manufacturer does not explicitly disclose the model used for postprocessing calculations to derive the complex permittivity from the measured reflection coefficient. However, the manufacturer's application note [36] cites the work of Blackham and Pollard [92] in the context of deriving the MUT permittivity from the reflection coefficient measured by the coaxial probe. This citation implies the use of polynomial model of the load admittance, with coefficients optimized for the exact probe geometry. In our work, the permittivity values obtained by the two methods were compared. This comparison served to verify the validity of the hypothesis that the admittance of the probe and MUT could be modeled using a simple capacitive-load model.

Furthermore, the permittivity values obtained from the measurements were compared with reference values for deionized water and saline (NaCl) solutions, which served as the MUTs, in order to validate the overall validity of the measurement setup. The dielectric permittivity of NaCl solutions can be characterized by the Cole–Cole dispersion model, provided that the dispersion parameters ε_∞, ε_s, τ, α, and σ_s are known. For each concentration c of saline, these parameters were computed using polynomial equations that were derived and validated in [93]. The exception to this was ε_∞, which maintained a constant value of 5.2 for both water and all saline solutions. The equations used for the calculation of Cole–Cole parameters for saline solution of concentration c (in moles per liter, M) were as follows:

$$\varepsilon_\mathrm{s} = \varepsilon_\mathrm{s\_water}(1 - 3.742 \times 10^{-4}tc + 0.034c^2 - 0.178c + 1.515 \times 10^{-4}t - 4.929 \times 10^{-6}t^2), \tag{4.31}$$

$$\tau = \tau_{water}(1.012 - 5.282 \times 10^{-3}tc + 0.032c^2 - 0.01c - 1.724 \times 10^{-3}t + 3.766 \times 10^{-5}t^2)\,, \tag{4.32}$$

$$\alpha = -6.348 \times 10^{-4}tc - 5.1 \times 10^{-2}c^2 + 9 \times 10^{-2}c\,, \tag{4.33}$$

$$\sigma_s = 0.174tc - 1.582c^2 + 5.923c\,. \tag{4.34}$$

Here, $\varepsilon_\mathrm{s\_water}$ = 78.36, τ_water = 8.27×10^{-12} s, and t represents the temperature in degrees Celsius. The values derived from these calculations are presented in Table 4.1. These parameters were input into the single pole Cole–Cole model (as per Equation 3.1) to calculate the complex permittivity of each saline solution. The real and imaginary components of the complex permittivity were then extracted and utilized as reference values for comparison and for the simulation models.

Table 4.1. Cole–Cole parameters of the analyzed saline solutions.

Saline Concentration	$\boldsymbol{\varepsilon_\infty}$	$\boldsymbol{\varepsilon_s}$	$\boldsymbol{\alpha}$	$\boldsymbol{\sigma_s}$ **[S/m]**	$\boldsymbol{\tau}$ **[ps]**
0.154 M	5.2	76.220	8.033×10^{-12}	1.020×10^{-2}	8.033
0.25 M	3.2	74.912	7.930×10^{-12}	1.535×10^{-2}	7.930
0.5 M	5.2	71.741	7.686×10^{-12}	2.432×10^{-2}	7.686
1 M	5.2	66.398	7.297×10^{-12}	2.313×10^{-2}	7.297

Figure 4.3. shows the measurement results for a 0.5 M saline solution. Both the real and imaginary components of the permittivity are represented by three distinct lines: the measurement result obtained from the embedded postprocessing of the measured reflection coefficient in the measurement software, the measurement result derived from postprocessing of the reflection coefficient using the simple capacitive-load model and the Cole–Cole dispersion model for the exact concentration of the saline solution. The measurement results were plotted using a moving average with a frequency span of ±125 MHz at each frequency point. This approach smoothed the lines by eliminating minor fluctuations that do not reflect actual result variations but are instead attributable to imperfections in the measurement setup.

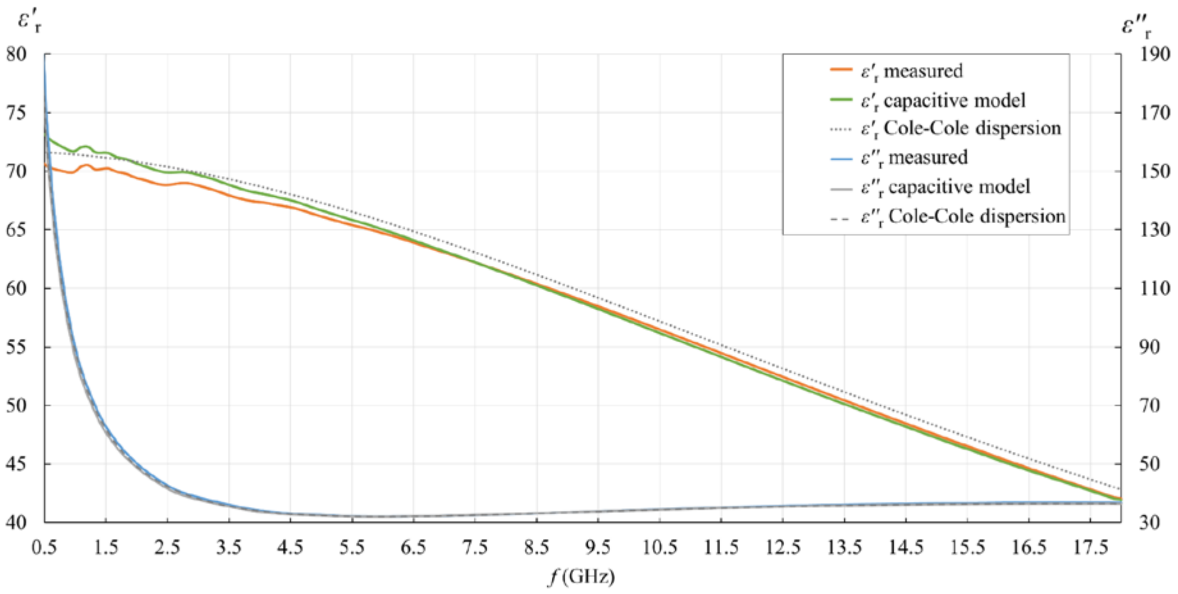

Figure 4.3. ε' and ε'' results for 0.5 M saline obtained from the: measurement software ("measured"), postprocessing with simple capacitive-load model ("capacitive model") and dispersion model ("Cole–Cole dispersion").

As observed in Figure 4.3., both measured values slightly and systematically differ from the Cole–Cole dispersion model. This trend is more pronounced with higher ionic concentrations of the saline. The discrepancies can be attributed to temperature fluctuations of the measured MUT during handling and measurement. Also, the difference could be explained by the known fact that measurement accuracy diminishes as the permittivity of the MUT deviates further from the reference liquid used in the calibration process, which in this case was deionized water. Regardless, the accuracy of the Slim Form Probe is declared at ±10%, and the difference between the measured values and the dispersion models falls within this accuracy. Consequently, the minor discrepancies between the measured results and the dispersion models were not the focus of this part of the study. Instead, the results obtained from the measurement software were considered as the accurately measured values (and thus as the reference values for comparisons), disregarding their deviation from the Cole–Cole dispersions. Therefore, the difference between the result obtained by postprocessing using the simple capacitive-load model and the result obtained by the measurement software was deemed an error. The relative error of the simple capacitive-load model for ε' and ε'' is shown in Figure 4.4. Due to the equivalent conductivity σ being directly proportional to ε'', the relative error of ε'' is equivalent to the relative error of σ. These relative errors, presented in Figure 4.4., equate to zero for water, as water was used as the calibration standard for both postprocessing methods.

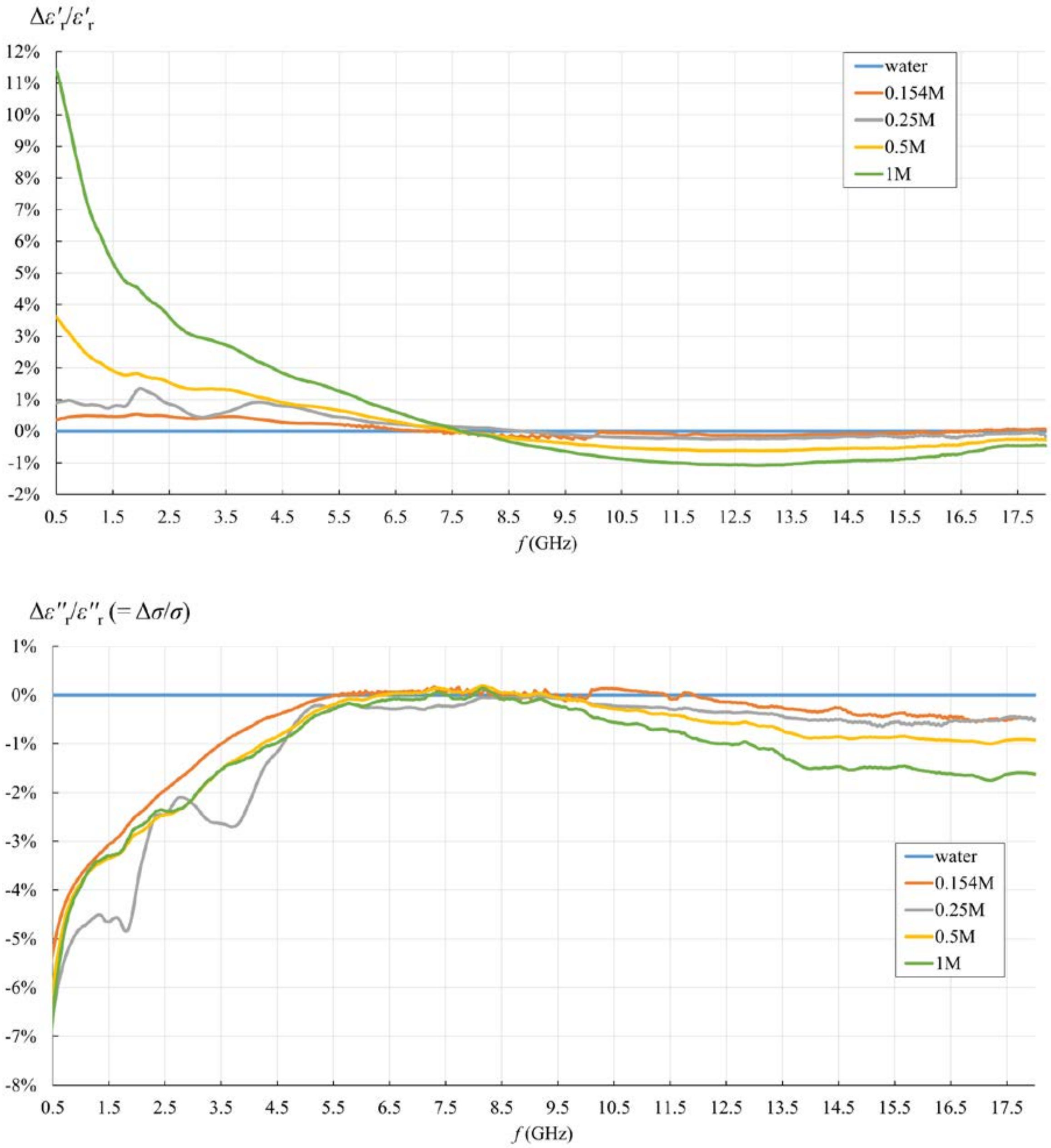

Figure 4.4. ε' (top) and ε'' (bottom) relative error of the simple capacitive-load model with respect to the measurement result obtained from the measurement software, for water and saline solutions.

Figure 4.4. reveals that the most pronounced discrepancy occurred in the lower part of the frequency span, specifically below ca. 7.5 GHz. Here, the simple capacitive-load model consistently yielded marginally higher ε' and lower ε'' compared to the actual measured value. The difference between the models is inversely proportional to the frequency for low frequencies and directly proportional to the ion concentration of the saline. Due to the ionic origin of this phenomenon, it was more prominent at low frequencies and diminished as the

frequency increased. This low-frequency phenomenon requires additional components to model the load accurately, which are not included in the simple capacitive-load model. The manufacturer does not specify whether their measurement software accounts for this effect or implements any corrections during postprocessing. Figure 4.4 reveals that the magnitude of the relative error of the real part of the permittivity calculated with the capacitive model, remained within ca. 0.5% for physiological saline, around 1% for 0.25 M saline, less than 4% for 0.5 M saline, and exceeded 11% for 1 M saline at the lowest frequency. In terms of ε'', the difference again manifested in the lower part of the frequency range, specifically below ca. 5.5 GHz, but exhibited the opposite sign: the simple capacitive-load model systematically yielded slightly lower results than the actual measured value. Once again, the error amplified towards the low frequencies, reaching a maximum magnitude of nearly 7% at the lowest frequency. This suggests that the relative error is inversely proportional to frequency at low frequencies. However, the error for ε'' at low frequencies did not significantly depend on the ion concentration in the saline. The magnitude of this error was not significant below 18 GHz: less than 1% for all concentrations lower than 1 M and less than 2% for the highest NaCl concentration of 1 M. It is noteworthy that the error slightly increased with frequency. This might be associated with the emergence of radiation from the probe end. However, due to the frequency limit of our setup, we were not able to determine the significance of this error above 18 GHz.

Upon the successful validation of the simple capacitive-load model in the initial phase of the study, the investigation proceeded to its second phase. This second phase of the study was the validation of the simulation of the complete measurement process. We examined the agreement of the coaxial probe simulation results, which were obtained by two entirely different numerical methods applied on the identical probe model, followed by the postprocessing calculations that were validated in the initial phase of the study. The objective of this study was to analyze the error occurring when using the simple capacitive-load model for postprocessing of the simulation data in dependence on the ionic concentration of the MUT.

Moreover, two simulation methods and solvers were used to enable comparison between them, which was also one of the aims of this study. Not only do the two numerical methods originate from different software packages, but they also diverge in their approaches to the electromagnetic problem: one resolves it in the frequency domain, while the other does so in the time domain. The MoM was selected as a frequency-domain solver method implemented in FEKO, and the FIT was chosen as a time-domain solver implemented in CST. Initially, the Slim

Form Probe was modeled in the software, after which the MUT volume was incorporated into the probe model. Analogous to the measurements, the permittivity of the MUT was set to the value of either water or saline solutions. The Debye dispersion was used to model the permittivity of water and the Cole–Cole dispersion was used for modeling the permittivity of saline solutions. Subsequently, electromagnetic simulations were conducted up to 18 GHz for each MUT, yielding the reflection coefficient at the probe input port. Finally, the permittivity of the MUT was de-embedded from the reflection coefficient using the simple capacitive-load model.

The permittivity of the MUT, derived as the final result of the comprehensive simulation process, was compared to the MUT permittivity initially set in the software model. This comparison served to authenticate the entirety of the modeling and simulation methodology. Figure 4.5. illustrates the relative error between the set permittivity and the value obtained by the postprocessing with the simple capacitive-load model. As FEKO operates in the frequency domain, the results are represented by discrete frequency points corresponding to the simulations performed. Conversely, the results obtained with CST using a time-domain solver span the frequency range continuously, as depicted by the colored lines in Figure 4.5.

The agreement between the results obtained by FEKO, CST, and theoretical dispersion models depends on both the frequency and ionic concentration. At lower concentrations of 0.154 M and 0.25 M, FEKO and CST exhibited substantial agreement on $\varepsilon_{\mathrm{r}}'$, aligning with the dispersion within a relative error of less than 1%. At 0.5 M, FEKO and CST closely paralleled each other above 2 GHz, with the error magnitude only marginally surpassing 1% across the majority of the frequency range and peaking at ca. 2%. For 1 M saline, FEKO and CST had a maximum error magnitude of ca. 2.5% for frequencies above 4 GHz. At lower frequencies, CST error increased to a maximum of over 4%, while the FEKO error magnitude peaked at over 7% at 1 GHz.

For $\varepsilon_{\mathrm{r}}''$, two distinct frequency ranges can be observed, below and above 3 GHz. Below 3 GHz, FEKO and CST diverged, with FEKO exhibiting a positive error reaching up to ca. 3–4% maximum, and CST error being negative with a magnitude up to ca. 2–3%. The error below 3 GHz did not appear to be strongly influenced by the concentration. The error above 3 GHz for both solvers increased with NaCl concentration. At lower concentrations of 0.154 M and 0.25 M, the error magnitude above 3 GHz remained within 1% and ca. 1.5%, respectively. At 0.5 M, the error magnitude above 3 GHz reached a maximum of slightly over 2%, while for 1 M, the maximum was ca. 3.5%. In conclusion, the simple capacitive-load model yielded only negligible errors, both for the frequency-domain and for the time-domain solvers. We also concluded that the time-domain solver (FIT in CST) was superior for this analysis compared to the frequency-domain solver (MoM in FEKO), owing to its ability to provide continuous results across the entire frequency range with exceptional precision.

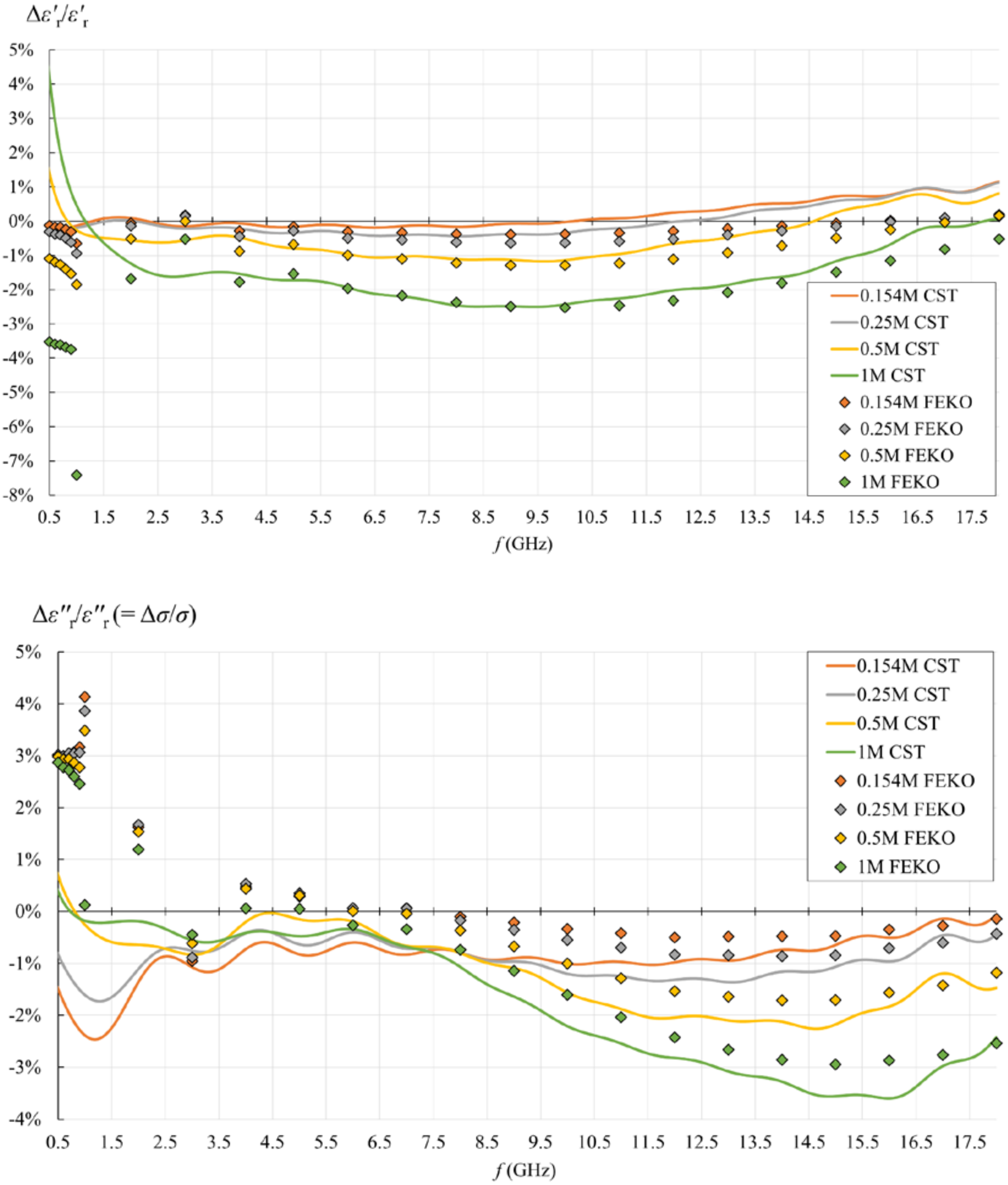

Figure 4.5. ε′ (top) and ε″ (bottom) relative error of the simple capacitive-load model with respect to the set permittivity value.

In both measurements and simulations, the error associated with the simple capacitive-load model was found to be proportional to the ionic concentration of the MUT. For the physiological saline, the deviation of the capacitive model from the accurate results was negligible. This is a critical conclusion, as our primary research interest is in dielectric measurements of biological materials, and the physiological saline closely approximates the biological materials with high water content.

By validating the simulation of the complete measurement process, which consists of computer electromagnetic modeling and simulations followed by the postprocessing calculations using the simple capacitive-load model, we are able to confidently employ this simulation method in our future work when investigating various dielectric measurement scenarios and the associated phenomena. This will be particularly beneficial for studies on biological tissues, where the realizations of the measurement scenarios can be extremely demanding, thus greatly benefiting from an accurate simulation method.

However, all the conclusions drawn are applicable within the studied frequency range, encompassing the lowest and middle parts of the declared probe frequency range. The highest part of the probe frequency range will be the subject of future studies. Even though our study [91] expanded the upper frequency range of the analysis with respect to previous studies, the frequency range of the Slim Form Probe extends even further beyond the frequencies analyzed. The upper frequency limit corresponds to the excitation of higher-order modes within the coaxial line. Below this limit, the TEM (Transverse Electromagnetic) mode is the only propagating mode. In the TEM mode, the electric field lines extend radially from the center conductor across the entire coaxial line, as depicted in Figure 4.6a, with the exception of the vicinity of the probe aperture where fringing fields are present.

The first higher-order mode to propagate in a coaxial line is the TE_{11} (Transverse Electric) mode, as illustrated in Figure 4.6b, with a cutoff frequency as referenced in [77]:

$$f_c \approx \frac{2c}{\sqrt{\varepsilon_r}\,\pi\,(D+d)}. \tag{4.35}$$

In the equation, d represents the diameter of the center conductor, and D signifies the inside diameter of the outer conductor. Both d and D are annotated in Figure 4.6. It is evident from the Equation 4.35 that a reduction in the size of the coaxial probe results in an increase in its cutoff frequency.

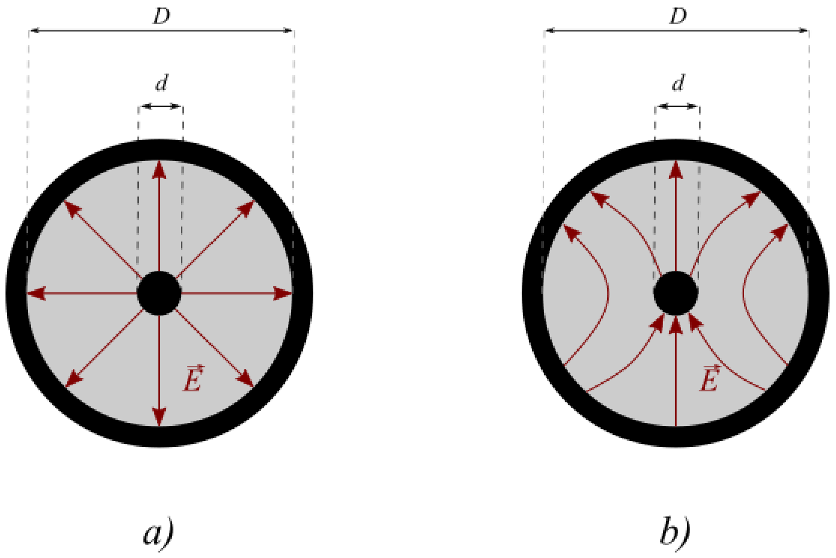

Figure 4.6. Electric field lines in a coaxial cable operating in a) TEM mode b) TE_{11} mode.

The upper frequency limits of several of the most commonly used coaxial probes are shown in Table 4.2. It is clear that during our research done on the Keysight Slim Form Probe geometry, we did not approach its upper frequency limit.

Table 4.2. Calculated upper frequency limits given for common commercial coaxial probes.

Type of coaxial probe	d [mm]	D [mm]	ε_r	Calculated f_c [GHz]	Maximum frequency from the datasheet [GHz]
Keysight Slim Form	0.51	1.68	2.08	60.43	50
DAK 3,5	0.93	3.5	2.53	27.09	20
DAK 12	2.18	12	2.53	8.46	3
DAK 1.2E	0.28	1.2	3.04	73.96	67
RG401 (used in [84])	1.63	5.28	2.08	19.15	18

While our results were limited to 18 GHz due to the limitations of the equipment used, the frequencies explored are still relevant as they encompass several biological dispersions, which are crucial in understanding the interaction between electromagnetic fields and biological tissues. Moreover, the frequencies investigated are commonly used in medical treatments such as microwave ablation and hyperthermia. Additionally, the frequencies are of interest for dosimetry studies, which are essential for assessing the exposure of humans to non-ionizing radiation. Beyond the results and conclusions, the value of our research lies in the established methodology. We utilized a simple capacitive model in our calibration, providing a simple and reliable method for de-embedding the permittivity from the reflection coefficient. This methodology can be readily adapted and updated if future research indicates so.

5. SCIENTIFIC CONTRIBUTIONS OF PUBLICATIONS

This chapter compiles abstracts of the published papers, along with an overview of the scientific contributions of each paper. Additionally, the contributions of the doctoral candidate are emphasized in every individual publication using the CRediT - Contributor Roles Taxonomy [94]. The taxonomy organizes authors' contributions within 14 predefined roles. The roles describe each contributor's exact contribution to the publication and are listed in Table 5.1 [94]. Not all fourteen roles must be listed and credited for every publication.

Table 5.1. CRediT roles and definitions.

ROLE	DEFINITION
CONCEPTUALIZATION	Ideas; formulation or evolution of overarching research goals and aims
METHODOLOGY	Development or design of methodology; creation of models
SOFTWARE	Programming, software development; designing computer programs; implementation of the computer code and supporting algorithms; testing of existing code components
VALIDATION	Verification, whether as a part of the activity or separate, of the overall replication/ reproducibility of results/experiments and other research outputs
FORMAL ANALYSIS	Application of statistical, mathematical, computational, or other formal techniques to analyze or synthesize study data
INVESTIGATION	Conducting a research and investigation process, specifically performing the experiments, or data/evidence collection
RESOURCES	Provision of study materials, reagents, materials, patients, laboratory samples, animals, instrumentation, computing resources, or other analysis tools
DATA CURATION	Management activities to annotate (produce metadata), scrub data and maintain research data (including software code, where it is necessary for interpreting the data itself) for initial use and later reuse

WRITING - ORIGINAL DRAFT	Preparation, creation and/or presentation of the published work, specifically writing the initial draft (including substantive translation)
WRITING - REVIEW & EDITING	Preparation, creation and/or presentation of the published work by those from the original research group, specifically critical review, commentary or revision – including pre-or postpublication stages
VISUALIZATION	Preparation, creation and/or presentation of the published work, specifically visualization/ data presentation
SUPERVISION	Oversight and leadership responsibility for the research activity planning and execution, including mentorship external to the core team
PROJECT ADMINISTRATION	Management and coordination responsibility for the research activity planning and execution
FUNDING ACQUISITION	Acquisition of the financial support for the project leading to this publication

5.1. Publication 1: Complex Permittivity of Ex-Vivo Human, Bovine and Porcine Brain Tissues in the Microwave Frequency Range

5.1.1. Abstract

Accurate knowledge about the dielectric properties of biological tissues in the microwave frequency range may lead to advancement of biomedical applications based on microwave technology. However, the published data are very scarce, especially for human brain tissues. The aim of this work was to measure and report the complex permittivity of brain white matter, grey matter and cerebellum. Complex permittivity was measured on human, bovine and porcine brain tissues in the microwave frequency range from 0.5 to 18 GHz using an open-ended coaxial probe. The results present a valuable addition to the available data on the brain tissue complex permittivity. Some noticeable variations between the results lead to several conclusions. Complex permittivity variation within the same tissue type of the individual species was comparable to interspecies variation. The difference was prominent between human brains obtained from autopsies, while bovine brains obtained from healthy animals showed very similar complex permittivity. We hypothesize that the difference might have been caused by the basic pathologies of the patients, where the associated therapies could have affected the

brain water content. We also examined the effect of excised tissue degradation on its complex permittivity over the course of three days, and the results suggest the gradual dehydration of the samples.

5.1.2. Scientific Contributions

The main scientific contribution of this publication are the new models of complex dielectric permittivity of brain tissue (grey matter, white matter, and cerebellum) based on Cole–Cole parameters obtained by systematic measurement experiments in the microwave frequency range on ex vivo tissue samples of animal and human brains. Previous Cole–Cole permittivity models of brain tissues that were commonly used for human dosimetry studies and were actually based on compiled measurement results primarily done on animal tissues. The new models are more sophisticated than the existing ones as they are developed for each individual measured species. Consequently, models of human brain tissue permittivity (grey matter, white matter, and cerebellum) are based exclusively on measurements of the human brain, which have not been carried out before, except for grey matter in a very narrow frequency band.

5.1.3. Authors Contribution

Authors: Anđela Matković (A.M.), Anton Kordić (A.K.), Antonia Jakovčević (A.J.) and Antonio Šarolić (A.Š.)
Author Contributions: Conceptualization, A.Š. and A.K.; methodology, A.Š., A.M., A.K. and A.J.; formal analysis, A.M. and A.Š.; investigation, A.M., A.Š., A.K. and A.J.; writing—original draft preparation, A.M., A.Š. and A.K.; writing—review and editing, A.M., A.Š., A.K. and A.J.; supervision, A.Š.; project administration, A.Š.

5.1.4. Supplementary Materials

The numerical values of the measured permittivity are made available in the form of downloadable Excel tables, as Supplementary Materials, and they include:

- human white matter, grey matter and cerebellum permittivity for brains H1 and H2, with the average permittivity of human white matter, grey matter and cerebellum;
- bovine white matter and grey matter permittivity for brains B1, B2 and B3, and cerebellum permittivity for brain B1, with the average permittivity of bovine white matter and grey matter;

- porcine white matter and grey matter permittivity;
- human white and grey matter permittivity for brain H1 measured along the course of three days;
- Cole–Cole models for the average permittivity of each tissue.

The following supporting information can be downloaded at: https://www.mdpi.com/article/10.3390/diagnostics12112580/s1.

5.2. Publication 2: The Effect of Freezing and Thawing on Complex Permittivity of Bovine Tissues

5.2.1. Abstract

The aim of this study was to investigate how the freezing and thawing of biological tissues affect their complex permittivity in the microwave frequency range from 0.5 MHz to 18 GHz. We measured the complex permittivity of ex vivo bovine tissues, including brain white and grey matter, liver, and muscle, using an open-ended coaxial probe. Bovine tissues were chosen for their availability and similarity to human tissue permittivity. The samples were measured at 25 °C, before they were frozen either in a commercial freezer below -18 °C or in liquid nitrogen, nominally at -196 °C. The measured permittivity before freezing was compared to the permittivity measured after freezing and thawing the tissues back to 25 °C. Statistical analysis of the results showed a statistically significant change in permittivity after freezing and thawing by both methods for all the measured tissues, at least in some parts of the measured frequency range. The largest difference was observed for the white matter, while the liver had the smallest percent change.

5.2.2. Scientific Contributions

The main scientific contribution of this publication is exploration of a novel method of long-term preservation of the permittivity of biological tissues based on a rapid freezing process to an extremely low temperature using liquid nitrogen. An experimental analysis was conducted with the evaluation and comparison of the permittivity of biological tissues before freezing and after thawing for the purpose of developing and testing the proposed method. The new method was compared with the method of slow freezing using a conventional freezer. For the first time, the possibility of preserving the permittivity of brain tissue was tested using both methods.

5.2.3. Authors Contribution

Authors: Anđela Matković (A.M.) and Antonio Šarolić (A.Š.)
Author Contributions: Conceptualization, A.Š. and A.M.; methodology, A.Š. and A.M.; formal analysis, A.M. and A.Š.; investigation, A.M. and A.Š.; writing—original draft preparation, A.M. and A.Š.; writing—review and editing, A.M. and A.Š.; supervision, A.Š.; project administration, A.Š.

5.3. Publication 3: Dielectric Permittivity Measurement Using Open-Ended Coaxial Probe—Modeling and Simulation Based on the Simple Capacitive-Load Model

5.3.1. Abstract

The study aim was to validate that dielectric permittivity measurement using the open-ended coaxial probe can be reliably modeled using electromagnetic modeling and simulations, followed by the postprocessing calculations based on the simple capacitive-load model. Saline solutions with various NaCl concentrations were used as materials under test (MUTs) to investigate how ionic conductivity affects the model validity. Two different solvers and simulation methods were used: FEKO for the frequency domain and CST for the time domain. Furthermore, we performed physical experiments with the same probe and MUTs, again implementing the capacitive-load model on the measurement data to observe the model’s validity. Relative error of the capacitive-load model with respect to the reference permittivity values, both in measurements and simulations, was within 10% for all cases except for the measured ε'_r of 1M solution at the lowest frequencies. The model yielded average relative errors well below 1% for the physiological saline, which is relevant for biological materials. The error increased for higher concentrations and for the lowest simulated frequencies but was within the declared measurement accuracy of the probe itself. This makes the simple capacitive-load model valid for all analyzed concentrations in the microwave frequency range from 0.5 to 18 GHz.

5.3.2. Scientific Contributions

The main scientific contribution of this publication is the development of a new simulation model of the entire process of measuring complex dielectric permittivity with an open-ended coaxial probe, which includes modeling of the probe, the measured material, and subsequent processing of the measured reflection coefficient to obtain the complex dielectric permittivity as the final result, and validation of the complete model by measurements.

5.3.3. Authors Contribution

Authors: Antonio Šarolić (A.Š.) and Anđela Matković (A.M.)
Author Contributions: Conceptualization, A.Š.; methodology, A.Š.; formal analysis, A.Š. and A.M.; investigation, A.Š. and A.M.; writing—original draft preparation, A.Š. and A.M.; writing—review and editing, A.Š. and A.M.; supervision, A.Š.; project administration, A.Š.

6. CONCLUSION

The first publication presented in this thesis introduces the developed permittivity models for three distinct brain tissues: grey matter, white matter, and cerebellum. These models are based on the Cole–Cole parameters obtained by systematic measurements in the microwave frequency range. The models are given for three different species: human, bovine, and porcine. As the previous Cole–Cole models for brain tissues were based on the compiled measurement results primarily conducted on animal tissues, the scientific contribution of the presented models lies in their development for each individual measured species. For the first time, the dispersion models for human brain tissues are exclusively based on the measurements of the human brain, which have not been carried out before, with the exception of grey matter in a very limited frequency band.

As the first study revealed the necessity of tissue preservation during measurements, the subsequent research was aimed at exploring how the freezing and thawing of brain tissues affects their permittivity in the microwave frequency range. The main scientific contribution of the second publication was the exploration of a novel method of long-term preservation of the permittivity of several biological tissues based on a rapid freezing process to an extremely low temperature using liquid nitrogen. The new method was compared with the method of slow freezing using a conventional freezer. For the first time, the possibility of preserving the permittivity of brain tissue was tested using both methods. Our results suggest that both freezing methods produce a statistically significant change in permittivity, at least in some part of the measured frequency range for all the studied tissues. Nevertheless, depending on the application and the preferred frequency range, the permittivity change might be acceptable for some tissues.

As the measurements of biological tissues proved to be a complex task with numerous confounding variables, the third publication of this thesis introduced a novel simulation model of the entire process of measuring complex dielectric permittivity with an open-ended coaxial probe. It included modeling of the probe, the measured material, and subsequent processing of the measured reflection coefficient to obtain the complex dielectric permittivity as the final result, and validation of the complete model by measurements. The model yielded negligible average relative errors in both measurements and simulations for the physiological saline, which closely approximates the biological materials with high water content.

In summary, these interconnected findings collectively advance the understanding of dielectric permittivity measurements, particularly for measurements of biological tissues. They have a significant contribution in the advancement of bioelectromagnetics for applications such as medical imaging, tissue engineering, and cancer detection, among others. They highlight the importance of accurate modeling and simulation methods as a faster and more attainable alternative for evaluating the confounders of the measurement method, considering that such analysis requires a large number of experiments in a wide parameter space. The developed simulation model of the permittivity measurement method using OECP can thus be used to analyze the confounders of permittivity measurements of biological tissues including the brain tissues. The permittivity models of brain tissues developed in our measurement study can be used to define the MUT in such simulation studies. The importance of the OECP measurement method simulations is additionally augmented by the difficulty of measuring numerous biological samples due to complexity of preserving their permittivity, as demonstrated in our work.

The future research will aim to expand the frequency range in both measurements and computer simulations. The low frequency limit is restricted by the emergence of probe ionic polarization, while the high frequency constraint is the occurrence of probe radiation and higher order modes. These phenomena are expected to be incorporated in the developed model in the future work. Additional possible direction of the future work is the use of the developed simulation methodology for the analysis of the heterogeneous MUTs. This is particularly relevant given that the specifications provided by commercial probe manufacturers are typically given for measurement setups with homogeneous materials. However, in reality many biological tissues exhibit considerable heterogeneity, which can significantly impact the accuracy and reliability of the measurement results. Therefore, it is important to conduct further analysis of the probe’s performance when used in configurations involving heterogeneous materials.

BIBLIOGRAPHY

[1] M. Koutsoupidou *et al.*, “Dielectric permittivity of human blood of different lactate levels measured at millimeter waves,” in *2019 41st Annual International Conference of the IEEE Engineering in Medicine and Biology Society (EMBC)*, Berlin, Germany: IEEE, Jul. 2019, pp. 1183–1186. doi: 10.1109/EMBC.2019.8857488.

[2] J. Shi, S. Seo, and J. Wang, “Monitoring Water Content of Blood During Hemodialysis Based on Complex Permittivity Measurement,” *IEEE Sensors J.*, vol. 20, no. 13, pp. 7347–7353, Jul. 2020, doi: 10.1109/JSEN.2020.2978220.

[3] M. Mizuno *et al.*, “Dielectric property measurements of corneal tissues for computational dosimetry of the eye in terahertz band in vivo and in vitro,” *Biomed. Opt. Express*, vol. 12, no. 3, p. 1295, Mar. 2021, doi: 10.1364/BOE.412769.

[4] E. Iaccheri, M. Varani, and L. Ragni, “Cost-Effective Open-Ended Coaxial Technique for Liquid Food Characterization by Using the Reflection Method for Industrial Applications,” *Sensors*, vol. 22, no. 14, p. 5277, Jul. 2022, doi: 10.3390/s22145277.

[5] V. Guihard, F. Taillade, J.-P. Balayssac, B. Steck, J. Sanahuja, and F. Deby, “Permittivity measurement of cementitious materials with an open-ended coaxial probe,” *Construction and Building Materials*, vol. 230, p. 116946, Jan. 2020, doi: 10.1016/j.conbuildmat.2019.116946.

[6] A. Mavrovic *et al.*, “Dielectric characterization of vegetation at L band using an open-ended coaxial probe,” *Geosci. Instrum. Method. Data Syst.*, vol. 7, no. 3, pp. 195–208, Jul. 2018, doi: 10.5194/gi-7-195-2018.

[7] L. D’Alvia, E. Piuzzi, A. Cataldo, and Z. Del Prete, “Permittivity-Based Water Content Calibration Measurement in Wood-Based Cultural Heritage: A Preliminary Study,” *Sensors*, vol. 22, no. 6, p. 2148, Mar. 2022, doi: 10.3390/s22062148.

[8] S. A. Komarov, A. S. Komarov, D. G. Barber, M. J. L. Lemes, and S. Rysgaard, “Open-Ended Coaxial Probe Technique for Dielectric Spectroscopy of Artificially Grown Sea Ice,” *IEEE Trans. Geosci. Remote Sensing*, vol. 54, no. 8, pp. 4941–4951, Aug. 2016, doi: 10.1109/TGRS.2016.2553110.

[9] A. Vergnano, A. Godio, C. M. Raffa, F. Chiampo, J. A. Tobon Vasquez, and F. Vipiana, “Open-Ended Coaxial Probe Measurements of Complex Dielectric Permittivity in Diesel-Contaminated Soil during Bioremediation,” *Sensors*, vol. 20, no. 22, p. 6677, Nov. 2020, doi: 10.3390/s20226677.

[10] T. Reinecke, L. Hagemeier, H. Spehlbrink, S. Guenther, M. Klintschar, and S. Zimmermann, “Open-ended coaxial probe for the quantification of edema in human brain tissue,” *Sensors and Actuators B: Chemical*, vol. 204, pp. 763–769, Dec. 2014, doi: 10.1016/j.snb.2014.08.045.

[11] B. Matthieu, R. Jerome, B. Stephane, and L. Gabriel, “Evolution of the complex permittivity of biological tissue at microwaves ranges: Correlation study with burn depth,” in *2014 36th Annual International Conference of the IEEE Engineering in Medicine and*

Biology Society, Chicago, IL: IEEE, Aug. 2014, pp. 4054–4057. doi: 10.1109/EMBC.2014.6944514.

[12] Y. Hayashi, N. Miura, N. Shinyashiki, and S. Yagihara, "Free water content and monitoring of healing processes of skin burns studied by microwave dielectric spectroscopy *in vivo*," *Phys. Med. Biol.*, vol. 50, no. 4, pp. 599–612, Feb. 2005, doi: 10.1088/0031-9155/50/4/003.

[13] H. N. Mayrovitz, "Assessing Lower Extremity Lymphedema Using Upper and Lower Extremity Tissue Dielectric Constant Ratios: Method and Normal Reference Values," *Lymphatic Research and Biology*, vol. 17, no. 4, pp. 457–464, Aug. 2019, doi: 10.1089/lrb.2018.0039.

[14] C. Aydinalp, S. Joof, and T. Yilmaz, "Towards Non-Invasive Diagnosis of Skin Cancer: Sensing Depth Investigation of Open-Ended Coaxial Probes," *Sensors*, vol. 21, no. 4, p. 1319, Feb. 2021, doi: 10.3390/s21041319.

[15] K. R. Foster and J. L. Schepps, "Dielectric Properties of Tumor and Normal Tissues at Radio through Microwave Frequencies," *Journal of Microwave Power*, vol. 16, no. 2, pp. 107–119, Jan. 1981, doi: 10.1080/16070658.1981.11689230.

[16] Y. Cheng and M. Fu, "Dielectric properties for non-invasive detection of normal, benign, and malignant breast tissues using microwave theories: Microwave properties of breast tissues," *Thorac Cancer*, vol. 9, no. 4, pp. 459–465, Apr. 2018, doi: 10.1111/1759-7714.12605.

[17] A. Fornes-Leal, C. Garcia-Pardo, M. Frasson, V. Pons Beltrán, and N. Cardona, "Dielectric characterization of healthy and malignant colon tissues in the 0.5–18 GHz frequency band," *Phys. Med. Biol.*, vol. 61, no. 20, pp. 7334–7346, Oct. 2016, doi: 10.1088/0031-9155/61/20/7334.

[18] C. Hessinger Nee Reimann *et al.*, "Dielectric Contrast Between Normal and Tumor Ex-Vivo Human Liver Tissue," *IEEE Access*, vol. 7, pp. 164113–164119, 2019, doi: 10.1109/ACCESS.2019.2951617.

[19] G. Fiorentini *et al.*, "A Narrative Review of Regional Hyperthermia: Updates From 2010 to 2019," *Integr Cancer Ther*, vol. 19, p. 153473542093264, Jan. 2020, doi: 10.1177/1534735420932648.

[20] L. M. Ellis, S. A. Curley, and K. K. Tanabe, Eds., *Radiofrequency ablation for cancer: current indications, techniques, and outcomes*. New York: Springer, 2004.

[21] K. Imajo, Y. Ogawa, M. Yoneda, S. Saito, and A. Nakajima, "A review of conventional and newer generation microwave ablation systems for hepatocellular carcinoma," *J Med Ultrasonics*, vol. 47, no. 2, pp. 265–277, Apr. 2020, doi: 10.1007/s10396-019-00997-5.

[22] International Commission on Non-Ionizing Radiation Protection (ICNIRP), "Guidelines for Limiting Exposure to Electromagnetic Fields (100 kHz to 300 GHz)," *Health Physics*, vol. 118, no. 5, pp. 483–524, May 2020, doi: 10.1097/HP.0000000000001210.

[23] IEEE Standards Coordinating Committee, "IEEE Standard for Safety Levels with Respect to Human Exposure to Electric, Magnetic, and Electromagnetic Fields, 0 Hz to 300 GHz," IEEE, New York, NY, USA, IEEE Std C95.1^{TM}-2019, 2019. doi: 10.1109/IEEESTD.2019.8859679.

[24] Keysight Technologies, "N1501A Dielectric Probe Kit Technical Overview," USA, 5992–0264EN, 2020.

[25] A. La Gioia *et al.*, “Open-Ended Coaxial Probe Technique for Dielectric Measurement of Biological Tissues: Challenges and Common Practices,” *Diagnostics*, vol. 8, no. 2, p. 40, Jun. 2018, doi: 10.3390/diagnostics8020040.

[26] Keysight Technologies, “N9927A FieldFox Handheld Microwave Vector Network Analyzer, 18 GHz,” Keysight. Accessed: Feb. 06, 2024. [Online]. Available: https://www.keysight.com/zz/en/product/N9927A/fieldfox-a-handheld-microwave-vector-network-analyzer-18-ghz.html

[27] Keysight Technologies, “N1500A Materials Measurement Suite - Technical Overview,” 2021.

[28] S. Gabriel, R. W. Lau, and C. Gabriel, “The dielectric properties of biological tissues: III. Parametric models for the dielectric spectrum of tissues,” *Phys. Med. Biol.*, vol. 41, no. 11, pp. 2271–2293, Nov. 1996, doi: 10.1088/0031-9155/41/11/003.

[29] P. A. Hasgall *et al.*, “IT’IS Database for thermal and electromagnetic parameters of biological tissues, Version 4.1.” Feb. 2022. [Online]. Available: itis.swiss/database

[30] M. Savazzi, J. M. Felicio, J. R. Costa, C. A. Fernandes, and R. C. Conceicao, “Study of Freezing and Defrosting Effects on Complex Permittivity of Biological Tissues,” *Antennas Wirel. Propag. Lett.*, vol. 20, no. 12, Art. no. 12, Dec. 2021, doi: 10.1109/LAWP.2021.3102842.

[31] Dassault Systèmes, “CST Studio Suite 3D EM simulation and analysis software.” Accessed: Oct. 04, 2022. [Online]. Available: https://www.3ds.com/products-services/simulia/products/cst-studio-suite/

[32] Altair Engineering Inc., “Altair Feko.” Accessed: Oct. 04, 2022. [Online]. Available: https://www.altair.com/feko/

[33] S. J. Orfanidis, “Electromagnetic Waves and Antennas.” [Online]. Available: https://www.ece.rutgers.edu/~orfanidi/ewa/

[34] V. Knapp and P. Colić, *Uvod u električna i magnetska svojstva materijala*. Zagreb: Školska knjiga, 1990.

[35] V. Raicu and Y. Feldman, Eds., *Dielectric relaxation in biological systems: physical principles, methods, and applications*, First edition. Oxford, United Kingdom: Oxford University Press, 2015.

[36] Keysight Technologies, “Basics of Measuring the Dielectric Properties of Materials,” Application Note 5989–2589EN, 2015.

[37] P. Debye, *Polar Molecules*. New York, USA: The Chemical Catalog Company, Inc., 1929.

[38] K. S. Cole and R. H. Cole, “Dispersion and Absorption in Dielectrics I. Alternating Current Characteristics,” *The Journal of Chemical Physics*, vol. 9, no. 4, pp. 341–351, Apr. 1941, doi: 10.1063/1.1750906.

[39] D. W. Davidson and R. H. Cole, “Dielectric Relaxation in Glycerol, Propylene Glycol, and n-Propanol,” *The Journal of Chemical Physics*, vol. 19, no. 12, pp. 1484–1490, Dec. 1951, doi: 10.1063/1.1748105.

[40] S. Havriliak and S. Negami, “A complex plane representation of dielectric and mechanical relaxation processes in some polymers,” *Polymer*, vol. 8, pp. 161–210, Jan. 1967, doi: 10.1016/0032-3861(67)90021-3.

[41] Y. Yamada, “Dielectric Properties of Textile Materials: Analytical Approximations and Experimental Measurements—A Review,” *Textiles*, vol. 2, no. 1, pp. 50–80, Jan. 2022, doi: 10.3390/textiles2010004.

[42] N. Nasir and M. Al Ahmad, “Cells Electrical Characterization: Dielectric Properties, Mixture, and Modeling Theories,” *Journal of Engineering*, vol. 2020, pp. 1–17, Jan. 2020, doi: 10.1155/2020/9475490.

[43] P. Siwach, E. Levy, L. Livshits, Y. Feldman, and D. Kaganovich, “Water is a biomarker of changes in the cellular environment in live animals,” *Sci Rep*, vol. 10, no. 1, p. 9095, Jun. 2020, doi: 10.1038/s41598-020-66022-9.

[44] C. Cametti, S. Marchetti, C. M. C. Gambi, and G. Onori, “Dielectric Relaxation Spectroscopy of Lysozyme Aqueous Solutions: Analysis of the δ-Dispersion and the Contribution of the Hydration Water,” *J. Phys. Chem. B*, vol. 115, no. 21, pp. 7144–7153, Jun. 2011, doi: 10.1021/jp2019389.

[45] K. C. Yaw, “Measurement of Dielectric Material Properties,” Rohde & Schwarz, RAC0607-0019_1_4E, 2012.

[46] M. Bailey and C. Swift, “Input Admittance of a Circular Waveguide Aperture Covered by a Dielectric Slab,” *IEEE Trans. Antennas Propagat.*, vol. 16, no. 4, pp. 386–391, Jul. 1968, doi: 10.1109/TAP.1968.1139207.

[47] SPEAG, Schmid & Partner Engineering AG, “DAK – Dielectric Assessment Kit Product Line.” Accessed: Oct. 18, 2021. [Online]. Available: https://speag.swiss/products/dak/overview/

[48] C. Gabriel, S. Gabriel, and E. Corthout, “The dielectric properties of biological tissues: I. Literature survey,” *Phys. Med. Biol.*, vol. 41, no. 11, pp. 2231–2249, Nov. 1996, doi: 10.1088/0031-9155/41/11/001.

[49] S. Gabriel, R. W. Lau, and C. Gabriel, “The dielectric properties of biological tissues: II. Measurements in the frequency range 10 Hz to 20 GHz,” *Phys. Med. Biol.*, vol. 41, no. 11, pp. 2251–2269, Nov. 1996, doi: 10.1088/0031-9155/41/11/002.

[50] A. Peyman and C. Gabriel, “Cole–Cole parameters for the dielectric properties of porcine tissues as a function of age at microwave frequencies,” *Phys. Med. Biol.*, vol. 55, no. 15, pp. N413–N419, Aug. 2010, doi: 10.1088/0031-9155/55/15/N02.

[51] A. Peyman and C. Gabriel, “Dielectric properties of porcine glands, gonads and body fluids,” *Phys. Med. Biol.*, vol. 57, no. 19, pp. N339–N344, Oct. 2012, doi: 10.1088/0031-9155/57/19/N339.

[52] K. Sasaki, E. Porter, E. A. Rashed, L. Farrugia, and G. Schmid, “Measurement and image-based estimation of dielectric properties of biological tissues —past, present, and future—,” *Phys. Med. Biol.*, vol. 67, no. 14, p. 14TR01, Jul. 2022, doi: 10.1088/1361-6560/ac7b64.

[53] M. C. Steel and R. J. Sheppard, “Dielectric properties of mammalian brain tissue between 1 and 18 GHz,” *Phys. Med. Biol.*, vol. 30, no. 7, pp. 621–630, Jul. 1985, doi: 10.1088/0031-9155/30/7/001.

[54] M. Thurai, V. D. Goodridge, R. J. Sheppard, and E. H. Grant, “Variation with age of the dielectric properties of mouse brain cerebrum,” *Phys. Med. Biol.*, vol. 29, no. 9, pp. 1133–1136, Sep. 1984, doi: 10.1088/0031-9155/29/9/009.

[55] A. Kraszewski, M. A. Stuchly, S. S. Stuchly, and A. M. Smith, "In vivo and in vitro dielectric properties of animal tissues at radio frequencies," *Bioelectromagnetics*, vol. 3, no. 4, pp. 421–432, 1982, doi: 10.1002/bem.2250030405.

[56] E. C. Burdette, P. G. Friederich, R. L. Seaman, and L. E. Larsen, "In Situ Permittivity of Canine Brain: Regional Variations and Postmortem Changes," *IEEE Trans. Microwave Theory Techn.*, vol. 34, no. 1, pp. 38–50, Jan. 1986, doi: 10.1109/TMTT.1986.1133278.

[57] D. Xu, L. Liu, and Z. Jiang, "Measurement of the Dielectric Properties of Biological Substances Using an Improved Open-Ended Coaxial Line Resonator Method," *IEEE Trans. Microwave Theory Techn.*, vol. 35, no. 12, pp. 1424–1428, Dec. 1987, doi: 10.1109/TMTT.1987.1133870.

[58] M. A. Stuchly, T. W. Athey, S. S. Stuchly, G. M. Samaras, and G. Taylor, "Dielectric properties of animal tissues in vivo at frequencies 10 MHz – 1 GHz," *Bioelectromagnetics*, vol. 2, no. 2, pp. 93–103, 1981, doi: 10.1002/bem.2250020202.

[59] S. B. Baumann, D. R. Wozny, S. K. Kelly, and F. M. Meno, "The electrical conductivity of human cerebrospinal fluid at body temperature," *IEEE Trans. Biomed. Eng.*, vol. 44, no. 3, pp. 220–223, Mar. 1997, doi: 10.1109/10.554770.

[60] J. Latikka, T. Kuurne, and H. Eskola, "Conductivity of living intracranial tissues," *Phys. Med. Biol.*, vol. 46, no. 6, pp. 1611–1616, Jun. 2001, doi: 10.1088/0031-9155/46/6/302.

[61] G. Schmid, G. Neubauer, and P. R. Mazal, "Dielectric properties of human brain tissue measured less than 10 h postmortem at frequencies from 800 to 2450 MHz," *Bioelectromagnetics*, vol. 24, no. 6, pp. 423–430, Sep. 2003, doi: 10.1002/bem.10123.

[62] G. Schmid, R. Überbacher, T. Samaras, M. Tschabitscher, and P. R. Mazal, "The dielectric properties of human pineal gland tissue and RF absorption due to wireless communication devices in the frequency range 400–1850 MHz," *Phys. Med. Biol.*, vol. 52, no. 17, pp. 5457–5468, Sep. 2007, doi: 10.1088/0031-9155/52/17/024.

[63] A. Matković, A. Kordić, A. Jakovčević, and A. Šarolić, "Complex Permittivity of Ex-Vivo Human, Bovine and Porcine Brain Tissues in the Microwave Frequency Range," *Diagnostics*, vol. 12, no. 11, p. 2580, Oct. 2022, doi: 10.3390/diagnostics12112580.

[64] L. Crocco, I. Karanasiou, M. L. James, and R. C. Conceição, Eds., *Emerging Electromagnetic Technologies for Brain Diseases Diagnostics, Monitoring and Therapy*. Cham: Springer International Publishing, 2018. doi: 10.1007/978-3-319-75007-1.

[65] I. Saied, T. Arslan, S. Chandran, C. Smith, T. Spires-Jones, and S. Pal, "Non-Invasive RF Technique for Detecting Different Stages of Alzheimer's Disease and Imaging Beta-Amyloid Plaques and Tau Tangles in the Brain," *IEEE Trans. Med. Imaging*, vol. 39, no. 12, Art. no. 12, Dec. 2020, doi: 10.1109/TMI.2020.3011359.

[66] M. J. Burfeindt, E. Zastrow, S. C. Hagness, B. D. Van Veen, and J. E. Medow, "Microwave beamforming for non-invasive patient-specific hyperthermia treatment of pediatric brain cancer," *Phys. Med. Biol.*, vol. 56, no. 9, pp. 2743–2754, May 2011, doi: 10.1088/0031-9155/56/9/007.

[67] G. Schooneveldt *et al.*, "Hyperthermia Treatment Planning Including Convective Flow in Cerebrospinal Fluid for Brain Tumour Hyperthermia Treatment Using a Novel Dedicated Paediatric Brain Applicator," *Cancers*, vol. 11, no. 8, p. 1183, Aug. 2019, doi: 10.3390/cancers11081183.

[68] T. Drizdal, M. M. Paulides, N. van Holthe, and G. C. van Rhoon, “Hyperthermia treatment planning guided applicator selection for sub-superficial head and neck tumors heating,” *International Journal of Hyperthermia*, vol. 34, no. 6, pp. 704–713, Aug. 2018, doi: 10.1080/02656736.2017.1383517.

[69] M. Kroesen *et al.*, “Feasibility, SAR Distribution, and Clinical Outcome upon Reirradiation and Deep Hyperthermia Using the Hypercollar3D in Head and Neck Cancer Patients,” *Cancers*, vol. 13, no. 23, p. 6149, Dec. 2021, doi: 10.3390/cancers13236149.

[70] E. Michel, D. Hernandez, and S. Y. Lee, “Electrical conductivity and permittivity maps of brain tissues derived from water content based on T_1 -weighted acquisition,” *Magn. Reson. Med.*, vol. 77, no. 3, pp. 1094–1103, Mar. 2017, doi: 10.1002/mrm.26193.

[71] J. M. Gullett *et al.*, “The association of white matter free water with cognition in older adults,” *NeuroImage*, vol. 219, p. 117040, Oct. 2020, doi: 10.1016/j.neuroimage.2020.117040.

[72] A. Shahzad, “Investigation of the effect of dehydration on tissue dielectric properties in ex vivo measurements,” p. 10, 2017.

[73] J. Bonello, L. Farrugia, and C. V. Sammut, “Effects of preservative solutions on the dielectric properties of biological tissue,” in *2017 International Conference on Electromagnetics in Advanced Applications (ICEAA)*, Verona, Italy: IEEE, Sep. 2017, pp. 1216–1219. doi: 10.1109/ICEAA.2017.8065488.

[74] A. Kordić, A. Matković, A. Jakovčević, and A. Šarolić, “Preliminary measurements of dielectric properties of excised human tissues and the associated challenges thereof,” in *BioEM 2021*, Ghent, Belgium, Sep. 2021, pp. 584–589.

[75] A. Matković and A. Šarolić, “The Effect of Freezing and Thawing on Complex Permittivity of Bovine Tissues,” *Sensors*, vol. 22, no. 24, p. 9806, Dec. 2022, doi: 10.3390/s22249806.

[76] L. Chen, C. K. Ong, C. P. Neo, V. V. Varadan, and V. K. Varadan, *Microwave electronics: measurement and materials characterisation*. Chichester: John Wiley, 2004.

[77] J. S. Bobowski and T. Johnson, “Permittivity measurements of biological samples by an open-ended coaxial line,” *Progress In Electromagnetics Research B*, vol. 40, pp. 159–183, 2012, doi: 10.2528/PIERB12022906.

[78] J. P. Dunsmore, *Handbook of microwave component measurements: with advanced VNA techniques*, Second edition. Hoboken, NJ: John Wiley & Sons, Inc, 2020.

[79] S. S. Stuchly, M. A. Rzepecka, and M. F. Iskander, “Permittivity Measurements at Microwave Frequencies Using Lumped Elements,” *IEEE Trans. Instrum. Meas.*, vol. 23, no. 1, pp. 56–62, 1974, doi: 10.1109/TIM.1974.4314218.

[80] M. M. Brady, S. A. Symons, and S. S. Stuchly, “Dielectric Behavior of Selected Animal Tissues in Vitro at Frequencies from 2 to 4 GHz,” *IEEE Trans. Biomed. Eng.*, vol. BME-28, no. 3, pp. 305–307, Mar. 1981, doi: 10.1109/TBME.1981.324707.

[81] M. A. Stuchly, M. M. Brady, S. S. Stuchly, and G. Gajda, “Equivalent circuit of an open-ended coaxial line in a lossy dielectric,” *IEEE Trans. Instrum. Meas.*, vol. IM–31, no. 2, pp. 116–119, Jun. 1982, doi: 10.1109/TIM.1982.6312533.

[82] M. M. Brady, S. A. Symons, and S. S. Stuchly, “Dielectric Behavior of Selected Animal Tissues in Vitro at Frequencies from 2 to 4 GHz,” *IEEE Trans. Biomed. Eng.*, vol. BME-28, no. 3, pp. 305–307, Mar. 1981, doi: 10.1109/TBME.1981.324707.

[83] N. Marcuvitz, *Waveguide handbook*. New York: McGraw-Hill, 1951.

[84] T. P. Marsland and S. Evans, “Dielectric measurements with an open-ended coaxial probe,” *IEE Proc. H Microw. Antennas Propag. UK*, vol. 134, no. 4, p. 341, 1987, doi: 10.1049/ip-h-2.1987.0068.

[85] I. J. Bahl and S. S. Stuchly, “Effect of Finite Size of Ground Plane on the Impedance of a Monopole Immersed in a Lossy Medium,” *Electronics Letters*, vol. 15, no. 22, pp. 728–729, 1979.

[86] G. Deschamps, “Impedance of an antenna in a conducting medium,” *IRE Trans. Antennas Propag.*, vol. 10, no. 5, pp. 648–650, Sep. 1962, doi: 10.1109/TAP.1962.1137923.

[87] J. P. Grant, R. N. Clarke, G. T. Symm, and N. M. Spyrou, “A critical study of the open-ended coaxial line sensor technique for RF and microwave complex permittivity measurements,” *J. Phys. E: Sci. Instrum.*, vol. 22, no. 9, pp. 757–770, Sep. 1989, doi: 10.1088/0022-3735/22/9/015.

[88] J. R. Mosig, J.-C. E. Besson, M. Gex-Fabry, and F. E. Gardiol, “Reflection of an open-ended coaxial line and application to nondestructive measurement of materials,” *IEEE Trans. Instrum. Meas.*, vol. IM–30, no. 1, pp. 46–51, Mar. 1981, doi: 10.1109/TIM.1981.6312437.

[89] G. Ruvio, M. Vaselli, V. Lopresto, R. Pinto, L. Farina, and M. Cavagnaro, “Comparison of different methods for dielectric properties measurements in liquid sample media,” *Int J RF Microw Comput Aided Eng*, vol. 28, no. 3, Art. no. 3, Mar. 2018, doi: 10.1002/mmce.21215.

[90] J. Z. Bao, C. C. Davis, and M. L. Swicord, “Microwave dielectric measurements of erythrocyte suspensions,” *Biophysical Journal*, vol. 66, no. 6, pp. 2173–2180, Jun. 1994, doi: 10.1016/S0006-3495(94)81013-6.

[91] A. Šarolić and A. Matković, “Dielectric Permittivity Measurement Using Open-Ended Coaxial Probe—Modeling and Simulation Based on the Simple Capacitive-Load Model,” *Sensors*, vol. 22, no. 16, p. 6024, Aug. 2022, doi: 10.3390/s22166024.

[92] D. V. Blackham and R. D. Pollard, “An Improved Technique for Permittivity Measurements Using a Coaxial Probe,” *IEEE Transactions on Instrumentation and Measurement*, vol. 46, no. 5, pp. 1093–1099, 1997, doi: 10.1109/19.676718.

[93] A. Peyman, C. Gabriel, and E. H. Grant, “Complex permittivity of sodium chloride solutions at microwave frequencies,” *Bioelectromagnetics*, vol. 28, no. 4, pp. 264–274, May 2007, doi: 10.1002/bem.20271.

[94] National Information Standards Organization, “CRediT - Contributor Roles Taxonomy,” CRediT. Accessed: Feb. 05, 2024. [Online]. Available: https://credit.niso.org/

APPENDIX A

Title	Complex Permittivity of Ex-Vivo Human, Bovine and Porcine Brain Tissues in the Microwave Frequency Range
Authors	Anđela Matković, Anton Kordić, Antonia Jakovčević, Antonio Šarolić
Journal	Diagnostics
Impact factor	3.6
Volume and number	12, 11
Year	2022
Article number	2580
DOI	10.3390/diagnostics12112580
Abstract	Accurate knowledge about the dielectric properties of biological tissues in the microwave frequency range may lead to advancement of biomedical applications based on microwave technology. However, the published data are very scarce, especially for human brain tissues. The aim of this work was to measure and report the complex permittivity of brain white matter, grey matter and cerebellum. Complex permittivity was measured on human, bovine and porcine brain tissues in the microwave frequency range from 0.5 to 18 GHz using an open-ended coaxial probe. The results present a valuable addition to the available data on the brain tissue complex permittivity. Some noticeable variations between the results lead to several conclusions. Complex permittivity variation within the same tissue type of the individual species was comparable to interspecies variation. The difference was prominent between human brains obtained from autopsies, while bovine brains obtained from healthy animals showed very similar complex permittivity. We hypothesize that the difference might have been caused by the basic pathologies of the patients, where the associated therapies could have affected the brain water content. We also examined the effect of excised tissue degradation on its complex permittivity over the course of three days, and the results suggest the gradual dehydration of the samples.

diagnostics

Article

Complex Permittivity of Ex-Vivo Human, Bovine and Porcine Brain Tissues in the Microwave Frequency Range

Anđela Matković [1,*], Anton Kordić [2], Antonia Jakovčević [3] and Antonio Šarolić [1]

[1] FESB, University of Split, HR-21000 Split, Croatia
[2] Department of Neurosurgery, University Hospital Centre Zagreb, HR-10000 Zagreb, Croatia
[3] Department of Pathology and Cytology, University Hospital Centre Zagreb, HR-10000 Zagreb, Croatia
* Correspondence: andjela.matkovic@fesb.hr

Abstract: Accurate knowledge about the dielectric properties of biological tissues in the microwave frequency range may lead to advancement of biomedical applications based on microwave technology. However, the published data are very scarce, especially for human brain tissues. The aim of this work was to measure and report the complex permittivity of brain white matter, grey matter and cerebellum. Complex permittivity was measured on human, bovine and porcine brain tissues in the microwave frequency range from 0.5 to 18 GHz using an open-ended coaxial probe. The results present a valuable addition to the available data on the brain tissue complex permittivity. Some noticeable variations between the results lead to several conclusions. Complex permittivity variation within the same tissue type of the individual species was comparable to interspecies variation. The difference was prominent between human brains obtained from autopsies, while bovine brains obtained from healthy animals showed very similar complex permittivity. We hypothesize that the difference might have been caused by the basic pathologies of the patients, where the associated therapies could have affected the brain water content. We also examined the effect of excised tissue degradation on its complex permittivity over the course of three days, and the results suggest the gradual dehydration of the samples.

Keywords: dielectric properties measurement; complex permittivity; microwave gigahertz (GHz) frequency range; open-ended coaxial probe; biological tissues; white matter; grey matter; cerebellum; human, bovine and porcine brain

check for updates

Citation: Matković, A.; Kordić, A.; Jakovčević, A.; Šarolić, A. Complex Permittivity of Ex-Vivo Human, Bovine and Porcine Brain Tissues in the Microwave Frequency Range. *Diagnostics* **2022**, *12*, 2580. https://doi.org/10.3390/diagnostics12112580

Academic Editor: Lorenzo Crocco

Received: 22 August 2022
Accepted: 20 October 2022
Published: 25 October 2022

1. Introduction

Interaction of electromagnetic field with a biological tissue crucially depends on the tissue's dielectric properties, i.e., its complex permittivity. The permittivity is a complex quantity that describes the dielectric polarization (i.e., the ability of a material to store the electric energy) and losses in a material exposed to electric or electromagnetic field. Accurate knowledge of the complex permittivity of biological tissues may lead to advancement of medical diagnostic and therapeutic applications, either inventing new ones, or improving the existing ones. Brain tissues are especially interesting in this respect, as they are relatively underrepresented in the published studies reporting biological tissue complex permittivity measurement, yet various beneficial applications are possible when knowing the exact dielectric properties.

For example, well defined dielectric properties in the microwave frequency range are crucial for microwave imaging and all related procedures relying on microwave electromagnetic (EM) radiation. Accordingly, medical applications would significantly benefit from precise dielectric characterization of biological tissues in the microwave, or more precisely, in the gigahertz (GHz) frequency range. Microwave imaging is based on the perturbation of the EM field inside the human body that occurs as a result of interaction with biological tissues. The applicability of the described imaging procedure on brain tissues is based on the existence of a significant contrast in dielectric permittivity of healthy tissues and pathological tissues or conditions (such as hemorrhage after a stroke) [1]. A great example is a recent paper published by Saied et al. [2] that describes a novel approach of detecting Alzheimer's disease by comparing the dielectric properties of a healthy brain with a brain sample from a patient with severe Alzheimer's disease. Another vivid example of this is the newly developed microwave scanner that enables detection and differentiation of a brain stroke (intracranial hemorrhage or ischemia) by means of microwave technology [3–5]. A diagnostic approach combining the aforementioned microwave imaging with brain biomarkers could potentially achieve even higher sensitivity and specificity [6]. Another notable example is the possibility of differentiation between benign and malignant tissues, as already described in papers relating to microwave breast imaging [7] and intraoperative margin-assessment devices [8], thus enabling total or near total tumor removal whilst sparing the healthy tissue. Also, an application very much worth mentioning is microwave beamforming for hyperthermia treatment [9] i.e., heating tumors using microwave EM radiation to the fever range temperatures of ca. 40–44 °C [10]. It is a procedure that should be carefully planned, where accurate knowledge of dielectric properties of brain tissues (especially the cerebellum in pediatric patients as the majority of tumors occur in the posterior fossa region that contains the cerebellum) is paramount because this approach utilizes constructive interference of electromagnetic waves and its selective absorption to achieve localized heating only in the target tumor tissue [9]. However, to do successful hyperthermia treatment planning, even non-target tissues should be well defined e.g., cerebrospinal fluid for brain tumor hyperthermia as shown in [10]. Likewise, exact permittivity of brain tissues is also necessary for hyperthermia treatment planning for non-brain head and neck tumors to avoid unnecessary heating of brain tissues [11]. This results in improved patient treatment quality, reproducibility, operator handling and patient safety [12] as well as it being a cost-effective option [13]. One of the more recent hyperthermia studies of the head and neck region showed the importance of the relationship between the absorbed electromagnetic power and tumor response [14], a subject that could be resolved by deeper understanding of physical properties of target tissues including the dielectric properties.

Microwave ablation, as another microwave-based technique, has been used since 1994 in liver and pancreatic tumors, but was recently used to treat brain and skull-base tumors [15]. Treatment of brain and skull-base tumors with microwave ablation reported in [15] deemed it as a safe and viable alternative for high-risk brain tumor resection surgery. The treatment planning and designing of microwave applicators for both hyperthermia and ablation using computer simulations would be impossible without accurately modeling the dielectric parameters of all tissues involved in the procedure, i.e., both the target and the surrounding tissues. The former was very recently shown in [16] where the microwave hyperthermia treatment of brain tumors was modeled and simulated using finite element method (FEM), with the brain tissue complex permittivity as the input parameter.

Lastly, dielectric properties of human tissues are the crucial data when analyzing the potentially harmful effects of electromagnetic radiation on the human body. In the microwave frequency range, the main harmful effect is the unwanted heating due to deposition of electromagnetic energy into the tissues [17]. In this case, contrary to medical hyperthermia and ablation, the heating is unwanted and thus considered harmful. Nevertheless, the physical mechanism is the same and depends on the tissue complex permittivity.

Research, innovation and implementation of microwave technology applications in medicine greatly benefit from anatomically realistic computer models of the human body [18], which can then be used in computer electromagnetic simulations (such as [19]). The models are built using high-resolution volumetric elements, where each element is assigned its dielectric properties, so that the microwave propagation inside the body can be faithfully simulated using computer simulations. Without the knowledge about dielectric properties measured at various temperatures, at multiple frequencies and on various subjects, it is difficult to know whether the models appropriately reflect the dielectric properties of the tissues.

The most commonly cited source of dielectric properties for various tissues (including the brain tissues) is still the one from Gabriel [20], from 1996. However, it is actually a compilation of measurement results from different species, mostly based on ovine tissue measurements. The most comprehensive compilation of physical properties of various tissues, which includes complex permittivity, is provided by [21], here referred to as the IT'IS database. The IT'IS database was chosen as our main reference for comparison given that the database is regularly updated with new data as it becomes available (e.g., last update was done in February 2022) and is thus cited by various recent publications on dielectric properties of tissues. However, most of the dielectric properties of tissues in the IT'IS database are still referenced to Gabriel [20], including also the brain tissues measured in this study. Accordingly, the reference dielectric properties of brain tissues have not been updated since 1996 as a result of lack of published data.

As the measured dielectric data for brain tissues is poorly covered in the literature, especially for human brain tissues, the aim of this work is to report the measurement data for dielectric properties of brain tissues for several species including humans, providing enough supporting information about our measurement protocol and tissue properties. We report here the measurements of complex permittivity of white matter and grey matter (both from cerebrum) and cerebellum of human, bovine and porcine brains at 25 °C, over the frequency range of 0.5 GHz to 18 GHz. We trust that this data will be of use to researchers that aim to realistically model the brain tissues as well as to simply compare the measurement data.

2. Materials and Methods

2.1. Complex Permittivity

Complex permittivity of the material $\hat{\varepsilon}$ expressed in farads per meter [F/m] is a physical quantity that describes the reaction of a material to the applied electric field. The real part ε' is a measure of a material's ability to store electrical energy, i.e., to be polarized. The imaginary part ε'' corresponds to the effective losses in the material. The permittivity is often normalized to the permittivity of a vacuum (ε_0), obtaining the so-called relative permittivity, denoted by the dimensionless complex quantity $\hat{\varepsilon}_r$ defined by its real and imaginary parts:

$$\hat{\varepsilon}_r = \frac{\hat{\varepsilon}}{\varepsilon_0} = \varepsilon_r' - j\varepsilon_r''. \tag{1}$$

Therefore, the actual quantities measured in this paper are the real and the imaginary part of the relative permittivity: ε_r' and ε_r'', respectively. The losses described by the imaginary part of the permittivity arise from two different mechanisms of dissipation. The first mechanism of loss is due to the free charges, either electrons or ions, inside the material. The second loss mechanism is due to the dielectric polarization losses caused by the alternating electric field that continuously reorients dipoles. The resulting macroscopically measurable conductivity σ [S/m] thus encompasses both losses and is expressed as:

$$\sigma = \omega\varepsilon_0\varepsilon_r'' \ , \tag{2}$$

where ω is the angular frequency.

It is worth noting that in some references (e.g., in [21]), the term "permittivity" refers only to the real part of the complex relative permittivity, ε_r', while the losses are presented by conductivity σ rather than by the imaginary part of the complex relative permittivity, ε_r''. Nevertheless, as the permittivity is indeed a complex physical quantity defined above, in this paper, like in most physics textbooks, the term "permittivity" denotes the complex permittivity $\hat{\varepsilon}$, or, in the context of normalization to a dimensionless quantity, the term "permittivity" is equivalent to the complex relative permittivity $\hat{\varepsilon}_r$, and will be used accordingly throughout this paper.

Frequency dependence of a biological tissue permittivity is commonly expressed using the Cole–Cole empirical formula [22] which models the dispersion and absorption in lossy dielectrics:

$$\hat{\varepsilon}_r = \varepsilon_\infty + \sum_{i=1}^{N} \frac{\varepsilon_{s,\,i} - \varepsilon_\infty}{1 + (j\omega\tau_i)^{1-\alpha_i}} + \frac{\sigma_i}{j\omega\varepsilon_0}, \tag{3}$$

where ε_s is the static dielectric constant, and ε_∞ is the "infinite frequency" (i.e., the high frequency) dielectric constant. N is the number of Cole–Cole poles that model different relaxation regions, while τ is the associated relaxation time and α is a measure of the broadening of the dispersion. Each relaxation region is the manifestation of a polarization mechanism characterized by a different time constant.

As the dominant relaxation mechanism in the frequency range of this study is the relaxation of the water molecules, the Cole–Cole model can be reduced to a single pole model:

$$\hat{\varepsilon}_r = \varepsilon_\infty + \frac{\varepsilon_s - \varepsilon_\infty}{1 + (j\omega\tau)^{1-\alpha}} + \frac{\sigma}{j\omega\varepsilon_0}, \tag{4}$$

where the parameters of the pole refer to the water relaxation. Accordingly, we derived the single pole Cole–Cole models to fit each set of the averaged measurement data, for each species and each tissue, as an additional representation of our measurement results.

2.2. Measurement Method

The measurements were performed using the open-ended coaxial probe method, described in detail in [23]. An open-ended coaxial probe is a precisely machined segment of a straight rigid coaxial transmission line. The probe input port with its associated coaxial connector is on one end, leaving the other end open to be pressed against the material under test (MUT). The electric field lines are formed between the electrodes at the open end, closing dominantly through the MUT. The termination load at the end of the coaxial line is thus determined by the permittivity of the MUT. The reflection coefficient of the entire line terminated by the MUT can be measured at the probe input port by a vector network analyzer (VNA). VNA performs a one-port reflection measurement by sending the test signal into the probe input port, measuring the reflection coefficient Γ. The reflection coefficient Γ is a complex quantity defined by its real and imaginary part, i.e., by its amplitude and phase. MUT dielectric properties are extracted from the amplitude and the phase of the measured reflection coefficient.

We measured the permittivity using the slim form probe manufactured by Keysight Technologies (Santa Rosa, CA, USA) [23,24], having the outer diameter of 2.2 mm. Its operating frequency range is from 500 MHz to 50 GHz. As our measurements of the reflection coefficient were done with N9927A FieldFox handheld network analyzer (Keysight Technologies Inc.) [25], which has an upper frequency limit of 18 GHz, this study was performed from 500 MHz to 18 GHz. The slim form probe was selected as a common choice for tissue measurements [26] due to its small diameter, which helps to distinguish different tissues in a heterogeneous sample. As a usual practice when measuring biological tissues, the probe open end was in all cases pressed against the sample with its entire surface. The declared accuracy of the probe for both ε_r' and ε_r'' is ±10%.

To extract the permittivity of a material from the measured reflection coefficient, postprocessing calculations have to be made. For the slim form probe, these calculations are incorporated in the software Keysight Materials Measurement Suite N1500A [27] provided by the probe manufacturer, accompanying the probe. The calculation method is based on solving the equivalent model of the probe termination load admittance, which includes all electromagnetic phenomena occurring in the probe and MUT. Thus, in order to determine the parameters of the load model, the measurement must first be calibrated using three known loads: open (without any MUT, open end is in the air), short (open end is shorted by a conductive sheet), and a known liquid (water being most commonly used, as its dielectric dispersion is well-known). After a proper calibration, measurements on MUTs can be made.

2.3. Materials under Test

In this study, three types of brain tissues from different species were measured, namely: white matter and grey matter (both from cerebrum), and cerebellum. Although cerebellum also consists of white and grey matter, it has been treated here as a single tissue, which is a usual approach in the literature [20,21], considering the fact that white and grey matter are so intertwined in cerebellum that they are indistinguishable by the measuring probe.

The main challenge when measuring dielectric properties of brain tissues was obtaining freshly excised brains so that the natural deterioration of postmortem tissues, as well as the dehydration, would affect the results as minimally as possible. In total, we acquired two different human brains (labeled hereafter as H1 and H2), three different bovine brains (labeled hereafter as B1, B2 and B3), and one porcine brain (labeled hereafter as P). Cerebellum was intact only in both human brain specimens (H1 and H2) and in one bovine brain specimen (B1). Other animal brain specimens were split into two hemispheres during slaughter, which was especially damaging to the delicate cerebellum tissue located in the center so the measurements on cerebellum could not be performed. Example of the brain sample (B1) is shown in Figure 1 (measuring tape shown for scale).

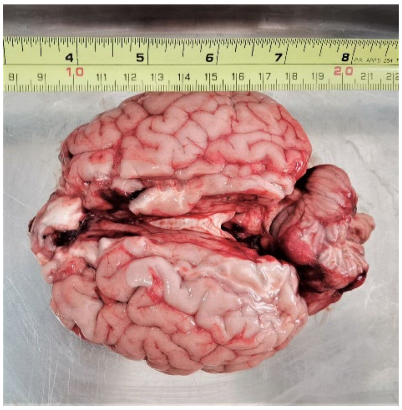

Figure 1. Bovine brain B1.

Human tissues were obtained from hospital autopsies at the Department of Pathology and Cytology, University Hospital Centre Zagreb. The study was performed under ethical approval from the Ethics Committee of the University Hospital Centre Zagreb.

Human brain H1 was from a male patient 50 years of age. Human brain H2 was from a female patient 84 years of age. The measurements were performed immediately after the autopsy (day 1), which was performed two days postmortem. Prior to autopsy, the bodies were kept in the refrigerator at 4 °C. The exact time between the death and the refrigeration at the pathology department is unknown, but a minimum of four hours is dictated by medical protocol. It is important to note that the brains were intact in the skull from the time of death to the day of autopsy. That is why the span of two days from death to measurements did not result in the dehydration of the brains. Neither of the patients had any disclosed brain pathologies noted in their medical record; however, both suffered from other pathologies that eventually led to lethal outcome, and were thus treated pharmaceutically prior to death. The human brain samples were either in the form of brain slices of around 1.5-centimeter thickness, exposing both white and grey matter, or in the form of ca. 2 cm × 2 cm × 2 cm cuboids consisting dominantly of white matter.

In addition to the measurements on day 1, the white and grey matter samples of brain H1 were measured on day 2 and day 3 from autopsy (four and five days postmortem) to examine the effects of the excised tissue degradation. The excised samples were kept in the refrigerator at 4 °C in sealed containers between the measurements. The samples were heated from 4 °C to 25 °C naturally, keeping them in sealed containers to avoid dehydration, by achieving thermal equilibrium with the room temperature, which was kept at 25 °C.

The age of the porcine specimen was not known, while all bovine specimens were under 12 months of age. Brains were obtained from the local butcher between 18 and 36 h from animal slaughter, depending on the brain. There was no dehydration or decomposition noticeable, presumably due to the short timespan from the slaughter and the fact that the brains were not dissected until we obtained them, while in the meantime they were kept wrapped and refrigerated at 1 °C. Before the measurements, we dissected all animal brains into coronal slices ca. 1.5 cm thick.

2.4. Measurement Setup

The slim form probe by Keysight Technologies Inc. was connected to the vector network analyzer FieldFox N9927A (Keysight Technologies Inc.) by a phase-stable coaxial cable Sucoflex 404 (HUBER+SUHNER AG, Herisau, Switzerland). The VNA was connected to a computer, and the measurements were controlled and performed using the manufacturer-provided software Keysight Materials Measurement Suite N1500A [27]. The measurements were performed from 500 MHz to 18 GHz with a 20 MHz step. During the measurements of human brains, the sweeping average was enabled on the VNA with averaging factor set to 10, meaning that the VNA automatically measured each measurement point consecutively 10 times, and then the average of those 10 measurements was calculated by the VNA for each measurement point. This procedure removes stochastic noise and obtains more accurate measurements. Unlike the animal brains which were measured in our lab, the human brains were measured out of our lab in a less controlled setting, which is why we made the choice of averaging to compensate for any possible instability of the measurement setup. VNA averaging was not performed with the animal samples, where more points were measured on each sample.

The probe was fixed to its stand in the vertical position and pressed onto the measured tissue. The samples were contained in a plastic dish on top of a polystyrene foam block that separated the dish with the sample from the metal laboratory jack underneath. The laboratory jack was used to lift the sample to the open end of the probe, so that the probe was tightly pressed against the sample to avoid air gaps between the probe and the sample. The walls of the dish as well as the laboratory jack underneath did not affect the measurement results. This was confirmed by several pilot measurements where the probe was put directly above the supporting structure without the biological sample. The measured permittivity of that setup was compared to the measurement of the open probe that was left in air, and no difference was found. The described measurement setup is shown in Figure 2.

The measurements were performed on homogeneous regions of either white or grey matter, when such regions were clearly visible on the sample. The regions with visually indistinguishable white and grey matter were avoided. Within these constraints, each sample was measured at as many points as possible to obtain better accuracy. The number of measurement points per tissue is shown in Table 1.

Table 1. The number of measurement points per tissue and species type.

Species	Brain	Age	White Matter	Grey Matter	Cerebellum
Human	H1	50 years	14	15	15
	H2	84 years	18	10	5
Bovine	B1	Under 12 months	72	70	13
	B2		38	32	-
	B3		38	32	-
Porcine	P1	Unknown	38	40	-

Figure 2. Measurement setup.

The number of measurement points reported in Table 1 corresponds to the measurements performed on different measurement points. These numbers were used to calculate the standard deviation for each sample.

Between measuring different samples, the probe was cleaned with 70% ethyl alcohol to prevent cross contamination and ensure the best results. The setup was also recalibrated in regular intervals with the refresh calibration option available in Keysight Materials Measurement Suite N1500A [27], where one calibration standard out of the three is chosen for recalibration. In our case, we chose to recalibrate with water as its properties gave the most stable results during the measurement process and, therefore, it was the most appropriate for recalibration. The room, water, and MUT temperatures were all kept at 25 °C during all measurements, while the temperature was controlled using a precise thermometer DTM3000 (LKM Electronics GmbH, Geratal, Germany).

3. Results

3.1. Human Brain Permittivity

In Figures 3–17, the colored lines represent the average of all measurements performed on a tissue, and the vertical bars show the associated standard deviation. The standard deviation is shown only at discrete frequency points for the sake of visual clarity. The colored lines showing the measurement results were additionally smoothed with a moving average spanning ±150 MHz. The smoothing was done to eliminate the small fluctuations that do not reflect the actual fluctuations of permittivity but are caused by the imperfections of the measurement setup. This smoothing procedure was performed on all the measured results in this study. Permittivity of human white matter for brains H1 and H2 is shown in Figure 3 in terms of its real and imaginary part, i.e., ε_r' and ε_r''. The brain of the older patient

(H2) displays significantly higher permittivity in both the real and imaginary parts. It is also noticeable that the standard deviation of H2 brain is much higher.

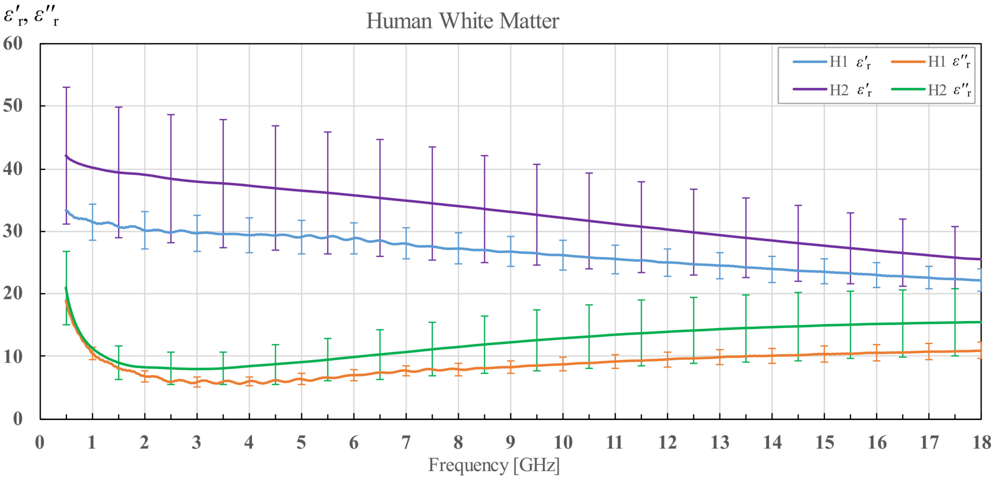

Figure 3. Permittivity of human white matter for brains H1 and H2 with corresponding standard deviations.

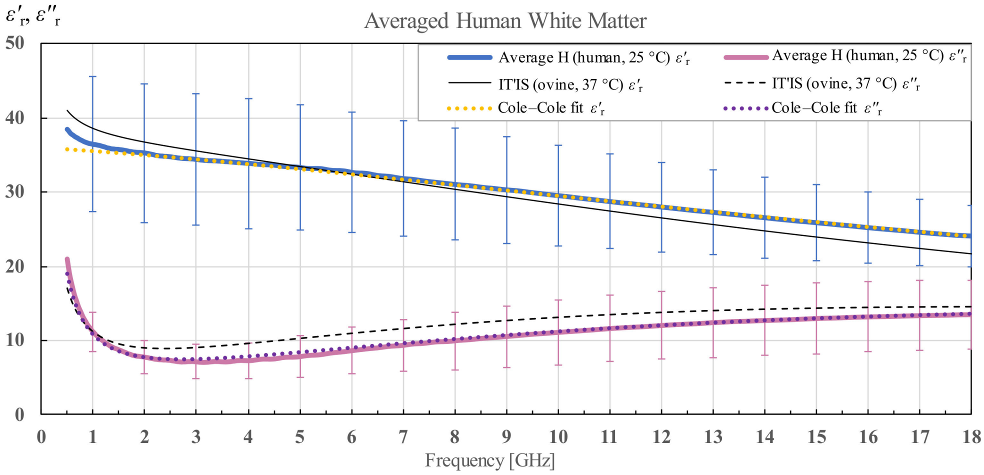

Figure 4. Average permittivity of human white matter with standard deviation and Cole–Cole fit, shown in comparison with the data from IT'IS database [21].

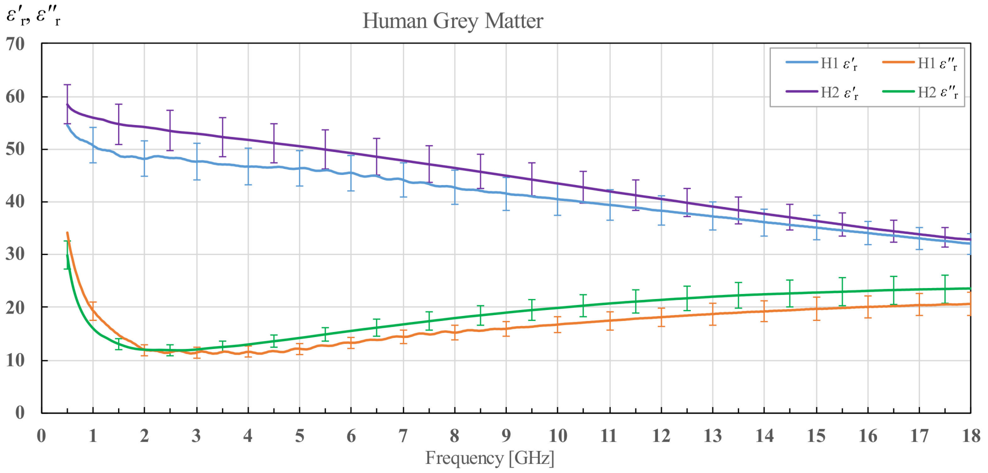

Figure 5. Permittivity of human grey matter for brains H1 and H2 with corresponding standard deviations.

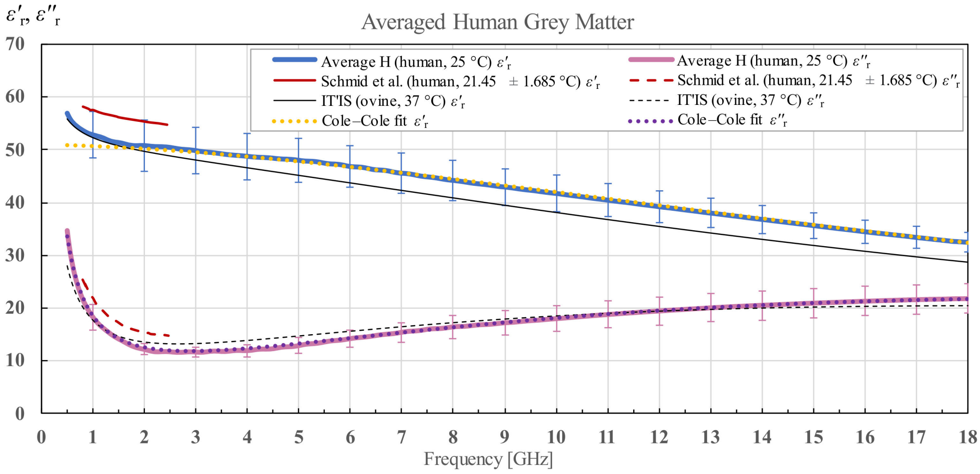

Figure 6. Average permittivity of human grey matter with standard deviation and Cole–Cole fit, shown in comparison with the data from IT'IS database [21] and Schmid et al. [28].

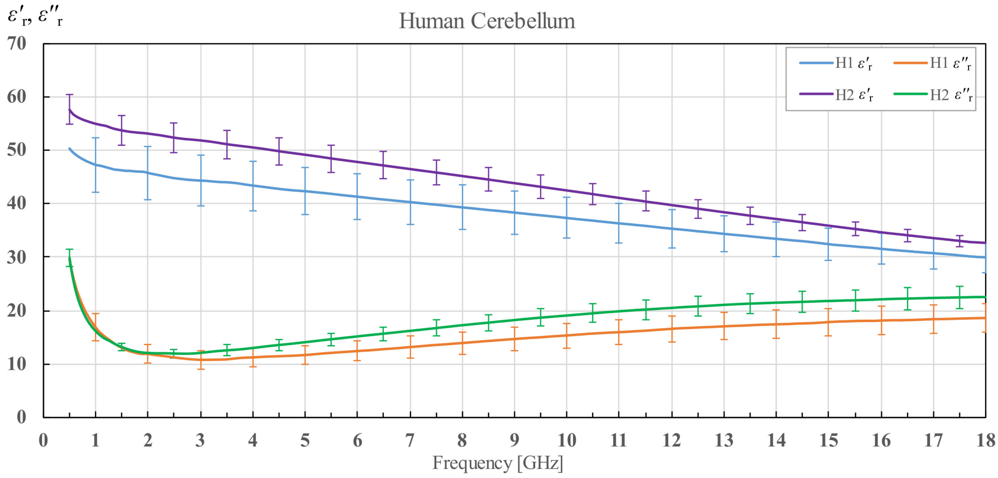

Figure 7. Permittivity of human cerebellum for brains H1 and H2 with corresponding standard deviations.

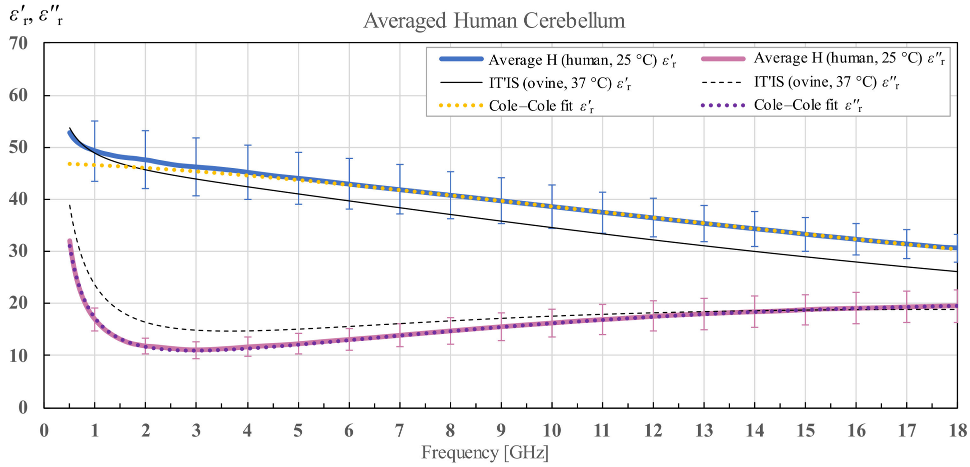

Figure 8. Average permittivity of human cerebellum with standard deviation and Cole–Cole fit, shown in comparison with the data from IT'IS database [21].

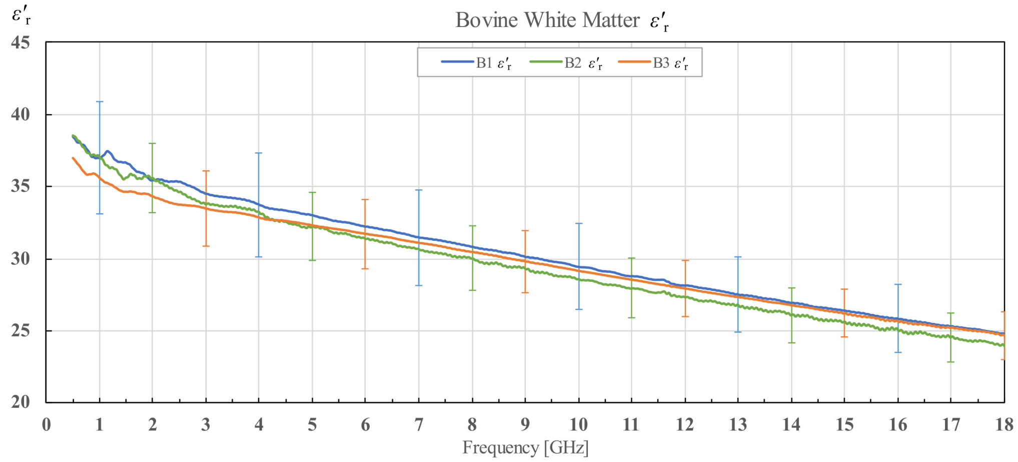

Figure 9. Real part of permittivity of bovine white matter for brains B1, B2 and B3 with associated standard deviations.

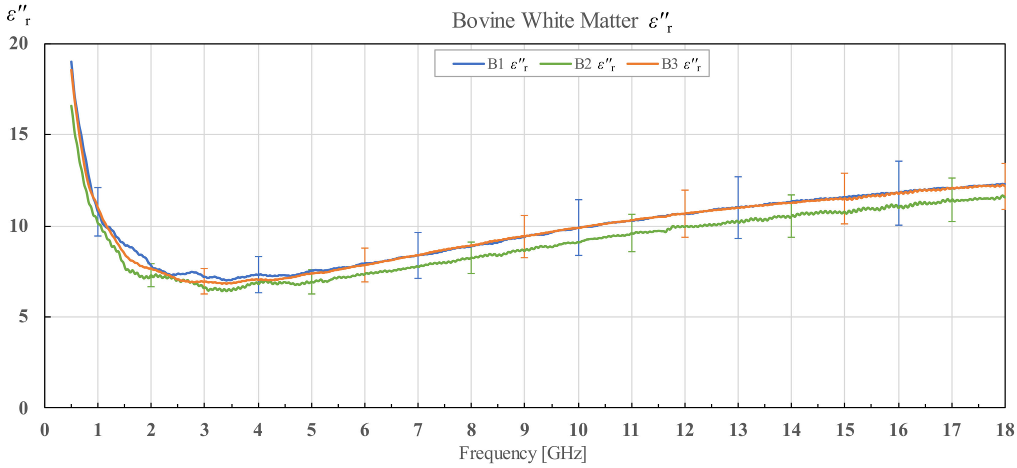

Figure 10. Imaginary part of permittivity of bovine white matter for brains B1, B2 and B3 with associated standard deviations.

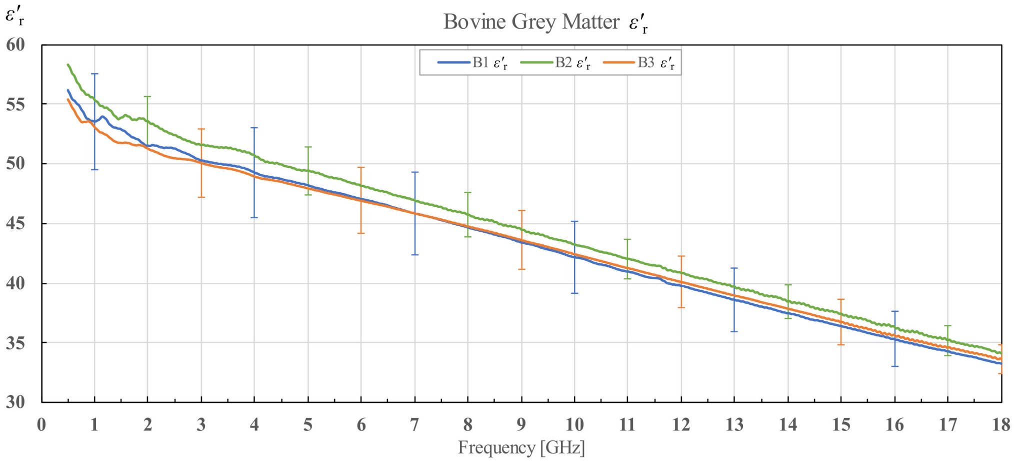

Figure 11. Real part of permittivity of bovine grey matter for brains B1, B2 and B3 with associated standard deviations.

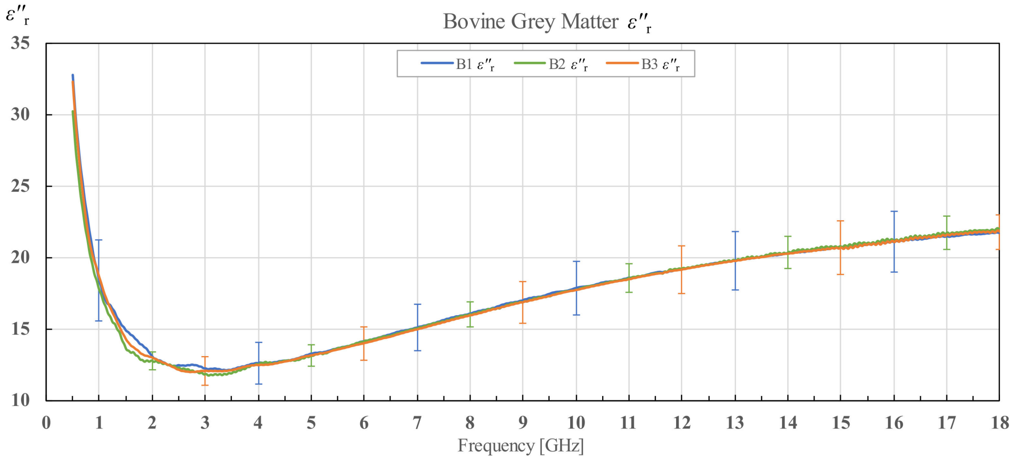

Figure 12. Imaginary part of permittivity of bovine grey matter for brains B1, B2 and B3 with associated standard deviations.

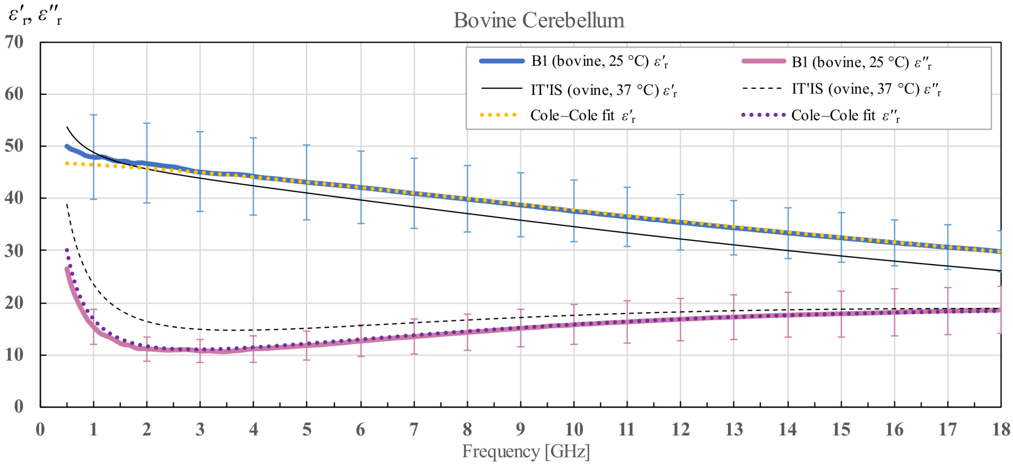

Figure 13. Permittivity of bovine cerebellum for brain B1 with standard deviation and Cole–Cole fit, shown in comparison with the data from IT'IS database [21].

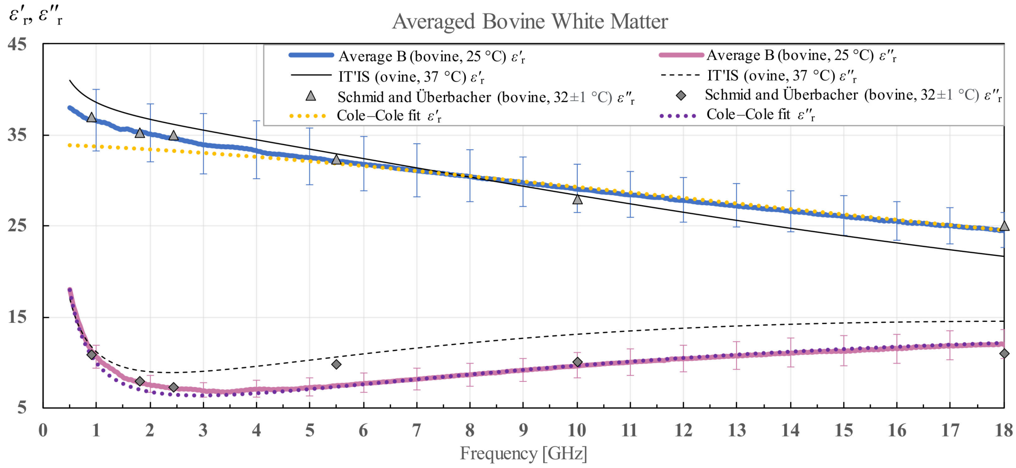

Figure 14. Average permittivity of bovine white matter with standard deviation and Cole–Cole fit, in comparison with the data from IT'IS database [21] and Schmid and Überbacher [29].

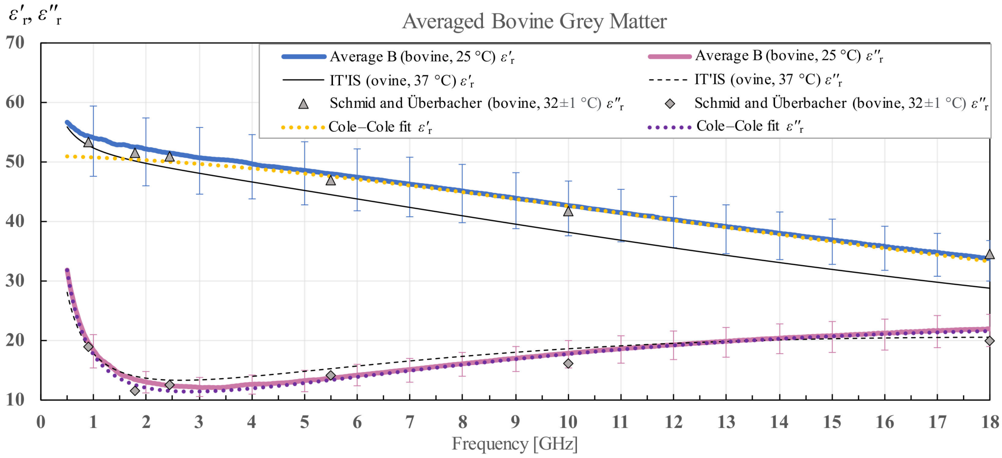

Figure 15. Permittivity of averaged bovine grey matter with standard deviation and Cole–Cole fit, in comparison with the data from IT’IS database [21] and Schmid and Überbacher [29].

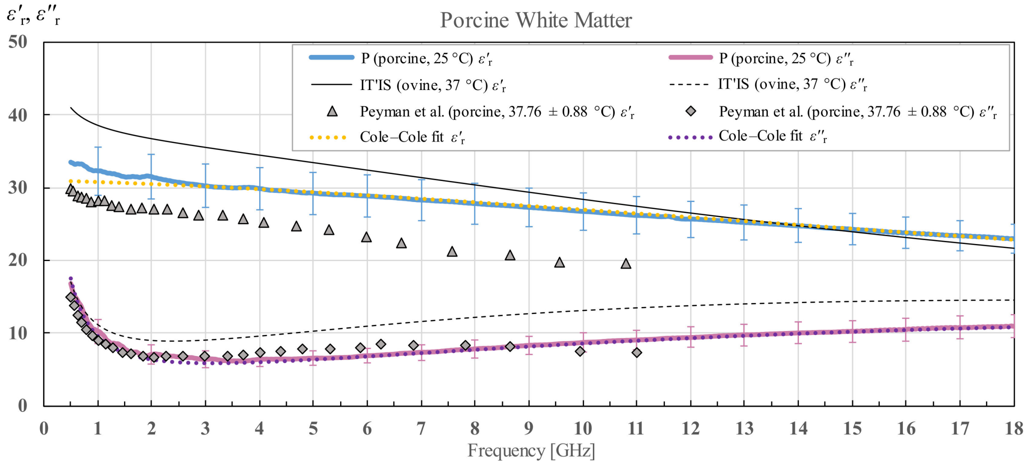

Figure 16. Permittivity of porcine white matter (P) with standard deviation and Cole–Cole fit, shown in comparison with the data from IT’IS database [21] and Peyman et al. [30].

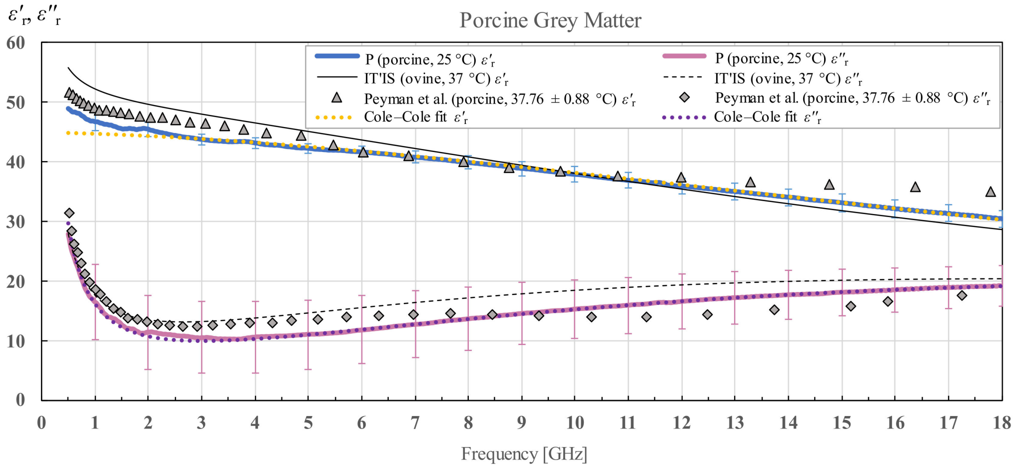

Figure 17. Permittivity of porcine grey matter (P) with standard deviation and Cole–Cole fit, shown in comparison with the data from IT’IS database [21] and Peyman et al. [30].

Additionally, Figure 4 shows the averaged results of white matter for human brains H1 and H2 with the associated overall standard deviation for human white matter measurements and Cole–Cole fit of the measured data according to (4). The results are compared to the permittivity data from the IT'IS database [21], shown in black for reference.

Figure 5 shows the permittivity of grey matter of brains H1 and H2. Again, the brain H2 has overall larger permittivity over the whole frequency range, but the difference is less prominent between the two brains for both the real and imaginary parts of the permittivity. Additionally, this time, the standard deviation is comparable between H1 and H2.

Figure 6 shows the averaged results of grey matter for human brains H1 and H2 with the associated standard deviation and Cole–Cole fit of the measured data according to (4) and the IT'IS data shown for reference. For the human grey matter, there is another suitable reference for comparison shown also on the chart, by Schmid et al. [28], who measured the human grey matter permittivity in a narrow frequency range from 800 MHz to 2450 MHz.

The results for cerebellum of both brain H1 and H2 are shown in Figure 7. The difference in cerebellum permittivity of the two brains is considerable. The results for human brain H1 are lower in permittivity for both the real and imaginary parts from brain H2. However, now the standard deviation of the averaged measurement results is larger for the brain H1, which is in contrast to the results for white matter.

Figure 8 shows the averaged cerebellum of both human brains along with the corresponding standard deviation and Cole–Cole fit of the measured data according to (4). The IT'IS data are displayed in black for comparison.

3.2. Bovine Brain Permittivity

The results for $\varepsilon_r\prime$ and ε_r'' of three different bovine brains (B1, B2 and B3), along with their corresponding standard deviations, are shown in Figures 9 and 10 for white matter, and Figures 11 and 12 for grey matter. The results for white and grey matter for brain B2 and B3 follow similar trendlines as the results for brain B1. Overall, all three measured brains have similar permittivity even though they are from different specimens.

The measurement results for cerebellum tissue of brain B1 are shown in Figure 13. It is immediately noticeable that the measured data for cerebellum have a much larger standard deviation than the measured data for white and grey matter. It is because cerebellum is composed of both white and grey matter which are tightly intertwined, so that white and grey matter in cerebellum cannot be discriminated by the probe. However, due to this heterogeneity, the measured results varied greatly from point to point. However, all three tissues follow the general trends of the previously reported literature data [21,29].

The averaged results and Cole–Cole fit of the measured data according to (4) for white and grey matter for all measurement points of the three bovine brains along with the standard deviation calculated for all samples are shown in Figures 14 and 15. IT'IS data [21] are shown in black for reference. For the bovine white and grey matter, there is a suitable reference for comparison shown also on the chart, by Schmid and Überbacher [29], who measured the bovine white and grey matter permittivity only at a few discrete frequency points shown in grey markers.

3.3. Porcine Brain Permittivity

The measured porcine brain white and grey matter permittivity and a Cole–Cole fit of the measured data according to (4) are shown in Figures 16 and 17 respectively. IT'IS data [21] is shown in black for reference. For the porcine white and grey matter, there is a suitable reference for comparison shown also on the chart, by Peyman [30], who measured the porcine white and grey matter permittivity in the similar frequency range, shown in grey markers.

We can notice that the grey matter has a substantially larger standard deviation of ε_r'' than ε_r', especially when taking into account the relative value of standard deviation with respect to the magnitude of ε_r''.

3.4. Interspecies Variability in Permittivity of White and Grey Matter and Cerebellum

Lastly, it is interesting to see comparative results for white and grey matter of all three species, as well as to compare human and bovine cerebellum data. Permittivity results of three different bovine brain tissues as well as two human brain tissues are averaged and only the average is shown in Figures 18–20. Averaged bovine brains are simply labeled as B and averaged human tissues as H. Comparison of the white matter for all three species is shown in Figure 18. Even though the three species show some variability in both the real and imaginary parts of complex permittivity, they show a similar sloping trend.

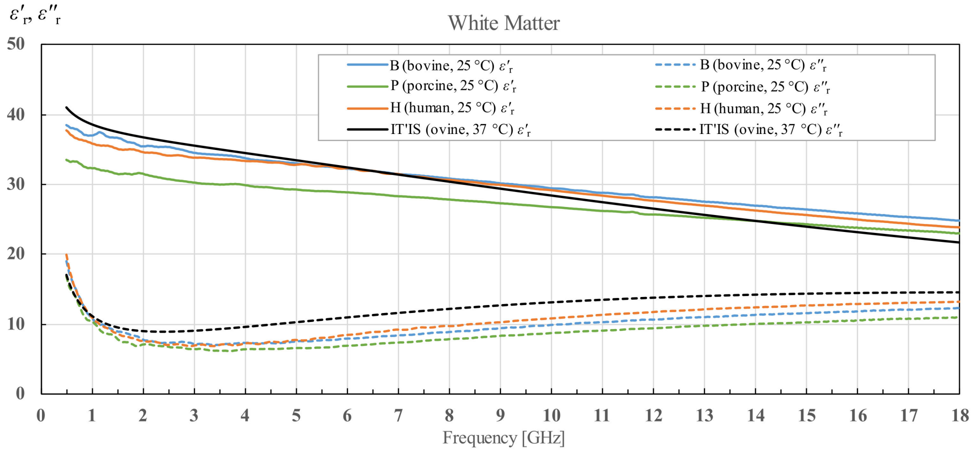

Figure 18. White matter permittivity comparison of averaged bovine brains (B), averaged human brains (H) and a porcine brain (P), as well as comparison with the published data from IT'IS database [21].

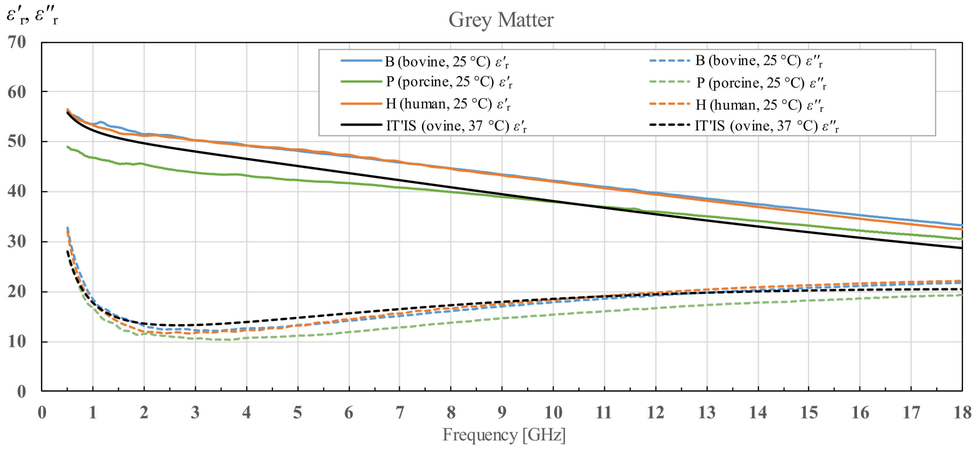

Figure 19. Grey matter permittivity comparison of averaged bovine brains (B), averaged human brains (H) and a porcine brain (P) as well as comparison with the published data from IT'IS database [21].

Results for grey matter for all three species are shown in Figure 19. Similar to the results for white matter, averaged permittivity of bovine brains matches the averaged permittivity of human brains. Again, porcine brain measurements differ from the aforementioned two. However, the sloping trend is similar for all three species.

Lastly, the permittivity of cerebellum is shown in Figure 20. As described in Section 2.3, cerebellum was measured only for brains H1, H2 and B1. The results for H1 and H2 are averaged and displayed as H, while the results for one bovine brain are displayed as B1.

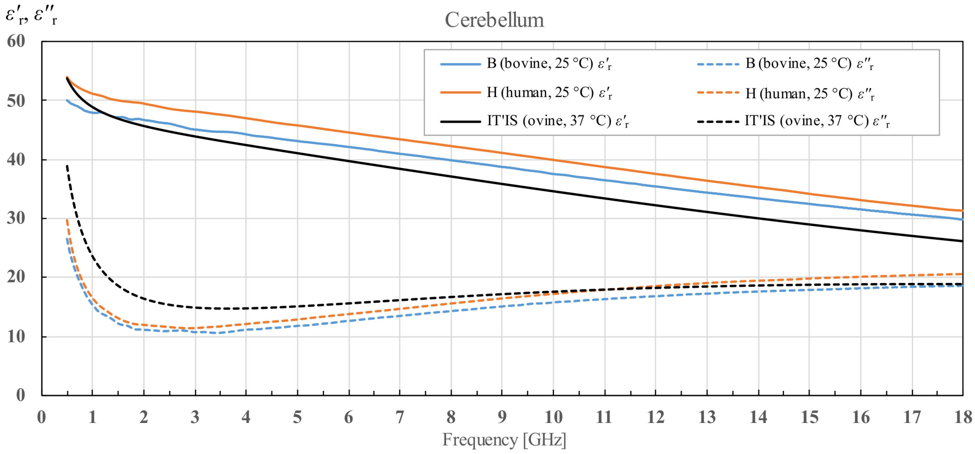

Figure 20. Cerebellum permittivity comparison of bovine brain (B1) and averaged human brains (H), as well as comparison with the published data from IT'IS database [21].

3.5. Human White and Grey Matter Permittivity on Day 2 and Day 3

For permittivity of H1 measured on day 2 and day 3, we calculated the percent change in permittivity relative to the permittivity measured on day 1 using Equations (5) and (6) for both white and grey matter separately.

$$\Delta\varepsilon'_{r(Day\ 2\ or\ Day\ 3)}\ [\%] = \frac{\varepsilon'_{r(Day\ 2\ or\ Day\ 3)} - \varepsilon'_{r(Day\ 1)}}{\varepsilon'_{r(Day\ 1)}} \cdot 100\%, \tag{5}$$

$$\Delta\varepsilon''_{r(Day\ 2\ or\ Day\ 3)}\ [\%] = \frac{\varepsilon''_{r(Day\ 2\ or\ Day\ 3)} - \varepsilon''_{r(Day\ 1)}}{\varepsilon''_{r(Day\ 1)}} \cdot 100\% \tag{6}$$

The calculated results as a function of frequency are shown in Figures 21 and 22. The fluctuations in the results visible under 8 GHz, and especially prominent for ε''_r, are due to the imperfections of the measurement setup. Besides the aforementioned fluctuations, it is worth noting that the difference in permittivity is fairly consistent throughout the measured frequency range. The percent change averaged across the measured frequency range is shown in Table 2.

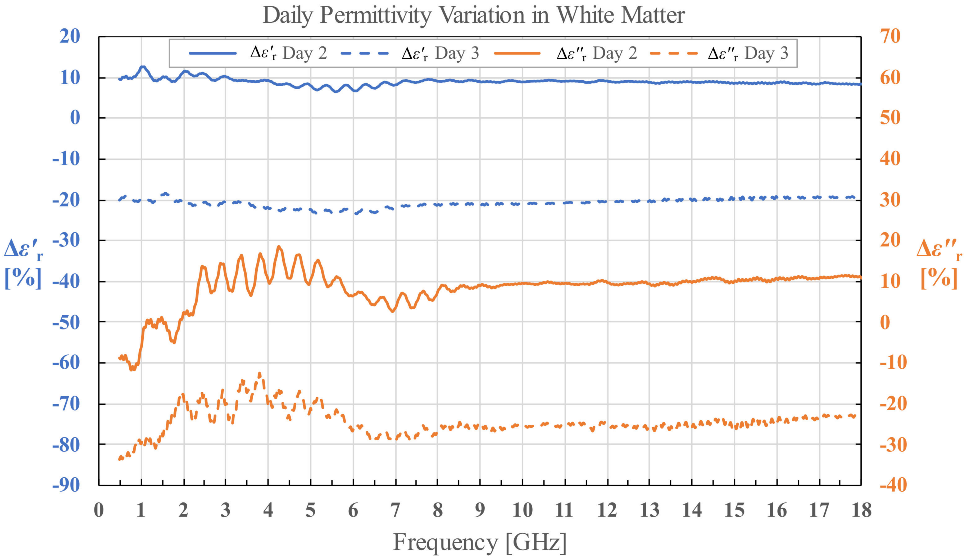

Figure 21. Permittivity change in human white matter for brain H1 on day 2 and day 3.

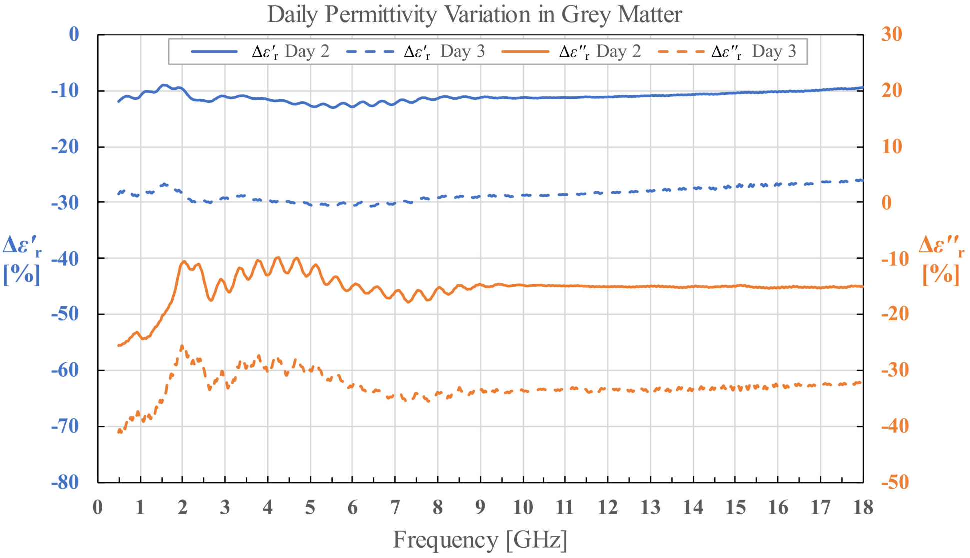

Figure 22. Permittivity change in human grey matter for brain H1 on day 2 and day 3.

Table 2. Average percent change in ε_r' and ε_r'' on day 2 and day 3 compared to day 1 for grey and white matter.

	Day 2		**Day 3**	
	$\varepsilon_r^{'}$	$\varepsilon_r^{''}$	$\varepsilon_r^{'}$	$\varepsilon_r^{''}$
Grey Matter	−11.19%	−15.29%	−28.55%	−32.81%
White Matter	8.97%	8.24%	−20.63%	−24.34%

3.6. Cole–Cole Models of the Data

The averaged measured permittivity for each species and each tissue was additionally depicted as a single pole Cole–Cole model in Figures 4, 6, 8 and 13–17. The Cole-Cole fits were derived in Microsoft Excel using Equation (4), producing the best fits predominantly based on the least-squares, with additional manual adjustments for a better fit at the highest measured frequencies. The derived parameters are listed in Table 3.

Table 3. Single pole Cole–Cole parameters for measured brain tissues.

		ε_∞	ε_s	α	σ	$\tau\,[ps]$
Porcine Brain	White Matter	5	31	0.09	0.47	5.4
	Grey Matter	3	45	0.05	0.8	6.2
Bovine Brain	White Matter	5	34	0.09	0.48	5.6
	Grey Matter	5	51	0.05	0.85	6.8
	Cerebellum	5	47	0.1	0.8	7.0
Human Brain	White Matter	2	36	0.13	0.5	5.8
	Grey Matter	5	51	0.05	0.9	7.1
	Cerebellum	3	47	0.08	0.83	6.5

3.7. Supplementary Materials

The numerical values of the measured permittivity presented in Sections 3.1–3.5 are made available in the form of downloadable Excel tables, as Supplementary Materials accompanying this paper, as follows:

- human white matter, grey matter and cerebellum permittivity for brains H1 and H2, with the average permittivity of human white matter, grey matter and cerebellum;

- bovine white matter and grey matter permittivity for brains B1, B2 and B3, and cerebellum permittivity for brain B1, with the average permittivity of bovine white matter and grey matter;
- porcine white matter and grey matter permittivity;
- human white matter permittivity for brain H1 measured along the course of three days;
- Cole–Cole models for the average permittivity of each tissue.

4. Discussion

4.1. Results Comparison with the Published Literature

4.1.1. General Remarks

Our measurement results were primarily compared with the IT'IS database [21], as it serves as the most comprehensive published reference on tissue permittivity and covers our whole measurement frequency range. The IT'IS data on white matter, grey matter and cerebellum permittivity originate from Gabriel [20]. The values for brain tissues in the frequency range from 500 MHz to 18 GHz in Gabriel [20] were compiled from the literature already published at that time (i.e., before 1996):

- rabbit specimen at 37 °C [31] (white and grey matter),
- mouse specimen at 37 °C [32] (grey matter),
- rat specimen in vivo at 32 °C [33] (grey matter),
- feline specimen in vivo at 36 °C [33] (grey matter),
- canine specimen in situ at 36 °C [34] (white and grey matter),
- canine specimen at 20 °C [35] (white and grey matter),
- feline specimen in vivo at 33 °C [36] (white and grey matter),
- canine specimen at 37 °C [37] (white and grey matter),

as well as from her own measurement results.

In study [20], Gabriel reported her own measurement results for ovine white matter, grey matter and cerebellum measured at 37 °C, as well as for human white matter and grey matter obtained from autopsies and measured also at 37 °C. While the ovine tissue results are reported in detail as comprehensive sets of measurement results measured in a continuous frequency range from 10 Hz to 20 GHz, the human tissues are reported only for a several frequency points. The final output of the Gabriel study [20] is a set of Cole-Cole models, i.e., the mathematical equations representing best fits for each tissue. These models are the basis for the IT'IS data. Gabriel states in [20] that the parameters of each model were adjusted to correspond to a close fit between the model and the most comprehensive data set available for the particular tissue. Observing the models for the white matter, grey matter and cerebellum in [20], they are mostly based on the ovine results, which are the most comprehensive data set for these particular tissues.

Accordingly, the difference between our results and IT'IS database could partly be explained by the difference in species. Additionally, the results compiled in [20] were all published for temperatures exceeding 30 °C with the exception of canine brain measurements from [35], which were done at 20 °C. Higher temperatures in general result in a lower real part of relative permittivity of biological tissues over the whole frequency range as well as increase of conductivity, i.e., rhe imaginary part of the permittivity [38]. Our results for $\varepsilon_r{\prime}$ are higher than the IT'IS data for H1 and H2 grey matter and cerebellum, H2 white matter, and grey matter for all three bovine brains. White matter from all three bovine brains as well as both white and grey matter from the porcine brain show lower permittivity than the IT'IS data up to some crossover frequency, after which they display higher permittivity. Similar occurrence is visible for H1 white matter, but as the crossover frequency is over 16 GHz, in most of the measured frequency range the permittivity is lower than the reported values from IT'IS. When it comes to the imaginary part of the relative permittivity, the results are systematically lower than the reported values from IT'IS for: H1 white and grey matter and cerebellum, all three bovine white matter measurements, B1 cerebellum and porcine white and grey matter. Other tissues again display crossover frequency below which the imaginary part of the permittivity is lower than the reported data. Those tissues are: H2 white and grey matter and cerebellum, and all three bovine grey matter measurements.

We are aware that our measured data is compared here with the data for different species at different temperatures. Hence, the comparison, although indicative, must be taken with some reservation. However, there are not enough published data on permittivity of brain tissues of various species measured at various temperatures in a relevant and continuous frequency range to make a direct comparison to a corresponding set of data. In general, the published data for all three measured tissues in this study are considerably dated and scarce. It is especially true for human tissues where, to the best of our knowledge, there are no reported data on human white matter, grey matter and cerebellum measured in the continuous frequency range of this study.

4.1.2. Human Tissues

Sparse data for human white and grey matter are presented in [20] in a graphical form; unfortunately, the logarithmic scale of the graphics is such that it is impossible to precisely extract those values, thus they cannot serve for comparison. Clearly, those values were not even meant to serve such a purpose, as the final output of [20] were the mathematical models described by Cole-Cole equations (and referenced later by IT'IS). We also compared our measured data with the usable data for human grey matter in the narrow frequency range from 800 MHz to 2450 MHz published in [28]. Our measurement results follow a similar trendline, but with a downward shift for both the real and imaginary parts of the permittivity. The reported temperature at the measurement points in [28] was from 18 °C to 25 °C with the mean of 21.35 °C, which is lower compared to our measurement temperature of 25 °C. The difference in permittivity could be explained by the difference in temperature as well as the difference in the measurement protocol. Measurements in [28] were performed over arachnoid membrane, which could result in higher measured permittivity values.

4.1.3. Bovine Tissues

Bovine white and grey matter was additionally compared with the reported results from Schmid and Überbacher [29], which reported the data at seven discrete frequency points, out of which six overlap with our measured frequency range (0.9 GHz, 1.8 GHz, 2.45 GHz, 5.5 GHz, 10 GHz and 18 GHz). The excised brain tissues were of either an adult animal or a young calf. Our measurement results are in better agreement with the results for young calves. This was to be expected as all three calves from our study were under 12 months of age, and thus better suit the reported results for young animals. The agreement between the data is satisfactory, especially when considering that their white and grey matter was measured at 32 °C.

4.1.4. Porcine Tissues

Porcine white and grey matter was additionally compared with the results published in [30]. The results from [30] were measured from 50 MHz to 20 GHz in vivo for pigs weighing around 50 kg and ex vivo for three different weight categories of pigs (10, 50 and 250 kg), and the tissues were measured as close to 37 °C as possible. Although we did not know the age of our specimen, we could conclude by the size of the brain that it was not a young porcine specimen. That is why we compared our results with the results for 250 kg pigs. Our results for white matter exhibit a higher real part of the permittivity, which is to be expected with the difference in tissue temperature, while the results for the imaginary part are lower up to 9 GHz, after which they are slightly higher than reported in [30]. A very similar trend for the imaginary part is noticeable for the results for grey matter where the crossover frequency is again around 9 GHz. The real part of the permittivity of grey matter measured in [30] is comparable to ours.

4.2. Interspecies Variability

There is a noticeable interspecies variability for all three measured brain tissues. The averaged results for the real part of the permittivity of bovine brain white and grey matter are similar to the averaged results for human brain white and grey matter. The imaginary part of the permittivity shows greater difference, but the results are still comparable. Both human and bovine white and grey matter show greater deviation from the porcine brain white and grey matter than from each other. The permittivity data for cerebellum are only available for human and bovine brains and they display noticeable difference between bovine and human cerebellum in the both real and imaginary parts of the permittivity. It should be remarked that the permittivity trends, with respect to frequency, are similar for all three measured species when comparing the same brain tissue.

4.3. Tissue Degradation over Time

Regarding the effects of tissue degradation over time in the stored samples, measured on H1 brain on day 2 and day 3, there is a clear trend of increase in magnitude of average change in permittivity from day 2 to day 3 in all measured tissues for both ε_r' and ε_r''. The results confirm that there is an increase in the tissue degradation over time. Observing the results for grey matter in Table 1, the decrease in ε_r' and ε_r'' (which correlates with the decrease in conductivity σ) for both day 2 and day 3 could be explained by the loss of water in the tissue, i.e., dehydration. The effect of water content on permittivity and conductivity of brain tissues was modeled in [39]. The same process of dehydration is an explanation for the results for white matter on day 3. The only exception are the results for white matter on day 2, where the permittivity increased with respect to the measured results on the fresh samples on day 1. The average standard deviation of the white matter measurements was not noticeably higher on day 2 to justify such a result. Unfortunately, this anomaly remained unnoticed at the time of measurements, i.e., until the results were processed. Thus, we can only speculate post festum that there was an unnoticed systematic error in this set of measurements, which resulted in a drift of the results; possibly due to an inadequately performed probe calibration. However, it must again be noted that the change in white matter permittivity measured on day 3 suggests that the decay of white matter increased with time, just like for the grey matter.

4.4. Intraspecies Variability

All three bovine brains show similar permittivity values for both grey and white matter, which is to be expected as they all originate from healthy specimens of similar age. Although the intraspecies variability between bovine grey and white matter is negligible, the human brain results suggest different conclusions. There is an apparent difference in all three measured tissues (grey and white matter and cerebellum), where the results for H2 are consistently higher than for H1 for both the real and imaginary parts of the permittivity.

4.4.1. Age-Related Factors

The most obvious difference between H1 and H2 is their age, although not necessarily the most important one. To the best of our knowledge, the only studies trying to directly link the dielectric properties to the age of the specimen are the studies [29,30,40]. However, all of them compare the difference between the young (immature) and the adult (fully matured) brain. On the other hand, our human brains were both fully matured, but one belonged to a middle-aged adult, while the other belonged to a senior adult. Therefore, the studies [29,30,40] cannot be confidently used in this context.

As there are no other appropriate studies done on age-related permittivity changes of brain tissues, we searched for studies researching the water content of brain tissues in older adults. The rationale for this is the known fact that the permittivity of biological tissues, in this frequency range, is dominantly determined by their water content. The higher the water content of a tissue, the higher permittivity it has, as demonstrated in [39]; as water has the largest permittivity value compared to any other tissue constituent. That is also why grey matter has overall larger permittivity and conductivity than white matter, as its water content is around 83%, compared to the 69% water content found in white matter [39]. Accordingly, our results suggest that all three brain tissues taken from brain H2 had a higher water content than those taken from H1. The study by Gullet et al. [41] showed that the extracellular free water within white matter increases with normal aging and can even be used as an indicator of cognitive decline. Free water refers to the water molecules that are freely diffusing without being hindered or restricted by tissue membranes. Increases in free water are connected with accumulation of extracellular water, which may occur due to processes such as atrophy, edema, or neurodegenerative disease. The increase in free water causes a decrease in white matter integrity [41]. Additionally, free water has a larger permittivity than bound water as bound water exhibits a permittivity value closer to that of dry matter, as reported in [42]. Thus, a reasonable explanation for the difference in permittivity of brains H1 and H2 could be in the changes that were ongoing in the elderly brain, causing it to have an increase in extracellular free water, especially because the biological tissue permittivity in the gigahertz frequency range is mostly influenced by the polarization of free water molecules [43].

4.4.2. Medical Condition of the Patients

Searching for potential causes of the difference in permittivity of brains H1 and H2, we paid additional attention to the medical condition of the deceased patients. Human brain H1 was from a male patient 50 years of age who died from dissection of abdominal aorta. Prior to his death, during hospitalization, the patient had acute renal insufficiency and hemodynamic instability, and was treated by means of intensive care therapy that included intubation and mechanical ventilation coupled with vasoactive therapy and intravascular volume replacement with 0.9% NaCl (saline) and colloid solutions. The presence of the aforementioned pathology, combined with the therapy used, could have easily caused the body fluid disbalance (oedema or dehydration) [44–46], thus changing the water content in the brain tissue. In this particular case the patient suffered from obvious loss of fluid that led to kidney failure. Also, an important factor to mention is that this patient had an MRI scan of the brain done during hospitalization that demonstrated combined ischemia and oedema of the brain stem (one of the brain parts most vulnerable to hypoxia; however, not the subject of analysis regarding its dielectric properties in this study) as a result of brain hypoperfusion hypoxic-ischemic injury [47].

Human brain H2 was from a female patient 84 years of age, that died from pulmonary oedema and had all the elements of hypotensive shock. One should note that in pulmonary oedema, as in this particular case, the patient had tachypnoea (very high number of inspirations/expirations in one minute). It is well known that tachypnoea leads to a lower amount of carbon dioxide (CO_2) in blood which then causes vasoconstriction of brain vessels and results in a reduced amount of cerebral blood volume, and thus reduces the brain water content [48]. This patient also received intensive care therapy measures because of hemodynamic instability, although to a lesser extent than the previously described patient due to the more rapid progression of disease that resulted in a lethal outcome.

The brain tissues H1 and H2 didn't show any macroscopic abnormalities, other than the visible atrophic changes on H2, however, within expectations according to the age of the patient. Also, the deceased patients did not have any disclosed brain pathologies in their medical records. Nevertheless, there is quite a real possibility that the basic pathology (non-primary brain pathologies: hypotensive or hypovolemic shock, acute renal dysfunction, pulmonary oedema et cetera), combined with intensive care therapy administered (volume replacement, vasoactive medications) could have led to changes in the brain water content, thus changing the dielectric properties of the tissues in question.

4.4.3. Tissue Variability

Lastly, it is worth noting that there is a factor of variability of the measured dielectric properties even when the tissues are considered homogenous. Therefore, the measured permittivity results can vary greatly when measured at different locations on the same specimen. The measurement study by Schmid et al. [28] states that the observed extent of standard deviation is around 6% for the real part of the permittivity and between 8% and 10% for the imaginary part of the permittivity. It is thought to be caused by the combination of biological variances in the tissue and by the differences in tissue temperature at the measurement sites. Similarly, Gabriel [20] states that their results' variability was in the range ±5%, and that the variation in tissue properties within a species may well exceed variations between species. That is an additional uncertainty factor that should be taken into consideration when comparing measurement results from seemingly identical specimens. The above applies not only to our measurement results, but also to all published results from the literature, which should always be taken with some reservation. The average standard deviations for measured brain tissues are shown in Table 4.

Table 4. Average standard deviation for measured white matter, grey matter and cerebellum of all measured brains.

Brain Sample	**White Matter**		**Grey Matter**		**Cerebellum**	
	ε_r'	ε_r''	ε_r'	ε_r''	ε_r'	ε_r''
H1	2.4	1.1	2.9	1.6	3.9	2.3
H2	8.1	4.5	3.1	1.9	2.1	1.5
B1	3.0	1.4	3.1	1.9	6.0	3.6
B2	2.1	0.9	1.7	0.9	-	-
B3	2.1	1.1	2.3	1.5	-	-
P	2.6	1.3	1.2	4.9	-	-

Comparing our results with the other published ex vivo permittivity data, we find that our standard deviations generally match those previously reported. For example, Fornes-Leal et al. [49] reported the standard deviation of measured permittivity of healthy colon tissues, varying from 2.33 to 3.12 for ε_r'' and from 0.09 to 2.68 for σ. It is important to note the difference between σ and ε_r'' as σ has a smaller absolute variation in value than ε_r''. Another, more recent example is the ex vivo measurement of ovine hearts in [50], where the mean standard deviation for ε_r' varies from 1.98 to 9.4 and from 0.04 to 0.35 for σ, depending on the measured part of the heart. Again, one should note the difference between σ and ε_r''. Consequently, the reported standard deviation of our data is within the expected standard deviation caused by the natural variation of the biological tissues that is also present in other reported ex vivo measurements.

5. Conclusions

The primary aim of this work was to report the measured dielectric permittivity of brain tissues, namely white matter, grey matter and cerebellum, in the microwave frequency range, from 0.5 to 18 GHz. Human, bovine and porcine brain samples were acquired and measured at the temperature of 25 °C. Human brain tissue permittivity is especially interesting for various medical uses; however, the measurement results in the literature are very scarce and dated. Therefore, the newly measured data certainly present a valuable addition to the knowledge about the human brain. The data containing permittivity values measured in this study are available as Supplementary Materials to this paper, to be freely used by other interested researchers.

Our results were compared with the published permittivity values for the corresponding tissues from the IT'IS database [21]. Furthermore, each species was compared with the suitable references for that species. The comparisons showed satisfactory overall agreement, while the observed differences led to important conclusions. The differences exist not only between our results and other references, but between the other references as well. This shows that the biological tissues exhibit variability in their permittivity within the same tissue type, which is a logical consequence of the natural variability of the tissue composition and physiological processes in the tissue specimen. This could be attributed to various factors, such as: age, health status, physiological condition, diet, postmortem sample handling etc. For most of the studies, these factors are mostly unknown or not disclosed. Therefore, each published data set, including our own, should be taken with some reservation. Accordingly, none of the references, not even those used here for comparison, can be considered as absolutely accurate data.

Regarding the inter- and intraspecies variations of our own measurement results, the interspecies differences were noticeable, but comparable to the standard deviation within the individual species.

In the course of this study, we used the opportunity to measure the same human white and grey matter samples over the course of three days, to examine the effects of tissue degradation on its permittivity. The trend suggested the loss of water content in the samples along the time course, despite keeping them in sealed containers in the refrigerator. This observation is in line with the expectations, and severely limits the usability of samples that are not freshly excised.

An important conclusion can be made based on the comparison between the two human brains obtained from autopsies. The two brains showed noticeable differences in their permittivity, which could be attributed not only to their age difference and natural tissue variability, but also to the medical conditions of the deceased patients. After analyzing their medical records, we conclude that there is quite a real possibility that the basic non-brain-related pathology of the patients, combined with intensive care therapy, could have led to changes in brain water content, potentially more significant than any age-related water content changes, thus affecting the dielectric properties of the brain tissues. Investigation of this hypothesis is far beyond the scope of this study; however, this important consideration, not previously mentioned in the literature, should be taken into account when measuring the permittivity of human brain tissues, as most of them would be derived from hospital autopsies and not from healthy individuals. As an argument supporting this hypothesis, the three bovine brains obtained from healthy animals of similar age showed very similar permittivity values.

Supplementary Materials: The following supporting information can be downloaded at: https://www.mdpi.com/article/10.3390/diagnostics12112580/s1, the measured permittivity data sets, described in Section 3.7.

Author Contributions: Conceptualization, A.Š. and A.K.; methodology, A.Š., A.M., A.K. and A.J.; formal analysis, A.M. and A.Š.; investigation, A.M., A.Š., A.K. and A.J.; writing—original draft preparation, A.M., A.Š. and A.K.; writing—review and editing, A.M., A.Š., A.K. and A.J.; supervision, A.Š.; project administration, A.Š. All authors have read and agreed to the published version of the manuscript.

Funding: This research received no external funding.

Institutional Review Board Statement: The study was conducted in accordance with the Declaration of Helsinki and approved by the Ethics Committee of University Hospital Centre Zagreb (Class: 8.1-20/48-2, no. 02/21 AG, date of approval: 24th of February 2020).

Informed Consent Statement: Not applicable.

Data Availability Statement: The measured permittivity data sets are available as Supplementary Materials accompanying this paper.

Acknowledgments: This study was performed within the research project "Measurements in Bioelectromagnetics (M-BEM)" supported by FESB, University of Split, and within the framework of COST Action MyWAVE CA17115. We gratefully acknowledge the organizational support of the Department of Pathology and Cytology, University Hospital Centre Zagreb.

Conflicts of Interest: The authors declare no conflict of interest.

References

1. Crocco, L.; Karanasiou, I.; James, M.L.; Conceição, R.C. (Eds.) *Emerging Electromagnetic Technologies for Brain Diseases Diagnostics, Monitoring and Therapy*; Springer International Publishing: Cham, Switzerland, 2018; ISBN 978-3-319-75006-4.
2. Saied, I.; Arslan, T.; Chandran, S.; Smith, C.; Spires-Jones, T.; Pal, S. Non-Invasive RF Technique for Detecting Different Stages of Alzheimer's Disease and Imaging Beta-Amyloid Plaques and Tau Tangles in the Brain. *IEEE Trans. Med. Imaging* **2020**, *39*, 4060–4070. [CrossRef] [PubMed]
3. Persson, M.; Fhager, A.; Trefna, H.D.; Yu, Y.; McKelvey, T.; Pegenius, G.; Karlsson, J.-E.; Elam, M. Microwave-Based Stroke Diagnosis Making Global Prehospital Thrombolytic Treatment Possible. *IEEE Trans. Biomed. Eng.* **2014**, *61*, 2806–2817. [CrossRef] [PubMed]
4. Ljungqvist, J.; Candefjord, S.; Persson, M.; Jönsson, L.; Skoglund, T.; Elam, M. Clinical Evaluation of a Microwave-Based Device for Detection of Traumatic Intracranial Hemorrhage. *J. Neurotrauma* **2017**, *34*, 2176–2182. [CrossRef] [PubMed]
5. El rube', I.; Heatley, D.; Abdel-Maguid, M. Detecting a Stroke-Affected Region in the Brain by Scanning with Low-Intensity Electromagnetic Waves in the Radio Frequency/Microwave Band. *Healthcare* **2021**, *9*, 1170. [CrossRef] [PubMed]
6. Vedin, T.; Bergenfeldt, H.; Holmström, E.; Lundager-Forberg, J.; Edelhamre, M. Microwave scan and brain biomarkers to rule out intracranial hemorrhage: Study protocol of a planned prospective study (MBI01). *Eur. J. Trauma Emerg. Surg.* **2022**, *48*, 1335–1342. [CrossRef]
7. Lazebnik, M.; Popovic, D.; McCartney, L.; Watkins, C.B.; Lindstrom, M.J.; Harter, J.; Sewall, S.; Ogilvie, T.; Magliocco, A.; Breslin, T.M.; et al. A large-scale study of the ultrawideband microwave dielectric properties of normal, benign and malignant breast tissues obtained from cancer surgeries. *Phys. Med. Biol.* **2007**, *52*, 6093–6115. [CrossRef]
8. Thill, M. MarginProbe ®: Intraoperative margin assessment during breast conserving surgery by using radiofrequency spectroscopy. *Expert Rev. Med. Devices* **2013**, *10*, 301–315. [CrossRef]
9. Burfeindt, M.J.; Zastrow, E.; Hagness, S.C.; Van Veen, B.D.; Medow, J.E. Microwave beamforming for non-invasive patient-specific hyperthermia treatment of pediatric brain cancer. *Phys. Med. Biol.* **2011**, *56*, 2743–2754. [CrossRef]
10. Schooneveldt, G.; Dobšíček Trefná, H.; Persson, M.; de Reijke, T.M.; Blomgren, K.; Kok, H.P.; Crezee, H. Hyperthermia Treatment Planning Including Convective Flow in Cerebrospinal Fluid for Brain Tumour Hyperthermia Treatment Using a Novel Dedicated Paediatric Brain Applicator. *Cancers* **2019**, *11*, 1183. [CrossRef]
11. Drizdal, T.; Paulides, M.M.; van Holthe, N.; van Rhoon, G.C. Hyperthermia treatment planning guided applicator selection for sub-superficial head and neck tumors heating. *Int. J. Hyperthermia* **2018**, *34*, 704–713. [CrossRef]
12. Prasad, B.; Kim, J.K.; Kim, S. Role of Simulations in the Treatment Planning of Radiofrequency Hyperthermia Therapy in Clinics. *J. Oncol.* **2019**, *2019*, 9685476. [CrossRef] [PubMed]
13. Datta, N.R.; Jain, B.M.; Mathi, Z.; Datta, S.; Johari, S.; Singh, A.R.; Kalbande, P.; Kale, P.; Shivkumar, V.; Bodis, S. Hyperthermia: A Potential Game-Changer in the Management of Cancers in Low-Middle-Income Group Countries. *Cancers* **2022**, *14*, 315. [CrossRef] [PubMed]
14. Kroesen, M.; van Holthe, N.; Sumser, K.; Chitu, D.; Vernhout, R.; Verduijn, G.; Franckena, M.; Hardillo, J.; van Rhoon, G.; Paulides, M. Feasibility, SAR Distribution, and Clinical Outcome upon Reirradiation and Deep Hyperthermia Using the Hypercollar3D in Head and Neck Cancer Patients. *Cancers* **2021**, *13*, 6149. [CrossRef] [PubMed]
15. Ramírez, A.; Rodríguez, P.; Gutiérrez, S.E.; Ávila, O. Preliminary experience in the management of brain and skull-base tumors with microwave ablation; feasibility guided by ultrasound, report from 23 cases. *Surg. Neurol. Int.* **2019**, *10*, 17. [CrossRef]
16. Redr, J.; Pokorny, T.; Drizdal, T.; Fiser, O.; Brunat, M.; Vrba, J.; Vrba, D. Microwave Hyperthermia of Brain Tumors: A 2D Assessment Parametric Numerical Study. *Sensors* **2022**, *22*, 6115. [CrossRef]
17. International Commission on Non-Ionizing Radiation Protection (ICNIRP) Guidelines for Limiting Exposure to Electromagnetic Fields (100 kHz to 300 GHz). *Health Phys.* **2020**, *118*, 483–524. [CrossRef]
18. Gosselin, M.-C.; Neufeld, E.; Moser, H.; Huber, E.; Farcito, S.; Gerber, L.; Jedensjö, M.; Hilber, I.; Gennaro, F.D.; Lloyd, B.; et al. Development of a new generation of high-resolution anatomical models for medical device evaluation: The Virtual Population 3.0. *Phys. Med. Biol.* **2014**, *59*, 5287–5303. [CrossRef]
19. ZMT Zurich MedTech, AG. Sim4Life. Available online: https://zmt.swiss/sim4life/ (accessed on 18 August 2022).
20. Gabriel, C. *Compilation of the Dielectric Properties of Body Tissues at RF and Microwave Frequencies*; Occupational and Environmental Health Directorate, Radiofrequency Radiation Division, Brooks Air Force Base: San Antonio, TX, USA, 1996.
21. Hasgall, P.A.; Di Gennaro, F.; Baumgartner, C.; Neufeld, E.; Lloyd, B.; Gosselin, M.C.; Payne, D.; Klingenböck, A.; Kuster, N. IT'IS Database for Thermal and Electromagnetic Parameters of Biological Tissues, Version 4.1. 2022. Available online: itis.swiss/database (accessed on 21 August 2022).
22. Cole, K.S.; Cole, R.H. Dispersion and Absorption in Dielectrics I. Alternating Current Characteristics. *J. Chem. Phys.* **1941**, *9*, 341–351. [CrossRef]
23. Šarolić, A.; Matković, A. Dielectric Permittivity Measurement Using Open-Ended Coaxial Probe—Modeling and Simulation Based on the Simple Capacitive-Load Model. *Sensors* **2022**, *22*, 6024. [CrossRef]
24. Keysight Technologies. *Keysight N1501A Dielectric Probe Kit 10 MHz to 50 GHz—Technical Overview*; Keysight Technologies: Santa Rosa, CA, USA, 2018.
25. Keysight Technologies. *Field Fox Handheld Analyzers—Technical Overview 2021*; Keysight Technologies: Santa Rosa, CA, USA, 2021.

26. La Gioia, A.; Porter, E.; Merunka, I.; Shahzad, A.; Salahuddin, S.; Jones, M.; O'Halloran, M. Open-Ended Coaxial Probe Technique for Dielectric Measurement of Biological Tissues: Challenges and Common Practices. *Diagnostics* **2018**, *8*, 40. [CrossRef]
27. Keysight Technologies. *N1500A Materials Measurement Suite—Technical Overview 2021*; Keysight Technologies: Santa Rosa, CA, USA, 2021.
28. Schmid, G.; Neubauer, G.; Mazal, P.R. Dielectric properties of human brain tissue measured less than 10 h postmortem at frequencies from 800 to 2450 MHz. *Bioelectromagnetics* **2003**, *24*, 423–430. [CrossRef] [PubMed]
29. Schmid, G.; Überbacher, R. Age dependence of dielectric properties of bovine brain and ocular tissues in the frequency range of 400 MHz to 18 GHz. *Phys. Med. Biol.* **2005**, *50*, 4711–4720. [CrossRef] [PubMed]
30. Peyman, A.; Holden, S.J.; Watts, S.; Perrott, R.; Gabriel, C. Dielectric properties of porcine cerebrospinal tissues at microwave frequencies: In vivo, in vitro and systematic variation with age. *Phys. Med. Biol.* **2007**, *52*, 2229–2245. [CrossRef] [PubMed]
31. Steel, M.C.; Sheppard, R.J. Dielectric properties of mammalian brain tissue between 1 and 18 GHz. *Phys. Med. Biol.* **1985**, *30*, 621–630. [CrossRef]
32. Thurai, M.; Goodridge, V.D.; Sheppard, R.J.; Grant, E.H. Variation with age of the dielectric properties of mouse brain cerebrum. *Phys. Med. Biol.* **1984**, *29*, 1133–1136. [CrossRef]
33. Kraszewski, A.; Stuchly, M.A.; Stuchly, S.S.; Smith, A.M. In vivo and in vitro dielectric properties of animal tissues at radio frequencies. *Bioelectromagnetics* **1982**, *3*, 421–432. [CrossRef]
34. Burdette, E.C.; Friederich, P.G.; Seaman, R.L.; Larsen, L.E. In Situ Permittivity of Canine Brain: Regional Variations and Postmortem Changes. *IEEE Trans. Microw. Theory Tech.* **1986**, *34*, 38–50. [CrossRef]
35. Xu, D.; Liu, L.; Jiang, Z. Measurement of the Dielectric Properties of Biological Substances Using an Improved Open-Ended Coaxial Line Resonator Method. *IEEE Trans. Microw. Theory Tech.* **1987**, *35*, 1424–1428. [CrossRef]
36. Stuchly, M.A.; Athey, T.W.; Stuchly, S.S.; Samaras, G.M.; Taylor, G. Dielectric properties of animal tissues in vivo at frequencies 10 MHz–1 GHz. *Bioelectromagnetics* **1981**, *2*, 93–103. [CrossRef]
37. Foster, K.R.; Schepps, J.L.; Stoy, R.D.; Schwan, H.P. Dielectric properties of brain tissue between 0.01 and 10 GHz. *Phys. Med. Biol.* **1979**, *24*, 1177–1187. [CrossRef]
38. Rossmann, C.; Haemmerich, D. Review of Temperature Dependence of Thermal Properties, Dielectric Properties, and Perfusion of Biological Tissues at Hyperthermic and Ablation Temperatures. *Crit. Rev. Biomed. Eng.* **2014**, *42*, 467–492. [CrossRef] [PubMed]
39. Michel, E.; Hernandez, D.; Lee, S.Y. Electrical conductivity and permittivity maps of brain tissues derived from water content based on T_1-weighted acquisition. *Magn. Reson. Med.* **2017**, *77*, 1094–1103. [CrossRef] [PubMed]
40. Mohammed, B.; Bialkowski, K.; Abbosh, A.; Mills, P.C.; Bradley, A.P. Closed-form equation to estimate the dielectric properties of biological tissues as a function of age: Dielectric Properties of Biological Tissues. *Bioelectromagnetics* **2017**, *38*, 474–481. [CrossRef] [PubMed]
41. Gullett, J.M.; O'Shea, A.; Lamb, D.G.; Porges, E.C.; O'Shea, D.M.; Pasternak, O.; Cohen, R.A.; Woods, A.J. The association of white matter free water with cognition in older adults. *NeuroImage* **2020**, *219*, 117040. [CrossRef]
42. Jones, S.B.; Sheng, W.; Or, D. Dielectric Measurement of Agricultural Grain Moisture—Theory and Applications. *Sensors* **2022**, *22*, 2083. [CrossRef]
43. Siwach, P.; Levy, E.; Livshits, L.; Feldman, Y.; Kaganovich, D. Water is a biomarker of changes in the cellular environment in live animals. *Sci. Rep.* **2020**, *10*, 9095. [CrossRef]
44. Lewis, S.R.; Pritchard, M.W.; Evans, D.J.; Butler, A.R.; Alderson, P.; Smith, A.F.; Roberts, I. Colloids versus crystalloids for fluid resuscitation in critically ill people. *Cochrane Database Syst. Rev.* **2018**, *8*, CD000567. [CrossRef]
45. Schrier, R.W.; Wang, W.; Poole, B.; Mitra, A. Acute renal failure: Definitions, diagnosis, pathogenesis, and therapy. *J. Clin. Investig.* **2004**, *114*, 5–14. [CrossRef]
46. Haller, M.; Schelling, G. Medizin aktuell: Aktuelle Strategien Klinischer Ernährung II. *Anaesthesist* **2000**, *49*, 349–352. [CrossRef]
47. DeSai, C.; Hays Shapshak, A. Cerebral Ischemia. In *StatPearls*; StatPearls Publishing: Treasure Island, FL, USA, 2022.
48. Zhang, Z.; Guo, Q.; Wang, E. Hyperventilation in neurological patients: From physiology to outcome evidence. *Curr. Opin. Anaesthesiol.* **2019**, *32*, 568–573. [CrossRef]
49. Fornes-Leal, A.; Garcia-Pardo, C.; Frasson, M.; Pons Beltrán, V.; Cardona, N. Dielectric characterization of healthy and malignant colon tissues in the 0.5–18 GHz frequency band. *Phys. Med. Biol.* **2016**, *61*, 7334–7346. [CrossRef] [PubMed]
50. Ištuk, N.; Porter, E.; O'Loughlin, D.; McDermott, B.; Santorelli, A.; Abedi, S.; Joachimowicz, N.; Roussel, H.; O'Halloran, M. Dielectric Properties of Ovine Heart at Microwave Frequencies. *Diagnostics* **2021**, *11*, 531. [CrossRef] [PubMed]

APPENDIX B

Title	The Effect of Freezing and Thawing on Complex Permittivity of Bovine Tissues
Authors	Anđela Matković, Antonio Šarolić
Journal	Sensors
Impact factor	3.9
Volume and number	22, 24
Year	2022
Article number	9806
DOI	10.3390/s22249806
Abstract	The aim of this study was to investigate how the freezing and thawing of biological tissues affect their complex permittivity in the microwave frequency range from 0.5 MHz to 18 GHz. We measured the complex permittivity of ex vivo bovine tissues, including brain white and grey matter, liver, and muscle, using an open-ended coaxial probe. Bovine tissues were chosen for their availability and similarity to human tissue permittivity. The samples were measured at 25 °C, before they were frozen either in a commercial freezer below -18 °C or in liquid nitrogen, nominally at -196 °C. The measured permittivity before freezing was compared to the permittivity measured after freezing and thawing the tissues back to 25 °C. Statistical analysis of the results showed a statistically significant change in permittivity after freezing and thawing by both methods for all the measured tissues, at least in some parts of the measured frequency range. The largest difference was observed for the white matter, while the liver had the smallest percent change.

sensors

Article

The Effect of Freezing and Thawing on Complex Permittivity of Bovine Tissues

Anđela Matković and Antonio Šarolić *

FESB, University of Split, HR-21000 Split, Croatia
* Correspondence: antonio.sarolic@fesb.hr

Abstract: The aim of this study was to investigate how the freezing and thawing of biological tissues affect their complex permittivity in the microwave frequency range from 0.5 MHz to 18 GHz. We measured the complex permittivity of ex vivo bovine tissues, including brain white and grey matter, liver, and muscle, using an open-ended coaxial probe. Bovine tissues were chosen for their availability and similarity to human tissue permittivity. The samples were measured at 25 °C, before they were frozen either in a commercial freezer below −18 °C or in liquid nitrogen, nominally at −196 °C. The measured permittivity before freezing was compared to the permittivity measured after freezing and thawing the tissues back to 25 °C. Statistical analysis of the results showed a statistically significant change in permittivity after freezing and thawing by both methods for all the measured tissues, at least in some parts of the measured frequency range. The largest difference was observed for the white matter, while the liver had the smallest percent change.

Keywords: complex permittivity measurement; open-ended coaxial probe; freezing and thawing of biological tissues; ex vivo bovine tissues; brain white and grey matter; muscle; liver; microwave frequency range

check for updates

Citation: Matković, A.; Šarolić, A. The Effect of Freezing and Thawing on Complex Permittivity of Bovine Tissues. *Sensors* **2022**, *22*, 9806. https://doi.org/10.3390/s22249806

Academic Editors: Raquel C. Conceição and Emily Porter

Received: 29 October 2022
Accepted: 10 December 2022
Published: 14 December 2022

1. Introduction

The number of applications of electromagnetic fields expands, both in the biomedical and wireless communications domains. Accordingly, there is a growing demand for the exact knowledge of the complex permittivity of human tissues in the widest possible frequency range. This requires new and extended measurement studies on human tissues. However, in vivo measurements of human internal organs are either unrealizable or are hindered by many difficulties; thus, ex vivo measurements are often performed, providing an obvious alternative. Furthermore, due to the limited availability of human tissue samples, the tissues of large mammals are often measured instead, and the obtained permittivity values are considered appropriate to model human tissues as well [1,2].

The motivation for this work came from our previous studies [1,3], which reported the results of the dielectric measurement campaign on excised human brain tissues obtained from hospital surgeries and autopsies. The timing of the samples' arrival was subordinate to the hospital schedule, while the measurement throughput was determined by the measurement logistics. Consequently, occasionally a problem would arise with the harmonization of the two throughputs, creating the need to store the tissue samples for a certain amount of time. Naturally, this requires resolving the issue of tissue degradation with time. During the said studies, tissue degradation was observed, both visibly on the tissue and on the complex permittivity measurement results, as dehydration and decomposition took place. Therefore, the studies reveal the need for tissue preservation, preferably over an extended period of time.

Freezing is a common method of preserving tissue from decomposition. It has even been used in the studies of tissue electric properties, such as in [4], where the tissue samples were initially stored in a freezer at −80 °C and subsequently thawed to room temperature before measurement. In the study [4], the samples were resected brain tumor tissues obtained from human patients. However, given that there were no published studies analyzing the effect of freezing and thawing on the conductivity of brain tissues or brain tumors, the authors could not confidently state that the tissue freezing and thawing process did not affect the measured conductivity.

Future extensive biological tissue measurement campaigns (aiming, e.g., to extend the frequency range of healthy tissues or to extend the knowledge of pathological tissues) would certainly benefit from a preservation protocol. Therefore, it is important to investigate how tissue freezing and thawing affects its complex permittivity. Due to differences in tissue composition, studies on the effects of freezing and thawing should be performed separately for different types of tissues.

Previously we reported the preliminary results of complex permittivity measurements of bovine and porcine brain and bovine liver before freezing in a commercial freezer and after thawing [5]. Here, we present a complete study focusing on bovine tissues only: the brain, liver, and muscle. Bovine tissues were chosen due to the availability of large healthy tissue samples. We expected that the changes in the bovine tissues' permittivity that would occur as a result of the freezing and thawing protocol would similarly influence the human tissues. Our recently published study [1] shows that the complex permittivity of bovine and human white matter and grey matter is very similar. As another example, a recent paper investigated the thermal and frequency dependence of dielectric properties of ex vivo liver tissue [6] from the aspect of microwave ablation medical procedures, measuring the bovine liver as well.

The issue of permittivity preservation after the freeze–thaw cycle was approached by a recent study [7] for three tissues: bovine liver, bovine fat, and chicken muscle. The permittivity of the three tissues was measured at room temperature, before and after freezing and thawing, in the frequency range of 0.5–8.5 GHz. The statistical analysis was performed at only three discrete frequencies. The study found significant differences in both ε' and ε'' for the bovine muscle at three analyzed frequencies (2.5, 4.5, and 6.5 GHz). The bovine liver had significant differences in the imaginary part for all three frequencies but only at 2.5 GHz for ε'. For the bovine fat tissue, ε' slightly decreased, and ε'' changed insignificantly, but both changes were not statistically significant. The authors concluded that the freeze–thaw cycle results in an increase in the complex permittivity for high-water content tissues, while low-water content tissues did not have a significant change in complex permittivity.

In comparison with the aforementioned study, we introduced liquid nitrogen as an additional fast-freezing method and expanded the upper-frequency limit to 18 GHz. Furthermore, we reported both the results and the statistics continuously in the whole frequency range instead of just in several discrete frequency points. Extending the frequency range is important due to the expansion of both medical and wireless communication technologies to ever higher frequencies. Unfortunately, in this study, we were limited to 18 GHz by the available instrumentation. The chosen microwave frequency range is highly utilized in various medical applications, from diagnostics (e.g., cancer detection and microwave imaging) to treatment (e.g., microwave ablation and medical hyperthermia), as well as in all generations of wireless technologies.

Another distinction of this study is the introduction of brain tissues into the experiment, as the brain tissue was the primary interest of our human tissue measurement campaign [1]. The muscle and liver are rather homogenous tissues that could serve well for additional investigation and control of the freezing and thawing method. On the other hand, to the best of our knowledge, the effect of freezing on the permittivity of brain tissues has never been previously studied, which makes this the first study to approach this topic. Additionally, we did not find any published references that examined the permittivity changes of biological tissues after freezing and thawing using liquid nitrogen.

2. Materials and Methods

2.1. Sample Handling and Preparation

Dielectric properties of a material are described by its complex dielectric permittivity:

$$\varepsilon = \varepsilon' - i\varepsilon''. \tag{1}$$

The real part ε' expresses the ability of the material to store the electric energy, while the imaginary part ε'' denotes the losses in the material, comprising of the material conductivity and the dielectric losses. We measured ε' and ε'' of ex vivo bovine tissues at the room temperature of 25 °C, first on the fresh ex vivo samples, then on the same samples after they were frozen and thawed back to the room temperature of 25 °C.

We acquired two entire bovine brains, two entire lobes of bovine livers from two different specimens, and two bovine muscles from two different specimens from a local butcher. After the initial measurements on fresh samples, they were either frozen below −18 °C with the use of a commercial freezer or frozen by immersing in liquid nitrogen, nominally at −196 °C. The bovine brain, muscle, and liver that were frozen and stored in the freezer are labeled as B1, M1, and L1, respectively, while the ones that were frozen and stored in the liquid nitrogen tanks are labeled as B2, M2, and L2.

Before bringing the samples to the lab, all the samples were kept fresh in the butcher's store for ca. 1 day after slaughter by refrigeration at 1 °C. The samples were immediately dissected upon bringing them to the lab. Both brains were first halved into the left and right hemispheres and were then dissected into coronal slices ca. 1.5 mm thick. Bovine liver and muscle were cut into $3 \times 3 \times 2$ cm^3 cuboids, which were visually entirely homogeneous. The size of the samples was chosen to obtain a maximum number of samples, each of them sufficiently large to satisfy the minimum sample size recommendation by the coaxial probe manufacturer (covered in Section 2.2) and to provide the space for multiple measurement points on each sample. Upon dissection, the cut samples were immediately stored in separate labeled airtight plastic containers and put in the refrigerator at 3 °C while they were waiting to be measured. Samples were sequentially taken out of the refrigerator and, while still in their sealed containers, heated to 25 °C with the help of the water bath. Each sample was measured at multiple points at 25 °C and then immediately put in a sealed container, either in the freezer, below −18 °C, or in the liquid nitrogen container, at −196 °C. The samples were left to freeze for 3 days and were then thawed back in the water bath set to the room temperature of 25 °C, and their permittivity was then measured again. Finally, the results were processed to compare the permittivity at the same temperature of 25 °C before freezing and after thawing.

2.2. Dielectric Measurement Setup

Measurements were carried out using FieldFox N9927A vector network analyzer (VNA) by Keysight Technologies (Santa Rosa, CA, USA) [8] connected to the Slim Form open-ended coaxial probe from Keysight's N1501A Dielectric Probe Kit (Keysight Technologies Inc., Santa Rosa, CA, USA) [9] by a phase-stable coaxial cable Sucoflex 404 (HUBER+SUHNER AG, Herisau, Switzerland). The VNA was connected to a computer where the measurements were performed using the manufacturer-provided software Keysight Materials Measurement Suite N1500A (Keysight Technologies Inc., Santa Rosa, CA, USA) [10]. The room and the tissue sample temperature during measurements were kept at 25 °C, and the temperature of the material under test was controlled using a precise thermometer DTM3000 (LKM Electronics GmbH, Geratal, Germany).

The measurement frequency range was limited at the upper limit by the VNA to 18 GHz, while the lower limit was 500 MHz, set by the Slim Form Probe lower frequency limit. Each measurement included 3501 linearly spaced frequency points from 500 MHz to 18 GHz. Several such measurements were performed on each tissue sample, moving the probe to different measurement points on the sample. The Slim Form Probe's outer diameter was just 2.2 mm, which allowed measuring of several points on each sample and distinguishing the tissue type on an inhomogeneous brain slice containing both the white and the grey matter. For these reasons, we did not use any wider probes.

The standard calibration procedure was performed with open, short, and deionized water measurements prior to each set of measurements. The probe was cleaned with 70% ethyl alcohol between the measurements to prevent cross-contamination and ensure the best results. After cleaning the probe with alcohol, we waited until the alcohol evaporated so as to not influence the results. The setup was recalibrated at regular intervals with deionized water.

The coaxial probe was fixed on the probe stand, and its open end was put in contact with a biological tissue sample. The sample was contained in a dish supported by thick layers of polystyrene foam on top of a precise weight scale. The scale was situated on top of a metal laboratory jack for *z*-axis adjustment so that the samples were lifted to the probe without disrupting the stability of the measurement setup. We did not notice any effect of the support structure on the measurement instability or inaccuracy. The measurement setup with each sample is shown in Figure 1.

(a) (b) (c) (d)

Figure 1. Measurement setup, including the dish with the sample supported by polystyrene on top of a weight scale for bovine (**a**) brain white matter, (**b**) brain grey matter, (**c**) liver, and (**d**) muscle.

Keysight recommends that the probe must be immersed in the material under test and surrounded by at least 5 mm of the material on all sides. Immersion is only attainable in liquid materials, as recommended by the manufacturer, while the usual practice when measuring biological tissues is to firmly press the probe against the tissue surface. Nevertheless, the liver samples were thick and homogeneous enough to allow the probe insertion into a sample by creating a tight insertion hole and achieving a configuration of the probe inserted into a homogeneous sample of the single tissue type. A similar approach was applied in [6], where the probe was inserted approximately 5 mm into the liver tissue. The inhomogeneous structure of the brain slices did not allow us to insert the probe as it would not be surrounded by only one tissue type (either white matter or grey matter) in sufficient volume; thus, the probe was just firmly pressed against the brain slice surface, either on the white matter or grey matter. The muscle samples, although homogenous, were too firm to successfully puncture with the coaxial probe without the severe compression of the sample, which would alter the results; therefore, the probe was only pressed against the muscle samples.

The precise weight scale in the setup was included to control the pressure that the probe exerted on the samples. This pressure was held constant as much as possible for each tissue type by fine adjustments of the laboratory jack height during the measurements, keeping the constant weight on the scale. The weight was kept at ca. 20 g after puncturing the liver, which translates to the constant pressure of ca. 50 kPa. The muscle samples were pressed with ca. 5 kPa, while both the white and grey matter were measured with the constant pressure of ca. 2.5 kPa, as the brain tissue was the most pliable of the three. These values were determined for each tissue type by observations to ensure firm contact between the probe and the tissue while avoiding significantly deforming the tissue, which depends on each tissue's plasticity and elasticity.

When performing measurements on the brain tissue, the measurements were performed on the homogeneous regions of either white or grey matter when such regions were clearly visible on the brain slice. It is worth noting that not all of the slices displayed such properties; thus, some of the slices were discarded. Additionally, the regions with visually undifferentiated inhomogeneities were avoided. An example of an acceptable region of white and grey matter for performing the measurements is shown in Figure 1a,b, respectively.

3. Results

The results were processed as the average of all the measurement points on all samples of the same tissue type, thus increasing the statistical strength of the results.

The results were separated into two categories: the percent permittivity change after freezing in a commercial freezer for samples B1, L1, and M1, and percent permittivity change after freezing in liquid nitrogen for samples B2, L2, and M2. The percent change was chosen over the absolute change, as the permittivity greatly varied with frequency; thus, the absolute change would not provide the information on the significance of the change. Additionally, polynomial fitting was performed to smooth out the narrowband fluctuations, which occurred due to the imperfections of the setup and did not reflect the actual change in permittivity due to the freezing process. Raw data are shown by the black solid or dotted line in Figures 2–9 for ε' and ε'', respectively. The polynomial fits of the raw data in Figures 2–9 are shown in a blue solid line for the change in ε' and an orange solid line for the change in ε''. Additionally, we added the limits of a statistical test to the charts for easier assessment of statistical significance. Dashed lines of the matching colors represent the limits of the *t*-test with a 95% confidence interval (CI). The actual test is described in Section 3.3.

3.1. B1, L1, and M1 Samples

Bovine brain B1 was measured on 17 slices that included a total of 72 measurement points for white matter and 70 points for grey matter before freezing to −18 °C, 73 measurement points for white matter, and 76 points for grey matter after thawing. Bovine liver L1 was measured on 15 different samples at 68 different points before freezing. The measurements on the 15 liver samples already showed that the difference between the liver samples was very small; thus, measuring the additional samples would not significantly increase the statistical strength. Therefore, the rest of the liver samples were frozen without measuring them to minimize the time of sample storage before freezing them. After thawing, 25 different liver samples were measured with 110 measurement points total. The bovine muscle M1 was measured on 21 different samples at 105 measurement points before freezing and 17 samples with 85 measurement points after thawing. The percent change in ε' and ε'' of the bovine tissues is presented in Figures 2–5.

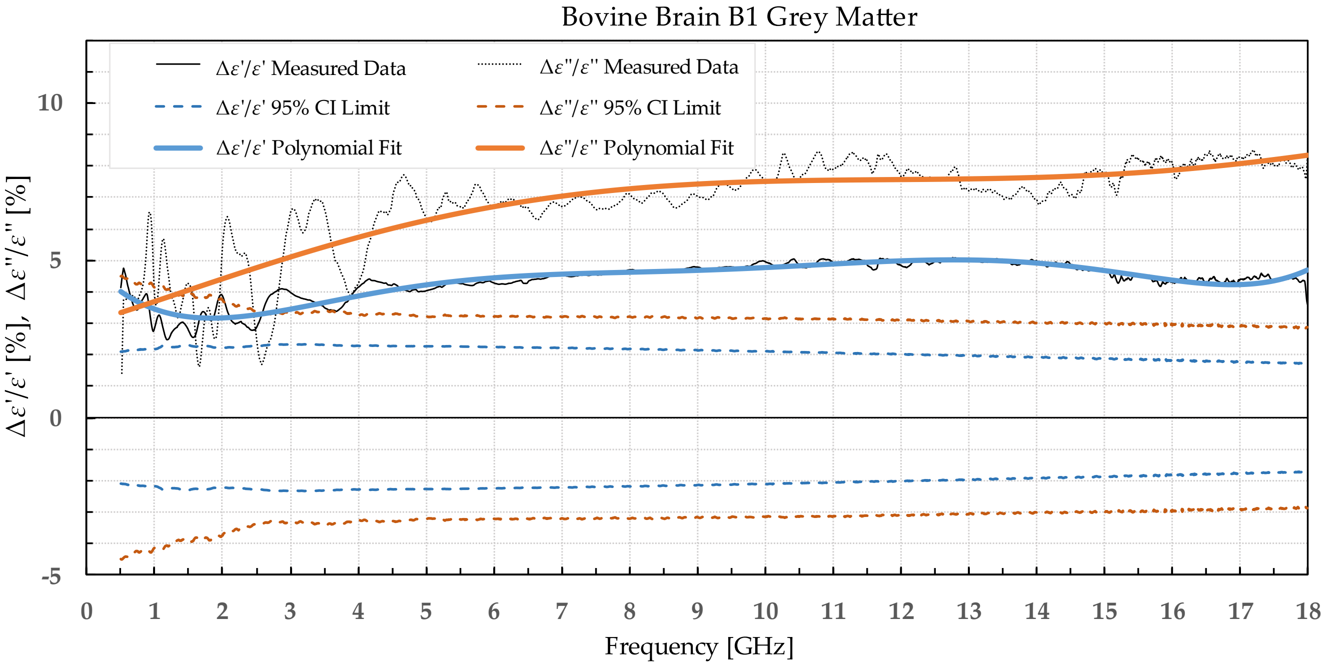

Figure 2. Percent change in ε' and ε'' for bovine grey matter before freezing below −18 °C in a commercial freezer and after thawing.

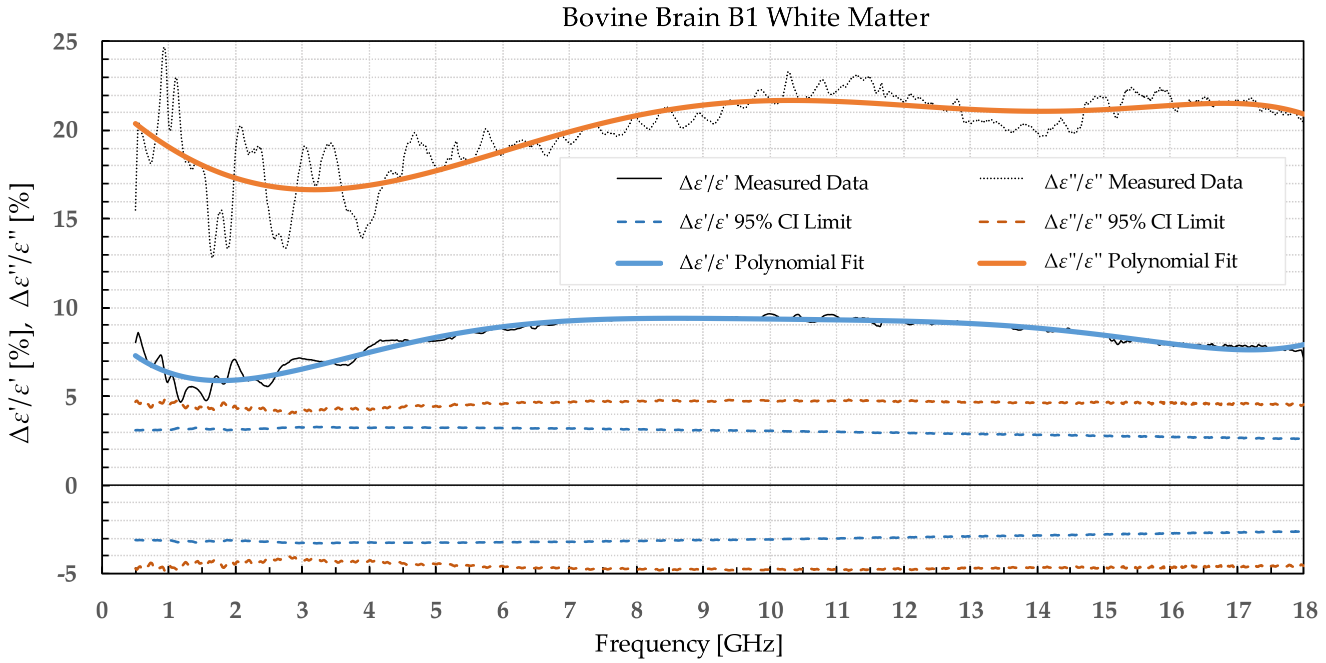

Figure 3. Percent change in ε' and ε'' for bovine white matter before freezing below −18 °C in a commercial freezer and after thawing.

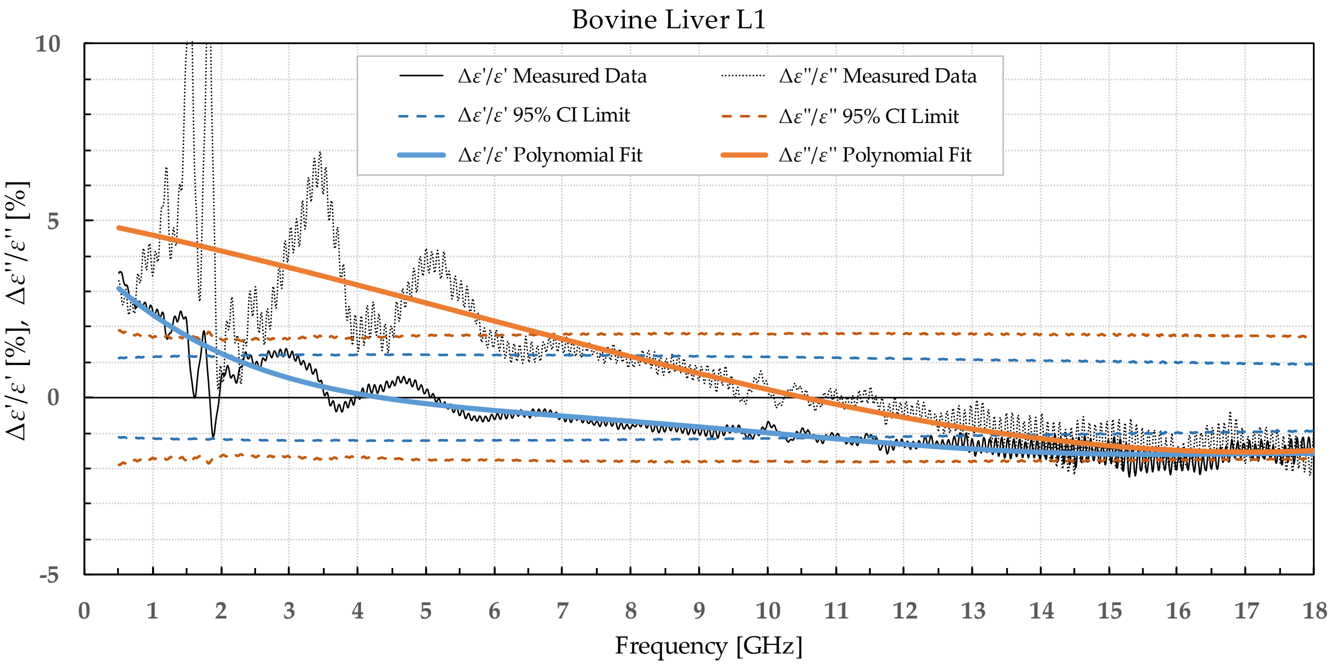

Figure 4. Percent change in ε' and ε'' for bovine liver before freezing below −18 °C in a commercial freezer and after thawing.

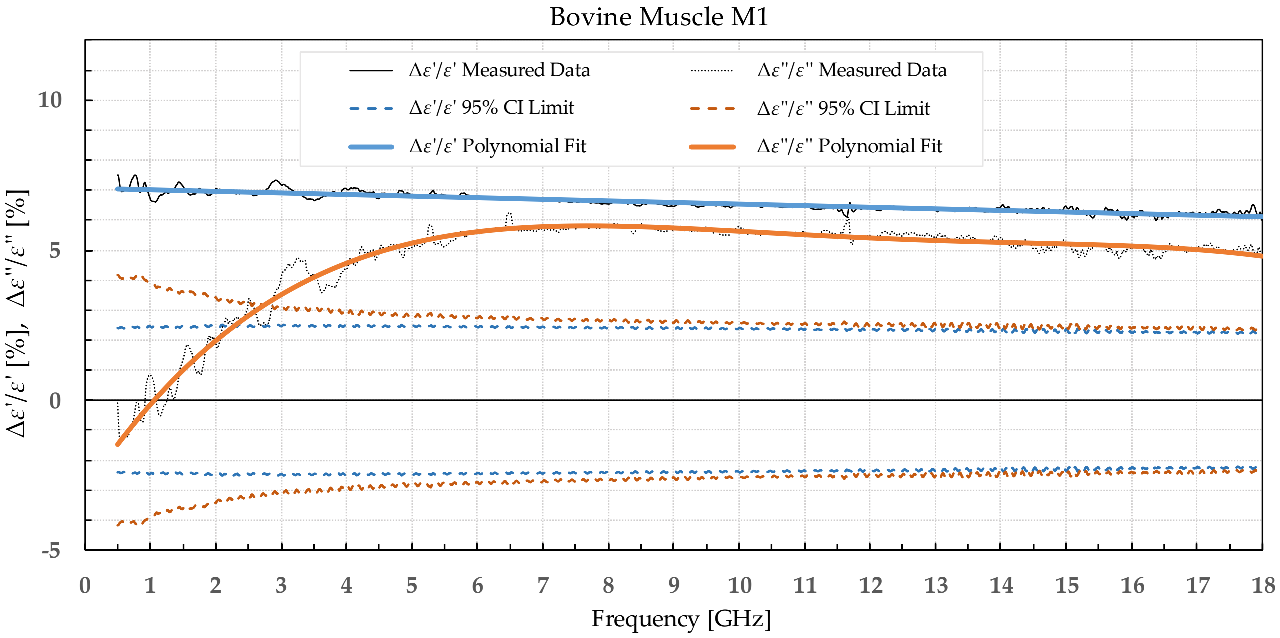

Figure 5. Percent change in ε' and ε'' for bovine muscle before freezing below −18 °C in a commercial freezer and after thawing.

3.2. B2, L2, and M2 Samples

Bovine brain B2 was measured on six slices that included 38 points for white matter and 32 points for grey matter, both before freezing at −196 °C and after thawing. Bovine liver L2 was measured on 10 different samples at 50 different points both before freezing in liquid nitrogen and after thawing back to 25 °C. Bovine muscle M2 was measured on 14 different samples totaling 80 different points both before freezing and after thawing. Figures 6–9 present the percent difference in complex permittivity for the bovine tissues frozen in liquid nitrogen. Additionally, we added the limits of a statistical test to the charts for easier assessment of statistical significance. The actual test is described in the next subsection.

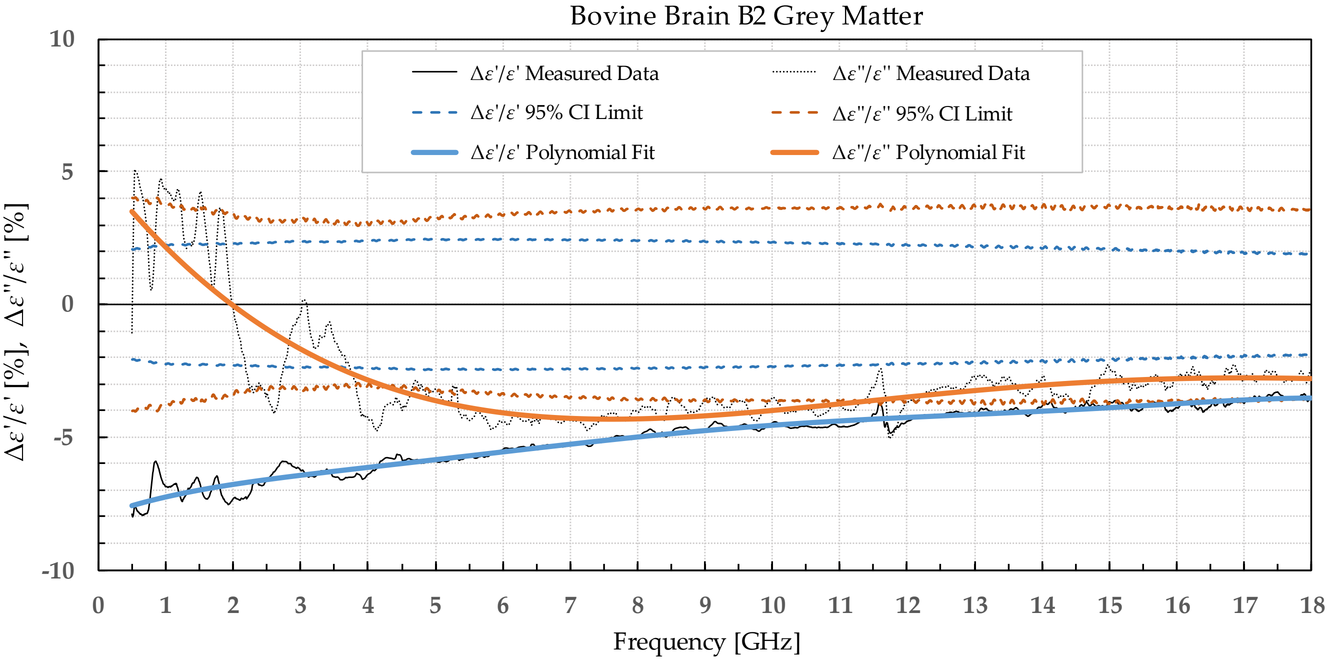

Figure 6. Percent change in ε' and ε'' for bovine grey matter before freezing in liquid nitrogen and after thawing.

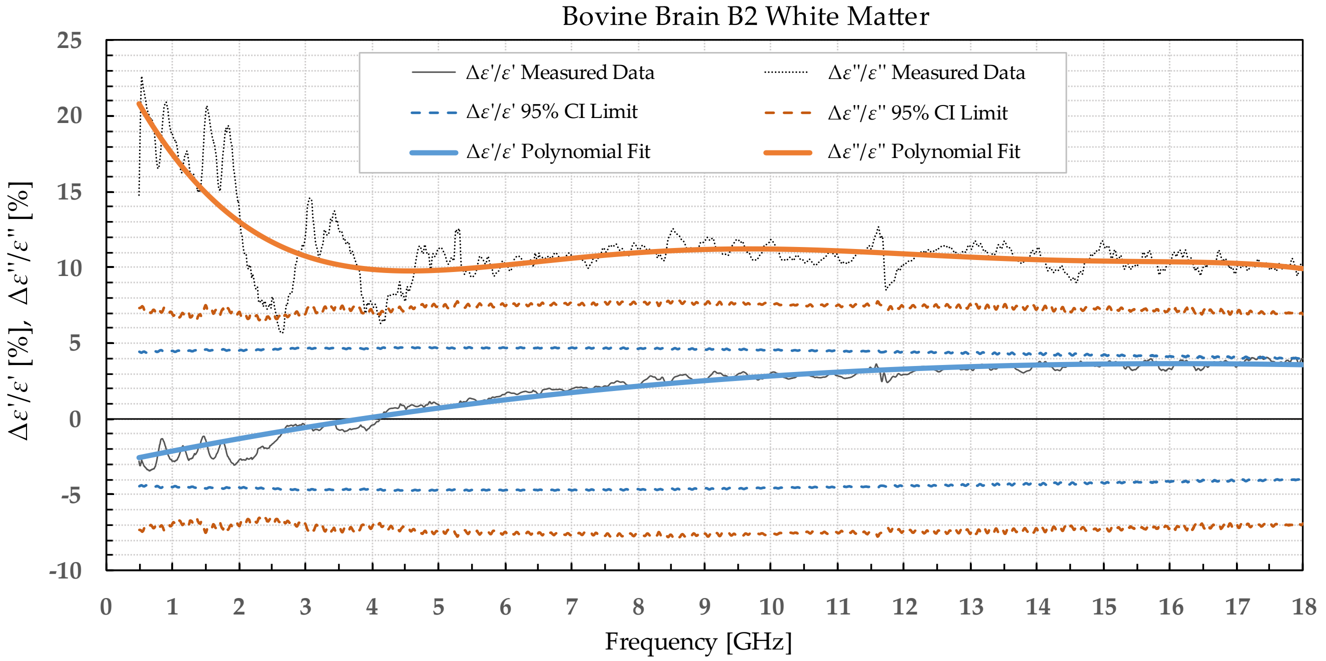

Figure 7. Percent change in ε' and ε'' for bovine white matter before freezing in liquid nitrogen and after thawing.

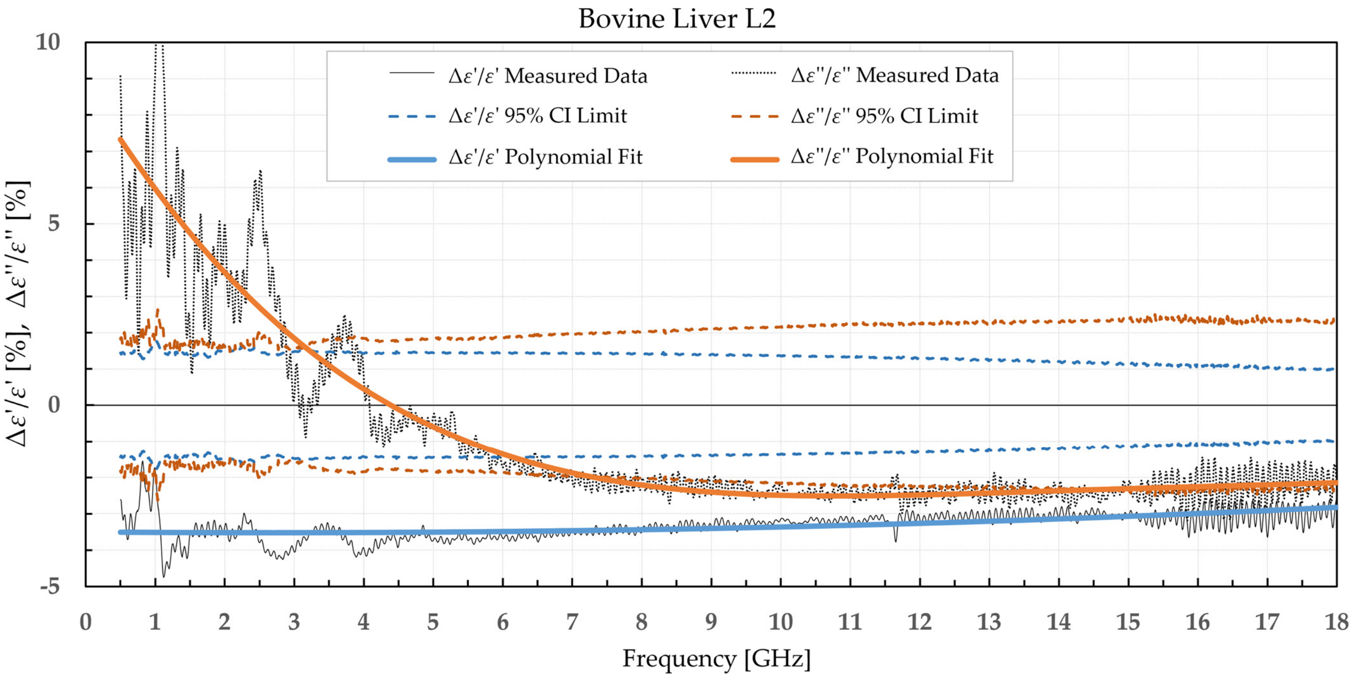

Figure 8. Percent change in ε' and ε'' for bovine liver before freezing in liquid nitrogen and after thawing.

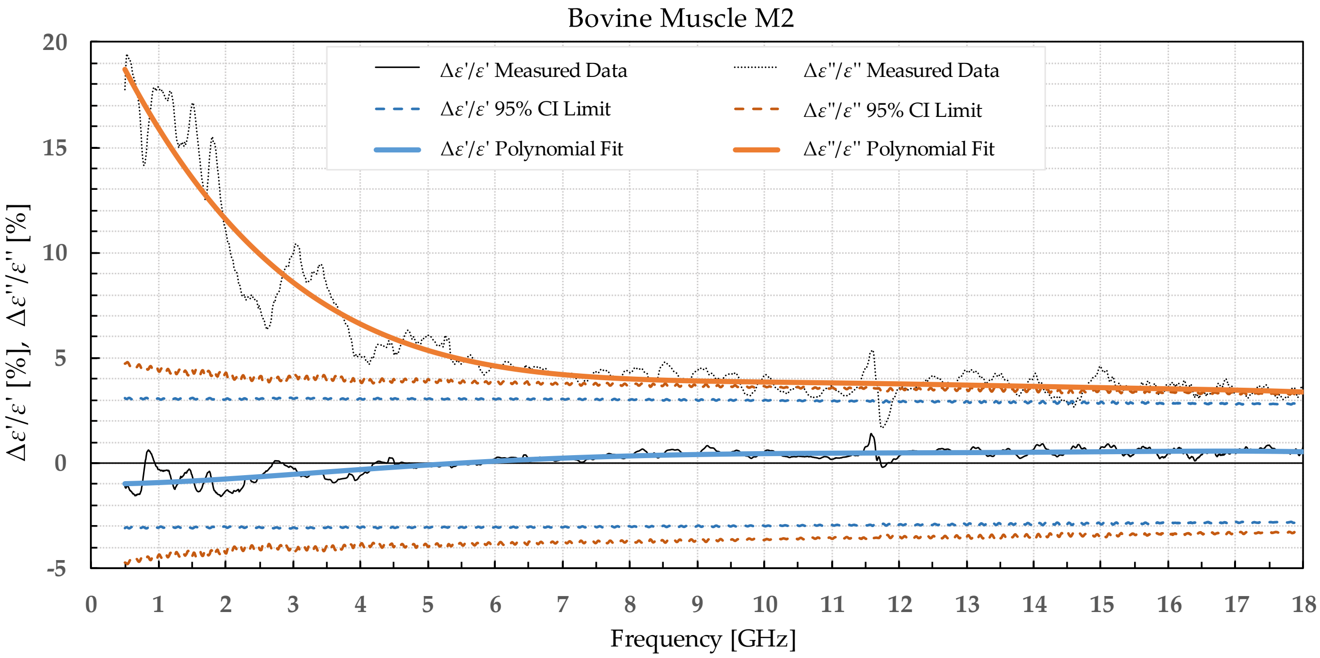

Figure 9. Percent change in ε' and ε'' for bovine muscle before freezing in liquid nitrogen and after thawing.

3.3. Statistical Analysis

We used the unpaired *t*-test to find the difference between the means of the two samples. Because the number of samples was not considered small, i.e., was over 30, the samples did not need to follow the normal distribution (although we expected that they actually would do). An additional requirement was that the two populations do not differ in the standard deviation, which was also satisfied, as shown in Table 1 which reports the standard deviation averaged over the entire measured frequency range. T-values were calculated for each frequency point of each tissue type and for each freezing method. The calculated values were compared to the values from the table of critical t-values chosen for a two-tailed test with a significance level of $\alpha = 0.05$, i.e., the confidence interval of 95% [11]. The limits of the decision criterion for statistical significance in the change of permittivity with the used 95% CI t-test are represented with dashed lines in Figures 2–9.

Table 1. Average standard deviations of ε' and ε'' for bovine tissues.

	Tissue Type	Before Freezing		After Thawing	
		ε'	ε''	ε'	ε''
Freezer	White Matter	3.11	1.53	2.54	1.39
	Grey Matter	3.18	2.13	2.44	1.59
	Liver	1.29	0.88	1.36	0.97
	Muscle	3.80	1.99	3.21	2.04
Liquid Nitrogen	White Matter	2.15	0.99	3.54	1.95
	Grey Matter	1.74	1.00	2.30	1.57
	Liver	0.93	0.47	1.52	1.05
	Muscle	4.42	2.57	3.63	2.20

4. Discussion

The agreement of our initial permittivity measurements prior to freezing the tissues with the previously published data [12,13] is satisfactory. The permittivity of the bovine liver and muscle has been measured in [12] from 500 MHz to 40 GHz at 37 °C. Even though our measurements were performed at 25 °C, due to the lack of the reported data for our specific tissue type, animal species, measurement frequency, and tissue temperature, we used their data for control and comparison. Our results for the bovine liver and muscle are comparable to the results in [12], taking into account that their measurements were performed at 37 °C. Bovine brain white matter and grey matter have been measured in [13] at 35 °C. The measured bovine brains were separated into two groups: adult animals, i.e., 16–24 months, and young animals, i.e., 4–6 months. Again, due to the lack of a more similar experimental setup and samples, we used their results for control and comparison. The results for both the grey and white matter are comparable to [13] for young calves when corrected for the difference in temperature.

As our preliminary results [5] indicated that freezing in a commercial freezer did, in fact, change the dielectric properties of the tissues, we also explored other freezing methods with faster freezing. Both methods of cooling the tissue to freezing temperatures and warming the tissue during thawing can cause the formation of damaging ice crystals. The ice formation during either cooling or warming differs between the methods, depending on how much time a method allows for the ice crystals to generate and grow. Therefore, it is possible to have a method with a sufficiently high cooling and warming rate where the ice formation will be suppressed [14]. That is why we also explored an additional freezing method by submerging the tissue samples in liquid nitrogen. Freezing by immersing in liquid nitrogen causes the process of freezing to happen much quicker than in a commercial freezer. Thus, by using two different freezing methods, in a commercial freezer and in liquid nitrogen, the effects of both slower and faster cooling rates on the sample permittivity were explored. During slow freezing, the extracellular water turned to ice, which is an almost completely pure substance, leaving the dissolved solutes in a reduced volume of solvent. The process inevitably changes the osmotic pressure and causes the intracellular water to flow outside the cell to restore the osmotic equilibrium, essentially dehydrating the cell and changing the permittivity [14]. Freezing with higher cooling rates should, in theory, prevent the described dehydration mechanism. However, cooling too quickly could cause intracellular ice formation that could rupture the membrane and lead to cell death. Between these two ends of the spectrum, there is an optimum cooling rate that minimizes both sources of freeze injury. Usually, cryopreservation is paired with cryoprotective agents to further reduce the damaging effects of frozen tissues during rapid freezing [15]. Unfortunately, the use of cryoprotectants on tissue samples would alter the dielectric properties, whereas the objective of this research was to find a way to preserve the permittivity, which is why our freezing protocol did not include the use of cryoprotectants.

The statistical analysis showed that the difference in permittivity before freezing and after thawing was not negligible. Overall, the most suitable tissue for freezing is the liver tissue which exhibited the smallest percent permittivity change for both freezing protocols. The most significant difference was observed for the white matter, where the difference in ε'' exceeded 20% at some frequency points.

The permittivity of both white and grey matter B1 displays a significant difference before and after freezing in the whole measured frequency range. The exception to this is ε'' below ca. 1 GHz, but this is practically insignificant. Freezing the brain B2 in liquid nitrogen and thawing caused a significant difference over the whole measured frequency range in ε'' of the white matter and ε' of the grey matter. ε' of the white matter did not display significant change over the whole frequency range, while the ε'' of the grey matter sporadically lingered around the set confidence interval limit at frequencies over 4.5 GHz.

When analyzing liver permittivity results, ε' of L1 did not display a significant change in the 2–11 GHz range, while ε'' displayed a significant difference for frequencies under 7 GHz. The liver L2 had a significant decrease in ε' over the whole measured range, while ε'' sporadically exceeded the chosen confidence interval and associated t-value under 3.5 GHz, between 7.5 and 13.5 GHz, and over 17.5 GHz.

Bovine muscle M1 displayed a significant increase in ε' over the whole measured frequency range, while ε'' showed a significant change over ca. 3 GHz. For the muscle frozen and stored in liquid nitrogen, M2, there were no significant differences in ε', while ε'' exhibited an increase over the whole frequency range but was especially prominent at the lowest measured frequencies.

Freezing the tissues in liquid nitrogen results in a decrease in ε' when compared to the same tissues frozen in a commercial freezer. The trends are not consistent between different tissues frozen with the same method. It was already observed in [16] that different tissues undergo different physical processes during a freeze–thaw cycle, which could also explain the difference in permittivity trends. Their preliminary investigations indicated that some tissues, such as the brain or spleen, soften after thawing because they have weak intercellular junctions or high extracellular water content and, therefore, lose their structure after thawing. Other tissues, such as skin or skeletal muscle, harden because their cells lose water and are unable to restore that water after thawing.

Comparing our measured permittivity difference for muscle and liver tissue before and after freezing with a similar study [7], there are several consistent observations. In their work, the permittivity of muscle tissue increased after thawing for both ε' and ε'' by 2.1% and 6.4% at 4.5 GHz, respectively. In our study, the increase in permittivity was 7% for ε' and 5% for ε'' for muscle frozen in a commercial freezer measured at 4.5 GHz. The trend of increase in permittivity was consistent between the studies, and both studies reported significant differences in both ε' and ε''. The difference in percentage could be explained by the different compositions of the chicken versus the bovine muscle. Their results for bovine liver showed an increase in permittivity by 2.6% for ε' and 8.9% for ε'' at 4.5 GHz. Our results at 4.5 GHz showed that the liver L1 had almost no change in ε' and 3% in ε''. Even though at first it appears that the results do not fully agree, it is worth noting that the statistical analysis of liver permittivity results in [7] found that there is a significant difference for ε'' but not for ε', and the same was observed in our study (Figure 4).

Unfortunately, unlike the muscle and liver tissue, which were measured before and after freezing in a similar study [7], there is no similar study on freezing the brain tissues to compare our results to.

5. Conclusions

To our knowledge, this is the first measurement study of permittivity change in brain tissue due to a freeze–thaw cycle. Our results suggest that both of the tested freezing methods produce a statistically significant change in permittivity, at least in some part of the measured frequency range. Nevertheless, depending on the application and the preferred frequency range, the permittivity change might be acceptable. If the acceptable percent change is set to, e.g., 10%, the measured permittivity change is satisfactory for liver, muscle (but only when frozen in a commercial freezer), and grey matter, while the permittivity change in white matter and muscle frozen in liquid nitrogen is not acceptable, but only due to the change in ε'' which exceeds the set limit.

The necessity for finding a tissue preservation method that would not significantly influence the complex permittivity still remains.

Author Contributions: Conceptualization, A.Š. and A.M.; methodology, A.Š. and A.M.; formal analysis, A.M. and A.Š.; investigation, A.M. and A.Š.; writing—original draft preparation, A.M. and A.Š.; writing—review and editing, A.M. and A.Š.; supervision, A.Š.; project administration, A.Š. All authors have read and agreed to the published version of the manuscript.

Funding: This research received no external funding.

Institutional Review Board Statement: Not applicable.

Data Availability Statement: Not applicable.

Acknowledgments: This study was performed within the research project "Measurements in Bioelectromagnetics (M-BEM)" supported by FESB, University of Split, and within the framework of COST Action MyWAVE CA17115. We kindly thank Vedrana Čikeš Čulić from University of Split, School of Medicine, for the logistical support and valuable advice on liquid nitrogen freezing.

Conflicts of Interest: The authors declare no conflict of interest.

References

1. Matković, A.; Kordić, A.; Jakovčević, A.; Šarolić, A. Complex Permittivity of Ex-Vivo Human, Bovine and Porcine Brain Tissues in the Microwave Frequency Range. *Diagnostics* **2022**, *12*, 2580. [CrossRef] [PubMed]
2. Hasgall, P.A.; Di Gennaro, F.; Baumgartner, C.; Neufeld, E.; Lloyd, B.; Gosselin, M.C.; Payne, D.; Klingenböck, A.; Kuster, N. IT'IS Database for Thermal and Electromagnetic Parameters of Biological Tissues. Version 4.1. 2022. Available online: https://www.itis.swiss/database (accessed on 28 November 2022).
3. Kordić, A.; Matković, A.; Jakovčević, A.; Šarolić, A. Preliminary Measurements of Dielectric Properties of Excised Human Tissues and the Associated Challenges Thereof. In Proceedings of the BioEM 2021, Ghent, Belgium, 26 September 2021; pp. 584–589.
4. Tha, K.K.; Katscher, U.; Yamaguchi, S.; Stehning, C.; Terasaka, S.; Fujima, N.; Kudo, K.; Kazumata, K.; Yamamoto, T.; Van Cauteren, M.; et al. Noninvasive Electrical Conductivity Measurement by MRI: A Test of Its Validity and the Electrical Conductivity Characteristics of Glioma. *Eur. Radiol.* **2018**, *28*, 348–355. [CrossRef] [PubMed]
5. Matković, A.; Kordić, A.; Šarolić, A. Investigation of Dielectric Permittivity Preservation after Freezing and Thawing the Bovine Brain, Porcine Brain and Bovine Liver. In Proceedings of the BioEM 2022, Nagoya, Japan, 19 June 2022; pp. 468–474.
6. Fallahi, H.; Sebek, J.; Prakash, P. Broadband Dielectric Properties of *Ex Vivo* Bovine Liver Tissue Characterized at Ablative Temperatures. *IEEE Trans. Biomed. Eng.* **2021**, *68*, 90–98. [CrossRef]
7. Savazzi, M.; Felicio, J.M.; Costa, J.R.; Fernandes, C.A.; Conceicao, R.C. Study of Freezing and Defrosting Effects on Complex Permittivity of Biological Tissues. *Antennas Wirel. Propag. Lett.* **2021**, *20*, 2210–2214. [CrossRef]
8. Keysight N9927A FieldFox Handheld Microwave Vector Network Analyzer, 18 GHz. Available online: https://www.keysight.com/zz/en/product/N9927A/fieldfox-a-handheld-microwave-vector-network-analyzer-18-ghz.html (accessed on 26 February 2022).
9. Keysight N1501A Dielectric Probe Kit. Available online: https://www.keysight.com/zz/en/product/N1501A/dielectric-probe-kit.html (accessed on 26 February 2022).
10. Keysight Technologies. *N1500A Materials Measurement Suite—Technical Overview*; Keysight Technologies: Santa Rosa, CA, USA, 2021.
11. Stommel, M.; Katherine, J.D. *Statistics for Advanced Practice Nurses and Health Professionals*; Springer Publishing Company: New York, NY, USA, 2014; pp. 307–308, ISBN 978-0-8261-9824-2.
12. Abdilla, L.; Sammut, C.; Mangion, L.Z. Dielectric Properties of Muscle and Liver from 500 MHz–40 GHz. *Electromagn. Biol. Med.* **2013**, *32*, 244–252. [CrossRef]
13. Schmid, G.; Überbacher, R. Age Dependence of Dielectric Properties of Bovine Brain and Ocular Tissues in the Frequency Range of 400 MHz to 18 GHz. *Phys. Med. Biol.* **2005**, *50*, 4711–4720. [CrossRef] [PubMed]
14. Fahy, G.M.; Wowk, B. Principles of Ice-Free Cryopreservation by Vitrification. In *Cryopreservation and Freeze-Drying Protocols*; Wolkers, W.F., Oldenhof, H., Eds.; Methods in Molecular Biology; Springer US: New York, NY, USA, 2021; pp. 27–97, ISBN 978-1-07-160783-1.
15. Wolkers, W.F.; Oldenhof, H. Principles Underlying Cryopreservation and Freeze-Drying of Cells and Tissues. In *Cryopreservation and Freeze-Drying Protocols*; Wolkers, W.F., Oldenhof, H., Eds.; Methods in Molecular Biology; Springer US: New York, NY, USA, 2021; pp. 3–25, ISBN 978-1-07-160783-1.
16. Schafer, A.T.; Kaufmann, J.D. What Happens in Freezing Bodies? Experimental Study of Histological Tissue Change Caused by Freezing Injuries. *Forensic Sci. Int.* **1999**, *102*, 149–158. [PubMed]

APPENDIX C

Title	Dielectric Permittivity Measurement Using Open-Ended Coaxial Probe—Modeling and Simulation Based on the Simple Capacitive-Load Model
Authors	Antonio Šarolić and Anđela Matković
Journal	Sensors
Impact factor	3.9
Volume and number	22, 16
Year	2022
Article number	6024
DOI	10.3390/s22166024
Abstract	The study aim was to validate that dielectric permittivity measurement using the open-ended coaxial probe can be reliably modeled using electromagnetic modeling and simulations, followed by the postprocessing calculations based on the simple capacitive-load model. Saline solutions with various NaCl concentrations were used as materials under test (MUTs) to investigate how ionic conductivity affects the model validity. Two different solvers and simulation methods were used: FEKO for the frequency domain and CST for the time domain. Furthermore, we performed physical experiments with the same probe and MUTs, again implementing the capacitive-load model on the measurement data to observe the model's validity. Relative error of the capacitive-load model with respect to the reference permittivity values, both in measurements and simulations, was within 10% for all cases except for the measured $\varepsilon'_{\mathrm{r}}$ of 1M solution at the lowest frequencies. The model yielded average relative errors well below 1% for the physiological saline, which is relevant for biological materials. The error increased for higher concentrations and for the lowest simulated frequencies but was within the declared measurement accuracy of the probe itself. This makes the simple capacitive-load model valid for all analyzed concentrations in the microwave frequency range from 0.5 to 18 GHz.

sensors

MDPI

Article

Dielectric Permittivity Measurement Using Open-Ended Coaxial Probe—Modeling and Simulation Based on the Simple Capacitive-Load Model

Antonio Šarolić * and Anđela Matković

FESB, University of Split, HR-21000 Split, Croatia
* Correspondence: antonio.sarolic@fesb.hr

Abstract: The study aim was to validate that dielectric permittivity measurement using the open-ended coaxial probe can be reliably modeled using electromagnetic modeling and simulations, followed by the postprocessing calculations based on the simple capacitive-load model. Saline solutions with various NaCl concentrations were used as materials under test (MUTs) to investigate how ionic conductivity affects the model validity. Two different solvers and simulation methods were used: FEKO for the frequency domain and CST for the time domain. Furthermore, we performed physical experiments with the same probe and MUTs, again implementing the capacitive-load model on the measurement data to observe the model validity. Relative error of the capacitive-load model with respect to the reference permittivity values, both in measurements and simulations, was within 10% for all cases except for the measured ε_r' of 1M solution at the lowest frequencies. The model yielded average relative errors well below 1% for the physiological saline, which is relevant for biological materials. The error increased for higher concentrations and for the lowest simulated frequencies but was within the declared measurement accuracy of the probe itself. This makes the simple capacitive-load model valid for all analyzed concentrations in the microwave frequency range from 0.5 to 18 GHz.

Keywords: dielectric permittivity measurement; open-ended coaxial probe; electromagnetic modeling and simulation; capacitive-load model; sodium chloride (NaCl) water solution; saline ionic conductivity; physiological saline; CST; FEKO; reflection coefficient de-embedding; microwave frequency range

check for updates

Citation: Šarolić, A.; Matković, A. Dielectric Permittivity Measurement Using Open-Ended Coaxial Probe—Modeling and Simulation Based on the Simple Capacitive-Load Model. *Sensors* **2022**, *22*, 6024. https://doi.org/10.3390/s22166024

Academic Editors: Raquel C. Conceição and Emily Porter

Received: 17 June 2022
Accepted: 10 August 2022
Published: 12 August 2022

1. Introduction

Dielectric permittivity of a biological tissue is the key parameter determining its interaction with the electromagnetic field in the radiofrequency (RF) and microwave (MW) frequency range [1]. Knowledge on dielectric permittivity is hence required to analyze how biological tissue responds to the imposed RF or MW electromagnetic field, either during biomedical procedures involving electromagnetic field applications or during inadvertent exposure. Systematic sets of results have been reported in [2–5]; however, these sets provide only limited data and are continuously challenged by newly reported results. In bioelectromagnetics, there is a constant need to perform more accurate measurements, to increase frequency range and resolution, to measure tissues at different temperatures, and to measure malignant and diseased tissues. In sensor applications, dielectric permittivity is measured in biological and non-biological materials to indirectly determine the concentration of a chemical ingredient that significantly affects the permittivity, such as water, salt, or glucose (e.g., [6–10]). In wireless communications, dielectric permittivity is a crucial parameter for analyzing electromagnetic wave propagation in materials (e.g., [11]). All of this makes dielectric permittivity measurement an important procedure that is used in various industries and that will be used even more as the associated measurement methods overcome their inherent limitations.

Lots of applications require the measurements to be non-destructive, which limits the possible designs of dielectric probes. When there is an additional requirement that the measurement must be broadband, the open-ended coaxial probe is the favored and widely accepted design [12–14]. It is based on the coaxial line, an inherently wideband structure, and the sensing is achieved by measuring the reflection from the probe open end which is only in surface contact with the material under test, making this method non-destructive.

In practical use, the coaxial probe dielectric measurement suffers from several uncertainties, a few of which are mentioned here. The probe response, although inherently wideband, is actually frequency-limited from both sides, meaning that the measurement error increases as the frequency decreases below or increases above the working frequency range [15]. The probe response to inhomogeneous materials is very complex and often unknown [16–19]. When measuring layered materials, the result depends on the probe sensing depth, which should be determined for the used probe [20–23]. When measuring biological tissues, the result also depends on the contact pressure, which should be regarded during the measurements [24,25]. The accuracy of the final measurement result additionally depends on the postprocessing method, which in turn depends on the chosen model of the open-end load impedance [15,26–29].

Consequently, these uncertainties and potential errors translate to the limitations of the coaxial probe, which can only be overcome by thorough analyses of various constraint factors. Such studies could be performed by physical experimentation; however, this is often demanding when experimenting in a wide space of parameters. Therefore, in order to facilitate such studies, it would be very useful to reliably model and simulate the complete measurement process, thus moving from physical experiments to computer simulations. Since the probe is measuring electromagnetic phenomena, the response of the probe is first determined by the electromagnetic modeling and simulation. Dielectric permittivity is then obtained from this response by postprocessing the results of electromagnetic simulation. Postprocessing is again based on modeling the actual load impedance even in an actual physical measurement process. The accuracy of this entire modeling and simulation therefore depends on the accuracy of the initial electromagnetic model, selected numerical method for electromagnetic simulation, and the selected postprocessing calculation model. Accordingly, modeling and simulation of the complete measurement process should be carefully prepared, performed, and validated in order to be used for relevant coaxial probe analyses.

The main aim of this paper was to demonstrate and to validate that the dielectric permittivity measurement method using open-ended coaxial probe in the microwave frequency range can be completely and reliably modeled and simulated using computer electromagnetic modeling and simulations followed by the postprocessing calculations based on the simple capacitive-load model within the typical measurement accuracy of the probe itself.

The previous state-of-the-art [15,26–30] suggests that the simple capacitive load successfully models the actual load if the frequencies are not as high as to cause radiation from the probe into the MUT. Accordingly, the validity of this model should be examined with respect to the probe dimensions, frequency range, and MUT characteristics.

The open-ended coaxial probe has been extensively electromagnetically modeled and simulated before; however, each study had its own choices of open-ended coaxial probe models, simulation methods, MUTs, and frequency ranges (e.g., [20,21,30–32]). In this study, we modeled the flangeless slim-form probe manufactured by Keysight Technologies. This choice was based on its convenience and the common acceptance for measurements of biological tissues due to its slim form and the absence of flange. This exact probe design is unique, considering the commercial probes in this frequency range. The probe technical characteristics are presented in Section 2.4. The frequency range of up to 18 GHz analyzed in this study is a considerable extension with respect to the previous studies, enabling the analysis of phenomena occurring at higher frequencies. The postprocessing calculations were based on the simple capacitive-load model, and the aim of this study was to analyze the error occurring when using such a model for postprocessing of simulation data in dependence on the ionic concentration of the MUT in the frequency range up to 18 GHz. This was done using sodium chloride (NaCl) solutions in deionized water with various NaCl concentrations as MUTs.

Moreover, two simulation methods and solvers were used to enable comparison between them, which was also one of the aims of this study. Furthermore, we also performed physical experiments with the analyzed exact slim-form probe and MUTs, again implementing the simple capacitive-load model on the measurement data, to observe the overall validity of such a postprocessing model when used to postprocess either measurement or simulation results.

The paper structure follows the study organization. Materials and methods are presented in Section 2, with subsections covering: the concept of the complete investigation; dielectric permittivity measurement method using open-ended coaxial probes in general; flangeless slim-form probe as the object of this study; description of materials under test; description of measurement parameters, description of simulation parameters, and description of the simple capacitive-load model. The results are presented in Section 3, with subsections for the measurement and the simulation results. The overall findings are further discussed in Section 4, with the conclusions given in Section 5.

2. Materials and Methods

2.1. Study Concept

2.1.1. Validation of the Simple Capacitive-Load Model by Physical Measurements

The first part of the study, i.e., validation of the simple capacitive-load model by physical measurements, examined how accurate the simple capacitive-load model is for modeling the coaxial open end terminated by a material under test (MUT), i.e., how the measurement results obtained by the simple capacitive-load model agree with the measurement results obtained by a more complex load model embedded in the manufacturer measurement software [33]. Dielectric permittivity of water and several saline solutions were physically measured by the open-ended coaxial probe. Generally, the measured permittivity value is obtained by postprocessing the raw measurement result, i.e., the measured open-end reflection coefficient. In this study, two methods were used for postprocessing, and the results were compared and discussed. The first method, regarded hereby as accurate and thus serving as a reference for comparisons, is the one embedded in the manufacturer-provided measurement software and uses a proprietary load model to calculate the complex permittivity from the reflection coefficient. The complex permittivity was then also calculated from the reflection coefficient by our own postprocessing calculations using the simple capacitive-load model, as the second method. The permittivity values obtained by the two methods were compared to check both the validity and the limitations of the hypothesis that the load could be modeled using a simple capacitive-load model. Finally, the measured permittivity values were additionally compared to the reference values of Debye and Cole–Cole dispersions (water and saline solutions, respectively), in order to verify the probe behavior and the overall validity of the measurement setup.

2.1.2. Validation of the Simulation of the Complete Measurement Process

The second part of the study, i.e., validation of the simulation of the complete measurement process, examined the agreement of the coaxial probe simulation results obtained by two entirely different numerical methods applied on the same probe model, followed by identical postprocessing calculations. Not only do the two numerical methods belong to two different software packages but they are also different in their approaches to the electromagnetic problem: one solves it in the frequency domain and the other one in the time domain. Method of moments (MoM) was chosen as a frequency-domain solver implemented in FEKO [34] and Finite Integration Technique (FIT) as a time-domain solver implemented in CST [35]. The slim-form probe was modeled first, then the MUT volume was added to the probe model. MUT permittivity was set to the value for water and then to the values for several saline solutions, in accordance with Debye dispersion for the water and Cole–Cole dispersion for the saline solutions. Then, the electromagnetic simulations were performed for each MUT, obtaining the reflection coefficient at the probe input port. Finally, we calculated the MUT permittivity from the reflection coefficient using the simple capacitive-load model. The calculated MUT permittivity, as the final output of the overall simulation process, was compared to the MUT permittivity initially set in the software model (Debye and Cole–Cole dispersions) in order to validate the modeling and simulation method as a whole.

The results were compared and discussed, allowing us to conclude the validity of the proposed method for modeling and simulation of the open-ended coaxial dielectric probe measurement method in the microwave frequency range based on the simple capacitive-load model.

2.2. Dielectric Permittivity

The dielectric permittivity $\hat{\varepsilon}$ of the material (in farads per meter, F/m) is a physical quantity that describes the response of the material to the imposed electric field. It is a complex quantity consisting of the real part ε', describing the polarization response of the material, and the imaginary part ε'', describing the losses in the material as the response to the imposed electric field. A material can be described by its relative permittivity $\hat{\varepsilon}_\mathrm{r}$ (hereafter written simply as ε_r), a dimensionless complex quantity which when multiplied by the vacuum permittivity ε_0 (in F/m) yields the complex permittivity $\hat{\varepsilon}$ (hereafter written simply as ε):

$$\hat{\varepsilon} = \varepsilon' - \mathrm{j}\varepsilon'' = \varepsilon_0 \cdot \left(\varepsilon'_\mathrm{r} - \mathrm{j}\varepsilon''_\mathrm{r}\right) = \varepsilon_0 \hat{\varepsilon}_\mathrm{r} \ . \tag{1}$$

Therefore, the actual quantities being measured are the real and the imaginary part of the relative permittivity: ε'_r and ε''_r, respectively. Their ratio is often referred to as the loss tangent tanδ, denoting the measure of losses in the material at a specific frequency:

$$\tan\delta = \frac{\varepsilon''}{\varepsilon\prime} = \frac{\varepsilon''_\mathrm{r}}{\varepsilon'_\mathrm{r}}. \tag{2}$$

The losses arise from the two different mechanisms of dissipation: dielectric losses arising from continuous reorientation of dipoles in the time-changing field and conduction losses due to electric conductivity of the material arising from free charges, either electrons or ions. Considering that both mechanisms form ohmic losses, they can be unified within a single resistance or conductance in the equivalent load model. Consequently, ε''_r is sometimes expressed in terms of the equivalent conductivity σ (in siemens per meter, S/m), which then incorporates both losses:

$$\sigma = \omega \varepsilon_0 \varepsilon''_\mathrm{r} \quad , \tag{3}$$

where ω is the angular frequency.

2.3. Open-Ended Coaxial Dielectric Probe Measurement Method in General

The open-ended coaxial probe is usually built as a precisely machined segment of a straight rigid coaxial transmission line. One end features the input port in the form of a coaxial connector, while the other end (the probe tip) is truncated and precisely machined as an open end. The open end is inserted into a MUT whose dielectric permittivity is being measured. The electric field lines form between the electrodes of the open end, penetrating the MUT. Thus, the MUT dominantly contains the electric field and determines the termination of the coaxial line. The resulting reflection coefficient can be measured at the probe input port by the vector network analyzer (VNA). VNA performs a one-port reflection measurement by sending the test signal into the probe input port, measuring the reflection from the probe tip inserted in the MUT in the form of the reflection coefficient Γ. The reflection coefficient Γ is a complex quantity defined by its real and imaginary part, i.e., by its amplitude and phase.

Considering that Γ is a function of ε_r and vice versa, the complex relative permittivity ε_r of the MUT can be derived from the reflection coefficient Γ using the postprocessing calculations. These calculations are incorporated in the software provided by the probe manufacturer, accompanying the probe, thus completing the whole measurement method provided to the probe user. The calculation method is based on the solution for the equivalent model of the probe termination load admittance. The probe manufacturers aim for the highest possible accuracy, leading to usage of complex models. Such complex models should preferably include all electromagnetic phenomena occurring in the probe and MUT—if not by analytical modeling of the phenomena, then at least implicitly by finding the best fitting function within the process of probe calibration. Thus, in order to determine the parameters of the load model, the measurement must first be calibrated using three known loads: open (without any MUT, open end is in the air), short (open end is shorted by a conductive sheet), and a known liquid (deionized water being most commonly used, as its dielectric dispersion is well-known).

In order to increase the measurement accuracy, the model should be as rigorous as possible while still allowing the calculations to be performed within a sensible time. The computation speed is an important aspect due to the fact that measurements are commonly performed in a wide frequency span, i.e., in a large number of frequency points, putting a strain on the computation time. Given all the considerations mentioned here, a number of models exist, while the probe manufacturers (such as [36,37]) use the complex ones they consider the most accurate and suitable to their probes. However, the simplest model would be the one taking into account only the capacitive susceptance at the probe open end. One of the aims of this paper was to analyze the validity of this simple model in the microwave frequency range from 0.5 to 18 GHz.

2.4. Slim-Form Probe

The object of our study was the slim-form probe—a widely used open-ended coaxial probe manufactured by Keysight Technologies—with all the specifications presented hereafter taken from [36]. It is built as a 200 mm long segment of a straight rigid coaxial transmission line. One end features the input port in the form of a 2.4 mm coaxial 50 Ω connector, while the other end is a flangeless open end having an outer diameter of 2.2 mm, according to the manufacturer specifications.

The inner diameters are not specified by the manufacturer; however, the probe has been commonly referenced [21,38] to conform to the geometry of the RG405 semirigid coaxial cable [39], having a characteristic impedance of 50 Ω. This conformance has been visually confirmed in this study as accurately as possible by the caliper measurements. Small deviations are possible, depending also on the relative permittivity of the cable dielectric, but these are considered too small to affect the modeling accuracy (having an order of magnitude 1/100 of the millimeter). Thus, the probe modeling in this study relied on RG405 dimensions while keeping the characteristic impedance at 50 Ω, as explained later.

The nominal frequency range of the probe from 500 MHz to 50 GHz is specified by the manufacturer [36]. Considering that the upper frequency limit of our VNA is 18 GHz, this study was performed from 500 MHz to 18 GHz. This range still covers most of the microwave applications nowadays, both in biomedicine and in communications.

The maximum frequency $f_{\max}$ of the probe is further limited by MUT properties according to the following equation given in the specifications [36]:

$$f_{\max} < \frac{|285 - 125j|}{\sqrt{|\varepsilon_r|}} \text{ GHz.} \tag{4}$$

A calculation check with the maximum $|\varepsilon_r|$ of MUTs used in this study confirmed that our measurements were not affected by this additional frequency limit.

According to [36], the measurement method with the slim-form probe assumes that the MUT is liquid or soft semi-solid, infinite in size, non-magnetic, isotropic, and homogeneous. It requires a sample size which allows minimum 5 mm insertion and 5 mm around the probe tip. The measured MUT should have ε_r' less than 100. These requirements were all satisfied for the MUTs used in this study.

The typical accuracy for both ε_r' and ε_r'' is declared in [36] simply as ±10% of the absolute value of the complex permittivity. The accuracy of our measurement results was actually better, as the results deviated less than 10% from the expected Debye and Cole–Cole values of MUTs.

In the probe specifications, the manufacturer does not explicitly disclose the model used for postprocessing calculations to derive the complex permittivity from the measured reflection coefficient. However, the manufacturer application note [40] referenced the paper [41] when mentioning the derivation of the MUT permittivity from the reflection coefficient measured by the coaxial probe, suggesting the use of polynomial model of the load admittance, with optimized coefficients.

2.5. Materials under Test

In order to validate the models analyzed in this study, we used well-defined materials whose dielectric properties can be modeled using Debye and Cole–Cole dispersion models: deionized water and sodium chloride (NaCl) solution in deionized water (saline).

Water is commonly used as a reference material, as its dielectric properties have been extensively studied. The frequency dispersion of the complex relative permittivity of water is described using Debye's empirical equation [42]:

$$\varepsilon_r(\omega) = \varepsilon_\infty + \frac{\varepsilon_s - \varepsilon_\infty}{1 + j\omega\tau}, \tag{5}$$

where ε_∞ is the relative permittivity at the high-frequency limit, ε_s is the low-frequency or static relative permittivity, and τ is the relaxation time of the water. Accordingly, the water permittivity can thus be determined, provided that said parameters are known.

Saline solutions, i.e., sodium chloride (NaCl) solutions in water, can be described by the Cole–Cole empirical equation [43], extended with the ionic conductivity term [44]:

$$\varepsilon_r(\omega) = \varepsilon_\infty + \frac{\varepsilon_s - \varepsilon_\infty}{1 + (j\omega\tau)^{1-\alpha}} + \frac{\sigma_i}{j\omega\varepsilon_0}, \tag{6}$$

where α is the distribution parameter and σ_i is the ionic electric conductivity.

Considering that water and NaCl solutions were used as the materials under test in this study, their permittivity could be calculated in advance by Equations (5) and (6), respectively. The calculated permittivity could thus serve as a reference value for simulations. The required Debye and Cole–Cole parameters ε_∞, ε_s, τ, α, and σ_i for the tested materials could be determined according to the saline concentrations and temperature.

Four saline solutions were used in the study, having NaCl concentrations of 0.154M, 0.25M, 0.5M, and 1M. The concentration of 0.154M refers to physiological saline (0.9% NaCl), commonly referred to as being isotonic to the biological tissue fluids [45], thus well-representing biological materials with high water content. This makes the study and its conclusions relevant and applicable for dielectric studies of biological samples. The other three saline solutions had larger NaCl concentrations, which increased their ionic conductivity, to observe its potential effect on the measurement results.

Dielectric permittivity of water can be described by Debye dispersion (5). We used the following Debye parameters from the well-accepted reference [46] (for 25 °C): $\varepsilon_\infty = 5.2$, $\varepsilon_{s\_water} = 78.36$, and $\tau_{water} = 8.27 \cdot 10^{-12}$ s to calculate the complex relative permittivity $\varepsilon_r(\omega)$ using Equation (5). Then, we extracted its real and imaginary parts $\varepsilon_r'(\omega)$ and $\varepsilon_r''(\omega)$ (respectively) to be used as reference values for comparison to the measurement and simulation results.

Dielectric permittivity of NaCl solutions can be described by Cole–Cole dispersion (6), provided that the dispersion parameters ε_∞, ε_s, τ, α, and σ_i are known. These parameters were calculated according to polynomial equations derived and validated in [44], with the exception of ε_∞ which does not differ between water and the analyzed saline solutions; thus, the value of $\varepsilon_\infty = 5.2$ for water could also be used for all the saline solutions. The model for concentrations below 1M from [44] was used for all four concentrations (0.154M, 0.25M, 0.5M, and 1M), as presented in the following equations:

$$\varepsilon_\mathrm{s} = \varepsilon_\mathrm{s\_water}\left(1 - 3.742 \cdot 10^{-4}tc + 0.034c^2 - 0.178c + 1.515 \cdot 10^{-4}t - 4.929 \cdot 10^{-6}t^2\right) \quad , \tag{7}$$

$$\tau = \tau_\mathrm{water}\left(1.012 - 5.282 \cdot 10^{-3}tc + 0.032c^2 - 0.01c - 1.724 \cdot 10^{-3}t + 3.766 \cdot 10^{-5}t^2\right) \quad , \tag{8}$$

$$\alpha = -6.348 \cdot 10^{-4}tc - 5.1 \cdot 10^{-2}c^2 + 9 \cdot 10^{-2}c \quad , \tag{9}$$

$$\sigma_\mathrm{i} = 0.174tc - 1.582c^2 + 5.923c \quad , \tag{10}$$

where t is the temperature in degrees Celsius (25 °C in this case), c is the saline concentration in moles per liter (M), and $\varepsilon_\mathrm{s\_water}$ and τ_water are the aforementioned values of static relative permittivity of water and the relaxation time of water, respectively. The resulting values are given in Table 1.

Table 1. Cole–Cole parameters of the analyzed saline solutions.

Saline Concentration	0.154M	0.25M	0.5M	1M
ε_s	76.22	74.912	71.741	66.398
τ [s]	8.033×10^{-12}	7.930×10^{-12}	7.686×10^{-12}	7.297×10^{-12}
α	1.020×10^{-2}	1.535×10^{-2}	2.432×10^{-2}	2.313×10^{-2}
σ_i [S/m]	1.543	2.469	4.741	8.691

These parameters were input in Equation (6) to calculate the complex relative permittivity $\varepsilon_\mathrm{r}(\omega)$ of each saline. Then, we extracted its real and imaginary parts $\varepsilon_\mathrm{r}'(\omega)$ and $\varepsilon_\mathrm{r}''(\omega)$ (respectively) to be used as reference values for the simulation models.

The same four saline solutions were used in measurements, with precisely prepared concentrations. The temperature of all samples was kept at the laboratory temperature of 25 °C, additionally stabilized by a water bath.

2.6. Measurements

The measurement setup was assembled according to the principles given above in Sections 2.3 and 2.4. The slim-form probe by Keysight Technologies Inc. (Santa Rosa, CA, USA) [36] was connected to the vector network analyzer FieldFox N9927A (Keysight Technologies Inc., Santa Rosa, CA, USA) by a phase-stable coaxial cable Sucoflex 404 (HUBER+SUHNER AG, Herisau, Switzerland). The VNA was connected to a computer, and the measurements were controlled and performed using the manufacturer-provided software Keysight Materials Measurement Suite N1500A (Keysight Technologies Inc., Santa Rosa, CA, USA) [33]. The room and the MUT temperature were kept at 25 °C, and the MUT temperature was controlled using a precise thermometer DTM3000 (LKM Electronics GmbH, Geratal, Germany).

The probe was fixed to its stand in the vertical position and inserted into liquid MUT, as shown in Figure 1. The liquid MUT was placed in a glass container, thus assuming the form of a cylinder, 29 mm high and 37 mm in diameter, while the probe insertion depth was kept at 10 mm. These dimensions exceed the aforementioned geometrical requirements given by the manufacturer related to the minimum insertion depth and MUT minimum size. The glass walls of the container did not affect the measurements, which was confirmed both by several pilot measurements with the larger containers, all yielding the same result, and as is later shown, by the results fitting the expected permittivity of the liquids in accordance with their dispersions (Debye dispersion for water and Cole–Cole dispersion for NaCl solutions).

Figure 1. The slim form inserted into a liquid MUT.

The output power was set to −10 dBm, and the intermediate frequency bandwidth was set to 100 Hz. The frequency range was set to cover the range from 500 MHz to 18 GHz, with linear stepping of 5 MHz. The measurements were calibrated by the open-short-water calibration sequence preceding each MUT measurement.

2.7. Simulations

2.7.1. Simulation Model

The basic model of the probe is shown in Figure 2a, as a segment of a coaxial line. At the upper end of the probe, the waveguide port was placed, allowing the measurement of the reflection coefficient. The lower end of the probe was the probe tip, i.e., the open end used for measuring the MUT permittivity. The original slim-form probe is 200 mm long from the open end to the connector. This separates the open end from the connector and the VNA cable (Figure 1), minimizing both the mechanical and the electromagnetic influence of the bulky attachment on the measurement occurring in the MUT. The sufficient probe length also provides the mechanical support for attaching the probe to the stand and keeping it mechanically stabilized (Figure 1). Furthermore, it also allows the insertion of the probe in tall and narrow containers. All these features were irrelevant for the simulations; thus, we minimized the length of the probe model to reduce the simulation burden. We set our model to the length of 11 mm to allow the 10 mm insertion into the MUT, which modeled the actual physical measurement setup within the MUT. The remaining length outside the MUT was arbitrarily chosen as 1 mm to provide a very short segment to which the input port was attached, 1 mm above the MUT border (Figure 2b).

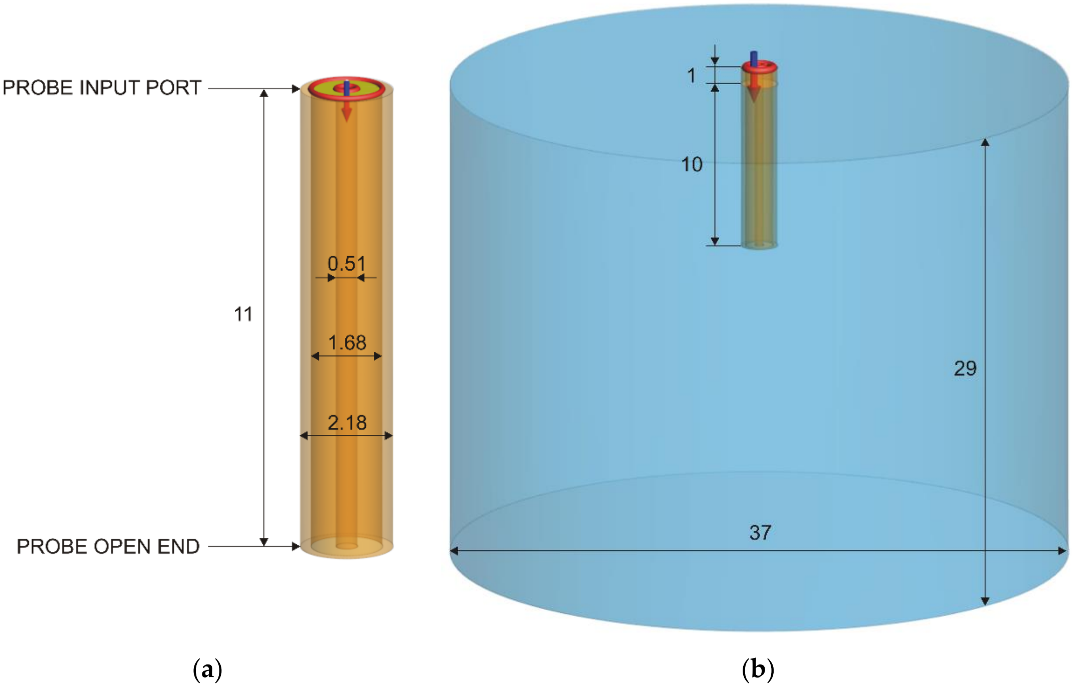

Figure 2. (**a**) The slim-form probe modeled as a coaxial line. (**b**) The model showing the probe inserted 10 mm deep into the MUT, with its input port outside the MUT. All measurements in millimeters.

Our simulation model of the slim-form probe exploited the fact that the slim-form probe dimensions conform to the geometry of a standard RG405 semi-rigid coaxial cable. According to, e.g., [39], these are: central conductor diameter 0.51 mm, dielectric diameter 1.68 mm, and shield outer diameter 2.18 mm, with PTFE (Teflon) as the dielectric. In this study, PTFE relative permittivity was set to $\varepsilon_r = 2.08$. PTFE loss tangent was set to zero, as the realistic loss tangent of PTFE is extremely small anyway, and the shortness of the line further reduces any significant losses in the coaxial line. The metallic parts, i.e., the central and the outer conductor, were modeled as perfect electric conductor (PEC). Using PEC as a material with infinite conductivity accelerated the simulations with respect to using realistic metallic materials. We initially compared the simulations of the probe model using PEC to those using metallic materials such as copper to observe if any difference exists in the results. The results were practically identical, concluding that PEC could be used further on, as an efficient approximation of metallic materials as its conductivity is so large that it can be approximated with infinity. After the initial simulations, the central conductor diameter was finely tuned to 0.50465 mm which yielded the accurate characteristic impedance of the coaxial line of 50 $\Omega \pm 0.01\ \Omega$ both in FEKO and in CST. This was the basic probe model which also served to simulate the open end without MUT, which was needed for the calibration.

MUT was added into the model as a vertical cylinder, 29 mm high and 37 mm in diameter, centered around the probe, with the probe inserted 10 mm deep into the cylinder (Figure 2b). The complex permittivity of the MUTs was set to their Debye and Cole–Cole values (water and saline solutions, respectively), previously calculated from 500 MHz to 18 GHz, as explained in Section 2.5. Both FEKO and CST allow the user to define the dispersive material by a table of ε_r' and ε_r'' frequency points.

2.7.2. Frequency Domain: Method of Moments in FEKO

The open-ended coaxial probe inserted in MUT was modeled and simulated using method of moments (MoM) implemented in electromagnetic simulation software package FEKO (Altair Engineering, Inc., Troy, MI, USA) [34]. The method of moments is the default and the most accurate method provided by FEKO, implementing a full wave solution of

Maxwell's integral equations in the frequency domain. MoM is an open domain method, i.e., it solves the problems involving radiation sources in free space. Accordingly, there are no problem boundaries to be defined but only the structure itself. Consequently, only the structure is discretized and not the space around it.

The structure volume elements, both metallic and dielectric, were defined by their surfaces, discretized by triangles. Modeling of dielectric media in MoM formulation was performed using the surface equivalence principle (SEP) enabled in FEKO. SEP introduces equivalent electric and magnetic currents on the surface of arbitrarily shaped closed dielectric bodies.

The frequency range of interest (500 MHz to 18 GHz) was covered by running simulations at discrete frequency points, from 500 MHz to 1 GHz with 100 MHz step, and from 1 to 18 GHz with 1 GHz step. The mesh size increased with the frequency and model complexity. After testing several grades of mesh refinement for the results convergence, we found the optimum mesh resulting with max. ~75k triangles at 18 GHz for the full model of the probe and MUT (Figure 3).

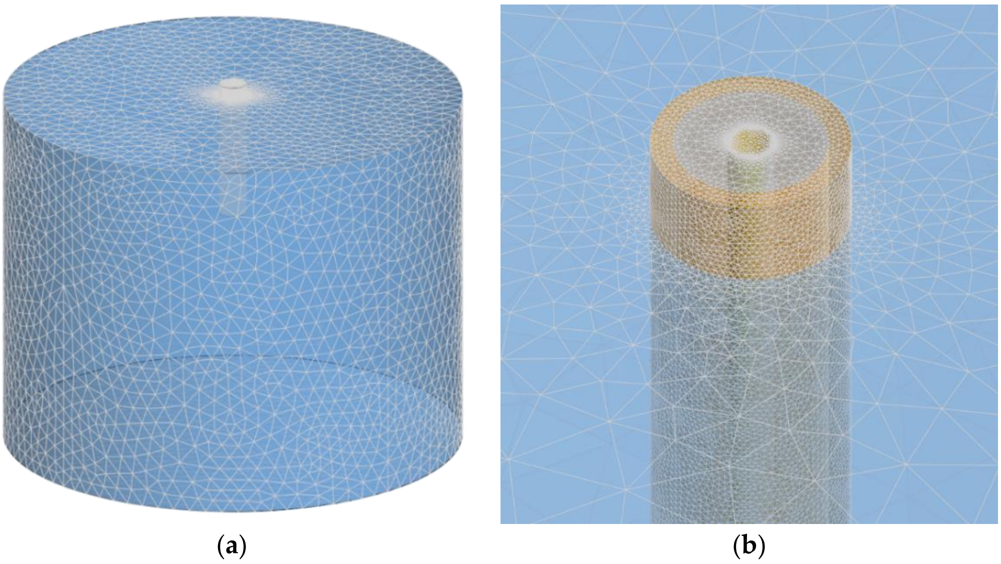
(**a**) (**b**)

Figure 3. (**a**) FEKO model mesh (probe in MUT). (**b**) Mesh detail around the probe input port.

2.7.3. Time Domain: Finite Integration Technique in CST

Aiming to additionally validate the electromagnetic simulation results with a different numerical method, we simulated the same models using a time-domain solver. Time-domain analysis not only complements the frequency-domain study but is also generally suitable and potentially less time-consuming for broadband problems such as this one. The Finite Integration Technique (FIT) implemented in electromagnetic simulation software package CST Studio Suite (Dassault Systèmes, Vélizy-Villacoublay, France) [35] was used as the numerical solver.

Mesh was based on hexahedra. The mesh density was increased near the model, as opposed to the model box edges where the boundary conditions were set as a perfectly matched layer. The probe itself consisted of 2.59 million mesh cells, while the entire model consisting of the probe immersed in MUT had between 31.8 and 33.7 million mesh cells, adequately representing the structure (Figure 4).

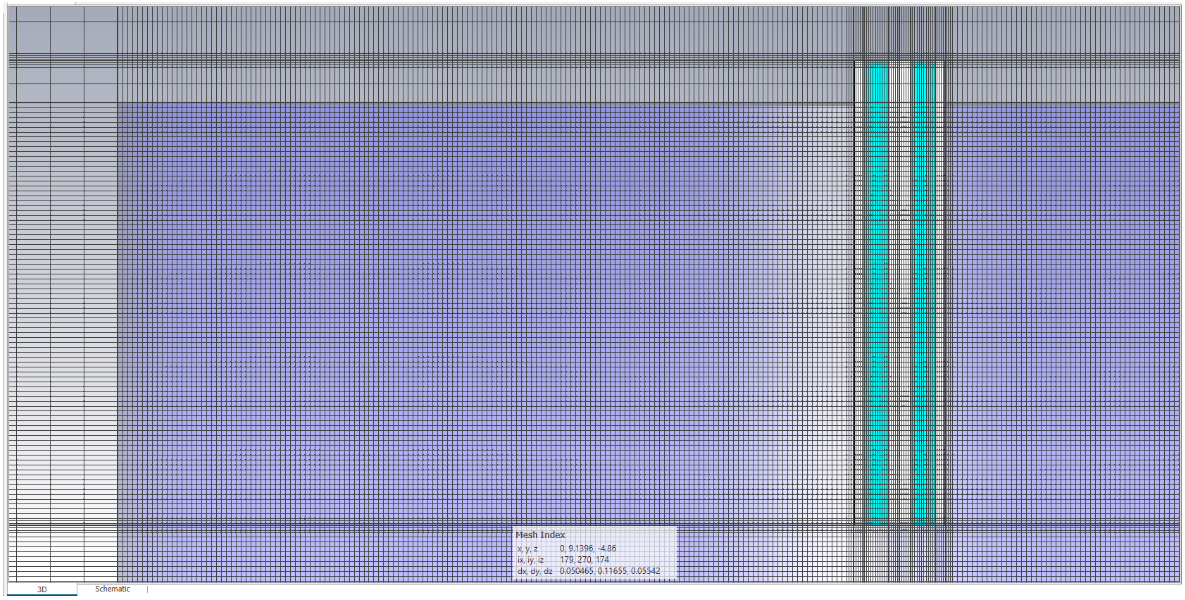

Mesh Index
x, y, z 0, 9.1396, -4.86
ix, iy, iz 179, 270, 174
dx, dy, dz 0.050465, 0.11655, 0.05542

Figure 4. CST model mesh cross-section, truncated on the right and on the bottom to ensure the visibility of the important features of the mesh, showing the cross-section of the whole probe and the upper-left part of MUT (compare to Figure 2b) surrounded by the model box.

For S-parameter calculations, the excitation signal for the transient analysis is defined by a Gaussian shape for which the Fourier spectrum entirely covers the defined frequency band of interest. The accuracy of results was set to −40 dB, and the maximum solver duration was set to 20 pulses. The set accuracy resulted in a total simulation time of just over 10 min for the probe only, 50 min for model with water as a MUT, and between 116 min and 163 min for the saline solutions.

2.8. Capacitive-Load Model

The probe open end inserted in MUT terminates the coaxial line, and the probe tip can thus be regarded as terminated by the load admittance Y, which inherently depends on the MUT permittivity ε_r. In order to derive the MUT relative permittivity ε_r from the reflection coefficient Γ measured at the probe input port, the function $\varepsilon_r = f(\Gamma)$ needs to be determined.

In general, the reflection coefficient at the line end is the function of the line termination load admittance Y, given the fixed characteristic admittance of the transmission line Y_0:

$$\Gamma_{\mathrm{MUT}} = \frac{Y_0 - Y}{Y_0 + Y}. \tag{11}$$

Equation (11) actually describes the reflection coefficient Γ_{MUT} at the probe open end, where the incident wave travelling inside the probe reflects from the interface with the MUT. On the other hand, VNA can only measure the reflection coefficient Γ at the probe input port (see Figure 2a). Assuming a lossless transmission line along the probe length, perfectly matched to the VNA, the two reflection coefficients differ only by their phase due to the phase shift from the probe tip to the probe input port, according to the following relation:

$$\Gamma = \Gamma_{\mathrm{MUT}} \frac{1 - \mathrm{jtg}\beta l}{1 + \mathrm{jtg}\beta l}, \tag{12}$$

where the fraction on the right describes the phase shift of the reflection coefficient in a lossless transmission line (i.e., along the probe) having a length of l, where $\beta = 2\,\pi/\lambda$, and λ is the wavelength inside the line. The assumption of a lossless line holds when the probe is made of low-loss materials and is too short for any significant losses to occur.

However, if the line has its own imperfections in terms of matching and losses, it has to be considered as a two-port network with its scattering matrix having parameters S_{11}, S_{12}, S_{21}, and S_{22}. At this point, for the sake of simplicity, Equation (12) stands as the special case of a scattering matrix of a matched lossless transmission line having S_{11} = S_{22} = 0 and S_{12} = S_{21} = $\mathrm{e}^{-\mathrm{j}\beta l}$. After establishing the dependencies $\Gamma = f\ (\Gamma_{\mathrm{MUT}})$ in (12) and $\Gamma_{\mathrm{MUT}} = f\ (Y)$ in (11), the last dependency to be established is $Y = f\ (\varepsilon_{\mathrm{r}})$, in order to finally determine the function $\varepsilon_{\mathrm{r}} = f\ (\Gamma)$.

The function $Y = f\ (\varepsilon_{\mathrm{r}})$ was determined by modeling the admittance of the probe end terminated by MUT. The model complexity can vary from the simplest one, a pure capacitive-load model $Y = \mathrm{j}\omega C$, to more complex ones including other components of the admittance. It has been shown in prior studies [26,47–49] that the simple capacitive load successfully models the actual load if the frequencies are not as high as to cause radiation from the probe into the MUT. Accordingly, in this model, the only physical phenomenon taken into account at the probe tip was the purely reactive electric field closing between the two conductors of the coaxial cable, forming the purely capacitive load. This is commonly satisfied within the nominal frequency range of a coaxial probe, which is anyhow limited at the high end by the occurrence of the higher modes of EM wave propagation in the coaxial line. Therefore, we used the simple capacitive-load model consisting of two capacitances:

$$Y = \mathrm{j}\omega C_{\mathrm{f}} + \mathrm{j}\omega\varepsilon C_0 = \mathrm{j}\omega C_{\mathrm{f}} + \mathrm{j}\omega\varepsilon_0\varepsilon_{\mathrm{r}}C_0 \tag{13}$$

where C_{f} is the fringing capacitance occurring within the probe dielectric and thus independent of MUT, and εC_0 is the capacitance arising from the electric field lines closing through the MUT (i.e., describing the electric energy stored in the MUT) and thus dependent on the MUT permittivity $\varepsilon = \varepsilon_0\varepsilon_{\mathrm{r}}$. Since the permittivity ε_{r} is a complex quantity as shown in (1), the admittance consists of both conductance and susceptance, despite calling this model a "capacitive-load model":

$$Y = \mathrm{j}\omega C_{\mathrm{f}} + \mathrm{j}\omega\varepsilon_0\left(\varepsilon_{\mathrm{r}}' - j\varepsilon_{\mathrm{r}}''\right)C_0 = \omega\varepsilon_0\varepsilon_{\mathrm{r}}''C_0 + \mathrm{j}\omega\left(C_{\mathrm{f}} + \varepsilon_0\varepsilon_{\mathrm{r}}'C_0\right) = G + \mathrm{j}B \quad . \tag{14}$$

The conductance thus describes the losses arising from the imaginary part of the MUT dielectric permittivity (as previously explained in Section 2.2).

It is obvious from (13) and (14) that $Y = f\ (\varepsilon_{\mathrm{r}})$, and vice versa, $\varepsilon_{\mathrm{r}} = f\ (Y)$, and from (11) and (12) that $\Gamma = f\ (Y)$, and vice versa, $Y = f\ (\Gamma)$; thus, there must exist a function $\varepsilon_{\mathrm{r}} = f\ (\Gamma)$, which can be used to calculate the MUT relative permittivity ε_{r} from the measured reflection coefficient Γ. Solving this function, according to the above given model, requires knowing the three unknowns which depend on the exact construction geometry of the probe: C_0, C_{f}, and the probe length l. This can be resolved by measuring the reflection coefficient for three known loads, as is commonly done by probe calibration, as mentioned in Section 2.3. This was the reasoning for the perfectly matched lossless probe.

Using the calibration data for three loads, the function $\varepsilon_{\mathrm{r}} = f\ (\Gamma)$ can actually be determined and expressed even without the need to determine the said unknowns. Such a procedure is especially useful for a general case of the scattering matrix, applicable to the realistic probes being neither perfectly matched nor lossless. Still, the same model can be used for the load admittance: a simple capacitive load described by (13). The calculation procedure has already been shown in the literature [47–49], where the probe was considered as a two-port network with its scattering matrix. The resulting function $\varepsilon_{\mathrm{r}} = f\ (\Gamma)$, in accordance with [48,49] is:

$$\varepsilon_{\mathrm{r}} = \frac{A_1\Gamma - A_2}{A_3 - \Gamma} \quad . \tag{15}$$

All the unknowns, including the scattering parameters in the general case, are contained within three unknowns A_1, A_2, and A_3, which are determined by calibration using three loads. The usual three loads for calibration are open, short, and a known liquid with relative permittivity ε_{L}, producing the reflection coefficients Γ_{O}, Γ_{S}, and Γ_{L}, respectively, during the calibration procedure. The unknowns A_1, A_2, and A_3 are then found from the calibration as (in accordance with [48,49]):

$$A_1 = \frac{\varepsilon_L(\Gamma_S - \Gamma_L) - (\Gamma_S - \Gamma_O)}{\Gamma_L - \Gamma_O} \quad , \tag{16}$$

$$A_2 = \frac{\varepsilon_L\Gamma_O(\Gamma_S - \Gamma_L) - \Gamma_L(\Gamma_S - \Gamma_O)}{\Gamma_L - \Gamma_O} \quad , \tag{17}$$

$$A_3 = \Gamma_S \quad . \tag{18}$$

All the quantities in Equations (15)–(18) are complex values.

The calibration was performed in this study throughout the frequency span of the measurements, calculating the unknowns A_1, A_2, and A_3 at each frequency point. This enabled us to calculate the permittivity using Equation (15) at each frequency point.

Besides performing the calculations (15)–(18) in the measurement part of the study, the same calculations were also used for postprocessing in the simulation part of the study. This postprocessing thus concluded the simulation of the complete measurement process: from modeling the probe and the MUT and obtaining the reflection coefficient for various MUTs by simulations to postprocessing using the simple capacitive-load model.

3. Results

3.1. Measurement Results

Figures 5–12 show the results of the first part of the study, described in Section 2.1.1. The measurement results are drawn, implementing a moving average with the frequency span of ±125 MHz at each frequency point to smooth the lines by eliminating the small fluctuations that do not reflect the actual result fluctuations but are caused by the imperfections in the measurement setup.

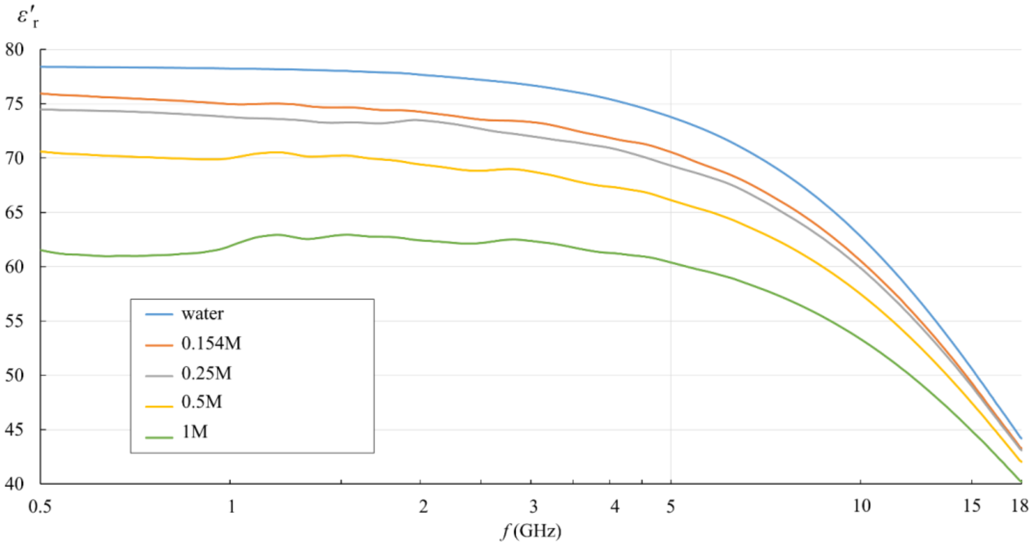

Figure 5. Measured ε'_r of water and saline solutions, as obtained from the measurement software (frequency in logarithmic scale).

Figures 5 and 6 show the measurement results for ε'_r and σ calculated by (3). They are displayed in the logarithmic scale for easier comparison with the published studies of NaCl solutions in water.

In Figures 5 and 6, the effect of the ionic concentration in the saline solutions can be observed. ε'_r decreased with the ionic concentration, shifting the whole curve downwards with respect to deionized water. Figure 6 shows the equivalent conductivity σ as defined by (3). The conductivity dominated the low frequency range and showed different values for different saline concentrations. At higher frequencies, the equivalent conductivity is a consequence of dielectric losses only, and thus converged towards deionized water.

In Figures 7–10, each quantity ($\varepsilon'_{\mathrm{r}}$ and $\varepsilon''_{\mathrm{r}}$) is represented with three lines:

- Measurement result as a final value obtained from the measurement software (where the postprocessing of the measured reflection coefficient was embedded in the measurement software);
- Measurement result obtained by postprocessing of the reflection coefficient using the simple capacitive-load model;
- Dispersion model (Debye dispersion for water and Cole–Cole dispersion for saline solutions).

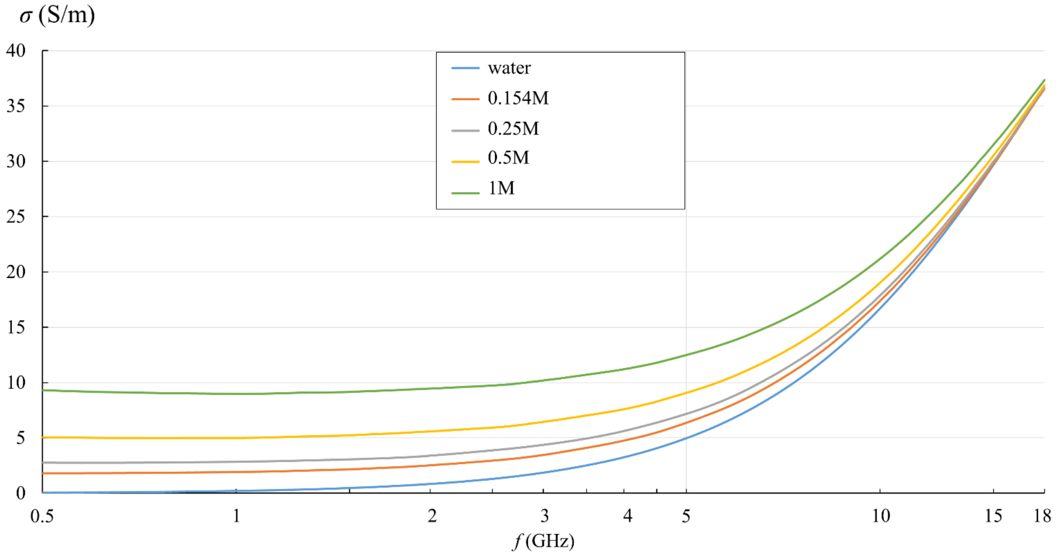

Figure 6. Measured σ of water and saline solutions, calculated from $\varepsilon''_{\mathrm{r}}$ (frequency in logarithmic scale).

Dispersion models are depicted in Figures 7–10 just to show the expected permittivity values for the measured MUTs, but they are not the focus of this part of the study. The dispersions were calculated according to the description given in Section 2.5. It can be observed in Figures 7–10 that the measured values slightly and systematically differed from Cole–Cole dispersion models (especially visible in Figures 7–10 for $\varepsilon'_{\mathrm{r}}$), more so as the ionic concentration increased. There might be several reasons for this. First, the dispersion models are not absolutely accurate. The models just approximate the realistic permittivity of the saline. Next, the model parameters depend on the temperature, where slight deviations are possible. Although the MUTs were stabilized in the water bath at 25 °C, the sample temperature slightly fluctuated around this value during its handling out of the bath and during the measurements. Furthermore, and most likely, the measurement accuracy deteriorates as MUT permittivity is further from the reference liquid used in the calibration process (which was deionized water). Anyway, the accuracy of the slim-form probe, described in Section 2.4, was itself declared at ±10%, and the systematic difference between the measured values and the dispersion models was within this declared accuracy. Accordingly, a slight difference between the measured results and the dispersion models was not of interest in this part of the study. Here, we just regarded the results obtained from the measurement software as the accurately measured values (hence as reference values for comparisons), ignoring their deviation from the dispersions. Therefore, the difference between the result obtained by postprocessing using the simple capacitive-load model and the accurate result can be considered as error. The relative error of the simple capacitive-load model with respect to the accurate value can be calculated for ε'_r and ε''_r as:

$$\varepsilon'_\mathrm{r} \text{ relative error } [\%] = \frac{\varepsilon'_{\mathrm{r(capacitive\ model)}} - \varepsilon'_{\mathrm{r(measured)}}}{\varepsilon'_{\mathrm{r(measured)}}} \cdot 100\% \;, \tag{19}$$

$$\varepsilon''_\mathrm{r} \text{ relative error}[\%] = \frac{\varepsilon''_{\mathrm{r(capacitive\ model)}} - \varepsilon''_{\mathrm{r(measured)}}}{\varepsilon''_{\mathrm{r(measured)}}} \cdot 100\% = \sigma \text{ relative error}[\%] \;. \tag{20}$$

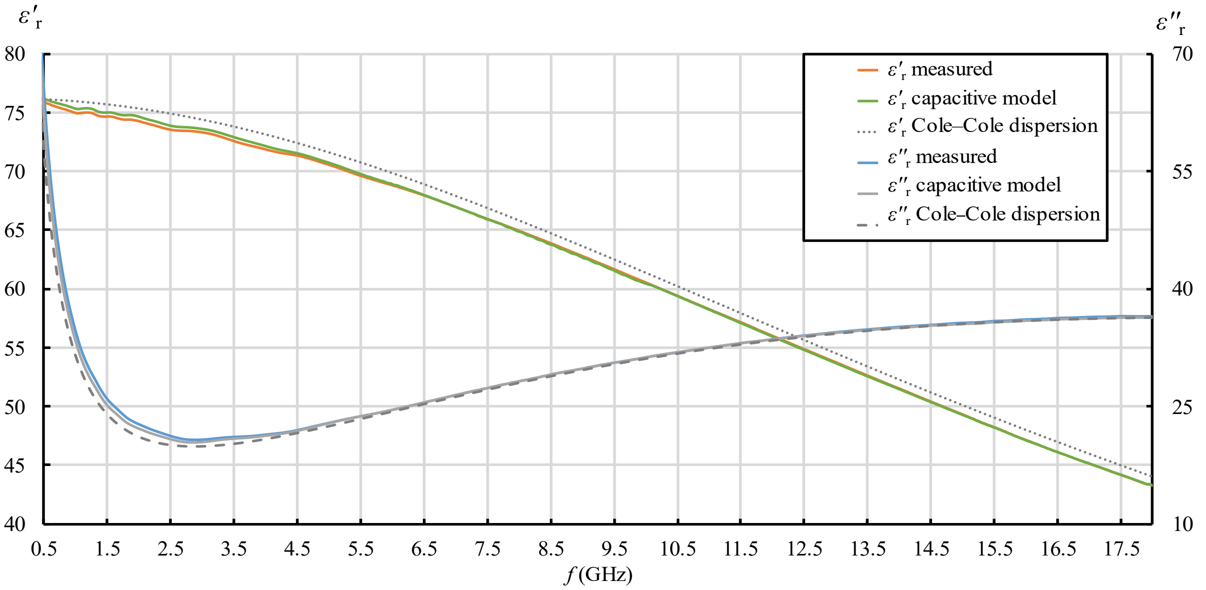

Figure 7. ε'_r and ε''_r for 0.154M (physiological) saline: measurement result as a final value obtained from the measurement software ("measured"); measurement result obtained by postprocessing the reflection coefficient using the simple capacitive-load model ("capacitive model") and dispersion model ("Cole–Cole dispersion").

Due to equivalent conductivity σ being directly proportional to ε''_r according to (3), ε''_r relative error is equal to σ relative error. These relative errors are presented in Figures 11 and 12. Both ε'_r and ε''_r relative errors equaled zero for water, as the water was used as the calibration standard both for the simple capacitive-load model and for the measurement software.

Figures 7–12 show interesting features when focusing on the comparison between the postprocessing methods, which was the research aim of this study. The most pronounced difference occurred in the lower part of the frequency span, below ca. 7.5 GHz, where the simple capacitive-load model systematically yielded slightly larger ε'_r than the actually measured value. The difference increased towards the low frequencies, which suggests that the difference between the models is inversely proportional to frequency at low frequencies for ε'_r. The difference also systematically increased with the ion concentration in the saline, suggesting that the error is connected to ionic polarization at the probe electrode surface. Due to the ionic origin of this phenomenon, it was more prominent at low frequencies and diminished as the frequency increased. However, comparing the measurement results with the dispersions, we concluded that the electrode polarization effect is not so prominent within the specified working frequency range of the slim-form probe. In any case, this low-frequency phenomenon requires additional components in (12) to model the load accurately, which are not included in the simple capacitive-load model. The manufacturer does not declare whether their measurement software models this effect or applies any corrections during postprocessing. Most likely, their measurement results suffer from the polarization error as well. Nevertheless, by regarding their measurement result as the accurate reference in this study, Figure 11 shows that the ε_r' relative error magnitude of the capacitive model stayed within ca. 0.5% for the physiological saline, around 1% for 0.25M saline, less than 4% for 0.5M saline, and exceeded 11% for 1M saline at the lowest frequency.

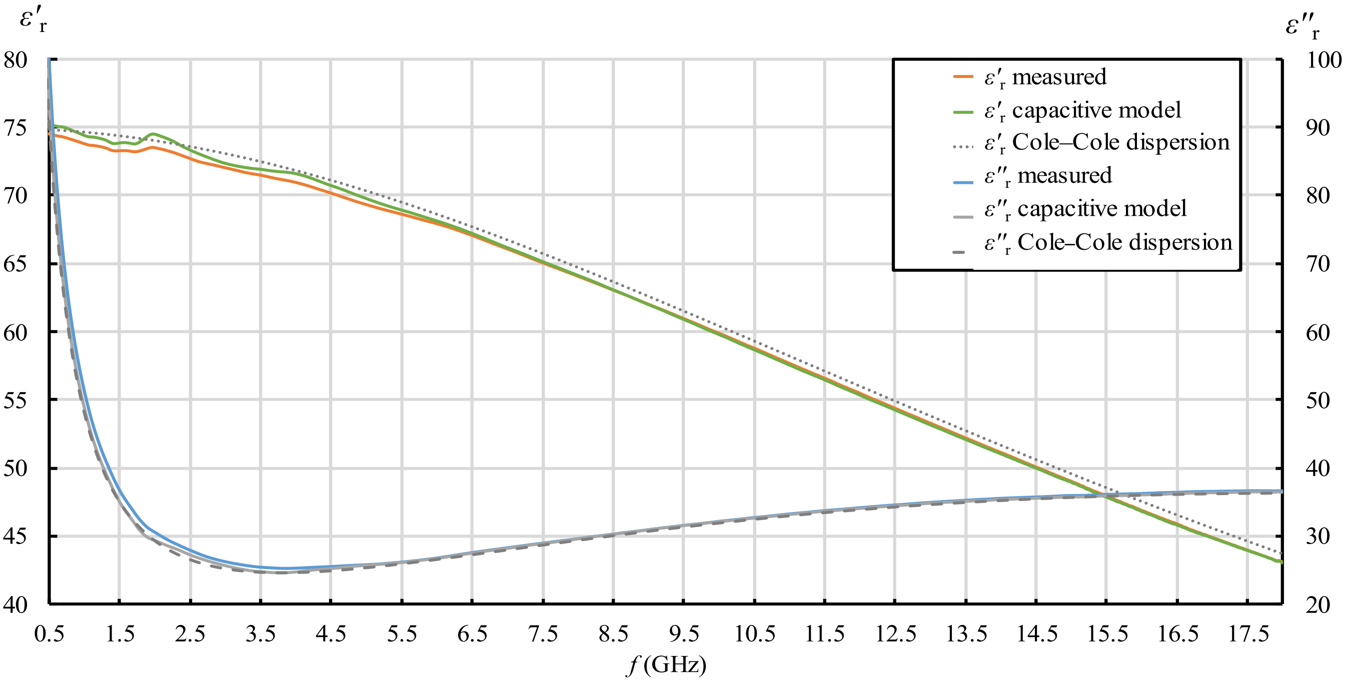

Figure 8. ε_r' and ε_r'' for 0.25M saline: measurement result as a final value obtained from the measurement software ("measured"); measurement result obtained by postprocessing the reflection coefficient using the simple capacitive-load model ("capacitive model") and dispersion model ("Cole–Cole dispersion").

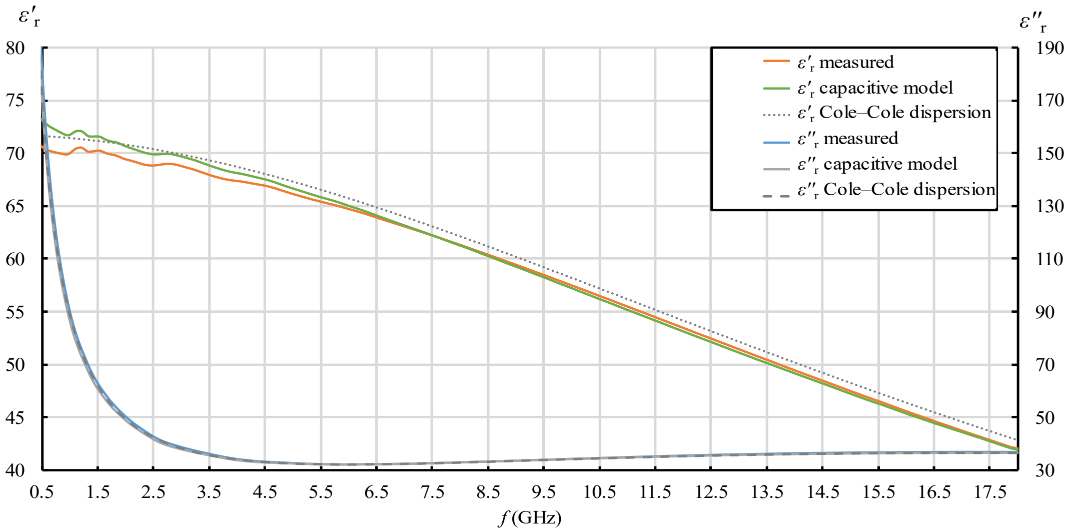

Figure 9. ε_r' and ε_r'' for 0.5M saline: measurement result as a final value obtained from the measurement software ("measured"); measurement result obtained by postprocessing the reflection coefficient using the simple capacitive-load model ("capacitive model") and dispersion model ("Cole–Cole dispersion").

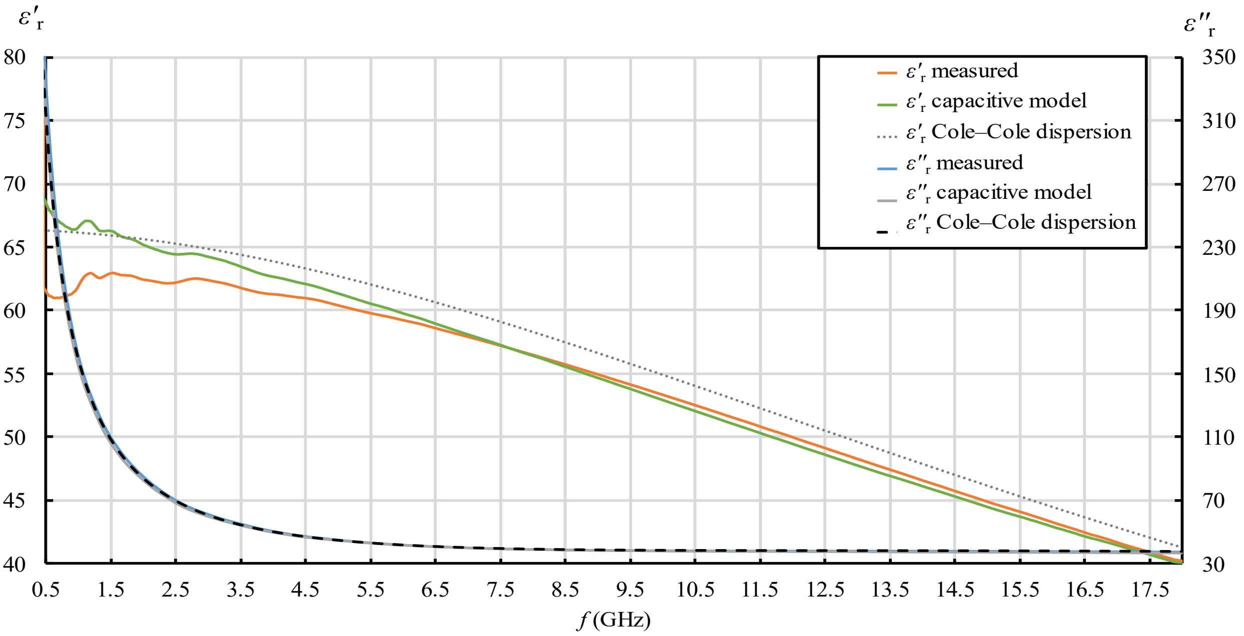

Figure 10. ε_r' and ε_r'' for 1M saline: measurement result as a final value obtained from the measurement software ("measured"); measurement result obtained by postprocessing the reflection coefficient using the simple capacitive-load model ("capacitive model") and dispersion model ("Cole–Cole dispersion").

Figure 11 also shows that the frequency of 7.5 GHz was a cross-over point, where the difference between the models diminished and then changed its sign: above 7.5 GHz, the simple capacitive-load model systematically yielded lower ε_r' than the actually measured value. However, the error magnitude stayed within ca. 1% even for the highest NaCl concentration and practically diminished towards the upper limit of the frequency span, overall suggesting a negligible error.

When it comes to ε_r'', the situation was somewhat different. Although the difference is barely visible in Figures 7–10 due to the y-axis scale, it is more clearly visible in Figure 12 where the difference again occurred in the lower part of the frequency span below ca. 5.5 GHz but had the opposite sign: the simple capacitive-load model systematically yielded slightly lower ε_r'' than the actually measured value. Again, the error increased towards the low frequencies, reaching the maximum magnitude of almost 7% at the lowest frequency, suggesting that the ε_r'' relative error is inversely proportional to frequency at low frequencies. However, the ε_r'' error at low frequencies apparently did not significantly depend on the ion concentration in the saline. Between ca. 5.5 GHz and 9 GHz, there was no difference between the models. Above 9 GHz, the difference appeared again, and the capacitive-load model started systematically yielding lower ε_r'' than the actually measured value. The magnitude of this error was not significant below 18 GHz: <1% for all concentrations lower than 1M and <2% for the highest NaCl concentration of 1M. It is worth noting that the error slightly increased with frequency. This might be connected with the appearance of radiation from the probe end, when the wavelength decreases and becomes comparable to the probe tip dimensions. However, due to the frequency limit of our setup, we were not able to determine the significance of this error above 18 GHz.

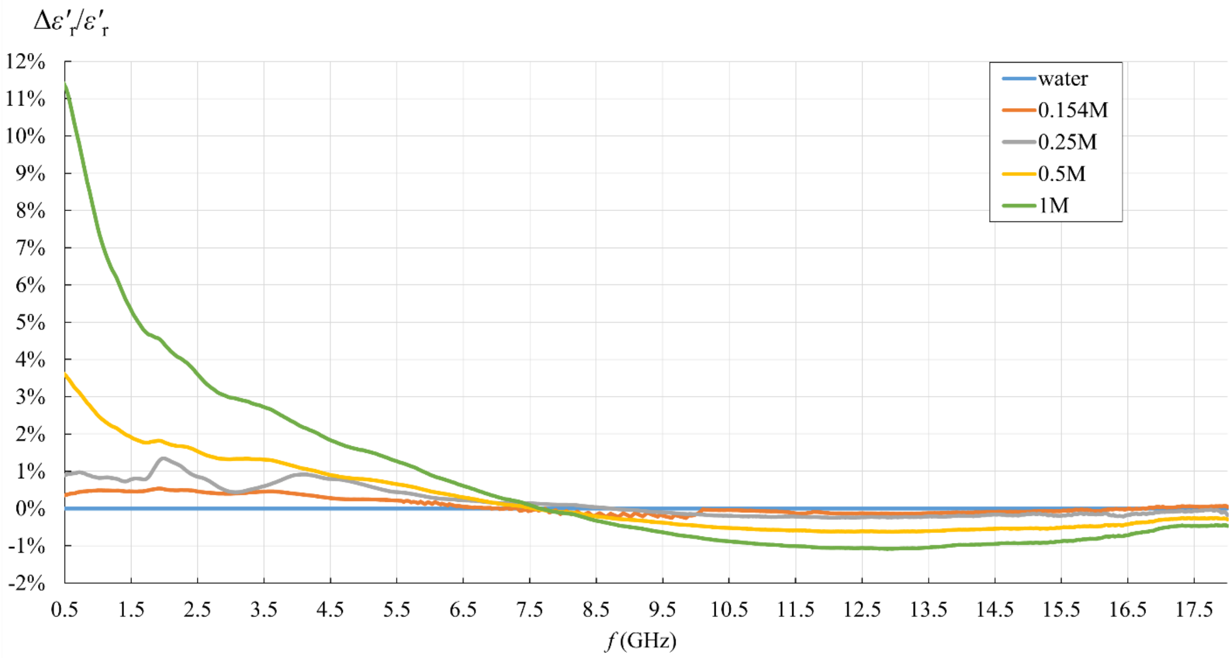

Figure 11. ε_r' relative error of the simple capacitive-load model with respect to the measurement result obtained from the measurement software, for water and saline solutions with different NaCl concentrations.

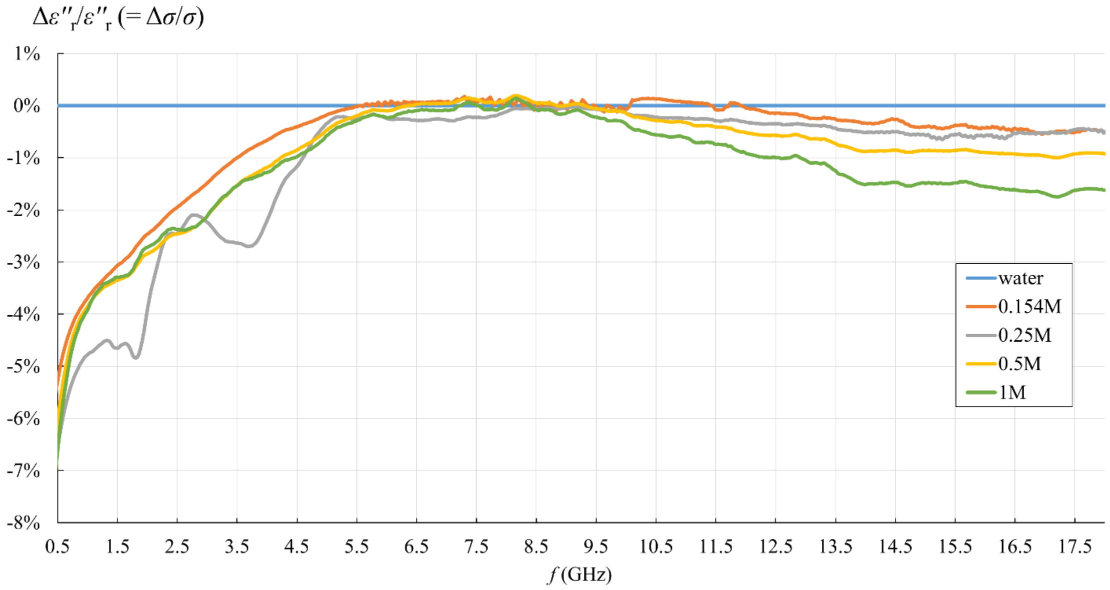

Figure 12. ε_r'' relative error of the simple capacitive-load model with respect to the measurement result obtained from the measurement software, for water and saline solutions with different NaCl concentrations.

3.2. Simulation Results with the Simple Capacitive-Load Model

Figures 13–16 show the results of the second part of the study, described in Section 2.1.2.

Figures 13 and 14 show the simulation results for ε_r' and ε_r'', as obtained by postprocessing of the reflection coefficient using the simple capacitive-load model. The reflection coefficient was obtained by simulations using FEKO and CST. FEKO is a frequency-domain method; therefore, the results are represented in Figures 13–16 by discrete frequency points for which the simulation was performed (as described in Section 2.7.2). CST is a time-domain method, and its results continuously covered the frequency span of the simulations (colored lines in figures). Both FEKO and CST results can be compared to the dispersion models, also shown in figures (dotted, dashed, and solid black lines).

In this simulation part of the study, the dispersion model represents the accurate permittivity, as this was the MUT permittivity value actually set in each simulation model. By comparing the simulation results to the dispersions, we can observe the validity of the overall simulation process, consisting of both the electromagnetic simulations and the postprocessing using the capacitive model. The postprocessing of the reflection coefficient should revert the simulation result right back to the permittivity initially set in the model.

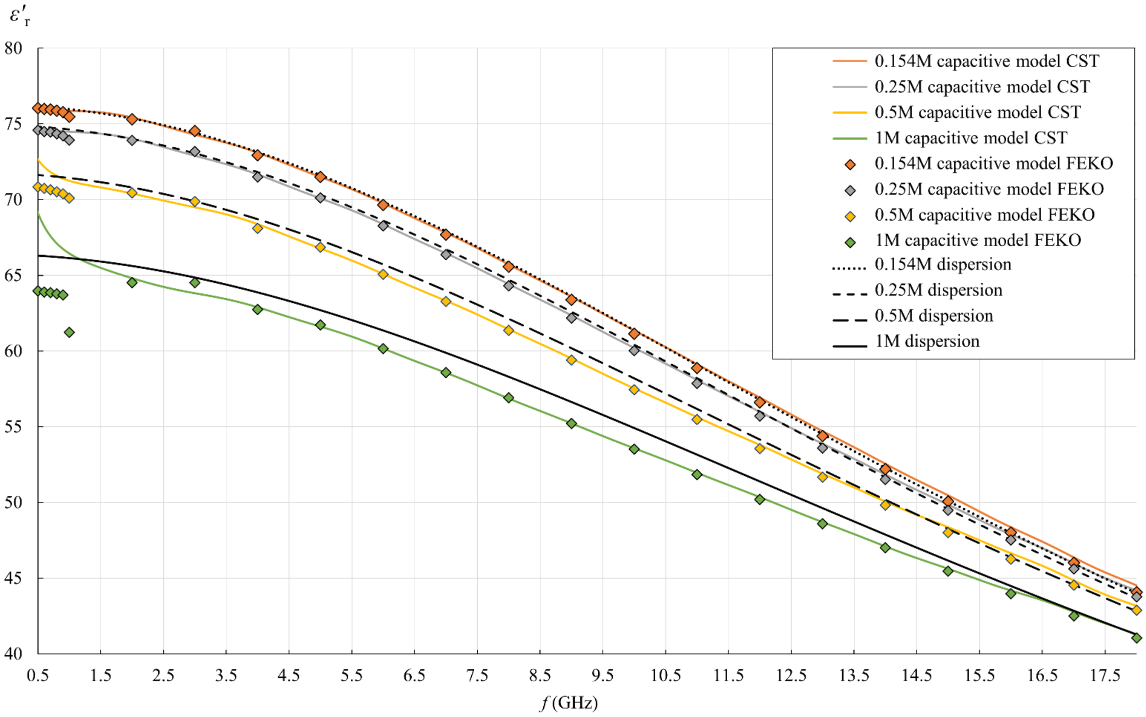

Figure 13. ε'_r for all saline solutions: simulation results obtained by postprocessing the reflection coefficient using the simple capacitive-load model ("capacitive model"), where the reflection coefficient was obtained by simulations either in CST (colored lines) or in FEKO (discrete points); Cole–Cole dispersion model ("dispersion"), which was the set ε'_r value for MUT in simulations (black lines).

Figures 13 and 14 clearly show the similarities and differences between the used simulation packages (CST and FEKO) and the associated methods, which was one of the research aspects of this study. The most obvious observation refers to their performance and output: the time-domain method (in CST) resolved the frequency range in just one simulation and provided a continuous curve. On the other hand, the frequency-domain method (in FEKO) required a large number of simulations to cover the same range, which is time-consuming and produces only the discrete points, thus potentially omitting the phenomena occurring between these frequency points. This makes the frequency-domain methods inferior when it comes to studying the broadband response, like in this study. Moreover, when the frequency span is so wide as in this study, it cannot be covered by a single model mesh in FEKO, i.e., the mesh parameters must be adapted to different frequencies, which is again time-consuming and causes additional errors if the model mesh is not adjusted properly. This might be the reason why FEKO results deviated from a smooth line at low frequencies (observable in Figure 13): it was obvious that discrete points do not form a smooth line below 2 GHz. The model mesh was indeed changed across that range. We did ensure the validity of the simulation results by refining the mesh until the result converged. Nevertheless, the final plot of the results shows discontinuities under 2 GHz. In the same range, $\varepsilon'_{\mathrm{r}}$ by FEKO fell lower than both the dispersion and CST. Perhaps FEKO models could be further refined to provide better agreement. However, this disagreement was quite small, while CST provided slightly better agreement with dispersions at low frequencies and produced a continuous wideband response. Accordingly, there was no rationale for further refinement of FEKO models.

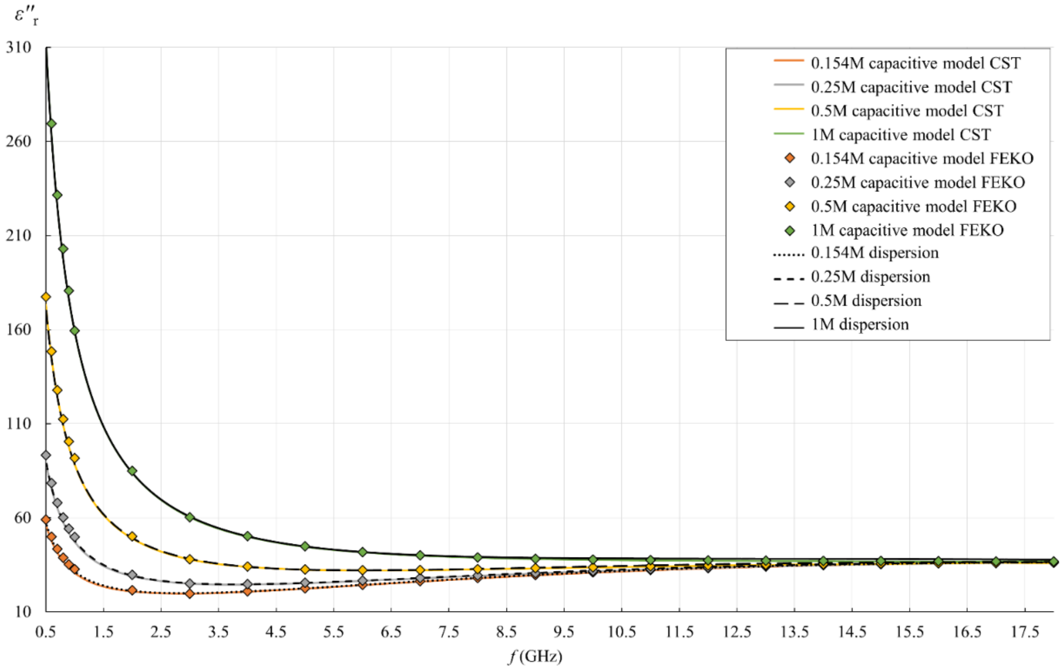

Figure 14. $\varepsilon''_{\mathrm{r}}$ for all saline solutions: simulation result obtained by postprocessing the reflection coefficient using the simple capacitive-load model ("capacitive model"), where the reflection coefficient was obtained by simulations either in CST (colored lines) or in FEKO (discrete points); Cole–Cole dispersion model ("dispersion"), which was the set $\varepsilon''_{\mathrm{r}}$ value for MUT in simulations (black lines).

Figures 15 and 16 show the relative error between the CST simulation, FEKO simulation, and dispersion, defined as:

$$\varepsilon'_{\mathrm{r}}\ \text{relative error}[\%] = \frac{\varepsilon'_{\mathrm{r(capacitive\ model)}} - \varepsilon'_{\mathrm{r(dispersion)}}}{\varepsilon'_{\mathrm{r(dispersion)}}} \cdot 100\%\ , \tag{21}$$

$$\varepsilon''_{\mathrm{r}}\ \text{relative error}[\%] = \frac{\varepsilon''_{\mathrm{r(capacitive\ model)}} - \varepsilon''_{\mathrm{r(dispersion)}}}{\varepsilon''_{\mathrm{r(dispersion)}}} \cdot 100\% = \sigma\ \text{relative error}[\%]\ . \tag{22}$$

The agreement between FEKO, CST, and dispersion depends on both frequency and ionic concentration. As seen in Figure 15, at lower concentrations of 0.154M and 0.25M, FEKO and CST agreed very well on $\varepsilon'_{\mathrm{r}}$, and also with the dispersion within the relative error of <1%. At 0.5M, FEKO and CST followed each other tightly above 2 GHz, while for both, the error magnitude only slightly exceeded 1% throughout most of the frequency range and reached the maximum of ca. 2% for FEKO at 1 GHz. For 1M saline, FEKO and CST followed each other tightly above 4 GHz where the maximum error magnitude reached ca. 2.5%. At lower frequencies, CST error increased to >4% maximum, while FEKO error magnitude reached the maximum of >7% at 1 GHz.

For $\varepsilon''_{\mathrm{r}}$, two frequency ranges can be observed, below and above 3 GHz. Below 3 GHz, FEKO and CST diverged, as FEKO exhibited positive error going up to ca. 3–4% maximum, and CST error was negative with magnitude up to ca. 2–3% maximum. The error below 3 GHz apparently did not strongly depend on the concentration. Above 3 GHz, FEKO and CST converged with each other above within 1% error for all concentrations. However, with respect to the dispersion, the error above 3 GHz for both of them increased with NaCl concentration. At lower concentrations of 0.154M and 0.25M, the error magnitude above 3 GHz stayed within 1% and ca. 1.5%, respectively. At 0.5M, the error magnitude above 3 GHz reached the maximum of slightly over 2%, while for 1M, the maximum was ca. 3.5%.

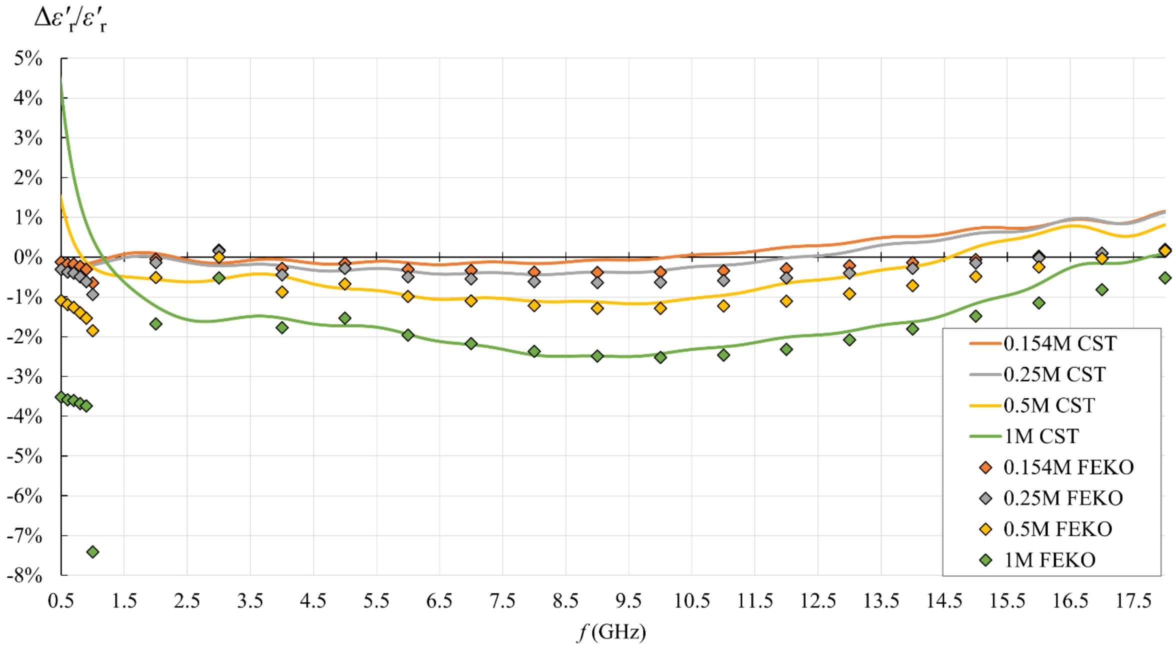

Figure 15. ε'_r relative error of the simple capacitive-load model (FEKO: discrete points; CST: solid lines) with respect to the set ε'_r value.

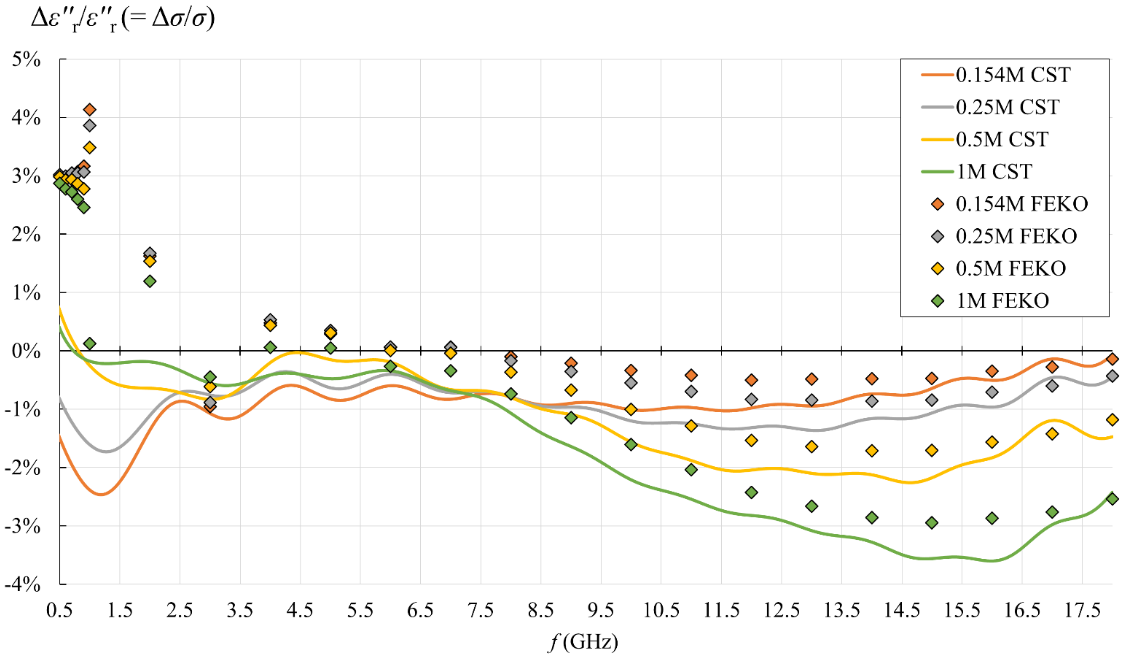

Figure 16. ε''_r relative error of the simple capacitive-load model (FEKO: discrete points; CST: solid lines) with respect to the set ε''_r value.

4. Discussion

4.1. Measurement Results with Respect to the Expected Saline Permittivity

Saline solutions are convenient MUTs to study the effect of ionic concentration on dielectric permittivity. The lowest concentration studied here (0.154M) is the so-called physiological saline [45], thus very relevant for translating the results of this study to biological materials with high water content. Furthermore, permittivity of NaCl solutions in water has been measured and modeled in the literature, e.g., [44,50–53]. However, this study does not perfectly overlap with those studies concerning the exact NaCl concentrations, saline temperature, and frequency range. The most similar parameters are in studies [44,53], bringing the results for the concentrations 0.2M, 0.5M, and 1M up to 20 GHz at 20 °C, and for 0.154M up to 50 GHz at 23 °C, respectively. Lots of similarities and similar trends can be observed. At similar concentrations and temperatures, ε_r', ε_r'', and σ are very similar in magnitude to the values in the literature and exhibit the exact same trends. The whole ε_r' lines in our study were systematically shifted slightly downwards and the whole σ lines slightly upwards with respect to other studies, which might be attributed to the slightly higher temperature in our study. However, our results showed the same trend of systematic deviation also from the models in Table 1 (calculated by (7)–(11)), more so as the ionic concentration increased. We are not aware of the cause of this phenomenon, other than those already mentioned in Section 3.1. However, it is worth noting that the model in (7)–(11) is based on the measurement results in [44], whose results are again slightly different from other studies and might also be slightly different from ours for unknown reasons. Nevertheless, considering that the results slightly vary between the previously published studies and that our results' deviation from the model was very small (less than 2% average error at concentrations lower than 1M), we were not concerned with this, especially since this is not a study on the accurate dielectric properties of saline solutions. Accordingly, we could conclude that our measurement method was validated by fairly accurate results for saline solutions, which was the aim of this comparison.

The next phenomenon to be observed is about the smoothness of ε_r', ε_r'', and σ lines. Unlike ε_r'' and σ lines, ε_r' lines were not smooth in the lower frequency range, and the line fluctuation was more observable at higher NaCl concentrations. This was also noticed and commented in [44,53]. In [44], this was commented as instability of the measurement in the presence of high conductivities at frequencies below a few hundred megahertz, and in [53], this was commented to be a consequence of the increased measurement uncertainty due to electrode polarization effect, which is again correlated with conductivity. The formation of electrical double layer at the electrodes due to ionic polarization is a well-known electrochemical effect [54], also described in the context of dielectric measurements, e.g., [15]. The double layer of electrical charges introduces additional capacitive and resistive components into the load seen by the probe. These depend on many factors: MUT composition, electrode material, shape and roughness, frequency, etc. Not only are they difficult to model but they tend to dominate the load impedance at lower frequencies, reducing the probe sensitivity to MUT and creating instabilities. As such, this is the major limiting factor for dielectric probes' lower frequency limit.

The same phenomenon causes the systematic deviation of ε_r' measurement results at low frequencies: measured ε_r' exhibits underestimation with respect to the expected trend of the line (the beginning of the line drops towards lower frequencies). This could be observed in our study, especially for higher concentrations of 0.5M and 1M (Figures 9 and 10, respectively), and also in [53] for a low concentration of 0.154M.

4.2. Measurement Results with Respect to the Use of Simple Capacitive-Load Model

This topic was the basic motivation for the measurement part of the study. The findings can be summarized in Figures 11 and 12. For the sake of this study, we took the final value obtained from the measurement software as the accurate result, i.e., the reference value for error calculation by Equations (19) and (20). Although this assumption of accuracy might be wrong, or at least has its limitations, there is no apparent reason to doubt that the manufacturer optimized the postprocessing method to their probe. A different approach to this issue would certainly require a separate study in that respect. In any case, if the accuracy of our reference results was jeopardized by the error embedded in the measured reflection coefficient (e.g., due to electrode polarization at low frequencies), the same error would have also been embedded in the result calculated by the capacitive model, as it used the same measured reflection coefficient as the input value. Thus, the errors in the pure measurement process are equal between the models and cancel out when calculating the relative error between the capacitive model and the result obtained from the measurement software.

The capacitive model was rather accurate in the upper frequency range, within ca. 1% relative error for ε_r' starting from ca. 6 GHz and within ca. 1.5% relative error for ε_r'' starting from ca. 4.5 GHz. Therefore, the validity of the capacitive model depends on the acceptable limit for the maximum relative error magnitude in the lower frequency range. Setting this limit to 10%, which corresponds to the declared probe accuracy, made the capacitive model acceptable for all analyzed concentrations up to 1M (the error exceeded 10% only at the lowest frequency for ε_r' for 1M). If better accuracy is required, the limit is imposed by ε_r'' error below 4.5 GHz, reaching almost 7%, and apparently does not depend on the concentration.

From the point of view of biological materials, the interest is focused on the 0.154M saline. Using the simple capacitive-load model for 0.154M saline produced only negligible error, less than 0.5% for ε_r' in the entire frequency range and for ε_r'' in the upper frequency range. The error increased only for ε_r'' in the lower frequency range, below 4.5 GHz, reaching the maximum magnitude of 5.3%.

Table 2 shows the maximum relative error magnitude, average relative error magnitude, and the standard deviation of the relative error magnitude for all concentrations.

Table 2. Measurement study—relative errors.

	Saline Concentration	**0.154M**	**0.25M**	**0.5M**	**1M**
ε_r'	Maximum relative error magnitude	0.5%	1.3%	3.6%	11.3%
	Average relative error magnitude	0.2%	0.3%	0.7%	1.6%
	Standard deviation of the relative error magnitude	0.2%	0.4%	0.9%	2.4%
ε_r''	Maximum relative error magnitude	5.3%	6.6%	6.1%	6.6%
	Average relative error magnitude	0.6%	1.0%	1.0%	1.2%
	Standard deviation of the relative error magnitude	1.0%	1.4%	1.1%	1.1%

Similar analyses of the capacitive model applicability have been published in [27,28]. In [27], 0.5M and 1M saline solutions were measured with an open-ended coaxial probe of similar dimensions (however, fabricated from a semirigid cable), then the result (i.e., the reflection coefficient) was postprocessed with the capacitive model and other load models (antenna model, virtual line model, and rational function). The capacitive model was found to give a much larger error than in our study in a similar frequency range (50 MHz–20.05 GHz). However, study [27] must be taken with some reservation, as the error was calculated against the theoretical permittivity for saline solutions, which was calculated according to Stogryn formulas for saline permittivity [50]. Stogryn model, although heavily cited in the literature, was partly disproved by Peyman et al. in [44], i.e., the model was observed to create significant and systematic error for larger NaCl concentrations. Actually, the Stogryn model is based on extrapolation from a reduced set of results and thus inherently has its limitations, which were spotted by Peyman et al. If the study [27] used the correct theoretical permittivity, the capacitive model error would be smaller. Furthermore, unlike the usual calibration of the probe at its open end and de-embedding the result using a general case of scattering matrix for the probe to include all imperfections (as in our study, see Section 2.8), in [27], the reflection coefficient measurement plane was at the probe connector, and then the reflection coefficient at the open end was calculated assuming a lossless line and using a theoretical expression for capacitances C_f and C_0. This procedure could have caused significant errors, which would then be included in their overall result of the capacitive model. Therefore, their conclusions about the error of the capacitive model should not be taken as accurate. The study [28] measured 0.15M saline from 50 MHz–2.6 GHz with a probe wider than ours but used the same procedure as our study: calibration with three loads at the open end, implicitly solving the scattering matrix of a two-port network representing the transmission line between the VNA and the open end. It showed a much smaller error of the simple capacitive-load model than [27], with the error magnitude comparable to ours at the lower frequencies (the study [28] did not reach the turnover frequency), except that our error for ε_r'' at the lower frequencies was even larger. The trend is also the same: slight overestimation of ε_r' and underestimation of ε_r'' at lower frequencies. Therefore, our results are consistent with the study [28].

4.3. Simulation Results with Respect to the Use of Simple Capacitive-Load Model

In measurements, we compared the capacitive model to the measurement result, which we regarded as accurate reference permittivity, although this assumption might have been wrong. Here, on the other hand, we had the reference permittivity that we set ourselves in the computer model, so it actually is the accurate permittivity. Another difference from measurements is that the reflection coefficient was obtained here by simulation; thus, its accuracy depends on the simulation accuracy. Therefore, all inaccuracies of the simulation, either due to model validity issues or due to numerical errors, are embedded in the reflection coefficient result, yielding an error that propagates in the permittivity calculated by the capacitive model. Accordingly, the error of the capacitive model vs. the reference permittivity includes not only the imperfections of the capacitive model but also the simulation errors. This might be the cause of discrepancy of trends between CST and FEKO at low frequencies: CST producing overestimation of ε_r' and underestimation of ε_r'', and vice versa for FEKO. In any case, here, the phenomena at low frequencies were not due to electrode polarization, as the simulations are not aware of that effect and do not take it into account.

Tables 3 and 4 show the maximum magnitude of the relative error, average relative error magnitude, and the standard deviation of the relative error magnitude for all concentrations, for both solvers. The error magnitudes were very similar, although the comparison should be taken with reservation because FEKO errors refer to the discrete frequency points only; thus, the comparison to CST is not straightforward.

Table 3. CST simulation study—relative errors.

	Saline Concentration	**0.154M**	**0.25M**	**0.5M**	**1M**
ε_r'	Maximum relative error magnitude	1.1%	1.1%	1.4%	4.2%
	Average relative error magnitude	0.3%	0.4%	0.7%	1.6%
	Standard deviation of the relative error magnitude	0.3%	0.3%	0.3%	0.7%
ε_r''	Maximum relative error magnitude	2.5%	1.7%	2.3%	3.6%
	Average relative error magnitude	0.9%	0.9%	1.2%	1.8%
	Standard deviation of the relative error magnitude	0.4%	0.3%	0.7%	1.3%

Table 4. FEKO simulation study—relative errors.

	Saline Concentration	**0.154M**	**0.25M**	**0.5M**	**1M**
ε_r'	Maximum relative error magnitude	0.7%	0.9%	1.8%	7.4%
	Average relative error magnitude	0.2%	0.4%	0.9%	2.4%
	Standard deviation of the relative error magnitude	0.1%	0.2%	0.5%	1.4%
ε_r''	Maximum relative error magnitude	4.1%	3.9%	3.5%	2.9%
	Average relative error magnitude	1.2%	1.3%	1.5%	1.8%
	Standard deviation of the relative error magnitude	1.3%	1.2%	1.0%	1.1%

Since CST simulation (with FIT) was superior for this analysis over FEKO simulation (with MoM) and provided continuous results over the entire frequency range, only CST results are discussed further.

Figures 15 and 16 show that the capacitive model was rather accurate throughout the frequency range, with the error increasing for higher concentrations and at the lowest frequencies. Setting the acceptable limit for the relative error magnitude to 10%, which corresponds to the declared probe accuracy, made the capacitive model valid for all analyzed concentrations in the entire frequency range. From the point of view of biological materials, the interest is focused on the 0.154M saline. Using the simple capacitive-load model for 0.154M produced only negligible error, less than 1% for ε_r' in the entire frequency range and for ε_r'' in the upper frequency range. The error increased only for ε_r'' in the lower frequency range, below 3.5 GHz, but stayed within 2.5% magnitude.

A similar simulation study was published in [30]. The same probe was simulated using CST, up to 5 GHz, with two biological MUTs, liver and fat. The liver and fat permittivities were taken from the literature and set in the simulation model. Liver is a more lossy material with higher permittivity than fat, having ε_r' of ca. 60 and σ of ca. 0.7 S/m at 500 MHz. These values are not very far from the values of the physiological saline and thus are comparable to our study. The magnitude of the average relative error in [30] was quantified at 1.9% for ε_r' and 2.1% for ε_r'' for liver, within the frequency limits of the simulation in [30]. Although the error is higher than in our study, we can regard the studies to be rather consistent.

It is worth noting that the simulation results systematically produced ε_r' lower than the dispersion (Figure 13), shifting the whole ε_r' curve downwards, more so as the ionic concentration increased. Although the dispersion was not a reference for the measurement study, it is interesting to observe the same phenomenon in measurement results (Figures 7–10), both with the capacitive model and with the measured value obtained from the measurement software. This cannot be attributed to the simple capacitive-load postprocessing, as the phenomenon also occurred with the measured value obtained from the measurement software. It also cannot be attributed to any polarization effect, since the simulation does not take polarization into account. We hypothesize that this might be related to the large difference in ε_r'' between the measured conductive MUTs and the calibration liquid (deionized water), but testing this hypothesis exceeds the scope of this study and will be addressed in future work.

5. Conclusions

Our study, consisting of the measurement and the simulation part, showed that the dielectric permittivity measurement method using open-ended coaxial probe in the microwave frequency range can be completely and reliably modeled and simulated using computer electromagnetic modeling and simulations followed by the postprocessing calculations. Furthermore, the study showed that the postprocessing calculations can be performed using the simple capacitive-load model, obtaining very accurate results.

When the simple capacitive-load model was used for postprocessing the measured reflection coefficients, the results were within the typical measurement accuracy of the probe itself. The main deficiency of the model showed up at the lowest part of the probe frequency range, where ionic polarization occurs at the probe electrodes, which is not taken into account by the model. However, the lowest part of the probe frequency range was critical even when using the probe with the manufacturer's measurement software.

When used for postprocessing the electromagnetic simulation results, the simple capacitive-load model yielded only negligible errors, both for the frequency-domain and for the time-domain solvers. We also concluded that the time-domain solver (FIT in CST) was superior for this analysis over the frequency-domain solver (MoM in FEKO) due to providing continuous results over the entire frequency range with excellent accuracy.

Both in measurements and in simulations, the error of the simple capacitive-load model was proportional to the ionic concentration of the MUT. For the physiological saline, the deviation of the capacitive model from the accurate results was negligible. This is an important conclusion, as our primary research interest is in dielectric measurements of biological materials, and the physiological saline approximates the biological materials with high water content.

All the conclusions are applicable in the studied frequency range, covering the lowest and the middle part of the declared probe frequency range. The highest part of the probe frequency range will be analyzed in future studies.

By validating the simulation of the complete measurement process, consisting of computer electromagnetic modeling and simulations followed by the postprocessing calculations using the simple capacitive-load model, in our future work, we will be able to confidently use this simulation method when studying various dielectric measurement scenarios and the associated phenomena. This will be especially useful for studies on biological tissues, where the realizations of the measurement scenarios can be very demanding, that will thus extremely benefit from an accurate simulation method.

Author Contributions: Conceptualization, A.Š.; methodology, A.Š.; formal analysis, A.Š. and A.M.; investigation, A.Š. and A.M.; writing—original draft preparation, A.Š. and A.M.; writing—review and editing, A.Š. and A.M.; supervision, A.Š.; project administration, A.Š. All authors have read and agreed to the published version of the manuscript.

Funding: This research received no external funding.

Institutional Review Board Statement: Not applicable.

Data Availability Statement: Not applicable.

Acknowledgments: This study was performed within the research project "Measurements in Bioelectromagnetics (M-BEM)" supported by FESB, University of Split and within the framework of COST Action MyWAVE CA17115.

Conflicts of Interest: The authors declare no conflict of interest.

References

1. Mehrotra, P.; Chatterjee, B.; Sen, S. EM-Wave Biosensors: A Review of RF, Microwave, Mm-Wave and Optical Sensing. *Sensors* **2019**, *19*, 1013. [CrossRef] [PubMed]
2. Hasgall, P.A.; Di Gennaro, F.; Baumgartner, C.; Neufeld, E.; Lloyd, B.; Gosselin, M.C.; Payne, D.; Klingenböck, A.; Kuster, N. *IT'IS Database for Thermal and Electromagnetic Parameters of Biological Tissues, Version 4.0*; IT'IS Foundation: Zürich, Switzerland, 2018.
3. Gabriel, C.; Gabriel, S.; Corthout, E. The Dielectric Properties of Biological Tissues: I. Literature Survey. *Phys. Med. Biol.* **1996**, *41*, 2231–2249. [CrossRef] [PubMed]
4. Gabriel, S.; Lau, R.W.; Gabriel, C. The Dielectric Properties of Biological Tissues: II. Measurements in the Frequency Range 10 Hz to 20 GHz. *Phys. Med. Biol.* **1996**, *41*, 2251–2269. [CrossRef]
5. Gabriel, S.; Lau, R.W.; Gabriel, C. The Dielectric Properties of Biological Tissues: III. Parametric Models for the Dielectric Spectrum of Tissues. *Phys. Med. Biol.* **1996**, *41*, 2271–2293. [CrossRef]
6. Jones, S.B.; Sheng, W.; Or, D. Dielectric Measurement of Agricultural Grain Moisture—Theory and Applications. *Sensors* **2022**, *22*, 2083. [CrossRef] [PubMed]
7. D'Alvia, L.; Piuzzi, E.; Cataldo, A.; Del Prete, Z. Permittivity-Based Water Content Calibration Measurement in Wood-Based Cultural Heritage: A Preliminary Study. *Sensors* **2022**, *22*, 2148. [CrossRef]
8. Chavanne, X.; Frangi, J.-P. Autonomous Sensors for Measuring Continuously the Moisture and Salinity of a Porous Medium. *Sensors* **2017**, *17*, 1094. [CrossRef]
9. Juan, C.G.; Potelon, B.; Quendo, C.; Bronchalo, E. Microwave Planar Resonant Solutions for Glucose Concentration Sensing: A Systematic Review. *Appl. Sci.* **2021**, *11*, 7018. [CrossRef]
10. Juan, C.G.; Bronchalo, E.; Potelon, B.; Quendo, C.; Sabater-Navarro, J.M. Glucose Concentration Measurement in Human Blood Plasma Solutions with Microwave Sensors. *Sensors* **2019**, *19*, 3779. [CrossRef]
11. Zhekov, S.S.; Franek, O.; Pedersen, G.F. Dielectric Properties of Common Building Materials for Ultrawideband Propagation Studies [Measurements Corner]. *IEEE Antennas Propag. Mag.* **2020**, *62*, 72–81. [CrossRef]
12. Stuchly, M.A.; Stuchly, S.S. Coaxial Line Reflection Methods for Measuring Dielectric Properties of Biological Substances at Radio and Microwave Frequencies—A Review. *IEEE Trans. Instrum. Meas.* **1980**, *29*, 176–183. [CrossRef]
13. Gregory, A.P.; Clarke, R.N. Dielectric Metrology with Coaxial Sensors. *Meas. Sci. Technol.* **2007**, *18*, 1372–1386. [CrossRef]
14. La Gioia, A.; Porter, E.; Merunka, I.; Shahzad, A.; Salahuddin, S.; Jones, M.; O'Halloran, M. Open-Ended Coaxial Probe Technique for Dielectric Measurement of Biological Tissues: Challenges and Common Practices. *Diagnostics* **2018**, *8*, 40. [CrossRef]

15. Bobowski, J.S.; Johnson, T. Permittivity Measurements of Biological Samples by an Open-Ended Coaxial Line. *Prog. Electromagn. Res. B* **2012**, *40*, 159–183. [CrossRef]
16. La Gioia, A.; O'Halloran, M.; Porter, E. Modelling the Sensing Radius of a Coaxial Probe for Dielectric Characterisation of Biological Tissues. *IEEE Access* **2018**, *6*, 46516–46526. [CrossRef]
17. La Gioia, A.; Salahuddin, S.; O'Halloran, M.; Porter, E. Quantification of the Sensing Radius of a Coaxial Probe for Accurate Interpretation of Heterogeneous Tissue Dielectric Data. *IEEE J. Electromagn. RF Microw. Med. Biol.* **2018**, *2*, 145–153. [CrossRef]
18. Brace, C.L.; Etoz, S. An Analysis of Open-Ended Coaxial Probe Sensitivity to Heterogeneous Media. *Sensors* **2020**, *20*, 5372. [CrossRef] [PubMed]
19. Aydinalp, C.; Joof, S.; Dilman, I.; Akduman, I.; Yilmaz, T. Characterization of Open-Ended Coaxial Probe Sensing Depth with Respect to Aperture Size for Dielectric Property Measurement of Heterogeneous Tissues. *Sensors* **2022**, *22*, 760. [CrossRef]
20. Meaney, P.M.; Gregory, A.P.; Epstein, N.R.; Paulsen, K.D. Microwave Open-Ended Coaxial Dielectric Probe: Interpretation of the Sensing Volume Re-Visited. *BMC Med. Phys.* **2014**, *14*, 3. [CrossRef]
21. Meaney, P.M.; Gregory, A.P.; Seppala, J.; Lahtinen, T. Open-Ended Coaxial Dielectric Probe Effective Penetration Depth Determination. *IEEE Trans. Microw. Theory Tech.* **2016**, *64*, 915–923. [CrossRef]
22. Šarolić, A.; Matković, A. Effect of the Coaxial Dielectric Probe Diameter on Its Permittivity Sensing Depth at 2 GHz—Simulation Study. In Proceedings of the 23rd International Conference on Applied Electromagnetics and Communications (ICECOM), Dubrovnik, Croatia, 30 September–2 October 2019; pp. 1–4.
23. Aydinalp, C.; Joof, S.; Yilmaz, T. Towards Non-Invasive Diagnosis of Skin Cancer: Sensing Depth Investigation of Open-Ended Coaxial Probes. *Sensors* **2021**, *21*, 1319. [CrossRef] [PubMed]
24. Maenhout, G.; Markovic, T.; Ocket, I.; Nauwelaers, B. Effect of Open-Ended Coaxial Probe-to-Tissue Contact Pressure on Dielectric Measurements. *Sensors* **2020**, *20*, 2060. [CrossRef] [PubMed]
25. Maenhout, G.; Markovic, T.; Nauwelaers, B. Controlled Measurement Setup for Ultra-Wideband Dielectric Modeling of Muscle Tissue in 20–45 °C Temperature Range. *Sensors* **2021**, *21*, 7644. [CrossRef]
26. Stuchly, M.A.; Brady, M.M.; Stuchly, S.S.; Gajda, G. Equivalent Circuit of an Open-Ended Coaxial Line in a Lossy Dielectric. *IEEE Trans. Instrum. Meas.* **1982**, *IM-31*, 116–119. [CrossRef]
27. Marsland, T.P.; Evans, S. Dielectric Measurements with an Open-Ended Coaxial Probe. *IEE Proc. H Microw. Antennas Propag.* **1987**, *134*, 341–349. [CrossRef]
28. Berube, D.; Ghannouchi, F.M.; Savard, P. A Comparative Study of Four Open-Ended Coaxial Probe Models for Permittivity Measurements of Lossy Dielectric/Biological Materials at Microwave Frequencies. *IEEE Trans. Microw. Theory Techn.* **1996**, *44*, 1928–1934. [CrossRef]
29. Ruvio, G.; Vaselli, M.; Lopresto, V.; Pinto, R.; Farina, L.; Cavagnaro, M. Comparison of Different Methods for Dielectric Properties Measurements in Liquid Sample Media. *Int. J. RF Microw. Comput. Aided Eng.* **2018**, *28*, e21215. [CrossRef]
30. Cavagnaro, M.; Ruvio, G. Numerical Sensitivity Analysis for Dielectric Characterization of Biological Samples by Open-Ended Probe Technique. *Sensors* **2020**, *20*, 3756. [CrossRef]
31. Gioia, A.L.; O'Halloran, M.; Elahi, A.; Porter, E. Investigation of Histology Radius for Dielectric Characterisation of Heterogeneous Materials. *IEEE Trans. Dielect. Electr. Insul.* **2018**, *25*, 1064–1079. [CrossRef]
32. Farshkaran, A.; Porter, E. Improved Sensing Volume Estimates for Coaxial Probes to Measure the Dielectric Properties of Inhomogeneous Tissues. *IEEE J. Electromagn. RF Microw. Med. Biol.* **2022**, *6*, 253–259. [CrossRef]
33. Keysight Technologies. *N1500A Materials Measurement Suite—Technical Overview*; Keysight Technologies: Santa Rosa, CA, USA, 2021.
34. Altair Feko. Available online: https://www.altair.com/feko/ (accessed on 6 May 2022).
35. CST Studio Suite 3D EM Simulation and Analysis Software. Available online: https://www.3ds.com/products-services/simulia/products/cst-studio-suite/ (accessed on 6 May 2022).
36. Keysight Technologies. *Keysight N1501A Dielectric Probe Kit 10 MHz to 50 GHz—Technical Overview*; Keysight Technologies: Santa Rosa, CA, USA, 2018.
37. DAK—Dielectric Assessment Kit Product Line. Available online: https://speag.swiss/products/dak/overview/ (accessed on 6 May 2022).
38. Šarolić, A. Open-Ended Coaxial Dielectric Probe Model for Biological Tissue Sensing Depth Analysis at 2 GHz. In Proceedings of the 2019 European Microwave Conference in Central Europe (EuMCE), Prague, Czech Republic, 13–15 May 2019; pp. 605–608.
39. Pasternack Enterprises. *086 Semi-Rigid Coax Cable with Copper Outer Conductor—Datasheet*; Pasternack Enterprises: Irvine, CA, USA, 2013.
40. Keysight Technologies. *Basics of Measuring the Dielectric Properties of Materials*; Application Note; Keysight Technologies: Santa Rosa, CA, USA, 2020.
41. Blackham, D.V.; Pollard, R.D. An Improved Technique for Permittivity Measurements Using a Coaxial Probe. *IEEE Trans. Instrum. Meas.* **1997**, *46*, 1093–1099. [CrossRef]
42. Debye, P. *Polar Molecules*; The Chemical Catalog Company Inc.: New York, NY, USA, 1929.
43. Cole, K.S.; Cole, R.H. Dispersion and Absorption in Dielectrics I. Alternating Current Characteristics. *J. Chem. Phys.* **1941**, *9*, 341–351. [CrossRef]

44. Peyman, A.; Gabriel, C.; Grant, E.H. Complex Permittivity of Sodium Chloride Solutions at Microwave Frequencies. *Bioelectromagnetics* **2007**, *28*, 264–274. [CrossRef] [PubMed]
45. Awad, S.; Allison, S.P.; Lobo, D.N. The History of 0.9% Saline. *Clin. Nutr.* **2008**, *27*, 179–188. [CrossRef]
46. Kaatze, U. Complex Permittivity of Water as a Function of Frequency and Temperature. *J. Chem. Eng. Data* **1989**, *34*, 371–374. [CrossRef]
47. Wei, Y.; Sridhar, S. Technique for Measuring the Frequency-dependent Complex Dielectric Constants of Liquids up to 20 GHz. *Rev. Sci. Instrum.* **1989**, *60*, 3041–3046. [CrossRef]
48. Bao, J.Z.; Davis, C.C.; Swicord, M.L. Microwave Dielectric Measurements of Erythrocyte Suspensions. *Biophys. J.* **1994**, *66*, 2173–2180. [CrossRef]
49. Bao, J.; Swicord, M.L.; Davis, C.C. Microwave Dielectric Characterization of Binary Mixtures of Water, Methanol, and Ethanol. *J. Chem. Phys.* **1996**, *104*, 4441–4450. [CrossRef]
50. Stogryn, A. Equations for Calculating the Dielectric Constant of Saline Water (Correspondence). *IEEE Trans. Microw. Theory Techn.* **1971**, *19*, 733–736. [CrossRef]
51. Gulich, R.; Köhler, M.; Lunkenheimer, P.; Loidl, A. Dielectric Spectroscopy on Aqueous Electrolytic Solutions. *Radiat. Environ. Biophys.* **2009**, *48*, 107–114. [CrossRef]
52. Gadani, D.H.; Rana, V.A.; Bhatnagar, S.P.; Prajapati, A.N.; Vyas, A.D. Effect of Salinity on the Dielectric Properties of Water. *Indian J. Pure Appl. Phys.* **2012**, *50*, 405–410.
53. Bakam Nguenouho, O.S.; Chevalier, A.; Potelon, B.; Benedicto, J.; Quendo, C. Dielectric Characterization and Modelling of Aqueous Solutions Involving Sodium Chloride and Sucrose and Application to the Design of a Bi-Parameter RF-Sensor. *Sci. Rep.* **2022**, *12*, 7209. [CrossRef] [PubMed]
54. Lvovich, V.F. *Impedance Spectroscopy: Application to Electrochemical and Dielectric Phenomena*; John Wiley & Sons Inc.: Hoboken, NJ, USA, 2012; ISBN 978-1-118-16407-5.

Curriculum Vitae

Anđela Matković was born in Split, Croatia, in 1995. After graduating from Grammar School for Natural Sciences and Mathematics in Split, Croatia, she enrolled for a bachelor's degree at the Faculty of Electrical Engineering, Mechanical Engineering and Naval Architecture in Split. Anđela received her BSc in Electrical Engineering and Information Technology in 2016 and MSc in Electronics and Computer Engineering in 2018, both from University of Split. She applied for a Ph.D. in Electrical Engineering in 2018 and has been working towards it to date. As a part of her doctoral studies, she has enrolled in several external courses from the TRIBE Ph.D. program at the School of Medicine. Her studies are integrated with her current employment as a teaching assistant at the University of Split.

Her research area is within the scope of electromagnetics with the focus on the dielectric permittivity measurements and electromagnetic modeling and simulation. She has authored and co-authored three journal papers and seven conference papers in various fields of electromagnetics.

Anđela is involved in the research field of bioelectromagnetics through *Measurements in bioelectromagnetics* (M-BEM) project. She was a management committee substitute in COST Action CA17115: *European network for advancing electromagnetic hyperthermic medical technologies* (MyWAVE) from 2018 to 2023. During her doctoral studies, Anđela has participated in the International School of Bioelectromagnetism *Alessandro Chiabrera* held in 2019 in Italy. She is a member of IEEE and its several societies: *Antennas and Propagation Society*, *Electromagnetic Compatibility Society*, *Engineering in Medicine and Biology Society* and *Microwave Theory and Techniques Society* as well as a member of *BioEM society* and *Croatian Biomedical Engineering and Medical Physics Society.*

Životopis

Anđela Matković rođena je 1995. godine u Splitu, Hrvatska. Nakon završavanja Prirodoslovno-matematičke gimnazije u Splitu, upisala je preddiplomski studij na Fakultetu elektrotehnike, strojarstva i brodogradnje na Sveučilištu u Splitu. Anđela je 2016. godine postala prvostupnica elektrotehnike i informacijske tehnologije, a 2018. godine magistrica elektronike i računalnog inženjerstva. Iste godine upisala je poslijediplomski studij iz elektrotehnike i informacijske tehnologije. U sklopu doktorskog studija upisala je nekoliko vanjskih kolegija TRIBE poslijediplomskog studija na Medicinskom fakultetu. Poslijediplomski studij joj je integriran s trenutnim radnim mjestom asistentice na Sveučilištu u Splitu.

Njezino područje istraživanja je u domeni elektromagnetizma s naglaskom na mjerenje dielektrične permitivnosti i elektromagnetsko modeliranje i simulacije. Autorica je i koautorica tri rada u časopisima i sedam konferencijskih radova iz različitih područja elektromagnetizma.

Anđela je uključena u istraživanja iz područja bioelektromagnetizma kroz projekt *Measurements in bioelectromagnetics* (M-BEM). Bila je zamjenski član u upravnom odboru COST akcije CA17115: *European network for advancing electromagnetic hyperthermic medical technologies* (MyWAVE) od 2018. do 2023. godine. Tijekom doktorskog studija Anđela je sudjelovala u Međunarodnoj školi bioelektromagnetizma *Alessandro Chiabrera* koja je održana 2019. godine u Italiji. Članica je IEEE-a i njegovih nekoliko društava: *Antennas and Propagation Society*, *Electromagnetic Compatibility Society*, *Engineering in Medicine and Biology Society* i *Microwave Theory and Techniques Society* kao i članica *BioEM* društva i Hrvatskog društva za biomedicinsko inženjerstvo i medicinsku fiziku.